EXPERIMENTAL AND DENSITY FUNCTIONAL THEORY INVESTIGATIONS ON THE STRUCTURAL AND ELECTRONIC PROPERTIES OF ACYCLOVIR AND THEOPHYLLINE HYDRATE MOLECULES

WANG SUH MIIN

MASTER OF ENGINEERING SCIENCE

FACULTY OF ENGINEERING AND GREEN TECHNOLOGY
UNIVERSITI TUNKU ABDUL RAHMAN
SEPTEMBER 2021

EXPERIMENTAL AND DENSITY FUNCTIONAL THEORY INVESTIGATIONS ON THE STRUCTURAL AND ELECTRONIC PROPERTIES OF ACYCLOVIR AND THEOPHYLLINE HYDRATE MOLECULES

By

WANG SUH MIIN

A dissertation submitted to the Department of Electronic Engineering,
Faculty of Engineering and Green Technology,
Universiti Tunku Abdul Rahman,
in partial fulfillment of the requirements for the degree of
Master of Engineering Science
September 2021

ABSTRACT

EXPERIMENTAL AND DENSITY FUNCTIONAL THEORY INVESTIGATIONS ON THE STRUCTURAL AND ELECTRONIC PROPERTIES OF ACYCLOVIR AND THEOPHYLLINE HYDRATE MOLECULES

Wang Suh Miin

Acyclovir (ACV) and theophylline (TP) drug compounds have gain high attentions in the study of polymorphism to improve their therapeutic performances, since both of them are the potent treatment solutions for global burden diseases of Herpes Simplex Virus (HZV), Varicella Zoster Virus (VZV), asthma, and chronic obstructive pulmonary disease (COPD). Surveys show that there is limited information about the Density Functional Theory (DFT) computational works on both compounds. So that, the work undertaken in this research study concerns the geometry structures and electronic properties investigations on the hydrated polymorphic forms of ACV (i.e. hydrated ACV-I, ACV-II, and ACV-III) and TP (i.e. anhydrous TP-I and monohydrated TP-II) active pharmaceutical ingredients (APIs) drug compounds. First, the polymorphism behaviors of ACV and TP compounds were observed from the crystal formation of ACV-I, TP-I, and TP-II via crystallization technique. The details of the crystal molecular structures were characterized through the single crystal X-ray diffraction experiment and acted as the main input sources for Density Functional Theory (DFT) computational calculations. Besides, Fourier transform infrared (FT-IR) and Ultraviolet-visible (UV-Vis) spectroscopy

techniques were conducted and used as the guiding references for DFT computational data. In this project, DFT/B3LYP/6-31G** and DFT/B3LYP/6-311G** level of calculations were chosen for ACV-I, ACV-II, and ACV-III molecular system, whereas DFT/B3LYP/6-31G and DFT/B3LYP/6-31G** level of theories were implemented for TP-I and TP-II molecular system. Geometry optimization calculations were performed to obtain the equilibrium structures of ACV-I, ACV-II, ACV-III, TP-I, and TP-II molecular system. Besides, single point calculations were carried out to determine the electronic properties (i.e. total energies, highest occupied molecular orbital-lowest unoccupied molecular orbital (HOMO-LUMO) energies, molecular electrostatic potential (MEP), natural bond orbital (NBO), and non-liner optical (NLO)) and FT-IR vibrational spectral of ACV-I, ACV-II, ACV-III, TP-I, and TP-II molecular system. From the computational data, ACV-I molecular system with computed total energies of -70358.746 eV (6-31G**) and -70376.691 eV (6-311G**), was dominated to be the most stable molecular structure among ACV-II and ACV-III molecular system. For TP-II molecular system, with total energies of -19517.293 eV (6-31G) and -19524.267 eV (6-31G**), it was found to be more stable than the TP-I molecular system. Besides, the computed HOMO-LUMO energy gaps of ACV-I and ACV-II using DFT/B3LYP/6-31G** and DFT/B3LYP/6-311G** methods were situated in the ranges of 4.889 eV to 5.012 eV, while for ACV-III molecular system were calculated to have ranges of 4.049 eV to 4.545 eV. Both of the computed HOMO-LUMO energy gaps of TP-I and TP-II using DFT/B3LYP/6-31G and DFT/B3LYP/6-31G** methods elucidated closer results within each other (i.e. 5.002 eV to 5.147 eV). For the NLO properties analysis, ACV-II molecular system with dipole moments of

14.822/14.600 Debye (6-31G**/6-311G**) and first hyperpolarizability of 6.690 x 10^{-29}/ 6.837 x 10^{-29} e.s.u (6-31G**/6-311G**), showed better NLO characteristic than ACV-I and ACV-III molecular system. For TP-I molecular system, the calculated dipole moments and first hyperpolarizability were reported to be 3.642/3.481 Debye (6-31G/6-31G**) and 7.598 x 10^{-30}/7.378 x 10^{-30} e.s.u (6-31G/6-31G**), whereas for TP-II molecular system were 2.562/2.332 Debye (6-31G/6-31G**) and 10.750 x 10^{-30}/10.130 x 10^{-30} e.s.u (6-31G/6-31G**). All the findings of the calculated FT-IR vibrational frequencies of ACV-I, ACV-II, ACV-III, TP-I, and TP-II molecular system met good agreement with the experimental and literature data. In additions, size effect studies were conducted on TP-I and TP-II molecular system. An increase in the molecular system size of TP has shown an impact on the accuracy of the computational data. Furthermore, rotational barrier studies were carried out on ACV-I, ACV-II, and ACV-III molecular system through the Potential Energy Surface (PES) scanning method to figure out the possible conformations of ACV molecules. The computed data elucidated that the extension of the bond distance C-O in the ACV molecule will result in unstable conformers. Noted that all the DFT computational findings in both ACV and TP polymorphic forms found satisfactory agreement with experimental data. In particular, the DFT results obtained in this work can be served as a complement for real system work and act as guideline resources for researchers in the future.

PUBLICATION

No	Title
1	Wang, S.M. and Toh, P.L., 2018. Geometry Structures and Electronic Properties on 2, 2-Dimenthyl-N-(phenylsulfonyl) acetamide using Density Functional Theory. *i-Manager's Journal on Material Science*, *6*(2), p.1.
2	Wang, S.M., Chng, L.M., Meepripruk, M. and Toh, P.L., 2019, September. Vibrational frequencies and electronic structures of 2-amino-1, 9-dihydro-9-[(2-hydroxuethoxy) methyl]-6H-purin-6-one using density functional theory method. In: *AIP Conference Proceedings*. AIP Publishing LLC, Vol. 2157, No. 1, p. 020010.
3	Wang, S.M., Chng, L.M. and Toh, P.L., 2020. FT-IR and Electronic Properties Investigations on Theophylline Molecular System: Density Functional Theory Calculation. *i-Manager's Journal on Material Science*, *8*(2), p.1.

ACKNOWLEDGEMENTS

I would like to thank everyone who had contributed to the successful completion of this project. I would like to express my gratitude to my research supervisor, Dr. Toh Pek Lan and co-supervisor, Dr Chng Lee Muei for their invaluable advice, guidance and their enormous patience throughout the development of the research. Besides my supervisors, I would like to extend my sincere thanks to Dr. Montha Meepripruk and also laboratory staffs.

In addition, I would also like to express my gratitude to my loving parent and friends who had helped and given me encouragement.

This work was supported in part by UTAR research fund (project: IPSR/RMC/UTARRF/2017-C2/T09).

APPROVAL SHEET

This dissertation entitled "**EXPERIMENTAL AND DENSITY FUNCTIONAL THEORY INVESTIGATIONS ON THE STRCUTURAL AND ELECTRONIC PROPERTIES OF ACYCLOVIR AND THEOPHYLLINE HYDRATE MOLECULES "** was prepared by WANG SUH MIIN and submitted as partial fulfillment of the requirements for the degree of Master of Engineering Science at Universiti Tunku Abdul Rahman.

Approved by:

(Dr. Ton Pek Lan)
Date: 30/9/2021
Supervisor
Department of Electronic Engineering
Faculty of Engineering and Green Technology
Universiti Tunku Abdul Rahman

(Dr. Chng Lee Muei)
Date: 1/10/21
Co-supervisor
Department of Chemical Engineering
Faculty of Engineering and Green Technology
Universiti Tunku Abdul Rahman

SUBMISSION SHEET

FACULTY OF ENGINEERING AND GREEN TECHNOLOGY

UNIVERSITI TUNKU ABDUL RAHMAN

Date: 30 September 2021

SUBMISSION OF DISSERTATION

It is hereby certified that **WANG SUH MIIN** (ID No: **18AGM00973**) has completed this dissertation entitled "**EXPERIMENTAL AND DENSITY FUNCTIONAL THEORY INVESTIGATIONS ON THE STRUCTURAL AND ELECTRONIC PROPERTIES OF ACYCLOVIR AND THEOPHYLLINE HYDRATE MOLECULES**" under the supervision of Dr Toh Pek Lan (Supervisor) from the Department of Electronic Engineering, Faculty of Engineering and Green Technology, and Dr Chng Lee Muei (Co-Supervisor)* from the Department of Chemical Engineering, Faculty of Engineering and Green Technology.

I understand that University will upload softcopy of my final dissertation in pdf format into UTAR Institutional Repository, which may be made accessible to UTAR community and public.

Yours truly,

_____

(*Wang Suh Miin*)

DECLARATION

I, WANG SUH MIIN, hereby declare that the dissertation is based on my original work except for quotations and citations which have been duly acknowledged. I also declare that it has not been previously or concurrently submitted for any other degree at UTAR or other institutions.

Name: Wang Suh Miin

Date: 30 September 2021

LIST OF TABLES

Table		Page
1.1	Polymorphic forms of ACV and TP drug compounds involved in the DFT computational calculations.	8
2.1	Polymorphic forms of ACV.	51
2.2	Polymorphic forms of TP.	54
3.1 (a)	Crystal data, data collection, and refinement of ACV-I.	74
3.1 (b)	Crystal data, data collection, and refinement of TP-I.	75
3.1 (c)	Crystal data, data collection, and refinement of TP-II.	76
3.1 (d)	Crystal data, data collection, and refinement of TP-III.	77
3.2	The MEP surface mapped plots isosurface display values of ACV-I, ACV-II, ACV-III, TP-I, TP-II, and TP-III molecular system.	89
4.1	Geometry parameters of intermolecular hydrogen bonds in ACV-I molecular system.	102
4.2 (a)	Experimental and optimized geometry parameters of ACV Molecule A in ACV-I molecular system.	104
4.2 (b)	Experimental and optimized geometry parameters of ACV Molecule B in ACV-I molecular system.	105
4.2 (c)	Experimental and optimized geometry parameters of ACV Molecule C in ACV-I molecular system.	106
4.3	Total energies, HOMO energies, LUMO energies, and HOMO-LUMO energy gaps of ACV-I molecular system.	110
4.4	Computed Mulliken atomic charges analysis (MPA) of ACV-I molecular system using DFT/B3LYP/6-31G** and DFT/B3LYP/6-311G** methods.	114
4.5	Computed dipole moment (μ) and first hyperpolarizability (βtot) of ACV-I molecular system using DFT/B3LYP/6-31G** and DFT/B3LYP/6-311G** methods.	122
4.6	Experimental and computational (unscaled and scaled) FT-IR vibrational frequencies of ACV-I molecular system.	126
4.7 (a)	Parts of the rotational barrier studies in ACV-I Molecule A using DFT/B3LYP/6-31G** and DFT/B3LYP/6-311G** methods.	135
4.7 (b)	Parts of the rotational barrier studies in ACV-I	136

	Molecule B using DFT/B3LYP/6-31G** and DFT/B3LYP/6-311G** methods.	
4.7 (c)	Parts of the rotational barrier studies in ACV-I Molecule C using DFT/B3LYP/6-31G** and DFT/B3LYP/6-311G** methods.	137
4.8 (a)	Experimental and optimized geometry parameters of ACV Molecule A in ACV-II molecular system.	145
4.8 (b)	Experimental and optimized geometry parameters of ACV Molecule B in ACV-II molecular system.	146
4.8 (c)	Experimental and optimized geometry parameters of ACV Molecule C in ACV-II molecular system.	147
4.9	Total energies, HOMO energies, LUMO energies, and HOMO-LUMO energy gaps of ACV-II molecular system.	149
4.10	Computed Mulliken atomic charges analysis (MPA) of ACV-II molecular system using DFT/B3LYP/6-31G** and DFT/B3LYP/6-311G** method.	152
4.11	Computed dipole moment (μ) and first hyperpolarizability (βtot) of ACV-II molecular system using DFT/B3LYP/6-31G** and DFT/B3LYP/6-311G** methods.	159
4.12	Computational (unscaled and scaled) FT-IR vibrational frequencies of ACV-II molecular system.	162
4.13 (a)	Parts of the rotational barrier studies in ACV-II Molecule A using DFT/B3LYP/6-31G** and DFT/B3LYP/6-311G** methods.	168
4.13 (b)	Parts of the rotational barrier studies in ACV-II Molecule B using DFT/B3LYP/6-31G** and DFT/B3LYP/6-311G** methods.	169
4.13 (c)	Parts of the rotational barrier studies in ACV-II Molecule C using DFT/B3LYP/6-31G** and DFT/B3LYP/6-311G** methods.	170
4.14 (a)	Experimental and optimized geometry parameters of ACV Molecule A in ACV-III molecular system.	177
4.14 (b)	Experimental and optimized geometry parameters of ACV Molecule B in ACV-III molecular system.	178
4.15	Total energies, HOMO energies, LUMO energies, and HOMO-LUMO energy gaps of ACV-III molecular system.	181
4.16	Computed Mulliken atomic charges analysis (MPA) of ACV-III molecular system using DFT/B3LYP/6-31G** and DFT/B3LYP/6-311G** methods.	185
4.17	Computed dipole moment (μ) and first	191

	hyperpolarizability (βtot) of ACV-III molecular system using DFT/B3LYP/6-31G** and DFT/B3LYP/6-311G** methods.	
4.18	Experimental and computational (unscaled and scaled) FT-IR vibrational frequencies of ACV-III molecular system.	194
4.19 (a)	Parts of the rotational barrier studies in ACV-III Molecule A using DFT/B3LYP/6-31G** and DFT/B3LYP/6-311G** methods.	199
4.19 (b)	Parts of the rotational barrier studies in ACV-III Molecule B using DFT/B3LYP/6-31G** and DFT/B3LYP/6-311G** methods.	200
4.20 (a)	Comparison between the experimental (single crystal X-ray diffraction) geometry parameters of TP-I with Ebisuzaki *et al.* (1997) molecular system.	204
4.20 (b)	Comparison between the computed electronic properties of TP-I with Ebisuzaki *et al.* (1997) molecular system using DFT/B3LYP/6-31G and DFT/B3LYP/6-31G** method.	205
4.21	The experimental and optimized geometry parameters for TP-I molecular system.	209
4.22	Total energies, HOMO energies, LUMO energies and HOMO-LUMO energy gaps, and global descriptors of TP-I molecular system.	213
4.23	Computed Mulliken atomic charges analysis (MPA) of TP-I molecular system using DFT/B3LYP/6-31G and DFT/B3LYP/6-31G** method.	216
4.24 (a)	Donor-acceptor interactions and second-order perturbation energies of TP-I molecular system using DFT/B3LYP/6-31G method.	223
4.24 (b)	Donor-acceptor interactions and second-order perturbation energies of TP-I molecular system using DFT/B3LYP/6-31G** method.	224
4.25	Computed dipole moment (μ) and first hyperpolarizability (βtot) of TP-I molecular system using DFT/B3LYP/6-31G and DFT/B3LYP/6-31G** methods.	227
4.26	Experimental and computational (unscaled and scaled) FT-IR vibrational frequencies of TP-I molecular system.	230
4.27 (a)	Optimized geometry structures of TP-I, 3[TP-I] and 5[TP-I] molecular system based on size effect study using DFT/B3LYP/6-31G method.	235

4.27 (b)	Optimized geometry structures of TP-I, 3[TP-I] and 5[TP-I] molecular system based on size effect study using DFT/B3LYP/6-31G** method.	236
4.27 (c)	Computed electronic properties of TP-I, 3[TP-I] and 5[TP-I] molecular system based on size effect study using DFT/B3LYP/6-31G level of theory.	241
4.27 (d)	Computed electronic properties of TP-I, 3[TP-I] and 5[TP-I] molecular system based on size effect study using DFT/B3LYP/6-31G** level of theory.	241
4.28 (a)	Lattice parameters of TP-II and TP-III molecular system.	244
4.28 (b)	Comparison between the experimental (single crystal X-ray diffraction) geometry parameters of TP-II with TP-III molecular system.	245
4.29	The experimental and optimized geometry parameters of TP-II molecular system.	249
4.30	Total energies, HOMO energies, LUMO energies, HOMO-LUMO energy gaps, and global descriptors of TP-II molecular system.	252
4.31	Computed Mulliken atomic charges analysis (MPA) of TP-II molecular system using DFT/B3LYP/6-31G and DFT/B3LYP/6-31G** method.	255
4.32 (a)	Donor-acceptor interactions and second order perturbation energies of TP-II molecular system using DFT/B3LYP/6-31G method.	262
4.32 (b)	Donor-acceptor interactions and second order perturbation energies of TP-II molecular system using DFT/B3LYP/6-31G** method.	263
4.33	Computed dipole moment (μ) and first hyperpolarizability (βtot) of TP-II molecular system using DFT/B3LYP/6-31G and DFT/B3LYP/6-31G** methods.	265
4.34	Experimental and computational (unscaled and scaled) FT-IR vibrational frequencies of TP-II molecular system.	267
4.35 (a)	Optimized geometry structures of TP-II, 3[TP-II], 5[TP-II], 7[TP-II], and 9[TP-II] molecular system based on size effect study using DFT/B3LYP/6-31G method.	273
4.35 (b)	Optimized geometry structures of TP-II, 3[TP-II], 5[TP-II], 7[TP-II], and 9[TP-II] molecular system based on size effect study using DFT/B3LYP/6-31G** method.	274

4.35 (c)	Computed electronic properties of TP-II, 3[TP-II], 5[TP-II], 7[TP-II], and 9[TP-II] molecular system based on size effect study using DFT/B3LYP/6-31G level of theory.	279
4.35 (d)	Computed electronic properties of TP-II, 3[TP-II], 5[TP-II], 7[TP-II], and 9[TP-II] molecular system based on size effect study using DFT/B3LYP/6-31G** level of theory.	279
4.36	The computed electronic properties (i.e. total energies, frontier molecular energies, dipole moment, and first hyperpolarizabilities) of ACV-I, ACV-II, and ACV-III molecular system.	284
4.37	The computed electronic properties (i.e. total energies, frontier molecular energies, dipole moment, and first hyperpolarizabilities) of TP-I and TP-II molecular system.	288

LIST OF FIGURES

Figures		Page
2.1 (a)	The single crystal X-ray diffractometer.	37
2.1 (b)	The single crystal X-ray diffraction pattern.	37
2.2	The instruments in FT-IR.	41
2.3	The instruments in UV-Vis spectroscopy.	45
2.4 (a)	Cartesian coordinate of a water molecule.	58
2.4 (b)	Internal coordinate of a water molecule.	58
2.5	The model of Potential Energy Surface (PES).	60
3.1	Research flow chart.	69
3.2 (a)	The heating process of the ACV mixture in Part A (deep blue solution) and Part B (light blue solution).	71
3.2 (b)	Filtration process of the ACV mixture.	71
3.2 (c)	Pure ACV powder obtained from the end of Part A.	71
3.2 (d)	The crystal sample of ACV-I obtained from the end of Part B.	71
3.3 (a)	The crystal sample of TP-I. (1.07 g of TP with 40 ml of H_2O)	72
3.3 (b)	The crystal sample of TP-II. (0.1 M of TP)	72
3.3 (c)	The crystal sample of TP-III. (TP + ACV in the ratio of 2:1 with 0.1 M acetic acid)	72
3.4	Bruker APEX-II CCD diffractometer.	73
3.5 (a)	Mixture of solid crystal with KBr powder in the ratio of 1:10.	79
3.5 (b)	A thin film compressed by the hydraulic compressor.	79
3.5 (c)	The FT-IR spectrometer.	79
3.6 (a)	10 mg of crystal samples mixed with 100 ml of deionised water.	80
3.6 (b)	Sample solutions were socked in the Ultrasonic water bath.	80
3.6 (c)	The 1 cm thick glass cuvette.	80
3.6 (d)	The DR 6000 UV-Vis spectrophotometer.	80
3.7 (a)	The unit cell of ACV-I.	83
3.7 (b)	The unit of ACV-II.	83
3.7 (c)	The unit of ACV-III.	83
3.7 (d)	The unit of TP-I.	83
3.7 (e)	The unit of TP-II.	83
3.7 (f)	The unit of TP-III.	83
3.8 (a)	The single molecular structure of ACV-I.	85
3.8 (b)	The single molecular structure of ACV-II.	85

3.8 (c)	The single molecular structure of ACV-III.	85
3.8 (d)	The single molecular structure of TP-I.	85
3.8 (e)	The single molecular structure of TP-II.	85
3.8 (f)	The single molecular structure of TP-III.	85
3.9	The HOMO surface mapped plot sample of TP-III molecular system.	87
3.10	The MEP surface mapped plot sample of ACV-III molecular system.	89
3.11	Single molecular of ACV with side chain rotation 0° to 360° .	90
3.12 (a)	The molecular size effect study on TP-I with three TP molecules.	91
3.12 (b)	The molecular size effect study on TP-I with five TP molecules.	91
3.12 (c)	The molecular size effect study on TP-II with three TP monohydrate molecules.	92
3.12 (d)	The molecular size effect study on TP-II with five TP monohydrate molecules.	92
3.12 (e)	The molecular size effect study on TP-II with seven TP monohydrate molecules.	92
3.12 (f)	The molecular size effect study on TP-II with nine TP monohydrate molecules.	92
4.1 (a)	The complete unit cell of ACV-I.	95
4.1 (b)	Labelling and numbering details in ACV-I single molecular system.	96
4.2 (a)	Parts of the geometry parameters (i.e. bond distances, bond angles, and dihedral angles) of ACV-I Molecule A.	100
4.2 (b)	Parts of the geometry parameters (i.e. bond distances, bond angles, and dihedral angles) of ACV-I Molecule B.	100
4.2 (c)	Parts of the geometry parameters (i.e. bond distances, bond angles, and dihedral angles) of ACV-I Molecule C.	101
4.2 (d)	The hydrogen bond interactions in ACV-I molecular system.	101
4.3 (a)	LUMO and HOMO surface mapped plots of ACV-I molecular system using DFT/B3LYP/6-31G** method.	111
4.3 (b)	LUMO and HOMO surface mapped plots of ACV-I molecular system using DFT/B3LYP/6-311G** method.	111
4.4	MPA analysis of ACV-I molecular system using	116

	DFT/B3LYP/6-31G** and DFT/B3LYP/6-311G** methods.	
4.5 (a)	The MEP surface mapped plots of ACV-I molecular system using DFT/B3LYP/6-31G** method.	119
4.5 (b)	The MEP surface mapped plots of ACV-I molecular system using DFT/B3LYP/6-311G** method.	119
4.6	Experimental FT-IR vibrational spectrum of ACV-I molecular system.	127
4.7 (a)	Potential Energy Surface of ACV-I Molecule A using DFT/B3LYP/6-31G** and DFT/B3LYP/6-311G** methods.	132
4.7 (b)	Potential Energy Surface of ACV-I Molecule B using DFT/B3LYP/6-31G** and DFT/B3LYP/6-311G** methods.	133
4.7 (c)	Potential Energy Surface of ACV-I Molecule C using DFT/B3LYP/6-31G** and DFT/B3LYP/6-311G** methods.	134
4.8 (a)	The complete unit cell of ACV-II.	139
4.8 (b)	Labelling and numbering details in ACV-II single molecular system.	139
4.9 (a)	Parts of the geometry parameters (i.e. bond distances, bond angles, and dihedral angles) of ACV-II Molecule A.	142
4.9 (b)	Parts of the geometry parameters (i.e. bond distances, bond angles, and dihedral angles) of ACV-II Molecule B.	142
4.9 (c)	Parts of the geometry parameters (i.e. bond distances, bond angles, and dihedral angles) of ACV-II Molecule C.	143
4.10 (a)	LUMO and HOMO surface mapped plots of ACV-II molecular system using DFT/B3LYP/6-31G** method.	150
4.10 (b)	LUMO and HOMO surface mapped plots of ACV-II molecular system using DFT/B3LYP/6-311G** method.	150
4.11	MPA analysis of ACV-II molecular system using DFT/B3LYP/6-31G** and DFT/B3LYP/6-311G** methods.	154
4.12 (a)	The MEP surface mapped plots of ACV-II molecular system using DFT/B3LYP/6-31G** method.	157
4.12 (b)	The MEP surface mapped plots of ACV-II molecular system using DFT/B3LYP/6-311G**	157

method.
4.13 (a) Potential Energy Surface of ACV-II Molecule A using DFT/B3LYP/6-31G** and DFT/B3LYP/6-311G** methods. 165
4.13 (b) Potential Energy Surface of ACV-II Molecule B using DFT/B3LYP/6-31G** and DFT/B3LYP/6-311G** methods. 166
4.13 (c) Potential Energy Surface of ACV-II Molecule C using DFT/B3LYP/6-31G** and DFT/B3LYP/6-311G** methods. 167
4.14 (a) The complete unit cell of ACV-III. 172
4.14 (b) Labelling and numbering details in ACV-III single molecular system. 172
4.15 (a) Parts of the geometry parameters (i.e. bond distances, bond angles, and dihedral angles) of ACV-III Molecule A. 174
4.15 (b) Parts of the geometry parameters (i.e. bond distances, bond angles, and dihedral angles) of ACV-III Molecule B. 175
4.16 (a) LUMO and HOMO surface mapped plots of ACV-III molecular system using DFT/B3LYP/6-31G** method. 182
4.16 (b) LUMO and HOMO surface mapped plots of ACV-III molecular system using DFT/B3LYP/6-311G** method. 182
4.17 MPA analysis of ACV-III molecular system using DFT/B3LYP/6-31G** and DFT/B3LYP/6-311G** methods. 186
4.18 (a) The MEP surface mapped plots of ACV-III molecular system using DFT/B3LYP/6-31G** method. 189
4.18 (b) The MEP surface mapped plots of ACV-III molecular system using DFT/B3LYP/6-311G** method. 189
4.19 (a) Potential Energy Surface of ACV-III Molecule A using DFT/B3LYP/6-31G** and DFT/B3LYP/6-311G** methods. 197
4.19 (b) Potential Energy Surface of ACV-III Molecule B using DFT/B3LYP/6-31G** and DFT/B3LYP/6-311G** methods. 198
4.20 (a) The complete unit cell and single molecule for TP-I. 203
4.20 (b) Labelling and numbering details in TP-I single 203

molecule.
4.21 Parts of the geometry parameters (i.e. bond distances, bond angles, and dihedral angles) of TP-I molecular system. 207
4.22 (a) LUMO and HOMO surface mapped plots of TP-I molecular system using DFT/B3LYP/6-31G method. 214
4.22 (b) LUMO and HOMO surface mapped plots of TP-I molecular system using DFT/B3LYP/6-31G** method. 214
4.23 MPA analysis of TP-I molecular system using DFT/B3LYP/6-31G and DFT/B3LYP/6-31G** methods. 217
4.24 (a) MEP surface mapped plots of TP-I molecular system using DFT/B3LYP/6-31G method. 220
4.24 (b) MEP surface mapped plots of TP-I molecular system using DFT/B3LYP/6-31G** method. 220
4.25 Experimental FT-IR vibrational spectrum of TP-I molecular system. 231
4.26 (a) Molecular structure of 3[TP-I] molecular system involved in the size effect study. 233
4.26 (b) Molecular structure of 5[TP-I] molecular system involved in the size effect study. 233
4.27 (a) Bond distances for experimental, computed TP-I, 3[TP-I] and 5[TP-I] molecular system using DFT/B3LYP/6-31G method. 237
4.27 (b) Bond distances for experimental, computed TP-I, 3[TP-I] and 5[TP-I] molecular system using DFT/B3LYP/6-31G** method. 238
4.28 (a) The complete unit cell and single molecule of TP-II and TP-III. 244
4.28 (b) Labelling and numbering details in TP-II single molecule. 246
4.29 Parts of the geometry parameters (i.e. bond distances, bond angles, and dihedral angles) of TP-II molecular system. 248
4.30 (a) LUMO and HOMO surface mapped plots of TP-II molecular system using DFT/B3LYP/6-31G method. 253
4.30 (b) LUMO and HOMO surface mapped plots of TP-II molecular system using DFT/B3LYP/6-31G** method. 253
4.31 MPA analysis of TP-II molecular system using 256

	DFT/B3LYP/6-31G and DFT/B3LYP/6-31G** methods.	
4.32 (a)	The MEP surface mapped plots of TP-II molecular system using DFT/B3LYP/6-31G method.	259
4.32 (b)	The MEP surface mapped plots of TP-II molecular system using DFT/B3LYP/6-31G** method.	259
4.33	Experimental FT-IR vibrational spectrum of TP-II molecular system.	268
4.34 (a)	The molecular structure of 3[TP-II] molecular system involved in the size effect study.	269
4.34 (b)	The molecular structure of 5[TP-II] molecular system involved in the size effect study.	270
4.34 (c)	The molecular structure of 7[TP-II] molecular system involved in the size effect study.	270
4.34 (d)	The molecular structure of 9[TP-II] molecular system involved in the size effect study.	271
4.35 (a)	Bond distances for experimental, computed TP-II, 3[TP-II], 5[TP-II], 7[TP-II], and 9[TP-II] molecular system using DFT/B3LYP/6-31G method.	275
4.35 (b)	Bond distances for experimental, computed TP-II, 3[TP-II], 5[TP-II], 7[TP-II], and 9[TP-II] molecular system using DFT/B3LYP/6-31G** method.	276
4.36	The molecular electrostatic potential (MEP) surface mapped plots of ACV-I, ACV-II, and ACV-III molecular system.	284
4.37	The HOMO and LUMO 3D surface mapped plots of ACV-I, ACV-II, and ACV-III molecular system.	285
4.38	The molecular electrostatic potential (MEP) surface mapped plots of TP-I and TP-II molecular system.	288
4.39	The HOMO and LUMO 3D surface mapped plots of TP-I and TP-II molecular system.	289

LIST OF ABBREVIATIONS

3D	Three-dimensional
ACV	Acyclovir
APIs	Active Pharmaceutical Ingredients
B3LYP	Becke-3-Lee-Yang-Parr
BSC	Biopharmaceutical Classification System
cAMP	Adenosine monophosphate
cGMP	Guanosine monophosphate
CCD	Charge-coupled Device
CIF	Crystallographic Information Framework
CCDC	Cambridge Crystallographic Data Centre
CCCBDB	Computational Chemistry Comparison and Benchmark DataBase
DFT	Density Functional Theory
DMF	Dimethylformamide
FDA	Food and Drug Administration
FFT	Fourier Transform
FMOs	Frontier Molecular Orbitals
FT-IR	Fourier Transform Infrared
GGA	Generalised Gradient Approximation
GTOs	Gaussian-type Orbitals
GUD	Genital Ulcer Disease
HF	Hartree-Fock
HIV	Human Immunodeficiency Virus

HOMO	Highest Occupied Molecular Orbital
HSV-1	Herpes Simplex Virus Type 1
HSV-2	Herpes Simplex Virus Type 2
IR	Infrared
ICH	International Conference on Harmonization
ICT	Intramolecular Charge Transfer
KBr	Potassium Bromide
LDA	Local Density Approximation
LUMO	Lowest Unoccupied Molecular Orbital
MO	Molecular Orbital
MEP	Molecular Electrostatic Potential
MPA	Mulliken Population Analysis
NBO	Natural Bond Orbital
NLO	Non-linear Optical
NMR	Nuclear Magnetic Resonance
PBC	Periodic Boundary Condition
PES	Potential Energy Surface
PNA	p-Nitroaniline
SCF	Self-consistent Field
STOs	Slater-type Orbitals
TK	Thymidine Kinase
TN	Theophyllinium Nitrate
TP	Theophylline
TCM	Theophyillinium Chloride Monohydrate
TInP	Theophylline –InP Diamantine

UV-Vis	Ultraviolet-Visible
VZV	Varicella Zoster
WHO	World Health Organization

LIST OF SYMBOLS

$\hat{\mathrm{H}}$	Hamiltonian operator
$\hat{\mathrm{H}}_e$	Electronic Hamiltonian operator
Ψ	Wave function
ψ	Wave function
ψ_{HP}	Hartree product wave function
E	Total energy
E_0	Lowest/ground state total energy
E_{ee}	Electron-electron repulsion term
E_{eN}	Electron-nuclear attraction term
E_T	Kinetic energy term of electrons
E_V	Potential energy of nuclear-electron attraction and nuclear-nuclear repulsion
E_J	Electron-electron repulsion term
E_{xc}	Exchange and correlation term
E_x	Exchange interaction term between electrons
E_c	Correlation interaction term between electrons
T	Kinetic energy of electron
T_e	Kinetic energy of electron
R_n	Nuclear coordinates
r_n	Electron coordinates
V_{ee}	Electron-electron repulsion
V_{eN}	Electron-nuclear attraction

T_N	Kinetic energy of nuclei
V_{NN}	Nuclear-nuclear repulsion
i	Electron i
j	Electron j
A	Nuclear A
B	Nuclear B
∇^2	Laplacian operator
r_{ij}	Distance between electrons
r_{iA}	Distance between electron and nuclear
R_{AB}	Distance between nuclei
M_A	Mass of Nuclear A
Z_A	Charge of Nuclear A
$X(\vec{x})$	Electron orbital functions
$\varphi(\vec{r})$	Spatial orbital of electrons
$\alpha(\omega)$	Spin up of electrons
$\beta(\omega)$	Spin down of electrons
$f(x_1)$	Fock operator
$J_i(x_1)$	Coulomb repulsion between electrons
$K_j(x_1)$	Exchange integral between electrons
φ_i	Molecular orbital
$c_{\mu i}$	Molecular orbital expansion coefficients
Φ_μ	Set of known function
n_r	Electron densities

$e_{xc}^{unif}(n)$	Exchange and correlation energy per particle in homogenous electron gas with partially uniform density (n)
$\tau(r)$	Kinetic energy density of the Kohn-Sham orbitals
λ	Wavelength
λ_{max}	Highest peak of wavelength
d	Interplanar spacing
θ	Diffraction angle of X-ray
σ	Sigma bonding orbital
π	Pi bonding orbital
n	Non-bonding/Lone pair orbital
LP	Lone pair
σ^*	Sigma anti-bonding orbital
π^*	Pi anti-bonding orbital
A_{sb}	Absorbance of sample
I_0	Intensity of light passed through the reference cell
I	Intensity of light passed through the target sample
ε	Molar absorbtivity
C	Molar concentration of solute
L	Path length of sample cell
ΔE	Band gap energy
h	Planck's constant

v	Frequency
c	Speed of light
IE	Ionization energy
EA	Electron affinity
η	Hardness
μ	Chemical potential
S	Softness
χ	Electronegativity
ω	Electrophilicity index
$V(r)$	Interaction energy
$E(2)$	Stabilisation energy
q_i	Occupancy in donor orbital
$F(i,j)$	Off-diagonal NBO Fock matrix elements
$\varepsilon_i \varepsilon_j$	Orbital energies diagonal elements
μ_0	Dipole moment
β_{tot}	First hyperpolarizability

TABLE OF CONTENTS

ABSTRACT **iii**
PUBLICATION **vi**
ACKNOWLEDGEMENTS **vii**
APPROVAL SHEET **viii**
SUBMISSION SHEET **ix**
DECLARATION **x**
LIST OF TABLES **xi**
LIST OF FIGURES **xvi**
LIST OF ABBREVIATIONS **xxii**
LIST OF SYMBOLS **xxv**
TABLE OF CONTENTS **xxix**
CHAPTER 1 **1**
INTRODUCTION 1
1.2 Problem Statement 9
1.3 Objectives 11
1.4 Significance of the Study 12
CHAPTER 2 **13**
LITERATURE REVIEW 13
2.1 Ab-initio 13
2.1.1 Schrödinger Equation 14
2.1.2 Hartree-Fock (HF) Theory 16
2.1.3 Basis Set 19
2.1.4 Density Functional Theory (DFT) 22
2.1.5 Functionals 25
2.2 Polymorphism 29
2.2.1 Formation of polymorphs 31
2.2.2 Characterization of polymorphs 32
2.3 Active Pharmaceutical Ingredients (APIs) 45
2.3.1 Acyclovir (ACV) 47
2.3.2 Theophylline (TP) 52
2.4 Geometry Optimization 56
2.5 Potential Energy Surface (PES) 58
2.6 Molecular Orbital (MO) 60

2.7 Molecular Electrostatic Potential (MEP) 63
2.8 Natural Bond Orbital (NBO) 64
2.9 Non-linear Optical (NLO) Properties 65
CHAPTER 3 **68**
METHODOLOGY 68
3.1 Flow of Research 68
3.2 Materials and Chemicals 69
3.3 Experimental Part 70
3.3.1 Crystal Formation in Acyclovir (ACV) Drug Compound 70
3.2.2 Crystal Formation in Theophylline (TP) Drug Compound 72
3.3.3 Single Crystal X-ray Diffraction Experiment 73
3.3.4 Fourier Transform Infrared (FT-IR) Spectroscopy 78
3.3.5 Ultraviolet-Visible (UV-Vis) Analysis 79
3.4 Computational Studies 81
3.4.1 Computational Method and Software 81
3.4.2 Input Source Preparation 81
3.4.3 Density Functional Theory (DFT) Computational Calculations 86
CHAPTER 4 **93**
RESULTS AND DISCUSSIONS 93
Polymorphism Organic Compound 1: Acyclovir (ACV) 93
4.1: Acyclovir Hydrate (ACV-I) ($3[C_8H_{11}N_5O_3]\cdot 2[H_2O]$) 94
4.2: Acyclovir Hydrate (ACV-II) $3[C_8H_{11}N_5O_3]\cdot 2[H_2O]$ 139
4.3: Acyclovir Hydrate (ACV-III) $2[C_8H_{11}N_5O_3]\cdot 4[H_2O]$ 172
Polymorphism Organic Compound 2: Theophylline 202
4.4: Pure Theophylline Compound (TP-I) ($C_7H_8N_4O_2$) 203
4.5: Theophylline Monohydrate Compound (TP-II) ($C_7H_8N_4O_2 \cdot H_2O$) 243
Comparison on the Polymorphisms of Acyclovir (ACV) and Theophylline (TP) Molecular System 281
4.6: Comparison on the Computed Electronic Properties of ACV-1, ACV-II, and ACV-III Molecular System 281
4.7: Comparison on the Computed Electronic Properties of TP-I and TP-II Molecular System 286
CHAPTER 5 **290**
CONCLUSION 290
5.2 Recommendation 293
REFERENCES **294**

CHAPTER 1

INTRODUCTION

The phenomena of polymorphism in matter have been observed for ages. Perhaps, the early incident observed by Klaproth (Haleblian and McCrone, 1969) in 1788 during the crystal formations of calcite and aragonite from calcium carbonate does not trigger the awareness of polymorphism phenomena in chemical substances. Until 1809, Humphrey Davy (Haleblian and McCrone, 1969; Bhatia *et al.*, 2018) noticed the physicochemical properties distinction between two carbon-based graphite and diamond. Undoubtedly, Davy's study had inspired people about the concept of polymorphism in chemical substances. Polymorphism phenomena refer to the ability of a chemical compound to exist in more than one crystal structure forms, regardless of either chemical structure or composition (Haleblian and McCrone, 1969; Karpinski, 2006; Raza *et al.*, 2014; Prasanthi *et al.*, 2016; Lin, 2020; Nogueira *et al.*, 2020). It is a widespread phenomenon in the chemical world as more than 59% of chemical substances exhibit polymorphism characteristics (Prasanthi *et al.*, 2016).

To date, the study of polymorphism in chemical substances has aroused lots of attentions from different background researchers since any variation in the polymorphic forms of a chemical substance may alter the physicochemical properties such as solubility, colour, melting point, dissolution rate, stability, and so on (Bauer, 2008; Marques *et al.*, 2013; Ainurofiq *et al.*, 2020; Nogueira *et al.*,

2020). A fatal lesson faced by a US pharmaceutical company- Abbott Laboratories reminded people about the impact and importance of polymorphism phenomena in the pharmaceutical industry. The company suffered a market crisis due to the sudden appearance of new needle-shaped Ritanovir polymorph Form II (lower bioavailability) from the original commercial rod-shaped Ritanovir Form I, after two years of product launching in the market (World, 2007; Bauer, 2008; Dezena, 2020). Abbott Laboratories forced to withdraw back all the marketed anti-HIV Ritanovir drug since some batches of the drug started to fail the dissolution test and show clinical ineffectiveness. The ignorance of polymorphism investigation on Ritanovir drug caused Abbott Laboratories to lose 250 million dollars of sales including additional development cost (Lin, 2020). This served as a wake-up call for drug developers to have concern study on the phenomena of polymorphism in medicine because there are more than half of the active pharmaceutical ingredients (APIs) tend to exhibit polymorph easily (Karpinski, 2006; World, 2007; Raza *et al.*, 2014; Lin, 2020).

Every coin has two sides. Although the polymorphism phenomena in APIs sound like a tricky challenge for the pharmaceutical industry, it does contribute to the field of pharmaceutical functional applications. It might be a saboteur to the pharmaceutical industry if there is a lack of understanding of the formation of polymorphs. However, a good identification, analysis, and characterization of those possible formations of polymorphs may help drug developers to enhance the therapeutic performances of an APIs drug and also improves the processability of the drug in the downstream processes. For

example, paracetamol is found to have two polymorph forms (Form I and Form II). It is figured out that Form II exhibits better compressibility than Form I and more suitable for the tableting purpose (Aitipamula and Nangia, 2012; Raza *et al.*, 2014). In the case of antibiotic chloramphenicol palmitate, it is reported to have three different polymorphs (i.e. Form A, B, and C). Form C is the most unstable form while Form B shows better bioavailability than Form A. With the same dosage of administration, Form B able to reach higher serum levels than Form A (Raza *et al.*, 2014; Censi and Di Martino, 2015; Prasanthi *et al.*, 2016). In fact, the occurrence of polymorphism behaviors in pharmaceutical drug compounds not only shows profound influence on the efficacy of therapeutic performance but also concerned about the safety and legal issues.

In the past decades, the astronomical development in computer technologies accompanies with rigorous improvement in theoretical algorithms had offered researchers an alternative way in the study of polymorphism in chemical substances. This quantum chemistry computational concept lies between the border of both physics and chemistry. It is a branch of theoretical chemistry that employ quantum mechanics and incorporated with efficient computational programs to solve and explain several interesting chemical problems and intricate reaction mechanism in chemical substances (Narayan, 2012; Nyakung'U, 2015). Among all, the Density Functional Theory (DFT) computational method is by far the most popular technique employed by researchers in the study of polymorphism in APIs drug compounds, due to its excellent computational performances in terms of system size, data accuracy, simulation cost, and time (Yin, 2009; Beran, 2016; Murti, 2017; Tandon,

Chakraborty and Suhag, 2019). In the pharmaceutical industry, it is a matter of observation that drug discovery and development processes are costly (800 million to 1000 million US dollars) and time-consuming (12 to 15 years) (Narayan, 2012). The emergence of the Density Functional Theory computational method is definitely a great help to the pharmaceutical industry. Rather than a sequence of complicated laboratory works, the first principle Density Functional Theory computational method able to predict and determine the molecular atomic structures, electronic properties, and spectroscopic signatures of a condensed matter system by just providing it the basic molecular geometry structural information without any other adjustable parameters (Yin, 2009; Li, 2012). Nogueira *et al.* (2020) noticed the intermolecular interactions and stability disparities between three polymorph forms of 1-Methylhydantoin. Rodríguez-López *et al.* (2016) successfully determined another five possible conformational polymorphic forms of 1, 4-bis (triisopropylsilyl) buta-1, 3-diyne polymorphs. Wang *et al.* (2018) observed the Raman and terahertz vibrational spectra differences in three polymorphic forms of 2-thiobarbituric acid (TBA) compound. For now, the Density Functional Theory computational method serves as a powerful guiding and analytic tool for both experimentalists and theorists, since it can evaluate and monitor the interrelationships between crystalline structures and properties related to the nature of reactions (i.e. intra/inter-molecular interactions, hydrogen bonding, conductivity, polarization, stability, charge transport activity and so on) (Narayan, 2012; Beran, 2016; Abbaz, T., Bendjeddou, A. and Villemin, 2019).

In this research work, two different heterocyclic APIs drug compounds –

acyclovir (ACV) and theophylline (TP) are chosen. The acyclovir ($C_8H_{11}N_5O_3$) drug compound plays a vital role in the treatment of Herpes Simplex Virus Type 1 (HSV-1), Type 2 (HSV-2), and Varicella Zoster (VZV) diseases (Masuda *et al.*, 2012; Sarkar and Rohani, 2015; Cai *et al.*, 2017; Poole and James, 2018), while the theophylline ($C_7H_8N_4O_2$) drug compound shows significant therapeutic application in respiratory diseases such as asthma and chronic obstructive pulmonary disease (COPD) (Aitipamula *et al.*, 2009; Zhang and Fischer, 2011; Novena *et al.*, 2017; Gong *et al.*, 2018). Although the current pharmaceutical performances of ACV and TP have considerable efficacy, they still have drawbacks. It has been reported that the ACV drug compound has low solubility, permeability, and bioavailability (Masuda *et al.*, 2012; Yan *et al.*, 2013; Nalla and Chinnala, 2017; Shamshina *et al.*, 2017). A higher dosage of ACV drug during the treatment will cause side-effects to the human body (i.e. rash, headache, diarrhoea, and nausea) (Nalla and Chinnala, 2017). For the case of the theophylline drug compound, its low physical stability, solubility, bioavailability, and narrow therapeutic index properties hinder its medical application (Andrei, 2011; Novena *et al.*, 2017; Jilani *et al.*, 2020). A heavy dosage of theophylline drug leads to anxiety, diarrhoea, heart palpitation, and restlessness in the human body.

Recently, more and more researchers elucidate lots of interest in the finding and study of polymorphism in both ACV and TP drug compounds (refer to chapter 2 section 2.3.1 and 2.3.2), due to the fact that Herpes Simplex Virus (HSV), asthma, and COPD are categorised as global burden diseases suffering by people worldwide. The HSV-1 and HSV-2 diseases are highly prevalence

lifelong infections. HSV-2 is the leading cause for Genital Ulcer Disease (GUD). It also increases the risk for Human Immunodeficiency Virus (HIV) acquisition (Looker *et al.*, 2015; Gottlieb *et al.*, 2019). Surveys reveal that there are an estimated of 3709 million of people worldwide below aged of 50 infected by HSV-1 in 2012 (Looker *et al.*, 2015; WHO, 2020). Besides, there are approximately 118 million of people reported to be newly infected by the disease in 2012 (Looker *et al.*, 2015). For HSV-2, there are 417 million of people between the ages of 15 to 49 get infected in 2012. This terrible number of cases accounted for 11.3% of global prevalence in 2012 (Looker *et al.*, 2015; Looker *et al.*, 2017; WHO, 2020). Furthermore, it is about 19.2 million of people found to be newly infected by HSV-2 in 2012 *(Looker et al.*, 2015). In chronic respiratory diseases, COPD and asthma have become the leading causes of worldwide mortality and morbidity. Studies reveal that there are approximately 3.2 million and 0.4 million of people died from COPD and asthma in 2015 (Soriano *et al.*, 2017). The mortality rate and prevalence of COPD increased by 11.6% and 44.2% from 1990 to 2015 (Soriano *et al.*, 2017). Currently, COPD is reported to be the 4th leading cause of death since 2000 (López-Campos *et al.*, 2016) and it will dominate to be 3rd by 2030 according to World Health Organization (WHO) (Ehteshami-Afshar *et al.*, 2016). As of 2015, there is an estimated of 174.5 million of people suffering from COPD (Soriano *et al.*, 2017). For asthma, with a total prevalence number of 358.2 million cases, the prevalence rate of asthma increased by 12.6% from 1990 to 2015 (Soriano *et al.*, 2017). Based on WHO, it is believed that the total number of asthma patients will increase to another 100 million by 2025 years (Ehteshami-Afshar *et al.*, 2016). From the above summary, it is obviously pointed out that the studies of

polymorphism in ACV and TP drug compounds are necessary in terms of public health issues. The physicochemical properties alteration ability among ACV and TP polymorphs give chances to drug developers and manufactures to further enhance and improve the efficacy and therapeutic performances of the drugs.

The works undertaken in this thesis can be divided into three main parts: (a) formation and characterization of ACV and TP polymorph crystals, (b) DFT computational study on the molecular structures, electronic properties (i.e. total energies, HOMO-LUMO energies, molecular electrostatic potential, natural bond orbital, and non-linear optical properties), and vibrational spectra of ACV and TP polymorphs, and (c) validation of computational results with experimental data. Table 1.1 summarises the crystal lattices and single molecular structures of ACV and TP polymorphs employed in the present work. All the computational calculations are mainly performed using the Gaussian 09 quantum mechanics computational software package (Frisch *et al.*, 2009) together with GaussView 5.0 (Frisch *et al.*, 2009) and Multifwn (Lu and Chen, 2012) software as the tools for data visualisation and analysis. DFT/B3LYP/6-31G** and DFT/B3LYP/6-311G** level of theories are selected for the computational calculations in ACV polymorphs (i.e. ACV-I, ACV-II, and ACV-III), whereas the DFT/B3LYP/6-31G and DFT/B3LYP/6-31G** level of calculations are used in the theoretical analysis of TP polymorphs (i.e. TP-I and TP-II). Additional Fourier transform infrared (FT-IR) spectroscopy and Ultraviolet-visible (UV-Vis) spectroscopy experiments are carried out and act as the comparative data and guiding reference for the computational findings.

Table 1.1: Polymorphic forms of ACV and TP drug compounds involved in the DFT computational calculations.

Compounds and Crystal Lattices		Single Molecular Crystal Strcutures
ACV-I		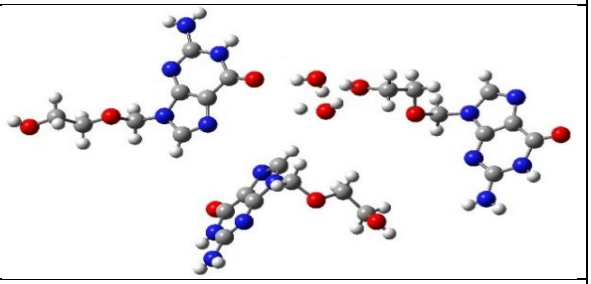
a = 10.765 Å	α = 90.000°	
b = 11.287 Å	β = 95.162°	
c = 25.455 Å	γ = 90.000°	
ACV-II		
a = 25.459 Å	α = 90.000°	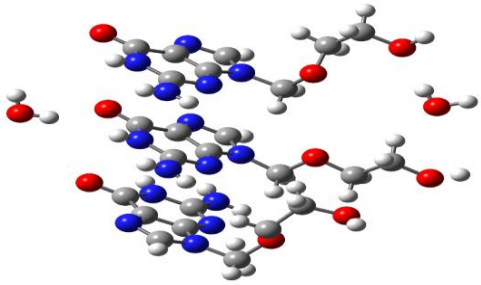
b = 11.282 Å	β = 95.160°	
c = 10.768 Å	γ = 90.000°	
ACV-III		
a = 6.900 Å	α = 82.595°	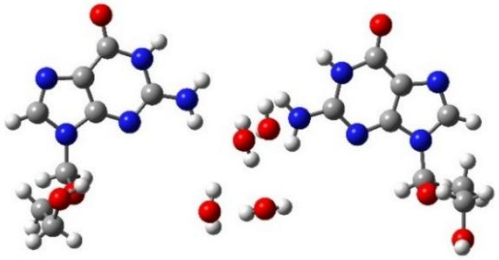
b = 11.417 Å	β = 82.395°	
c = 15.081 Å	γ = 89.368°	
TP-I		
a = 24.493 Å	α = 90.000°	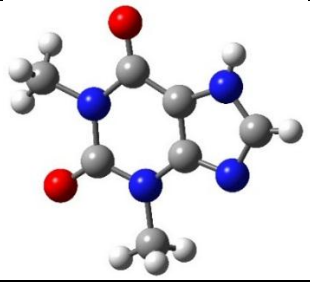
b = 3.812 Å	β = 90.000°	
c = 8.456 Å	γ = 90.000°	
TP-II		
a = 4.489 Å	α = 90.000°	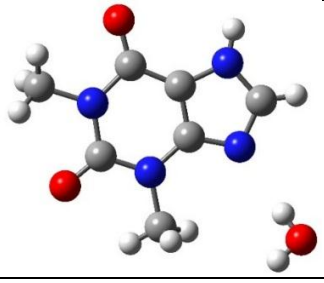
b = 15.408 Å	β = 98.591°	
c = 13.287 Å	γ = 90.000°	

1.2 Problem Statement

The study of polymorphism in active pharmaceutical ingredients (APIs) drug compounds is crucial since any alteration and changing in the polymorphic forms of the drug may affect its physicochemical properties and pharmaceutical performances such as solubility, stability, dissolution rate, and bioavailability (Bauer, 2008; Censi and Di, 2015; Ainurofiq *et al.*, 2020; Nogueira *et al.*, 2020). As the primary treatment choice for global burden diseases of Herpes Simplex Virus (HSV) and Varicella Zoster (VZV) infections (Masuda *et al.*, 2012; Sarkar and Rohani, 2015; Cai *et al.*, 2017; Gong *et al.*, 2018), the commercial acyclovir (ACV) drug compound is reported to have trouble in solubility and bioavailability (Cai *et al.*, 2017; Nalla and Chinnala, 2017; Shamshina *et al.*, 2017; Jilani *et al.*, 2020). A similar situation also faced by theophylline (TP) drug compound (Andrei, 2011; Novena *et al.*, 2017; Gottlieb *et al.*, 2019), which serves as the treatment for global burden diseases of asthma and chronic obstructive pulmonary disease (COPD) (Aitipamula *et al.*, 2009; Zhang and Fischer, 2011; Yan *et al.*, 2013; Novena *et al.*, 2017). In order to overcome the blemishes in ACV and TP drug compounds, researchers have put a lot of effort into the discovery and study of polymorphism behaviours in both compounds. However, literature surveys reveal that the theoretical investigation based on the molecular structures, electronic properties, and vibrational spectra for both ACV and TP polymorphs are still limited. The electronic properties of a condensed matter system govern and affect the properties of the material (Nyakung'U, 2015). Through Gaussian 09 quantum mechanics computational software package, the electronic properties study in a system can be identified

(Nyakung'U, 2015; Rodríguez-López, Nesterov and Youngblood, 2016; Poole and James, 2018). These findings not only explain the nature of chemical reactions in the system but also helps in the prediction of the new formation of polymorphs. Sometimes, experimentally monitor the energy differences between two polymorphs is a daunting challenge because majority of the polymorphs are found to have less than 0.021 eV of lattice energy difference (Rodríguez-López *et al.*, 2016). Consequently, the comprehensive understanding on the electronic properties of a compound using computational approach has become an indispensable part for material and drug researchers. In this work, the main focus is on the theoretical study of hydrated polymorphic forms of ACV and TP compounds using the Density Functional Theory computational method. As a pharmaceutical drug, ACV and TP compounds are exposed to water frequently during various processes (i.e. manufacturing, storing, and consuming) (World, 2007). This leads to a strong possibility in the formation of hydrated polymorphs in ACV and TP compounds. It is crucial to be aware that the selection of the DFT computational method largely impacts on the accuracy of computational data (Wang *et al.*, 2018). In order to verify and give confidence to the computational method selected on ACV and TP polymorphs, additional Fourier transform infrared (FT-IR) spectroscopy and Ultraviolet-visible (UV-Vis) spectroscopy experiments are carried out to act as comparative data with computational findings since there are limited reference resources about the DFT computational study on ACV and TP polymorphs.

1.3 Objectives

The objectives of this study are:

a) To prepare the crystal forms of acyclovir and theophylline hydrate compounds.

b) To characterize the physical structures of acyclovir and theophylline hydrate compounds.

c) To find the local energy minima of acyclovir and theophylline hydrate molecular systems using geometry optimization calculations.

d) To determine the geometric and electronic structures of acyclovir and theophylline hydrate molecules by performing single point calculations.

e) To compare the data obtained from Density Functional Theory (DFT) with experimental findings.

1.4 Significance of the Study

The present study provided microscopic fundamental understanding on the molecular structures, electronic properties (i.e. optimized total energies, computed HOMO-LUMO energies, molecular electrostatic potential, natural bond orbital, and non-linear optical properties), and vibrational spectra of three polymorphic forms of ACV (i.e. hydrated ACV-I, ACV-II, and ACV-III) and two polymorphic forms of TP (i.e. anhydrous TP-I and hydrated TP-II) molecular system. The possible conformers of ACV polymorphs are assessed by the rotational barrier study. The size effect study in the computational approach is determined by increasing the size of the single molecule in the TP polymorphs system. All the computational results obtained in this study can serve as a complement and provide a guideline for researchers in the study of polymorphism phenomena in ACV and TP compounds. The data comparison between computational results and experimental data confirmed the usability of the DFT/B3LYP computational method in the study of geometry and electronic properties of future ACV and TP polymorphism.

CHAPTER 2

LITERATURE REVIEW

2.1 Ab-initio

With the combination of chemistry, physics, mathematical calculation and computing technique, computational chemistry and physics has become an essential and useful method employed by researchers to solve several interesting chemical problems such as molecular energy, thermodynamic characteristic, vibrational frequency, molecular orbitals and so on (Tapre, 2013). Among all, Ab-initio computational calculation gains high popularity as it shows outstanding performance in data accuracy than other methods. The word "Ab-initio" derives from the Latin word, contains the meaning of "from first principles" (David, 1998; ChemViz, 2000; Gilbert, 2007). It determines and investigates the structures and properties of matter at the atomistic level based on the fundamental law of quantum mechanics – the Schrödinger equation (Gilbert, 2007; Tapre, 2013; Kattiet *al.*, 2017). There are two famous and well-known computational methods in Ab-initio calculation: Hartree-Fock (HF) method and Density Functional Theory (DFT) method (David, 1998). The former deals with electronic wave function while the latter deals with electronic density. A short glance of the fundamental understanding of HF and DFT computational methods is briefly discussed.

2.1.1 Schrödinger Equation

Physicists realize that atomic particles do not only behave in particle-like form but also in wave-like form naturally. The diffraction experiment carried out by Clinton Davisson and Lester Germer using nickel crystals confirmed the wave-like behaviour of atoms (Chan, 2013). Unfortunately, the wave function is not physically observable but can be understood via a sequence of mathematical constructs (Nyakung'U, 2015). In 1926, great achievement is done by Erwin Schrodinger with the introduction of the Schrödinger wave equation. The Schrödinger wave equation accurately describes the wave behaviour of a system through a mathematical approach and acts as the main fundamental law in quantum mechanics study (Chan, 2013; Daniel, 2014; O'Connor and Robertson, 2017). Besides, it also plays the role of the pioneer and precursor for the development of HF and DFT computational methods. Equation 2.1 shows the Schrödinger wave equation (Narayan, 2012; Daniel, 2014; Zobel, 2018).

$$\hat{\mathrm{H}}\Psi(r_1, r_2, \dots, r_n\,; R_1, R_2, \dots, R_n\,) = E\Psi(r_1, r_2, \dots, r_n\,;\, R_1, R_2, \dots, R_n)$$

(Equation 2.1)

The symbol $\hat{\mathrm{H}}$ is the Hamiltonian operator, Ψ is the wave function, E is the total energy of the system, R_n is the nuclear coordinates, and r_n is the electron coordinates. Noticed that the Hamiltonian operator ($\hat{\mathrm{H}}$) is the energy operator and can be further expanded as shown in Equation 2.2. It contains all the kinetic and potential energy operators that describe the interactions between electrons and nuclei in a molecular system (Zobel, 2018).

$$\hat{H} = \underbrace{-\frac{1}{2}\sum_{i}^{N}\nabla_i^2}_{T_e} + \underbrace{\sum_{i}^{N}\sum_{j\neq i}^{N}\frac{1}{r_{ij}}}_{V_{ee}} - \underbrace{\sum_{i}^{N}\sum_{A}^{M}\frac{Z_A}{r_{iA}}}_{V_{eN}} - \underbrace{\frac{1}{2}\sum_{i}^{M}\frac{1}{M_A}\nabla_A^2}_{T_N} + \underbrace{\sum_{A}^{M}\sum_{B\neq A}^{M}\frac{Z_A Z_B}{R_{AB}}}_{V_{NN}}$$

(Equation 2.2)

The T_e is the kinetic energy operator of the electron, V_{ee} represents the electron-electron repulsion, V_{eN} is the electron-nuclear attraction, T_N is the kinetic energy operator of nuclei and V_{NN} is the nuclear-nuclear repulsion. The ∇^2 is known as the Laplacian operator and can be presented as $\frac{\partial^2}{\partial x^2} + \frac{\partial^2}{\partial y^2} + \frac{\partial^2}{\partial z^2}$ (Daniel, 2014). Terms A and B count over the nuclei while terms i and j count over the electrons (Sena, 2010).

The substitution of Equation 2.2 into Equation 2.1 makes the Schrödinger wave equation becomes complicated and knotty. To overcome this situation, an important approximation known as Born-Oppenheimer Approximation is introduced to separate the motions of nuclei and electrons (Narayan, 2012). Based on the approximation, the mass of an atomic nucleus in a molecular system is thousands of times heavier than the electron (Narayan, 2012; Daniel, 2014; Zobel, 2018) and the motion of the nucleus is slow enough to be assumed in a stationary condition. Therefore, with constant nucleus position of R_n, the kinetic energy of the nucleus is said to be zero and has constant potential energy. This further simplifies the Hamiltonian operator ($\hat{H}$) by ignoring the kinetic and potential energy terms of nuclei (i.e. T_N and V_{NN}) and focuses on the electronic problems as shown in Equation 2.3. Equation 2.4 states the electronic Schrödinger wave equation after Born-Oppenheimer Approximation (Sena, 2010; Dixit and Antwerpen, 2012).

$$\hat{\mathrm{H}}_e = \underbrace{-\frac{1}{2}\sum_{i}^{N}\nabla_i^2}_{T_e} + \underbrace{\sum_{i}^{N}\sum_{j\neq i}^{N}\frac{1}{r_{ij}}}_{V_{ee}} - \underbrace{\sum_{i}^{N}\sum_{A}^{M}\frac{Z_A}{r_{iA}}}_{V_{eN}}$$

(Equation 2.3)

$$\hat{\mathrm{H}}_e\Psi(r_i) = E_e\Psi(r_i)$$

(Equation 2.4)

From the electronic Schrödinger wave equation, the energy state and related physicochemical properties of a system can be determined as if the mathematical treatment for the equation is available. However, the electronic Schrödinger wave equation is only solvable for hydrogen atoms and harmonic oscillators (Narayan, 2012). For any system that contains more than two particles (N-body system), the mathematical solution seems to be difficult and impossible.

2.1.2 Hartree-Fock (HF) Theory

It reached a bottleneck for computational chemistry and physics since the invoking of Born-Oppenheimer Approximation is not enough to obtain a satisfactory mathematical solution for many electrons (N-body) Schrödinger wave equation. Several approximations are proposed by researchers. One of the well-established solutions is the Hartree-Fock (HF) method. It adopted orbital approximation and "mean-field" approximation to minimize the complexity of the Schrödinger wave equation from N-electrons problem to N one-electron problem. Each of the electrons is described separately by its independent orbital wavefunction and the Coulombic interactions between electrons are defined under an effective mean-field from their average charges (Dixit and Antwerpen, 2012; Chan, 2013). In the HF method, the total wavefunction (Ψ) of a molecular

system is just the product of the single electron orbital wavefunctions (the Hartree Product) as shown in Equation 2.5 (Sherrill, 2000; Narayan, 2012; Rosa, 2014).

$$\psi_{HP}\,(x_1, x_2, \dots, x_N) = X_1(x_1)X_2(x_2)\dots X_N(x_N)$$

(Equation 2.5)

Noted that the electrons orbital functions ($X(x)$) in Equation 2.5 are not only consider to have three spatial coordinates but also in intrinsic spin coordinates as presented in Equation 2.6 and 2.7 (Sherrill, 2000; Rosa, 2014).

$$X(\vec{x}) = x(\vec{r}, \omega)$$

(Equation 2.6)

$$X(\vec{x}) = \begin{cases} \varphi(\vec{r})\alpha(\omega) \\ \varphi(\vec{r})\beta(\omega) \end{cases}$$

(Equation 2.7)

The $\varphi(\vec{r})$ represents the spatial orbital that describes the spatial distribution of electrons while $\alpha(\omega)$ and $\beta(\omega)$ represent the spin up and spin down of electrons. Unfortunately, the Hartree Product total wavefunction in Equation 2.5 does not obey the Pauli Exclusion Principle, where the electrons are distinguishable fermions and will be in antisymmetric wavefunction form during the interchange between electrons (Sherrill, 2000; Dixit and Antwerpen, 2012; Zobel, 2018). To overcome this problem, the Slater determinant is used to arrange all the electrons spin orbitals into antisymmetric wave-function form. Equation 2.8 shows the total wavefunction after the employment of Slater determinant (Sherrill, 2000; Sena, 2010; Rosa, 2014; Zobel, 2018) in HF theory.

$$\psi_{HP}\,(x_1, x_2, \dots, x_N) = \frac{1}{\sqrt{N!}} \begin{bmatrix} X_1(x_1) & X_2(x_1) & \cdots & X_N(x_1) \\ X_1(x_2) & X_2(x_2) & \cdots & X_N(x_2) \\ \vdots & \vdots & \ddots & \vdots \\ X_1(x_N) & X_2(x_N) & \cdots & X_N(x_N) \end{bmatrix}$$

(Equation 2.8)

According to the Variational theorem, the energy of an approximation wavefunction will always equal to or larger than the true lowest energy state E_0 of the system. This concept makes the finding of ground state energy of a molecular system mathematically possible (Rosa, 2014; Zobel, 2018). Equation 2.10 shows the energy expression of a molecular system after the combination of the concept of Slater determinant into Variational theorem. From the equation, each of the electrons is moving independently from other electrons and will experience the Coulomb potential from the nuclei and also from the N-1 other electrons (Sena, 2010; Rosa, 2014).

$$E_0 \leq \langle \psi | \hat{\mathrm{H}} | \psi \rangle$$

(Equation 2.9)

$$E = \sum_{i=1}^{N} < \psi_{HP} |\, h(i) \,| \psi_{HP} > + \sum_{i=1}^{N-1} \sum_{j=i}^{N} < \psi_{HP} \,| \frac{1}{r_{ij}} | \psi_{HP} >$$

(Equation 2.10)

The $h(i)$ represents the one-electron integral and the $\frac{1}{r_{ij}}$ represents the many electrons integral part. For now, the Hartree product wavefunction with Slater determinant and the energy expression is obtained. To get the approximated ground state energy of a system, the Lagrange multipliers method with the combination of Fock operator is applied and the complete and standard Hartree-Fock equation can be written as (Sherrill, 2000; Sena, 2010; Rosa, 2014)

$$f(x_1)\psi_i(x_1) = \epsilon_i \psi_i(x_1)$$

(Equation 2.11)

where,

$$f(x_1) = h(x_1) + \sum_j J_i(x_1) - \sum_i K_j(x_1)$$

(Equation 2.12)

$$J_i(x_1)\psi_i(x_1) = \{\int dx_2\, \psi_j^*(x_2)\psi_j(x_2)r_{12}^{-1}\}\psi_i(x_1)$$

(Equation 2.13)

$$K_j(x_1)\psi_i(x_1) = \{\int dx_2\, \psi_j^*(x_2)\psi_i(x_2)r_{12}^{-1}\}\psi_j(x_1)$$

(Equation 2.14)

The $f(x_1)$ is known as the Fock operator, $J_i(x_1)$ is the Coulomb operator that represents the interaction between electrons due to the mean-field effect and $K_j(x_1)$ is the exchange operator introduced by the Slater determinant wavefunction.

2.1.3 Basis Set

A basis set is a set of mathematical computational functions that combined in linear combinations to create and describe the molecular orbitals in a system (Hänninen, 2012; Li, 2012; Narayan, 2012). It is important because the electron wave-functions are presented in the form of electron orbitals (Li, 2012). Equation 2.15 represents the mathematical expression of the molecular orbital basis functions.

$$\varphi_i = \sum_{\mu=1}^{n} c_{\mu i}\Phi_\mu$$

(Equation 2.15)

From the equation, the unknown molecular orbital (φ_i) can be obtained from the linear combination of other known function Φ_μ. The term $c_{\mu i}$ refers to the molecular orbital expansion coefficients. There are two types of molecular orbitals basis functions, i.e. Slater-type orbitals (STOs) and Gaussian-type orbitals (GTOs) (Nyakung'U, 2015). For STOs, it provides a good approximation of atomic wavefunction but faces limitations when dealing with two-electron integrals (Nyakung'U, 2015). Accompany with computational efficiency consideration, the STOs are replaced by a mathematically more tractable combination of GTOs in electronic structure calculations (Foroushani, 2019). Initially, a minimum basis set is introduced. It contains only the smallest number of functions necessary to adapt the electron within an atom. For example, hydrogen required a minimum of a single s-function, whereas the elements in the second row of the periodic table required two s-functions and a set of p-function. A well-known typical minimum basis set is the STO-3G basis set. However, the minimum basis sets lose their popularity in the quantum computational study since they provide only a few or no electron correlation and find unsuitable for charge and lone pairs structures (Nyakung'U, 2015). To conquer this awkward situation, the split valence basis set is introduced. It describes the orbital into two main parts (i.e. the core shell and the valence shell). Generally, the split valence basis set has the format of "$N-MPG$", where N is the number of Gaussian primitives used to describe the core shell region, M is the Gaussian primitive for inner valence region, P is the Gaussian primitive for outer valence region, and the term G is defined as Gaussian-type orbitals (LibreTexts, 2020). The most common split valence basis sets are the 3-21G and 6-31G basis sets. In 3-21G, the core orbitals are described by three Gaussians

while the inner part and outer part valence shells are represented by two Gaussians and one Gaussian respectively. In 6-31G, the number of Gaussian primitives for core orbitals and inner valence orbitals are increased to six Gaussians and three Gaussians, whereas the outer valence orbitals remain one Gaussian primitive. The increase in the primitive number of basis set gives better flexibility in the construction of electron orbitals (i.e. angular freedom and multi-direction of electron distribution) (Narayan, 2012; Nyakung'U, 2015; Foroushani, 2019). Besides, there are two additional functions (i.e. polarized function and diffuse function) that can be employed in the basis sets. The polarized function uses asterisks symbol "∗" while the diffuse function uses the plus sign "+". In the 6-31G** basis set, the first "∗" represents the addition of d-type orbital function on heavy atoms, whereas the second "∗" indicates the addition of p-type orbital function on hydrogen atom (Foroushani, 2019). In the 6-31++G basis set, the first "+" indicates the addition of sp-diffuse functions on the heavy atom, whereas the second "+" represents the addition of the s-diffuse function on the hydrogen atom (Foroushani, 2019). Noted that both of the diffuse and polarized additional functions can be added together into the basis sets (i.e. 6-31++G**). For practical applications, the selection of a suitable basis set strongly depends on the computing system and methods. Normally, larger basis sets will result in heavy computational time and cost (Zobel, 2018).

2.1.4 Density Functional Theory (DFT)

The contributions achieved by Hartree-Fock (HF) computational method (i.e. replacing the total wavefunction (ψ) with single electron orbital wave function, defining the ground state energy using Variational principle, and self-consistent method (Köse, 2001)) had brought the quantum computation millstone to another level. However, the applications of the HF method are restricted, especially in larger molecular system. The complexity of the entity in dealing with wavefunction in the HF method caused the computational cost and time increase proportional with system size. In additions, the ignorance of correlation interactions between electrons reduces the accuracy of the computational data (Köse, 2001; Daniel, 2014). The emergence of the Density Functional Theory (DFT) computational method can be said to be a revolutionary improvement in the history of quantum computational fields. Although the Thomas Fermi Approximation introduced by Thomas and Fermi in 1927 seems to be immature and does not obey the Schrödinger wave equation (i.e. ignorance of the nuclear-electron, electron-electron energies, exchange, and correlation effects (Kurth *et al.*, 2003)), it does come out with a brand new and innovative idea in quantum computation fields, which replacing the complicated wavefunction by electron density ($n(r)$) in the calculation of the energy of an atom (E) (Köse, 2001; Tu, 2008; Chan, 2013). It acts as the predecessor of the DFT computational method. Equation 2.16 shows the basic conceptual root of the DFT computational method (Nyakung'U, 2015). In DFT, the total energy (E) of a system is a functional of the electron density ($n(r)$).

$$E\big(n(r)\big) = F\big(n(r)\big)$$

(Equation 2.16)

The foundation of the DFT method is based on the Hohenberg-Kohn Theorems and Kohn-Sham Theorem (Kurth *et al.*, 2003; Li, 2012; Daniel, 2014). In 1964, Hohenberg and Kohn introduce the Hohenberg-Kohn Theorem I and II that set forth the reliability of using electron density rather than wavefunction in the solution of complicated N-body Schrödinger wave equation (Kurth *et al.*, 2003; Tu, 2008; Sena, 2010; Dixit and Antwerpen, 2012). From the Hohenberg-Kohn Theorem I (Kurth *et al.*, 2003), the unique ground state energy (E_0) and properties of the N-body system depend only on the electron density (n_r) (Kurth *et al.*, 2003; Sena, 2010; Daniel, 2014; Zobel, 2018) and the ground state electronic energy can be defined as stated in Equation 2.17 (Tu, 2008).

$$E_0[n_r] = T[n_r] + E_{ee}[n_r] + E_{eN}[n_r]$$

(Equation 2.17)

Based on the Variational principle, the Hohenberg-Kohn Theorem II (Kurth *et al.*, 2003) mentions that the correct ground-state electron density can be obtained through the minimization of the total energy of the electronic system (Kurth *et al.*, 2003; Sena, 2010; Daniel, 2014; Zobel, 2018). Equation 2.18 states the correct ground state energy expression for the electronic system (Tu, 2008):

$$E_0 \leq E[n] = T[n] + E_{ee}[n] + E_{eN}[n]$$

(Equation 2.18)

However, both of the Hohenberg-Kohn theorems only prove that there is a true relationship between electron density and ground-state properties. There is still a lack of exact expression to interpret the kinetic part, electron-electron interaction part, and fermion characteristic of the electron in the system (Zhou,

2007; Tu, 2008; Dixit and Antwerpen, 2012; Svensson, 2015). In 1965, Kohn and Sham simplify the N-body system into a non-interaction electrons fictitious system under an effective potential, in which the electron density in the fictitious system can represent the ground state density of the real system (Tu, 2008; Daniel, 2014). Under this situation, the kinetic energy of the N-body system is the same as in the Hartree-Fock method and the Coulomb interaction (i.e. exchange and correlation interaction between electrons) is also included inside the fictitious system. Complementary with the Hohenberg-Kohn theorems and Kohn-Sham approach, the energy of the electronic system can now be express as written in Equation 2.19 (Kurth *et al.*, 2003; E., 2016).

$$\mathrm{E[n]} = E_T[n] + E_V[n] + E_J[n] + E_{xc}[n]$$

(Equation 2.19)

where E_T is the kinetic energy functional of non-interacting electron system, E_V is the potential energy of nuclear-electron attraction and nuclear-nuclear repulsion, E_J is the electron-electron repulsion (Coulomb self -interaction of electron density) and E_{xc} is the exchange and correlation functional (electron-electron interaction).

$$E_T[n] = -\frac{1}{2}\sum_i < \psi_i|\nabla^2|\psi_i >$$

(Equation 2.20)

$$E_J[n] = \frac{1}{2}\iint \frac{n(r)n(r')}{r-r'} d^3r d^3r'$$

(Equation 2.21)

$$E_V[n] = \int V_{ext}(r)n(r)d^3r$$

(Equation 2.22)

The first three terms ($E_T[n], E_V[n], and\ E_J[n]$) in Equation 2.19 are known as the universal functionals (non-interacting part) which suitable for every system. The only problem is the exchange and correlation term E_{xc} (interacting part), which is system dependence, undefined and difficult to solve (Köse, 2001; Kurth *et al.*, 2003; Sena, 2010; Chan, 2013). This issue is later solved by the exchange and correlation approximation functionals. Over the past decades, DFT computational method had replaced the HF theory and dominated as the most successful quantum computational method in the prediction and investigation of the electronic properties in solid compounds (Köse, 2001). By using electron density, the complicated 3N variable (N represents the number of electrons) of the wavefunction is replaced by 3 variable spatial coordinated (i.e. *x*, *y*, and *z*) (Sena, 2010). Hence, DFT computational method shows attractive computing performance in larger N-body system. It also provides a good balance among computational cost, time, and accuracy (Foroushani, 2019).

2.1.5 Functionals

As mentioned, there are no exact way but approximation to solve the exchange and correlation (E_{xc}) functional.

$$E_{xc}[n] = E_x[n] + E_c[n]$$

(Equation 2.23)

The E_x term represents the exchange interaction between electrons, while the E_c term represents the correlation interaction between electrons (Nyakung'U, 2015). In DFT, there are plenty of choices of exchange and correlation approximation functionals. According to Jacob's ladder diagram (Murti, 2017; Foroushani,

2019), the accuracy of the computational study is increasing in the ascending order of LDA < GGA < meta-GGA < Hybrid functionals. The computational cost and time also increase accordingly due to the addition of mathematical considerations inside the approximation calculations (Foroushani, 2019). In DFT computational study, the finding of good and suitable E_{xc} functional is significant and challenging (Foroushani, 2019). It directly influences the quality of the computational results.

2.1.5.1 Local density approximation (LDA)

The local density approximation (LDA) introduced by Kohn and Sham is the simplest approximation in E_{xc} functional (Dixit and Antwerpen, 2012). The word "local" indicates that the E_{xc} of the system is dependent only on the electron density at a certain point in space (Köse, 2001; Kurth *et al.*, 2003). It treats electron density as the homogenous electron gas. Equation 2.24 shows the exchange-correlation functional expression of LDA (Kurth *et al.*, 2003; E., 2016).

$$E_{xc}^{LDA}[n] = \int d^3r n(r) e_{xc}^{unif}(n(r))$$

(Equation 2.24)

The $e_{xc}^{unif}(n)$ represents the exchange and correlation energy per particle in homogenous electron gas with partially uniform density (n). The LDA functional finds high accuracy in the molecular system that has locally constant or slowly vary electron density characteristics (Köse, 2001; Dixit and Antwerpen, 2012). Unfortunately, most of the real electronic system are in inhomogeneous circumstances. Hence, the application of LDA functional is limited.

2.1.5.2 Generalised gradient approximation (GGA)

To improve the performance of approximation functional in E_{xc}, a more sophisticated approach is developed. In the generalised gradient approximation (GGA) functional, the mathematical approximation does not only consider the electron density (as in LDA) but also taking account of the electron density's gradient at each point (Köse, 2001). The gradient acts as the function that measures and determines the changes of the electron density due to the non-uniformity of the system (Nyakung'U, 2015). This concept full-fill the inhomogeneity in real case electronic system. Obviously, the uses of gradient corrections in GGA functional exhibits good improvement in DFT quantum computational, especially in the finding of binding energies in a system (Hänninen, 2012). Equation 2.25 shows the E_{xc} functional expression of GGA in the spin unpolarised system (Kurth *et al.*, 2003; E., 2016).

$$E_{xc}^{GGA}[n] = \int d^3r\, f(n(r), \nabla n(r))$$

(Equation 2.25)

Different from LDA which has unique input of e_{xc}^{unif} , the input function of GGA (f) has several formats depending on the type of GGA functionals choose (i.e. PBE and BLYP) (Kurth *et al.*, 2003). Besides, to further enhance the performance of GGA functional, an additional term based on the Kohn-Sham kinetic energy density is added in meta-GGA functional. Equation 2.26 describes the mathematical expression of meta-GGA functional (Kurth *et al.*, 2003).

$$E_{xc}^{meta-GGA}[n] = \int d^3r\, g(n(r), \nabla n(r), \tau(r))$$

(Equation 2.26)

Noted that the $\tau(r)$ represents the kinetic energy density of the Kohn-Sham orbitals and can be further elaborate as (Kurth *et al.*, 2003):

$$\tau(r) = \frac{1}{2}\sum_{i}^{occ} |\nabla\varphi_i(r)|^2$$

(Equation 2.27)

2.1.5.3 Hybrid functionals

Since both of the LDA and GGA functionals show less accuracy in the investigation of the electronic properties of a system (i.e. underestimate the band gaps of around 50% to 100%) (Kurth *et al.*, 2003; Dixit and Antwerpen, 2012), further improvement in the development of exchange and correlation approximation functional is necessary for more reliable and practical data. One of the most successful and accurate E_{xc} approximation functional is the hybrid functional, where the term "hybrid" indicated the mixture of Density Functional Theory (DFT) exchange-correlation with Hartree-Fock exchange (Köse, 2001; Sena, 2010; Nyakung'U, 2015). In hybrid functionals, the correlation energy from the LDA and GGA approximation functionals work together with the Hartree-Fock exchange energy term and the LDA/GGA exchange energy term.

$$E_{xc}^{B3LYP} = (1 - a_0)E_x^{LDA} + a_0(E_x^{HF}) + a_x(E_x^{B88}) + a_c(E_c^{LYP}) + (1 - a_c)(E_c^{VMN})$$

(Equation 2.28)

Among all, the hybrid functional of B3LYP is popular in the investigation of organic compounds. It able to provides satisfying computation data with considerable computing time. The B3LYP functional stands for Becke-3-Lee-

Yang-Parr, is the combination of conventional LDA, GGA (i.e. Becke-1988 (B88), Lee-Yang-Parr (LYP), Vosko, Wilks, Nusair (VWN)) functionals together with HF exchange percentage (Nyakung'U, 2015). Equation 2.28 shows the mathematical expression for B3LYP functional (Murti, 2017) and the coefficients of a_0, a_x, and a_c are 0.20, 0.81, and 0.72.

2.2 Polymorphism

The word "polymorph" comes from Greek language. "poly" stands for the meaning of "many" whereas "morph" represents "form" (Hunt, 2008; Gandhi *et al.*, 2019). The phenomena of polymorphism in chemical substance is not a recent new discovery but have been found long times ago. The contribution made by an English chemist named Smithson Tennant in 1796 based on diamond and charcoal confirmed the existence of polymorphism in chemical compounds. According to Smithson, he stated that "*diamond consists entirely of charcoal, differing from the usual state of the substances only by its crystallized form*" (Meenatchi *et al.*, 2015). This point of view was later supported by Humphry Davy around 1814, who initially questioned the idea of Smithson (Saranya *et al.*, 2018; shodhganga, 2021). Humphry originally stated that two compounds (i.e. diamond and charcoal) with identical chemical nature and composition must have the same physical properties. After a sequence of experimental works, Humphry noticed the significant properties differences between diamond and charcoal and accepted the idea delivered by Smithson.

To date, there is no any actual and satisfactory clarification on the

meaning of polymorphism. Different background researches have different versions of definitions for polymorphs (Nagabalasubramanian, 2012). A well-known and most frequently used explanation for polymorph can refer to the paper reported by Haleblian and McCrone in 1969 (Hunt, 2008; Prasana *et al.*, 2019). The authors stated that the polymorphism phenomena in chemical compounds refer to the ability of a solid compound to exist more than one crystalline forms which difference in structural arrangements or conformations in the crystal lattice (Hunt, 2008; Nagabalasubramanian, 2012; Bahgat and Fraihat, 2015; Prasana *et al.*, 2019). Besides, there are plenty of categorisations in the types of polymorphs. For chemical compounds that have identical chemical structures but different in crystal structures, they can be divided into packing polymorph and conformational polymorph. The packing polymorph refers to the chemical compounds that have identical conformation but different in crystal packing while the conformational polymorph is the opposite of packing polymorph. Moreover, some of the chemical compounds will form co-crystal, salt, and solvate that have chemical and crystal structures different at every composition. These types of polymorphism phenomena are not belonging to either packing polymorph or conformational polymorph, but categorised as Solvatomorph or Pseudopolymorph.

The diversity in the naming schemes of polymorphs sometimes will be very confused. According to U.S Food and Drug Administration, the term "polymorph" can be used for chemical compounds that have structural differences regardless of chemical structures or composition. Under this definition, the hydrated, solvate, and amorphous forms of chemical compounds

can be further simplified and unify as polymorph without detailed categorisation (Nagabalasubramanian, 2012). This idea is also supported by International Conference on Harmonization (ICH) (Dheivamalar *et al.*, 2016; Maache *et al.*, 2016). Even though a chemical compound has the ability to form several polymorphic forms, there is only one polymorphic form allow to appear in stable condition at specific circumstances (i.e. pressure, humidity, temperature, and so on) (shodhganga, 2021).

2.2.1 Formation of polymorphs

Crystallization is one of the useful methods employed by researchers to study the polymorphism phenomena in chemical compounds. Basically, the crystallization of chemical compounds is governed by two main steps (i.e. nucleation and crystal growth). The nucleation process can be categorised into primary nucleation and secondary nucleation (shodhganga, 2021). Primary nucleation refers to the formation of nuclei growth inside the solution while secondary nucleation refers to the seeding process. In the secondary nucleation process, there are already small crystal pieces of the target compound occurred in the solution that prepares for crystallization. Normally, the secondary nucleation method is applied in growing crystals for further modification purposes (shodhganga, 2021).

Several studies had carried out on the subject of polymorphism phenomena in chemical compounds through crystallization. For example, Sridhar and Ravikumar (2009) obtained three different polymorph forms of

lamotrigine drug compounds (i.e. pure lamotrigine, lamotrigine chloride salt, and lamotrigine nitrate salt) through crystallization technique. Chadha *et al.* (2013) also discovered another four new polymorphic forms of lamotrigine drug compound via the crystallization of lamotrigine drug compound with acetic acid, propionic acid, sorbic acid, and glutaric acid. Besides, Hall *et al.* (2018) obtained another new polymorphic form of lamotrigine, named lamotrigine ethanol monohydrate through crystallization method. Although the crystallization method has been widely used by researchers in the discovery of polymorphism in chemical compounds, it is still a challenging task faced by researchers where the possible polymorphic form obtain from the crystallization process is unpredictable. The crystal formation of chemical compounds strongly affected by several factors (i.e. type of solvent, concentration ratio between compound and solvent, temperature, humidity, cooling rate, stirring rate, pressure, and impurity) (Garg and Sarkar, 2016; Pumpo, 2016; Enkelmann *et al.*, 2019). Noted that any of the changes in these factors during the crystallization process may alter the properties of the final product. Therefore, it is difficult to indicate whether a compound will crystallize into one or several crystalline forms, or interacts with the solvent or other molecules in the solution to form crystal.

2.2.2 Characterization of polymorphs

Since the polymorphism phenomena occurred based on the difference in the crystalline structures of a chemical compound, structural analysis is a useful way to identify and investigate the presence of polymorphic forms in chemical substances. There are several choices of experimental methods used to

differentiate the polymorphs. For example, spectroscopic techniques such as Fourier transform infrared spectroscopy (FT-IR), Fourier transform raman spectroscopy (FT-Raman), UV-Vis Spectroscopy, and Nuclear magnetic resonance (NMR) analysis are able to provide fast and roughly idea about the formation of solvate polymorph but faced limitation when dealing with conformational polymorph. Among all, single crystal X-ray diffraction analysis is found to be the most appropriate method for the identification of polymorphism phenomena in chemical compounds since it can provide detailed information about the molecular and crystal geometry structure of the polymorph. In this research, the single crystal X-ray diffraction analysis is chosen as the primary method used to determine the formation of ACV and TP polymorphs based on the crystallized samples. Besides, FT-IR spectroscopy and UV-Vis spectroscopy are also carried out as supporting analysis to verify the reliability of computational results.

2.2.2.1 Single Crystal X-ray Diffraction Analysis

Three-dimensional (3D) arrangements of atoms define the unique structures and properties of materials. For example, diamond and graphite both consist of only carbon atoms. The divergence in the 3D arrangement of carbon atoms caused diamond to have different structures and physicochemical properties from graphite (American, 2007). This signified that structure determination in material is vital since it contains useful information about the properties and characteristics of the compound. However, human eyes are unable to directly identify the structural arrangements of material due to the limitation in the

resolution of wavelength but can obtain it through the X-ray crystallography method.

The history of X-ray crystallography can be traced back to the discovery of X-ray by Wilhelm Conrad Rontagen in 1895 (Hasegawa, 2012; *Wilhelm Conrad Röntgen- Biographical*, 2021). In 1912, Max von Laue introduced the concept of X-ray diffraction pattern during X-ray experiment with copper sulphate crystal (Hasegawa, 2012; Pumpo, 2016). One year later, being idealised by Max von Laue's study, William Henry Bragg and William Lawrence Bragg discovered Bragg's Law which describes the X-ray diffraction phenomena and makes the determination of the positions of atoms mathematically possible (Hasegawa, 2012). So far, there are two common types of X-ray diffraction methods (i.e. single crystal X-ray diffraction method and powder X-ray diffraction method) employed by researchers in the structural determination of material. For the powder X-ray diffraction method, it provides only one-dimensional information about the structure of the solid compound. It is useful when the target sample contains different structure from its parent sample and shows limitation when dealing with conformation polymorph that has identical crystal structure but different in arrangement. By contrast, single crystal X-ray diffraction method is a more complicated and time-consuming analysis since it interprets crystal data in three-dimensionality way. To date, the single crystal X-ray diffraction analysis still remains as the "golden standard" method used to elucidate and characterize the structure of material (Bond, 2016). It able to provide an absolute inside "look" of solid compounds at molecular level (Batsanov, 2010) where the powder X-ray diffraction unable to do it.

Single crystal X-ray diffraction can provide detailed information about the crystalline solid compound including crystal space group, lattice parameters, atomic coordinates, types of atoms, bond distances, bond angles, dihedral angles, and hydrogen bond interactions. This geometry information is significantly important and acts as the main input data for computational calculation in Density Functional Theory. Besides, it also excels in the detection of disorder and defect in crystal compounds. For example, Sun *et al.* (2002) discovered two disorder sites with 50:50 occupancy at the methyl group of theophylline molecule during their single crystal X-ray diffraction study on theophylline monohydrate polymorph. Evidently, the single crystal X-ray diffraction method shows outstanding performances in the determination and identification of polymorphism phenomena in pharmaceutical drug compounds since it is sensitive than other analysis methods (i.e. powder X-ray diffraction, FT-IR, and UV-Vis) (Bunaciu *et al.*, 2015). However, as the name suggested in single crystal X-ray diffraction technique, the target sample must be only in single crystal solid form. This caused the employment of single crystal X-ray diffraction analysis to be difficult since the formation of crystal with good quality and suitable size sometimes can be a tricky process.

The instrument used in the single crystal X-ray diffraction method is known as X-ray diffractometer. Figure 2.1 (a) shows the conceptual diagram of X-ray diffractometer taken from the paper written by Bond (2016). It consists of three basic components: X-ray source, goniometer, and X-ray detector (Bunaciu *et al.*, 2015; Bond, 2016). When a voltage is applied, the heated tungsten filament in the cathode ray tube will produce electrons and accelerate toward the

anode metal (i.e. Cu or Mo), resulting in the formation of X-ray source. The generated X-ray source will shoot the crystal sample and caused diffraction phenomena. This is the basic operation principle in X-ray diffraction techniques. As the incident ray passes through the crystal sample satisfied the condition in Bragg's Law, constructive interference will occur and a peak intensity of diffracted ray can be obtained (Bunaciu *et al.*, 2015). Those diffraction patterns contain important details about the structural content of the crystal sample at the molecular level because each of the solid crystalline compounds has its own unique "fingerprint" diffraction pattern (Pinar, 2017). Equation 2.29 represents the formula of Bragg's Law (Bunaciu *et al.*, 2015).

$$\lambda = 2dsin\theta$$

(Equation 2.29)

The symbol λ is the wavelength of X-ray, d represents the interplanar spacing that generating the diffraction and θ is the diffraction angle of X-ray. In additions, the goniometer in the X-ray diffractometer will simultaneously rotate the crystal sample and X-ray detector. This is to study and determine the diffraction patterns of the crystal sample in more detail multi-dimension areas where the Bragg's law is satisfied and useful diffracted X-rays pattern can be obtained. For X-ray detector, it is rotating in 2θ axis horizontally within the goniometer while the crystal sample is rotating under three types of axis (i.e. ω, ϕ, and χ). The ω-axis and χ-axis are about the horizontal and vertical rotation within the plane of the goniometer while the ϕ-axis is about the horizontal rotation on the mounting plane of the crystal sample. Figure 2.1 (b) illustrates the example of the diffraction pattern (dots structures) obtain from the technical article written by Hasegawa (2012). All the dots (diffracted rays) are detected, collected, and

recorded by the X-ray detector with the help of a charge-coupled device (CCD). The geometry position and intensity of the dots (diffracted rays) are important since they reveal the structural information (i.e. crystal orientation, lattice parameters, atoms types, and coordinates) of the crystal sample (Hasegawa, 2012; Pinar, 2017). Practically, the data collection process, rotation of goniometer, and interpretation of data are performed by researchers with the help of control software and data processing software with specific knowledge in the crystallography area in order to generate reliable output results.

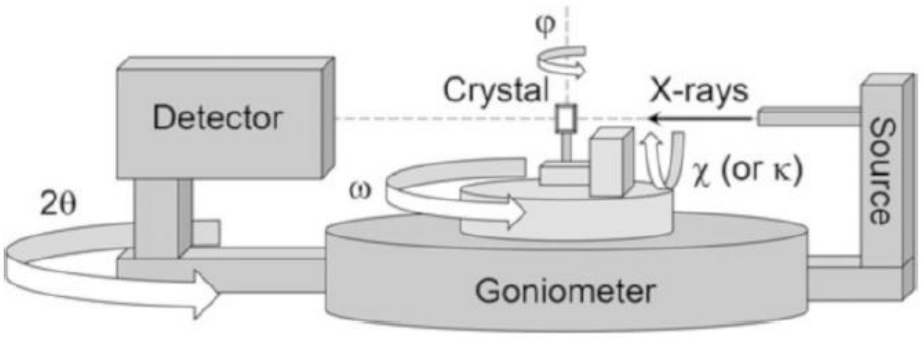

Figure 2.1 (a): The single crystal X-ray diffractometer (Bond, 2016).

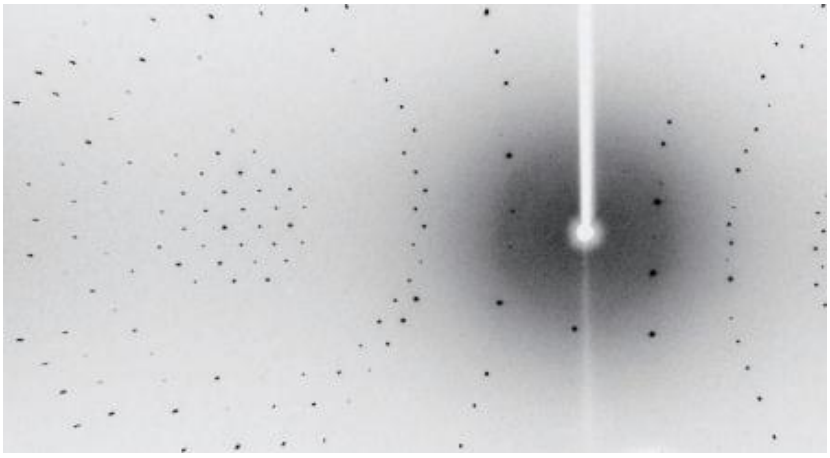

Figure 2.1 (b): The single crystal X-ray diffraction pattern (Hasegawa, 2012).

2.2.2.2 Fourier Transform Infrared (FT-IR) Spectroscopy

Fourier transform infrared (FT-IR) spectroscopy or sometimes known as vibrational spectroscopy, is one of the popular non-destructive analytic methods employed by researchers to identify unknown material (Duygu *et al.*, 2009; Bunaciu *et al.*, 2010). It offers wide ranges of applications based on its remarkable sensitivity in the detection of the change in functional groups (Bhattacharyya, 2015). For example, FT-IR is adopted for quality control purposes (Co., 2019). When a measured sample is contaminated, the changes in molecular structures and functional groups will cause disparity in the FT-IR vibrational spectrum with reference data. Thereby, largely simplified the quality checking process in the industry. Besides, it also has explicit importance usage in the determination of polymorphism phenomena in chemical compounds, especially for hydrate, solvate, and co-crystal types of polymorphs. As an example, the FT-IR absorption peaks between band regions 3500 cm^{-1} to 3700 cm^{-1} indicated the presence of hydrate polymorphic form in ampicilline since it shows different FT-IR vibrational spectrum with anhydrous ampicilline (Bunaciu *et al.*, 2010). The basic operating principle of FT-IR spectroscopy is briefly mentioned in the papers written by Babrah *et al.* (2007) and Bunaciu *et al.* (2010). It monitors and distinguishes the interactions different between bonded atoms at the molecular level based on their vibrational activities. This is because the energy generated by the infrared (IR) radiation is low and insufficient to cause electron transition in the target sample but enough for vibrational changes within molecules (Bunaciu *et al.*, 2010). During the FT-IR analysis, the IR radiations will be absorbed by the target sample at particular

frequencies, resulting in either stretching or bending vibrational interactions between the covalent bonded atoms. Those absorbed IR radiations are then plotted against with the wavelength of light in the form of absorption peaks. Each of the peaks in the FT-IR vibrational spectrum gives informative data about the types of functional groups presented in the target sample. Besides that, the intensity of the absorption peaks correspond to the number of functional groups in the target sample is also provided by the analysis (Co., 2019). Consequently, FT-IR spectroscopy has the ability to characterize chemical compounds through the probing on the chemical bond vibration patterns since each of the chemical substances has its own unique "biochemical fingerprint" of FT-IR spectrum diagram.

Commonly, the FT-IR instrument contains five elements: the source, interferometer, target sample, detector, and data interpreting software (Co., 2019). Figure 2.2 illustrates the basic idea of the FT-IR spectroscopy experiment (Co., 2019). Firstly, the infrared (IR) radiation generated from the black-body source will pass through an interferometer for "spectral encoding" purposes. At this step, the interferometer cooperates with the beam-splitter to produce an "interferogram" signal that contains all the unique information about every IR frequencies generated from the source. This process is necessary as it ensures the simultaneous measurement of IR frequencies in the target sample. In the form of "interferogram" signal, the IR radiations will then hit and pass through the target sample. Meanwhile, all the IR radiation activities (i.e. absorption and transmission) in the "interferogram" signal are measured and collected by an IR detector. After that, the FT-IR interpreting software will decode and analyse the

collected data in order to convert the “interferogram” format data into frequency spectrum format through Fourier Transform (FFT) mathematical method (Co., 2019).

There is three categorisations of infrared (IR) radiation ranges employed by researches during FT-IR analysis. The range are far-infrared (10 cm^{-1} to 400 cm^{-1}), mid-infrared (400 cm^{-1} to 4000 cm^{-1}), and near-infrared (4000 cm^{-1} to 13000 cm^{-1}) (Duygu *et al.*, 2009; Bunaciu *et al.*, 2010). Among three of them, researchers prefer to use mid-IR because vast majority of chemical substances tend to exhibit infrared bands in this range (Bunaciu *et al.*, 2010). For example, the FT-IR vibrational spectrum obtained by Meenatchi *et al.* (2015) using mid-IR ranges show satisfactory agreement with the structure of (E)-N’-(4-Isopropylbenzylidene) furan-2-carbohydrazide monohydrate ($C_{15}H_{18}N_2O_3$) compound. The authors realized that band regions 3112 cm^{-1} and 3134 cm^{-1} are correspondence to the C-H stretching vibration mode from the aromatic ring of $C_{15}H_{18}N_2O_3$ molecular system while band region 3424 cm^{-1} is related to N-H stretching vibration mode. Furthermore, Gandhi and Joshi (2018) confirmed the formation of strontium tartrate from the mixture of eosin with strontium chloride using mid FT-IR experiment since they obtained carbonyl group C=O stretching vibrational modes between band regions 1591 cm^{-1} to 1588 cm^{-1}. In additions, the authors also realized the presence of water molecule inside the strontium tartrate crystal because the absorption peak around 3400 cm^{-1} is assigned to O-H stretching vibrational mode. Unlike other methods, FT-IR spectroscopy is a more convenient and user-friendly technique. It allows the target sample to be prepared in either solid crystal, powder, or liquid states (Duygu *et al.*, 2009;

Bunaciu *et al.*, 2010).

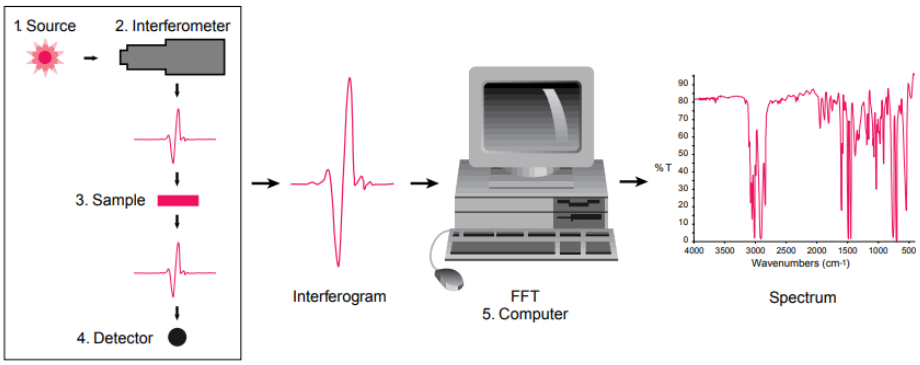

Figure 2.2: The instruments in FT-IR (Co., 2019).

2.2.2.3 Ultraviolet-Visible (UV-Vis) Spectroscopy

Ultraviolet-visible (UV-Vis) spectroscopy is a useful quantitative and qualitative analytic method applicable in huge ranges of chemical substances (Rocha *et al.*, 2018). It can be used to analyse the rate of reaction in chemical compounds based on the change in the concentration of chemical substances and the absorbance of UV-Vis radiation. It is also widely adopted for quality control purposes, especially in ink, paint, and dye industries (RSC, 2009). As an example, with the employment of the UV-Vis spectroscopy technique, Ramya *et al.* (2013) realized that storage temperature will evidently affect the quality of the lamotrigine drug compound. Besides, UV-Vis spectroscopy is also used for the study and determination of the dissolution rate in pharmaceutical drug compounds. In addition to the applications mentioned previously, UV-Vis analysis also elucidates outstanding performance in the determination of band gap energy which potent for photocatalysis study in chemical compounds (Rocha *et al.*,

2018). By using ethanol and water as the medium for UV-Vis spectroscopy analysis, Karabacak *et al.* (2012) successfully obtained 5.216 eV and 5.238 eV band gap energies for 4-butyl benzoic acid. The authors reported that both of the experimental band gap energy results are compatible with computational data. Barim and Akman (2019) also determined the band gap energy of N-(2-acetylbenzofuran-3-yl) acrylamide through the UV-Vis spectroscopy analysis. From the output data, the experimental absorption wavelength for N-(2-acetylbenzofuran-3-yl) acrylamide in dichloromethane and ethanol mediums are found to be 313 nm and 311 nm, which correspondence well with computational data (356 nm and 359 nm).

The UV-Vis spectroscopy is a type of absorption spectroscopy. Its working principle is based on the UV-Vis wavelength absorption behaviours of atoms inside the chemical compounds. During the analysis, the UV-Vis radiation beam covers a wide range of wavelengths. Each of the wavelengths consists of a particular amount of energy. When the light energy at a particular wavelength satisfied the condition for electron transition, the electrons in the target sample will be excited from a lower energy level (ground state) to a higher energy level (excitation state) (Holmes-Hampton *et al.*, 2014), resulting in the absorption of UV-Vis radiation wavelength. There are a total of six possible combinations of electron transitions in chemical compounds. For example, $\sigma \rightarrow \sigma^*, \sigma \rightarrow \pi^*, \pi \rightarrow \sigma^*, \pi \rightarrow \pi^*, n \rightarrow \sigma^*$, and $n \rightarrow \pi^*$. The σ represents the sigma bonding orbital, π represents the pi-bonding orbital, n represents the non-bonding orbital (lone pair) while symbol "$*$" indicates anti-bonding orbital (RSC, 2009). Commonly, the wavelengths used in the UV-Vis spectroscopy analysis are between the

ranges of 200 nm to 800 nm. This is because the wavelengths below 200 nm (vacuum UV-light) and above 800 nm (infrared light) show low practical usefulness in the UV-Vis spectroscopy experiment (Rocha *et al.*, 2018). Under these ranges, only $n \rightarrow \pi^*$ and $\pi \rightarrow \pi^*$ types of electron transitions are observable in the target sample. Equation 2.30 states the Beer-Lambert law for UV-Vis spectroscopy experiment, where A_{sb} is the absorbance of the sample, I_0 is the intensity of light passed through the reference cell (blank/background), I is the intensity of light passed through the target sample, ε is the molar absorbtivity, C is the molar concentration of solute and L is the path length of sample cell in centimetre unit.

$$A_{sb} = log_{10} \frac{I_0}{I} = \varepsilon CL$$

(Equation 2.30)

It acts as the main operating equation and perfectly describes the absorption phenomena in the target sample. As the target sample is shooting through by UV-Vis radiation beam, the decrease in the input UV radiation intensity (I) at a particular wavelength indicates the absorption activities of the target sample. Consequently, the absorbance of the target sample can be determined. Besides, the Beer-Lambert law equation also indicates that the absorbance will increase proportionally with the concentration of the target sample. Since it is well-known that the energy required for electrons to "jump" from the ground state to the excitation state is equal to the absorbed wavelength energy, the absorbed wavelength (λ) plays important role in the measurement of the band gap energy (ΔE). Equation 2.31 states the mathematical expression for the band gap energy, where h is the Planck's constant, v is the frequency, c is the speed of light, and λ is the wavelength.

$$\Delta E = hv = \frac{hc}{\lambda}$$

(Equation 2.31)

Figure 2.3 shows the instruments used in the UV-Vis spectroscopy experiment. (Soderberg, 2019). The UV-Vis spectrophotometer consists of three elements: source, sample, and detector. For the UV-Vis radiation source, it is generated by two different components (i.e. Tungsten lamp and Deuterium lamp). The former responsible for the generation of visible light while the latter takes part in the production of ultraviolet light. Both of the light sources are then directed into a monochromator to generate a UV-Vis radiation light source with wavelengths of 200 nm to 800 nm. After that, the UV-Vis radiation beam will hit the target sample and the absorption activities of the wavelengths will be detected and recorded by the detector. A UV-Vis transmittance graph will be generated (absorbance vs. wavelength) as the output result. From the plotted graph, the highest peak (λ_{max}) is the most interested point because it contains informative data about the target sample (Rocha *et al.*, 2018). Practically, the target sample for the UV-Vis spectroscopy experiment must be prepared in liquid state form. The water and alcohol are often selected as the dissolve solvents (blank) due to their excellent transparency ability in UV-Vis radiation. Sometimes, acetone and dimethylformamide (DMF) will be picked as an alternative solvent when dealing with chemical substances that are poorly soluble in water and alcohol. There exists of limitation in the usages of acetone and DMF, since both of them only suitable for chemical substances that have wavelength cut-off value above 320 nm (Rocha *et al.*, 2018).

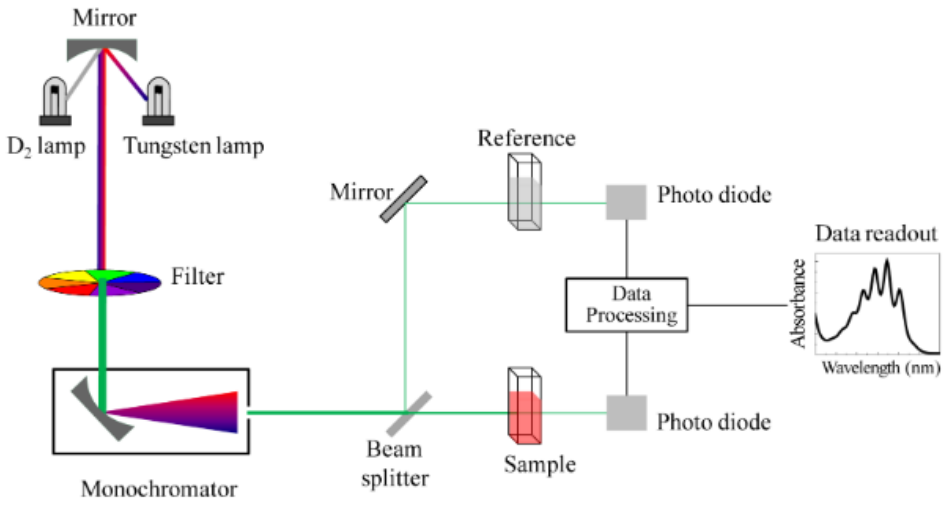

Figure 2.3: The instruments in UV-Vis spectroscopy (Soderberg, 2019).

2.3 Active Pharmaceutical Ingredients (APIs)

In medicine, there are usually have several components mix together to perform specific therapeutic effects. It can be divided into two main parts: active pharmaceutical ingredients (APIs) and excipient. The active pharmaceutical ingredients (APIs) refer to the part of a drug that is biologically active and is able to perform pharmacological activities during the treatment of disease (ScienceDaily, 2014; Stone, 2020; Corp, 2021; NPRA, 2021). On the contrary, the excipient represents the inactive part of the drug. It does not directly involve in the treatment process (Corp, 2021). Some of the examples of excipient in drug compounds are the colouring agents, absorption enhancers, wetting agents, and solvents. In this research study, both the acyclovir (ACV) and theophylline (TP) organic drug compounds are categorised as the family members of APIs.

According to the studies made by Raza *et al.* (2014) and Karpinski (2006), majority (more than 50%) of active pharmaceutical ingredients (APIs) tend to form polymorphism easily. The difference in the formation of polymorphism may affect the physicochemical properties of the APIs drug compounds in terms of melting point, stability, solubility, toxicity, hardness, dissolution rate, hygroscopicity, and so on. Consequently, the properties will affect the bioavailability, safety, and therapeutic performances of the APIs drug compounds (Fucke *et al.*, 2012). Besides, the polymorphism phenomena in APIs drug compounds not only show impacts in the drug performance but also in drug formulation and manufacturing processes. The drug formulation refers to the mixing of primary APIs components with suitable excipient substances. Each of the formulation recipes developed by drug developers may lead to different chemical functional groups presented inside the APIs drug compounds, depending on the polymorphism ability of APIs components with excipients. Moreover, some of the APIs drug compounds tend to form hydrate crystalline structures easily due to the hydrogen bonding phenomena and the availability of the various type of functional groups (ScienceDaily, 2014). The state of hydration in APIs drug compounds shows impacts on its physical properties, pharmaceutical performance, and drug processability (Chan *et al.*, 2014).

The study of polymorphism phenomena and hydrated behaviours of APIs drug compounds are significantly important, especially in the pharmaceutical industry. It helps to avoid the drug patent regulation issues and at the same time produces a drug compound with different formulation but has the same or better clinical performances. Normally, drug developers tend to formulate and produce

APIs drug compound that is biologically safe and has satisfactory therapeutic performance with stable pharmacokinetic and pharmacodynamics characteristics. There are some guidelines to identify the performance of polymorphism in APIs drug compounds. Polymorphic form with the lowest energy always has the greatest stable thermodynamic form. It will avoid the alteration of drug compound caused by the surrounding temperature, humidity, and so on which will bring cost damage and pharmaceutical performance defect during the development, manufacturing, delivery, and storage stages. Refer to the same reasons, the metastable forms should be avoided. Although the physical stability performances of metastable forms are good but they also exhibit poor chemical stability performance at the same time. Basically, the most thermodynamically stable crystalline structure of an APIs component will be considered and used in the formulation of commercial APIs drug products.

2.3.1 Acyclovir (ACV)

Gertrude Belle Elion who was the inventor and developer of ACV drug compound, was awarded the 1988 Nobel Prize in Medicine (Sarkar and Rohani, 2015). ACV with the IUPAC named of 2-amino-1, 9-dihydro-9-[(2-hydroxuethoxy) methyl]-6H-purin-6-one, has the chemical formula of $C_8H_{11}N_5O_3$. Even though ACV was being discovered past few decades, it still maintains its popularity and acts as the first-line treatment in α-type Herpes Viruses, including Herpes Simplex Virus Type 1 (HSV-1), Type 2(HSV-2), and Varicella Zoster (VZV) diseases (i.e. chickenpox, cold sore, and shingles) (Masuda *et al.*, 2012; Sarkar and Rohani, 2015; Cai *et al.*, 2017; Poole and James,

2018). The absence of 3'-hydroxyl group in the acyclic side chain of ACV inhibits the replication of viral DNA with the help of virus encoded thymidine kinase (TK). The enzyme TK converts the ACV into monophosphate derivative and triphosphate derivative forms during the diphosphorylation and triphosphorylation processes. The high concentration of ACV triphosphates in the HSV and VZV infected cells filled up the next space positions of the viral DNA polymerase. The lack of 3'-hydroxyl group in ACV triphosphates terminated the growth of viral DNA chains, subsequently turned the infected viral DNA polymerase become inactive (Herpesviruses, 2007; Salvaggio and Gnann Jr, 2017). ACV has the advantages of low HSV resistance and low cytotoxicity (Meepripruk *et al.*, 2016).

However, there are several problems encountered by ACV during the treatment sections. According to the Biopharmaceutical Classification System (BSC), ACV is categorised as a Class IV drug that has low bioavailability, low solubility, and low permeability (Masuda *et al.*, 2012). These factors strongly influence the in-vitro and in-vivo absorption activities of ACV. The oral bioavailability of ACV is just about 15% to 30% and the half-life for ACV is considered short with only three hours (Masuda *et al.*, 2012; Cai *et al.*, 2017). The plasma concentration of ACV occurred between 90 minutes to 150 minutes. Besides, the low transdermal absorption rate of ACV caused it unable to penetrate the skin easily (Yan *et al.*, 2013). Based on these characteristics, a challenging task faced by drug and material researchers is how to improve the physicochemical properties and therapeutic performances of the ACV drug compound.

Since ACV is categorised as an APIs drug compound, one of the reliable ways is through the formation of polymorphisms. Literature surveys reveal that the ACV drug compound has good ability in the formation of polymorphisms. For example, Birnbaum *et al.* (1984) synthesised one of the monoclinic hydrated polymorphic forms of ACV from aqueous dimethylformamide. This ACV polymorphic form was later used as the commercial form of the ACV drug compound. Lutker *et al.* (2011) discovered another three new ACV polymorphic forms (i.e. two monoclinic anhydrous forms and one triclinic hydrated form) via crystallization technique. Two years later, Terada *et al.* (2013) discovered an orthorhombic anhydrous form of ACV during the crystallization process of commercial ACV compound with N, N-dimethyl formamide solution and acetonitrile. Moreover, with the purpose of enhancing the solubility and permeability in the ACV drug compound, Yan *et al.* (2013) successfully obtained three different salt and co-crystal polymorphic forms of ACV using maleic acid, fumaric acid, and glutaric acid. The authors figured out that the ACV polymorphic forms with fumaric acid and glutaric acid show better permeability than commercial ACV form because both of them exhibit lower melting point and higher lipophilicity (lop P) value than commercial ACV. On the other hands, ACV polymorphic form with maleic acid shows lower permeability characteristic than commercial ACV. These signified that the study of polymorphism in APIs drug compounds is important because the formation of different polymorphic forms will not only enhance the pharmaceutical performances but may also degrade it. Sarkar and Rohani (2015) synthesised another new triclinic polymorphic form of ACV with fumaric acid which differs from the findings with Yan *et al.* (2013). Table 2.1 lists the examples of ACV

polymorphic forms discovered by researchers.

Table 2.1: Polymorphic forms of ACV.

Chemical Formula	Space Group	a (Å)	b (Å)	c (Å)	α (°)	β (°)	γ (°)
$3[C_8H_{11}N_5O_3].2[H_2O]$ (Birnbaum *et al.*, 1984)	Monoclinic	25.459	11.282	10.768	90.000	95.160	90.000
$C_{11}H_{13}N5O3.2[H_2O]$ (Suwińska *et al.*, 2001)	Triclinic	8.450	11.665	14.930	75.440	76.650	86.440
$C_8H_{11}N_5O_3$ (Lutker *et al.*, 2011)	Monoclinic	10.912	11.131	7.884	90.000	108.262	90.000
$C_8H_{11}N_5O_3$ (Lutker *et al.*, 2011)	Monoclinic	4.750	15.120	28.680	90.000	91.160	90.000
$C_8H_{11}N_5O_3.2[H_2O]$ (Lutker *et al.*, 2011)	Triclinic	6.800	11.332	14.937	82.722	82.502	89.323
$C_8H_{11}N_5O_3.2[H_2O]$ (Montha, 2012)	Triclinic	6.900	11.417	15.081	82.595	82.395	89.368
$C_8H_{11}N_5O_3.C_4H_6O_6$ (Masuda *et al.*, 2012)	Monoclinic	11.709	14.960	4.602	90.000	100.601	90.000
$C_8H_{11}N_5O_3$ (Terada *et al.*, 2013)	Orthorhombic	4.539	15.031	28.332	90.000	90.000	90.000
$C_8H_{11}N_5O_3$ (Terada *et al.*, 2013)	Monoclinic	10.940	11.184	8.116	90.000	108.628	90.000
$C_8H_{11}N_5O_3.2[H_2O]$ (Terada *et al.*, 2013)	Triclinic	6.838	11.368	14.942	82.845	82.419	89.326
$C_{12}H_{14}N_5O_7$ (Yan *et al.*, 2013)	Triclinic	8.753	12.863	14.033	67.419	86.643	74.314
$C_{14}H_{21}N_5O_{11}$ (Yan *et al.*, 2013)	Monoclinic	21.318	6.490	29.435	90.000	103.906	90.000
$C_8H_{11}N_5O_3.\ C_5H_8O_4$ (Yan *et al.*, 2013)	Triclinic	8.185	8.848	11.657	70.210	86.985	80.948
$C_{24}H_{36}N_{10}O_{17}$ (Sarkar and Rohani, 2015)	Triclinic	6.534	11.023	23.529	97.730	91.930	105.330

2.3.2 Theophylline (TP)

Theophylline (TP) or commonly known as methylxanthine, with the IUPAC named of 1, 3-dimethyl-7H-purine-2, 6-dione, has the chemical formula of $C_7H_8N_4O_2$. It was being discovered by Albert Kossel in 1888 from cocoa beans and tea leaves (Fucke *et al.*, 2012; Gong *et al.*, 2018). The first application of TP is used as a diuretic agent. Later, its bronchodilator properties were being discovered by researchers in 1922. TP is an FDA-approved drug compound which widely used in the treatment of respiratory diseases such as asthma and chronic obstructive pulmonary disease (COPD) (Aitipamula *et al.*, 2009; Zhang and Fischer, 2011; Gong *et al.*, 2018). It is mainly used as a muscle relaxant, vasodilator, and bronchodilator agent (Ebisuzaki *et al.*, 1997). As a PDE inhibitor, TP increases the concentration of intracellular cyclic 3', 5' adenosine monophosphate (cAMP) and cyclic 3', 5' guanosine monophosphate (cGMP) through the breakdown of cyclic nucleotides in muscle and inflammatory cells. These mechanisms work to relax the muscle and provide anti-inflammatory properties to the airway system (Barnes, 2013). Research studies reveal that the TP drug compound has low aqueous solubility and physical stability (Andrei, 2011). This caused a higher dosage of TP is required to achieve a maximal relaxation effect in muscle. Due to this reason, the clinical usage of TP is limited and made it become the third-line treatment in respiratory diseases (Barnes, 2013).

Although TP has several weaknesses, it still maintained its popularity in the pharmaceutical industry since TP is easily available from plants and cheap

in price. So far, drug and material researchers still put a lot of effort into the finding of suitable TP polymorphic forms in order to enhance the pharmaceutical performances and applications of TP. Zaitu *et al.* (1995) characterized one of the monoclinic hydrated polymorphic forms of TP via the crystallization of TP with 5-fluoro-uracil in water. Two years later, Ebisuzaki *et al.* (1997) successfully obtained a new orthorhombic anhydrous form of TP. Besides, with the purpose of improving the physical stability of the TP drug compound, Aitipamula *et al.* (2009) discovered a new triclinic co-crystal polymorphic form of TP through the crystallization technique of TP with gentisic acid and methanol. Zhang and Fischer (2011) synthesised another new monoclinic anhydrous polymorphic form of TP via the crystallization process of commercial TP with chloroform and methanol. Furthermore, Fucke *et al.* (2012) obtained four different polymorphic forms of TP (i.e. two orthorhombic anhydrous forms and two monoclinic hydrated forms). The authors realized the physicochemical properties differences (i.e. thermodynamic properties and the strength of hydrogen bonds) among four of the TP polymorphic forms. Kakkar *et al.* (2018) discovered six new co-crystal polymorphic forms of TP using picolinamide (PIC), 3,4-dichlorobenzoic acid (DCB), 4-chloro-3-nitrobenzoic acid (4C*l*3NB), 4-fluoro-3-nitrobenzoic acid (4F3NB), p-hydroxybenzamide (NBEN), and acetazolamide (ACZ). Table 2.2 tabulates the examples of TP polymorphic forms synthesised by researchers.

Table 2.2: Polymorphic forms of TP.

Chemical Formula	Space Group	a (Å)	b (Å)	c (Å)	α (°)	β (°)	γ (°)
$2[C_7H_8N_4O_2]. C_4H_3FN_2O_2. H_2O$ (Zaitu *et al.*, 1995)	Monoclinic	7.640	8.804	32.126	90.000	98.280	90.000
$C_7H_8N_4O_2$ (Ebisuzaki *et al.*, 1997)	Orthorhombic	24.612	3.830	8.501	90.000	90.000	90.000
$C_7H_8N_4O_2. H_2O$ (Sun *et al.*, 2002)	Monoclinic	4.468	15.355	13.121	90.000	97.792	90.000
$C_7H_8N_4O_2. C_7H_6O_4$ (Aitipamula *et al.*, 2009)	Triclinic	7.099	8.054	13.034	86.080	81.270	74.140
$C_7H_8N_4O_2$ (Zhang and Fischer, 2011)	Monoclinic	7.894	12.909	15.906	90.000	104.214	90.000
$C_7H_8N_4O_3$ (Fucke *et al.*, 2012)	Orthorhombic	13.087	15.579	3.863	90.000	90.000	90.000
$C_7H_8N_4O_4$ (Fucke *et al.*, 2012)	Orthorhombic	24.330	3.771	8.485	90.000	90.000	90.000
$C_7H_8N_4O_2. H_2O$ (Fucke *et al.*, 2012)	Monoclinic	4.461	15.321	13.053	90.000	97.511	90.000
$C_7H_8N_4O_2. H_2O$ (Fucke *et al.*, 2012)	Monoclinic	4.416	15.168	12.922	90.000	97.511	90.000
$C_7H_9N_4O_2^+. BF_4^-$ (Buist *et al.*, 2014)	Monoclinic	13.088	6.041	14.554	90.000	115.306	90.000
$C_7H_9N_4O_2^+. Cl^-. H_2O$ (Buist *et al.*, 2014)	Orthorhombic	13.866	6.462	11.363	90.000	90.000	90.000
$C_7H_9N_4O_2^+. Br^-. H_2O$ (Buist *et al.*, 2014)	Orthorhombic	14.012	6.615	11.530	90.000	90.000	90.000

Table 2.2 Continued.

Chemical Formula	Space Group	a (Å)	b (Å)	c (Å)	α (°)	β (°)	γ (°)
$C_7H_9N_4O_2^+$. Cl^- (Buist *et al.*, 2014)	Monoclinic	32.081	4.503	12.826	90.000	103.524	90.000
$2(C_7H_8N_4O_2).C_7H_7NO_3$ (Fernandes *et al.*, 2015)	Monoclinic	10.451	12.425	17.995	90.000	99.758	90.000
$C_7H_8N_4O_2$. $C_7H_7NO_2$ (Fernandes *et al.*, 2015)	Triclinic	7.021	8.779	13.108	96.893	90.832	115.464
$C_7H_8N_4O_2$. $2(C_7H_4Cl_2O_2)$ (Chan *et al.*, 2014)	Triclinic	10.191	10.459	12.777	98.98	108.898	108.434
$C_7H_8N_4O_2$. $C_4H_6N_4O_3S_2$ (Kakkar *et al.*, 2018)	Monoclinic	42.668	4.952	16.838	90.000	106.575	90.000
$C_7H_8N_4O_2$. $C_7H_7NO_2$ (Kakkar *et al.*, 2018)	Orthorhombic	8.022	14.308	25.258	90.000	90.000	90.000
$C_7H_8N_4O_2$. $C_7H_4FNO_4$ (Kakkar *et al.*, 2018)	Triclinic	7.203	14.913	16.014	63.098	86.349	84.677
$2(C_7H_8N_4O_2)$. $C_6H_6N_2O$ (Kakkar *et al.*, 2018)	Triclinic	8.060	9.605	14.240	96.817	99.412	103.672
$C_7H_8N_4O_2$. $C_7H_4ClNO_4$ (Kakkar *et al.*, 2018)	Triclinic	7.064	15.147	15.438	69.624	81.819	86.324

2.4 Geometry Optimization

Geometry optimization or sometimes known as geometry relaxation, is the energy minimization process that aims to find the equilibrium and stable ground-state geometry arrangement of atoms in a molecular system (Narayan, 2012; Nyakung'U, 2015; Ul-Haq, 2016; Abdullahi, 2018). The geometry optimization process tends to locate a stationary point on the Potential Energy Surface (PES) where the total energy of the system is said to be at a minimum. In computational chemistry, geometry optimization is necessary and important. It should be performed before starting any other computational analysis (*Computational Chemistry*, 2021). The main purpose of geometry optimization is to obtain the approximated ground-state molecular geometry structure that is closer or identical to the geometry arrangement of a substance that can be found naturally in the world (Nyakung'U, 2015; Ul-Haq, 2016). Under optimized conditions, the net interatomic force acting between atoms is approximately close to zero (Nyakung'U, 2015; Ul-Haq, 2016). This indicates that the pushing and pulling interactions between atoms are at a minimum state. Such conditions will lead to an equilibrium and stable (ground-state) form. This optimized geometry structure is useful for a variety of computational and experimental studies.

The convergence ability for geometry optimization calculation strongly depends on the initial input geometry. A sensible input geometry coordinates are employed and modified iteratively according to the computational software to reach a convergence situation. At each of the modified geometry structures, the total energy and the wave function are computed and calculated across the PES.

Computational software itself will decide the distance and direction for the next geometry optimization steps (Narayan, 2012). Refer to this reason, the use of suitable and appropriate atomic coordinates can speed up the computational time by reducing the optimization cycles. Hence, greatly improve the robustness of the geometry optimization process (Reveles and Köster, 2004). The most easier and logical way to perform geometry optimization is to use the experimental data obtained from single crystal X-ray diffraction techniques as the input source (Narayan, 2012). There are two ways to express the geometry coordinates for a molecular system (i.e. Cartesian coordinate and internal coordinate). The Cartesian coordinate expresses the atomic positions in x, y, z axes while the internal coordinate describes the geometry structure using bond distances, bond angles, and dihedral angles (Schlegel, 2011; Ul-Haq, 2016). As compared with the Cartesian coordinate format, the internal coordinate provides more descriptive information about the chemical structure and bonding scheme of a molecular system during geometry optimization calculation (Schlegel, 2011). Figure 2.4 (a) and (b) show the difference between Cartesian coordinate and internal coordinate in a water molecule.

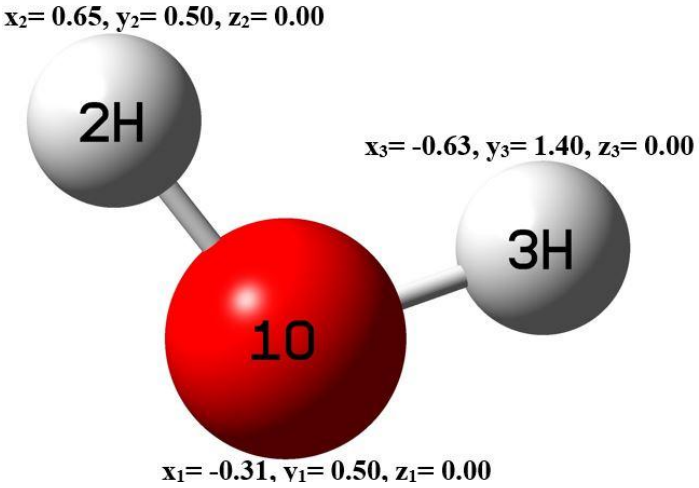

Figure 2.4 (a): Cartesian coordinate of a water molecule.

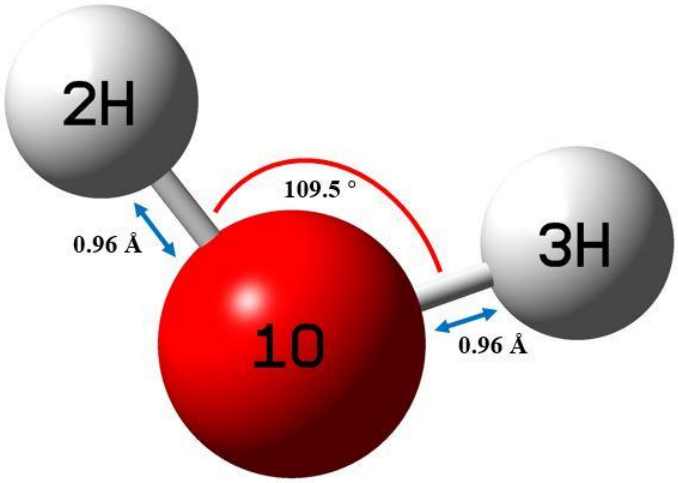

Figure 2.4 (b): Internal coordinate of a water molecule.

2.5 Potential Energy Surface (PES)

Potential Energy Surface (PES) is a mathematical representation that reveals the total energy of a molecular system as a function of molecular geometry (Schlegel, 2011). It helps to monitor the change of total energy and wave function based on

the variation in molecular geometry structure during the optimization process. By using single point energy calculation, each of the total energies and wave functions corresponding to different geometry structures is computed and move across the PES. The geometry optimization process is said to be complete and successful when a stationary point is found on the PES. A stationary point refers to the point where the force and gradient are equal to zero (Foresman and Frisch, 1996; Nyakung'U, 2015). Figure 2.5 shows the model for PES. It looks like a hilly landscape containing valleys, peaks, and mountain passes (Schlegel, 2011). In PES, the stationary point might locate at the global minima, local minima, and saddle point. Global minima represents the most stable geometry arrangement where the total energy of the system is at a minimum (ChemViz, 2000). Saddle point at minima indicates that the optimization calculation is complete at the transition state. Theoretically, a geometry optimization process is said to be completed when the force, force root-mean-square, next step displacement, and displacement root-mean-square are all equal to zero. Unfortunately, the practical values are not always reached exactly zero when it comes to the real geometry optimization process. So that several convergence criteria have been set up by computational software to determine the completeness of geometry optimization calculation. For example in Gaussian 09 software package, for any system that has a force below the cut-off value of 0.0005, force root-mean-square tolerance of 0.0003, next step displacement below cut-off value of 0.0018, and displacement root-mean-square cut off value of 0.0012, the geometry optimization is said to be done and converged (Foresman and Frisch, 1996).

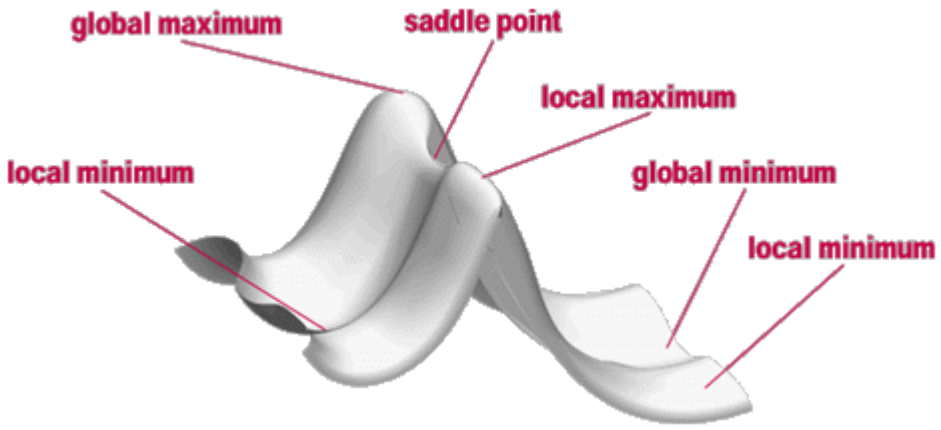

Figure 2.5: The model of Potential Energy Surface (PES) (Foresman and Frisch, 1996; *Studying Chemical Reactions with Gaussian*, 2021).

2.6 Molecular Orbital (MO)

Molecular orbitals (MOs) are formed by combining the atomic orbitals of atoms in a molecular system (Chemistry LibreTexts, 2016). Same with atomic orbitals, MO describes the wave-like behaviour of electrons in a molecule using a mathematical approach. MO is informative as it is able to determine the physicochemical properties of a molecular system. Besides, it is capable to predict the regions that have the possibility to obtain electrons. In this research work, the main concern MOs are the HOMO and LUMO which play dominant role in the determination of molecular properties. Sometimes, HOMO and LUMO are known as Frontier Molecular Orbitals (FMOs). HOMO is the acronym for the highest occupied molecular orbital while LUMO stands for the lowest unoccupied molecular orbital. HOMO is the outermost orbital containing electrons whereas LUMO is the innermost empty orbital (Ibeji *et al.*, 2016). In

FMOs, the excitation of one electron from the ground state to 1st excited state refers to the one electron absorption process from HOMO to LUMO (Drissi *et al.*, 2015). The HOMO energy measures the electron donating ability while the LUMO energy shows the electron gaining ability. Both the HOMO and LUMO energies are popular quantum chemical descriptors. The difference between HOMO and LUMO energies is known as the HOMO-LUMO energy gap. Three of them (i.e. HOMO energy, LUMO energy, and HOMO-LUMO energy gap) have significant features in the characterization and determination of chemical reactivity, kinetic stability, electronic, and optical properties of a molecular system (Bahgat and Fraihat, 2015; Rahmani *et al.*, 2018). Moreover, they also determine the way molecule interacts with other species (Narayan, 2012). For example, if a substance is said to have a narrow HOMO-LUMO energy gap, it will have low kinetic stability, high chemical reactivity, soft, and more polarizable (Bahgat and Fraihat, 2015; Ceylan *et al.*, 2016; Rajalakshmi and Nayak, 2017). In additions, HOMO energy is directly related to ionization energy while the LUMO energy has a direct relationship with electron affinity (Prasad and Ojha, 2018). According to Koopmans theorem, the global reactivity descriptors (i.e. ionization energy (IE), electron affinity (EA), hardness (η), chemical potential (μ), softness (S), electronegativity (χ), and electrophilicity index (ω)) can be obtained from HOMO and LUMO energy via the formulas (Asath *et al.*, 2017):

$$IE = -E_{HOMO}$$

(Equation 2.32)

$$EA = -E_{LUMO}$$

(Equation 2.33)

$$\eta = (IE - EA)/2$$

(Equation 2.34)

$$\mu = -(IE + EA)/2$$

(Equation 2.35)

$$S = 1/(2\eta)$$

(Equation 2.36)

$$\chi = (IE + EA)/2$$

(Equation 2.37)

$$\omega = \mu^2 S$$

(Equation 2.38)

These global descriptors have potent usage in the description of the chemical reactivity of a molecular system. The energy barrier of electrons can be obtained through electron affinity and ionization potential (Ceylan *et al.*, 2016). The ionization energy represents the amount of energy required to remove an electron from an occupied orbital while the electron affinity measures the amount of energy loss when an electron is added to an empty orbital (Asath *et al.*, 2017). The electronegativity and chemical potential determine the escaping ability of electrons (Ali *et al.*, 2017). Hardness and softness predict the chemical stability of a system (Ali *et al.*, 2017; Akbas *et al.*, 2018). The electrophilicity index represents the lowering energy caused by maximal electron flow between the donor electron and acceptor electron.

2.7 Molecular Electrostatic Potential (MEP)

Molecular electrostatic potential (MEP) is referring to the interaction energy ($V(r)$) between the molecular charge distributions with a unit positive test charge at a given point r (Orozco and Luque, 1996; Alipour and Mohajeri, 2010; Drissi *et al.*, 2015). Equation 2.39 presents the mathematical interpretation of MEP (Politzer *et al.*, 1985; Alipour and Mohajeri, 2010).

$$V(r) = \sum_{A} \frac{Z_A}{|R_A - r|} - \int \frac{\rho(r')dr'}{|r' - r|}$$

(Equation 2.39)

where $V(r)$ is the interaction energy, Z_A is the nuclear charge on atom A at point R_A and $\rho(r')$ represents the electronic density at point r. The formula elucidates that the polarity and sign on the MEP surface in a molecular system governs by the predominant effects from either nuclei charge distribution (positive) or electrons charge distribution (negative). So, the MEP surface serves as a useful illustration to explain the interaction and reactivity of a molecular system. The MEP visualises the sites for electrophilic and nucleophilic reactions in a molecular system (Rahmani *et al.*, 2018). It has significant applications in the prediction and study of the catalysis process, biological recognition process, and hydrogen bonding interaction scheme (Ceylan *et al.*, 2016; Kabouchi *et al.*, 2017).

The GaussView software package provides the graphical interpretation of the MEP surface. It uses colour scheme to differentiate the level of negativity in the electrostatic potential of a molecular system. The negativity of the electrostatic potential increases in the sequence colour from blue to green to

yellow to orange to red (Maache *et al.*, 2016). The blue colour region represents the less negative (most positive) electrostatic potential region which undergoes nucleophilic reaction. On the other hand, the red colour region represents the most negative (least positive) region where the electrophilic reaction will take place (shodhganga, 2021). The green colour region represents the neutral electrostatic potential site.

2.8 Natural Bond Orbital (NBO)

Natural bond orbital (NBO) analysis is a convenient and helpful method uses to understand the charge transfer and conjugative interaction in a molecular system (Bahgat and Fraihat, 2015; shodhganga, 2021). It provides detailed information about the interaction in both filled and emptied orbitals (Gandhi *et al.*, 2019; shodhganga, 2021). So that, NBO is able to enhance and give a strong perception about the molecular intra and inter bonding interactions (Bahgat and Fraihat, 2015; Maache *et al.*, 2016; Gandhi *et al.*, 2019). The NBO analysis computational study can be carried out using the NBO 3.1 program which is implemented in Gaussian 09 software package. In NBO analysis, the second-order Fock matrix contains several significant information (i.e. electron donor orbital, electron acceptor orbital, and stabilisation energy) that reveal the donor-acceptor and conjugation interaction in a molecular system. The stabilisation energy ($E(2)$) for each donor NBO (i) and acceptor NBO (j) related to delocalisation can be calculated using Equation 2.40 (Bahgat and Fraihat, 2015; Maache *et al.*, 2016; Gandhi *et al.*, 2019; shodhganga, 2021).

$$E\ (2) = q_i\ \frac{F(i,j)^2}{\varepsilon_i \varepsilon_j}$$

(Equation 2.40)

where $E(2)$ is the stabilisation energy, q_i represents the occupancy in donor orbital, $F(i,j)$ represents the off-diagonal NBO Fock matrix elements, and $\varepsilon_i \varepsilon_j$ is the orbital energies diagonal elements. The charge transfer interaction occurs through the overlapping of occupied Lewis-type electron donor (bonding or lone pair) NBO with unoccupied non-Lewis type electron acceptor (anti-bonding) NBO and caused stabilisation in the molecular system (Balachandran *et al.*, 2013; Dubey *et al.*, 2018; shodhganga, 2021). So that, the stabilisation energy explains the intensity of the donor-acceptor interaction. Higher in the stabilisation energy reflects the fact that the donating tendency from electron donors to electron receivers is more and the extent of conjugation in the molecular system is greater (shodhganga, 2021). These results in stronger charge transfer interaction between electron donors and acceptors (Dubey *et al.*, 2018).

2.9 Non-linear Optical (NLO) Properties

Non-linear optical (NLO) materials have immense applications in industries like telecommunications, optical signal processing, optical data storage, photonics, and laser technologies (Jawaher *et al.*, 2018; Varghese *et al.*, 2019). The study and discovery of NLO properties in chemical compounds have become the fore-front in current research especially in organic molecules. Organic compounds have a high tendency to induce the delocalisation of π electrons, making them exhibit high nonlinearities properties (Varghese *et al.*, 2019). Besides, the structural flexibility for device fabrications and ease of solution processability

in organic compounds make them become the potential target in the study of NLO (Islam and Chimni, 2016; Marinescu, 2018; Varghese *et al.*, 2019). The powerful development of computational algorithms in quantum chemistry has made a significant contribution to the study of NLO properties. The NLO properties of a chemical compound can be obtained through dipole moment (μ_0) and first hyperpolarizability (β_{tot}) studies. Dipole moment describes the fundamental property of a chemical compound based on the non-bonded type dipole-dipole intermolecular interaction (Rahmani *et al.*, 2018). It is useful in the determination of NLO properties in a molecular system (Ibeji *et al.*, 2016). Equation 2.41 shows the mathematical expression of the computed dipole moment (Dubey *et al.*, 2018; Jawaher *et al.*, 2018; Rahmani *et al.*, 2018; shodhganga, 2021).

$$\mu_0 = (\mu_x^2 + \mu_y^2 + \mu_z^2)^{\frac{1}{2}}$$

(Equation 2.41)

For the first hyperpolarizability, it is a 3rd rank tensor which can be presented by a 3 x 3 x 3 matrix. The Kleinman symmetry theory states that $\beta_{xyy} = \beta_{yxy} = \beta_{yyx}$ or $\beta_{yyz} = \beta_{yzy} = \beta_{zyy}$. So that the complicated 3D matrix with 27 components can be further reduced to 10 components (i.e. $\beta_{xxx}, \beta_{xxy}, \beta_{yyz}, \beta_{yyy}, \beta_{xxz}, \beta_{xyz}, \beta_{zzz}, \beta_{xzz}, \beta_{xyy}$ and β_{yzz}) in the calculation of β_{tot} (Thanthiriwatte and De Silva, 2002; Günay *et al.*, 2013; Rahmani *et al.*, 2018). Equation 2.42 lists the mathematical presentation of the computed first hyperpolarizability (β_{tot}) (Dubey *et al.*, 2018; Rahmani *et al.*, 2018; Varghese *et al.*, 2019).

$$\beta_{tot} = [(\beta_x{}^2 + \beta_y{}^2 + \beta_z{}^2)]^{\frac{1}{2}}$$

(Equation 2.42)

where,

$$\beta_x = \beta_{xxx} + \beta_{xyy} + \beta_{xzz}$$

(Equation 2.43)

$$\beta_y = \beta_{yyy} + \beta_{xxy} + \beta_{yzz}$$

(Equation 2.44)

$$\beta_z = \beta_{zzz} + \beta_{xxz} + \beta_{yyz}$$

(Equation 2.45)

Noted that several factors will influence the first hyperpolarizability. For example, the donor-acceptor mechanism, nature of substitutes, planarity influence, and conjugated π system of a chemical compound (Raja *et al.*, 2014). Normally, a good NLO material will have large β_{tot} value. In order to identify the NLO properties of a chemical compound, the well-known NLO materials (i.e. urea and p-Nitroaniline (PNA)) will choose as the β_{tot} threshold reference and served for comparative study with the target materials (Günay *et al.*, 2013; Rahmani *et al.*, 2018).

CHAPTER 3

METHODOLOGY

3.1 Flow of Research

This chapter describes the design procedures of both experimental (i.e. crystallization process, single crystal X-ray diffraction experiment, Fourier transform infrared (FT-IR) spectroscopy, and Ultraviolet-visible (UV-Vis) spectroscopy) and theoretical computations via Density Functional Theory (DFT) method. The work undertakes in this research study focus on two types of pharmaceutical drug compounds (i.e. acyclovir (ACV) and theophylline (TP)). Both of the drugs (i.e. ACV and TP) are classified as active pharmaceutical ingredients (APIs) which prone to form polymorphisms that may have different physicochemical properties. So, the characterizations and investigations on the polymorphic forms of ACV and TP using both experimental and computational methods are important and indispensable from one another. Figure 3.1 shows the research flow chart.

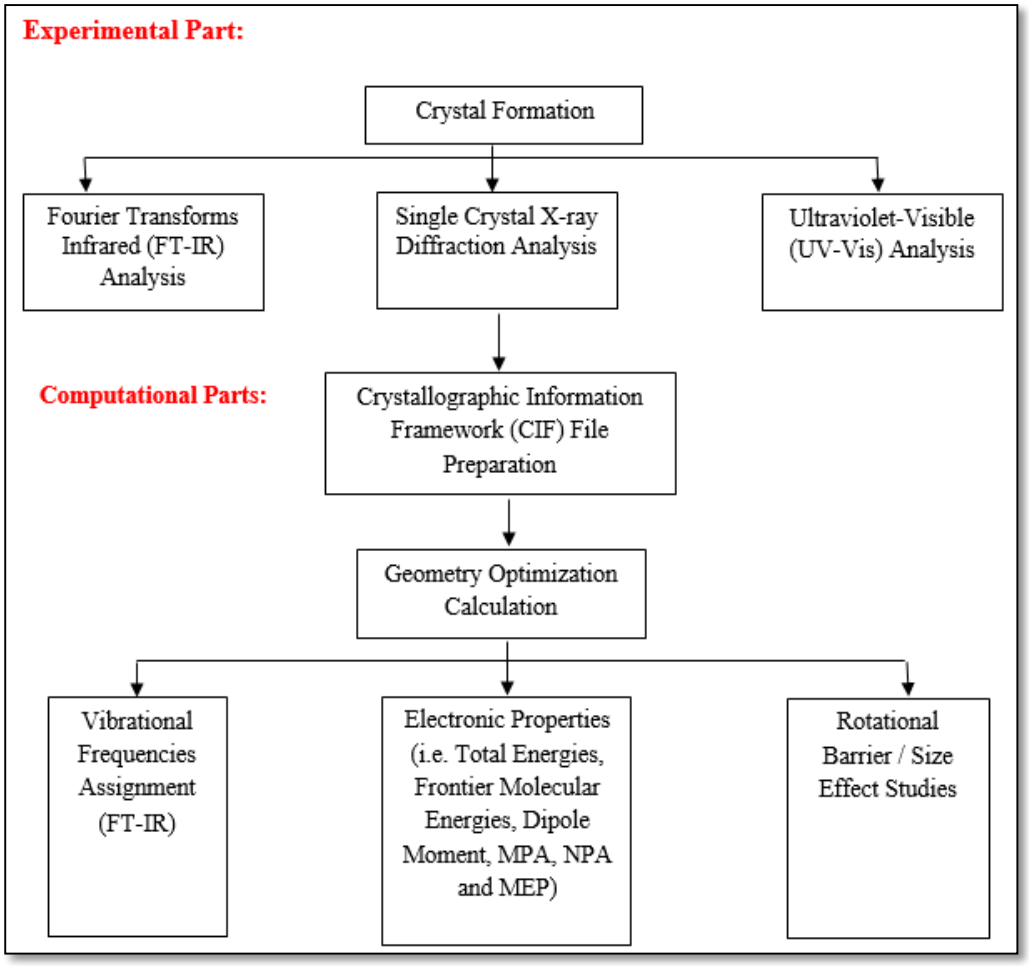

Figure 3.1: Research flow chart.

3.2 Materials and Chemicals

There are two main APIs drug compounds (i.e. acyclovir (AC) and theophylline (TP) involved in this research study. The 800 mg ACV drug tablet used in the crystallization part is purchased from Health Mate Pharmacy Sdn. Bhd., Malaysia with a brand named VIRLESS. Besides, the TP crystal samples are donated by Dr. Montha Meepripruk from Kamphaeng Phet Rajabhat University, Thailand.

3.3 Experimental Part

3.3.1 Crystal Formation in Acyclovir (ACV) Drug Compound

Part A: Preparation of ACV pure powder.

One blue tablet of 800 mg ACV was grinded into fine-powder form. 790 mg of ACV powder was mixed with 320 ml of deionised water at temperature around 37℃. The mixture was stirred evenly by a magnetic stirrer with 250 rpm. After that, the mixture was heated at temperature around 60℃ to 76℃ for 30 minutes. The hot mixture was then being filtered and undergo a continuously heating process to reduce the total volume of the mixture to around 20% left. After that, the mixture was left cooled down at room temperature for a week. At the end of the 7^{th} day, a white-blue colour of ACV pure powder was obtained. The ACV pure powder was ready to be used for the crystallization process.

Part B: Crystallization of ACV compound.

By using water as the solvent for the crystallization process, 0.042 g of ACV pure powder was mixed with 15 ml of deionised water at temperature around 70℃ and stirred evenly with 250 rpm for 40 minutes. After that, the hot mixture was being filtered and left cooled down at room temperature. To speed up the evaporation process, the solid-liquid state ACV mixture was then put into a 60℃ drying oven for hours. Light blue, tiny, and needle shape of acyclovir crystal (ACV-I) sample was obtained and ready for further instrumental testing to study the characteristics of the crystal formed. Figure 3.2 (a), (b), (c), and (d)

illustrate the set-up and products obtained from the crystallization process.

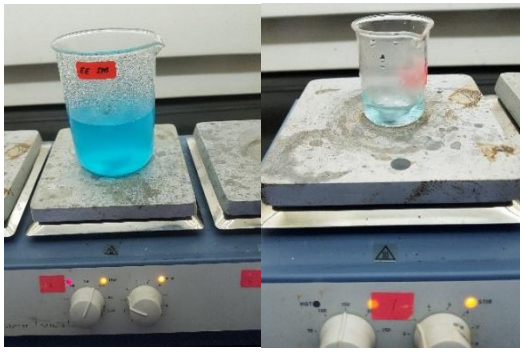

PART A **PART B**

Figure 3.2 (a): The heating process of the ACV mixture in Part A (deep blue solution) and Part B (light blue solution).

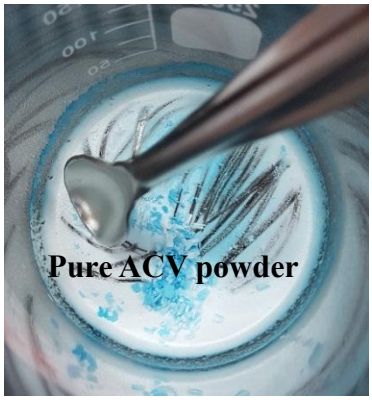

Figure 3.2 (c): Pure ACV powder obtained from the end of Part A.

Figure 3.2 (b): Filtration process of the ACV mixture.

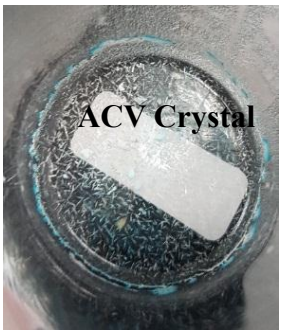

Figure 3.2 (d): The crystal sample of ACV-I obtained from the end of Part B.

3.2.2 Crystal Formation in Theophylline (TP) Drug Compound

Three TP crystal compounds with different types of solvents were donated by Dr. Montha Meepripruk. According to Dr. Meepripruk, two of the TP crystals (i.e. TP-I and TP-II) were the products that result from the mixing of TP drug compounds with water. Another one (i.e. TP-III) was the result of mixing TP and AVC drug compounds in the ratio [TP: ACV] of [2:1] with acetic acid. Figure 3.3 (a), (b), and (c) show the colourless, long needle-shaped TP crystal samples of TP-I, TP-II, and TP-III.

Figure 3.3 (a): The crystal sample of TP-I. (1.07 g of TP with 40 ml of H_2O)

Figure 3.3 (b): The crystal sample of TP-II. (0.1 M of TP)

Figure 3.3 (c): The crystal sample of TP-III. (TP + ACV in the ratio of 2:1 with 0.1 M acetic acid)

3.3.3 Single Crystal X-ray Diffraction Experiment

The four crystal samples (i.e. ACV-I, TP-I, TP-II, and TP-III) obtained in this research study were sent to Universiti Sains Malaysia (USM) Penang, Malaysia to perform the single crystal X-ray diffraction experiment. The crystal samples were characterized and identified using the Bruker APEX-II CCD diffractometer with MoKα type of radiation at room temperature. Figure 3.4 illustrates the Bruker APEX-II CCD diffractometer used by USM. The cell refinement and data reduction were carried out via the Bruker SAINT Programme. Besides, the structure was solved and refined by using SHELXS-97 and SHELXL-2014 computational software. Moreover, the molecular graphics were computed via the Bruker SHELXTL program. Table 3.1 (a), (b), (c), and (d) summarise the crystal data, collection, and refinement details of the ACV-I, TP-I, TP-II, and TP-III crystal compounds obtained from the single crystal X-ray diffraction output data.

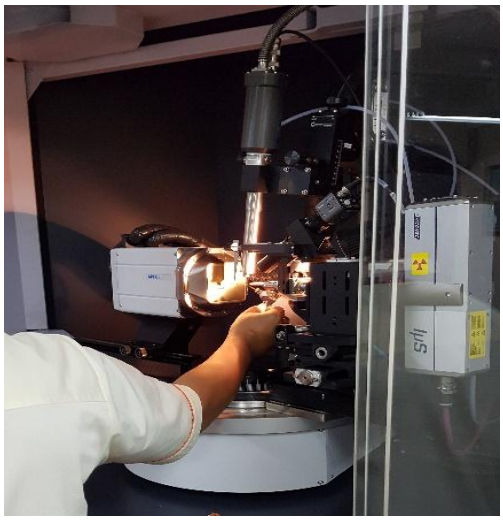

Figure 3.4: Bruker APEX-II CCD diffractometer.

Table 3.1 (a): Crystal data, data collection, and refinement of ACV-I.

ACV-I		
Crystal Data		
Chemical Formula		$3[C_8H_{11}N_5O_3].2[H_2O]$
Mr		316.30
Crystal System, space group		Monoclinic, P21/n
Temperature (K)		296
a, b, c (Å)		10.7647(4), 11.2869(4), 25.4548(10)
α, β, γ (°)		90.00, 95.162, 90.00
V (Å3)		3080.2(2)
Z		9
Radiation type		Mo Kα
μ (mm-1)		0.123
Crystal size (mm)		0.185 × 0.284 × 0.735 (Blue, Plate)
Data Collection		
Diffractometer		Bruker Apex-II CCD
No. of measured reflections		63184
No. of independent reflections		9055
No of [I > 2σ(I)] reflections		4746
Rint		0.0725
Refinement		
R [F2 > 2σ(F2)], ωR (F2), S		0.0769, 0.2638, 1.050
No. of reflections		9055
No of parameters		468
No of restraints		2
Δρmax, Δρmin (e Å-3)		1.294, –0.497
H-atom treatment		H atoms treated by a mixture of independent
		and constrained refinement

Table 3.1 (b): Crystal data, data collection, and refinement of TP-I.

TP-I		
Crystal Data		
Chemical Formula		$C_7H_8N_4O_2$
Mr		360.35
Crystal System, space group		Orthorhombic, P2c/-2n
Temperature (K)		293
a, b, c (Å)		24.493 (12), 3.8124 (19), 8.456 (4)
α, β, γ (°)		90.00, 90.00, 90.00
V (Å3)		789.6 (7)
Z		2
Radiation type		Mo Kα
μ (mm-1)		0.116
Crystal size (mm)		0.092 x 0.267 x 0.307 (Colourless, Plate)
Data Collection		
Diffractometer		Bruker Apex-II CCD
No. of measured reflections		5618
No. of independent reflections		1985
No of [I > 2σ(I)] reflections		1122
Rint		0.1261
Refinement		
R [F2 > 2σ(F2)], ωR (F2), S		0.1449, 0.2745, 1.287
No. of reflections		1985
No of parameters		120
No of restraints		1
Δρmax, Δρmin (e Å-3)		0.323, -0.311
H-atom treatment		H atoms treated by a mixture of independent
		and constrained refinement

Table 3.1 (c): Crystal data, data collection, and refinement of TP-II.

TP-II		
Crystal Data		
Chemical Formula		$C_7H_8N_4O_2.H_2O$
Mr		264.25
Crystal System, space group		Monoclinic, P21/n
Temperature (K)		296
a, b, c (Å)		4.4885 (7), 15.408 (3), 13.287 (2)
α, β, γ (°)		90.00, 98.591, 90.00
V (Å3)		908.6 (3)
Z		3
Radiation type		Mo Kα
μ (mm-1)		0.116
Crystal size (mm)		0.131 x 0.152 x 0.61 (Colourless, Block)
Data Collection		
Diffractometer		Bruker Apex-II CCD
No. of measured reflections		20107
No. of independent reflections		2695
No of [I > 2σ(I)] reflections		1852
Rint		0.0450
Refinement		
R [F2 > 2σ(F2)], ωR (F2), S		0.0551, 0.1630, 1.052
No. of reflections		2695
No of parameters		138
No of restraints		2
Δρmax, Δρmin (e Å-3)		0.202, -0.185
H-atom treatment		H atoms treated by a mixture of independent
		and constrained refinement

Table 3.1 (d): Crystal data, data collection, and refinement of TP-III.

TP-III		
Crystal Data		
Chemical Formula		$C_7H_8N_4O_2.H_2O$
Mr		264.25
Crystal System, space group		Monoclinic, P21/n
Temperature (K)		296
a, b, c (Å)		4.4988 (9), 14.451 (3), 13.329 (3)
α, β, γ (°)		90.00, 98.581, 90.00
V (Å3)		916.2 (3)
Z		3
Radiation type		Mo Kα
μ (mm-1)		0.115
Crystal size (mm)		-
Data Collection		
Diffractometer		Bruker Apex-II CCD
No. of measured reflections		17810
No. of independent reflections		2449
No of [I > 2σ(I)] reflections		1861
Rint		0.0386
Refinement		
R [F2 > 2σ(F2)], ωR (F2), S		0.0735, 0.1755, 1.195
No. of reflections		2449
No of parameters		141
No of restraints		2
Δρmax, Δρmin (e Å-3)		0.206, -0.279
H-atom treatment		H atoms treated by a mixture of independent
		and constrained refinement

3.3.4 Fourier Transform Infrared (FT-IR) Spectroscopy

Small amounts of ACV-I, TP-I, TP-II, and TP-III crystal samples were collected to investigate the functional groups via Fourier transform infrared (FT-IR) spectroscopy analysis (Perkin Elmer). Noted that all the procedures in the FT-IR experiment for the four crystal samples are identical. All the crystal samples were mixed with potassium bromide (KBr) powder in the ratio of [1:10] to dilute the experimental samples into the Nano-absorbing matrix. The mixture was grinded and compressed with a hydraulic pump for a few seconds to obtain the crystal-KBr pellet which was later used as the input sample for the FT-IR analysis. Mid-IR radiation region (400 cm^{-1} to 4000 cm^{-1}) was set in the FT-IR analysis. In order to obtain the actual IR absorption activities of the sample pellet without the influence of the environmental condition, background spectrum scanning was performed before starting the FT-IR experiment with the sample pellet. This background spectrum is important and acts as the comparative data to adjust the FT-IR vibrational spectrum result of the sample pellet. Figure 3.5 (a), (b), and (c) show the FT-IR instrument and sample preparation procedures.

Figure 3.5 (a): Mixture of solid crystal with KBr powder in the ratio of 1:10.

Figure 3.5 (b): A thin film compressed by the hydraulic compressor.

Figure 3.5 (c): The FT-IR spectrometer.

3.3.5 Ultraviolet-Visible (UV-Vis) Analysis

The Ultraviolet-visible (UV-Vis) spectral measurement was performed using DR 6000 UV-Vis spectrophotometer with four crystal samples (i.e. ACV-I, TP-I, TP-II, and TP-III) prepared in liquid solution forms. Deionised water was chosen as the blank and used to dissolve the crystal samples. 10 mg of crystal samples were dissolved in 100 ml of deionised water at room temperature. In order to ensure the complete dissolution of crystal samples into the water, the ultrasonic water bath technique was carried out for an hour without temperature adjustment. After that, clear and colourless solutions were obtained for the four crystal samples and ready for the UV-Vis spectroscopy analysis. During the UV-Vis measurement, the sample solutions were further diluted by deionised water with different ratios in order to determine the change in absorbance wavelength corresponding to the concentration of sample solutions. The mixture of the

sample solution was held by a glass-type cuvette with a thickness of 1 cm. Noted that bubble formation and fingerprint contamination had been avoided to produce an accurate and reliable result. The UV-Vis scanning ranges were set between 200 nm to 800 nm. Before scanning the sample solutions, the scanning of blank is necessary to remove the characteristic of the solvent used. Figure 3.6 (a), (b), (c), and (d) illustrate the sample preparation, sample holder (cuvette), and UV-Vis spectrophotometer used in this work.

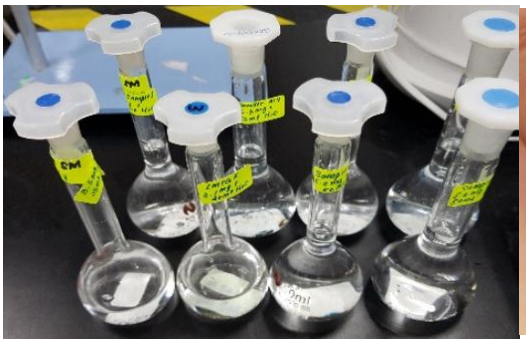

Figure 3.6 (a): 10 mg of crystal samples mixed with 100 ml of deionised water.

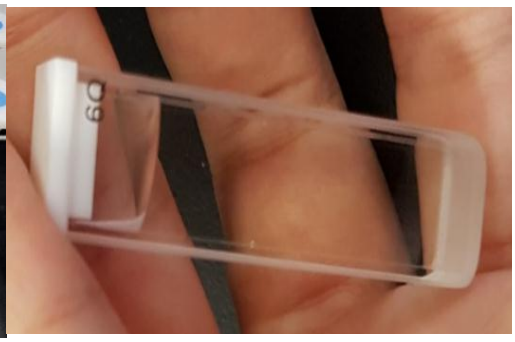

Figure 3.6 (c): The 1 cm thick glass cuvette.

Figure 3.6 (b): Sample solutions were socked in the Ultrasonic water bath.

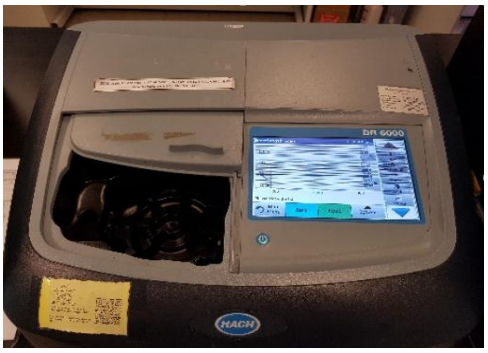

Figure 3.6 (d): The DR 6000 UV-Vis spectrophotometer.

3.4 Computational Studies

3.4.1 Computational Method and Software

In this research work, Density Functional Theory (DFT) was the main quantum mechanics computational method employed to study the ACV and TP polymorphism compounds. All the DFT computations were carried out using Gaussian 09 software package. The visualisation and analysis of results generated by the Gaussian 09 software package (Frisch *et al.*, 2009) were performed via the GaussView 5.0 (Frisch *et al.*, 2009) and Multifwn (Lu and Chen, 2012) softwares. The DFT calculations were carried out using Becke's Three Lee-Yang-Parr (B3LYP) hybrid functional together with different types of split valence basis sets (i.e. 6-31G, 6-31G**, and 6-311G**). The geometry structures, electronic properties, and vibrational frequencies of ACV and TP polymorphisms (i.e. ACV-I, ACV-II, ACV-III, TP-I, TP-II, and TP-III) were obtained and discussed in this study.

3.4.2 Input Source Preparation

The crystal data obtained from the single crystal X-ray diffraction analysis for ACV-I, TP-I, TP-II, and TP-III were converted into crystallographic information framework (CIF) files using the SHELEX program (Hübschle *et al.*, 2011) and acted as the main input sources for whole DFT computational calculations in this work. CIF formatted input file is necessary since it contains important information about the molecular geometry structures of ACV-I, TP-I, TP-II, and

TP-III. Besides, it is also the readable format for GaussView 5.0 software to prepare the computational input files used by the Gaussian 09 software package. In this research study, the computational calculations not only involved the crystal compounds (i.e. ACV-I, TP-I, TP-II, and TP-III) obtained from the single crystal X-ray experiment but also included another two hydrated ACV polymorphisms from other researcher's findings. The CIF files for the two additional ACV polymorphisms (i.e. ACV-II and ACV-III) were obtained from Cambridge Crystallographic Data Centre (CCDC) and Dr. Meepripruk. As a result, there were a total of six ACV and TP polymorphism compounds (i.e. ACV-I, ACV-II, ACV-III, TP-I, TP-II, and TP-III) involved in the DFT computational studies. Figure 3.7 (a), (b), (c), (d), (e), and (f) illustrate the complete single unit cell molecular structures for ACV-I, ACV-II, ACV-III, TP-I, TP-II, and TP-III under the visualisation of GaussView 5.0 software package.

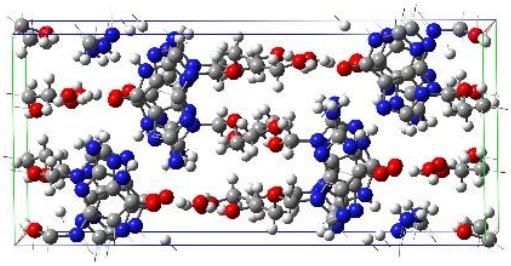

Figure 3.7 (a): The unit cell of ACV-I.

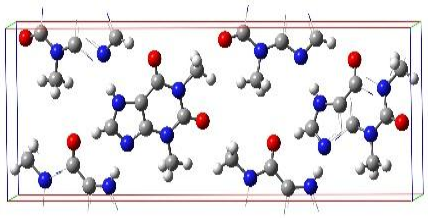

Figure 3.7 (d): The unit of TP-I.

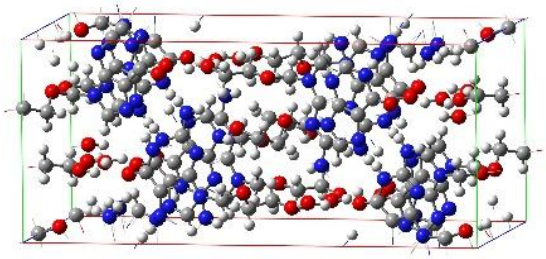

Figure 3.7 (b): The unit of ACV-II.

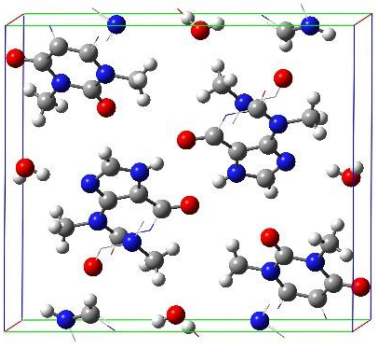

Figure 3.7 (e): The unit of TP-II.

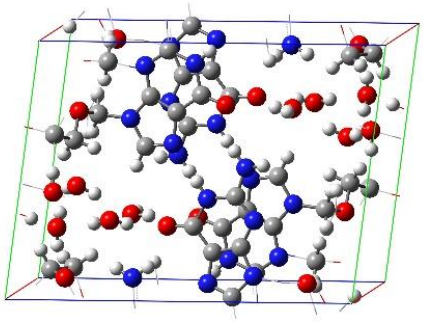

Figure 3.7 (c): The unit of ACV-III.

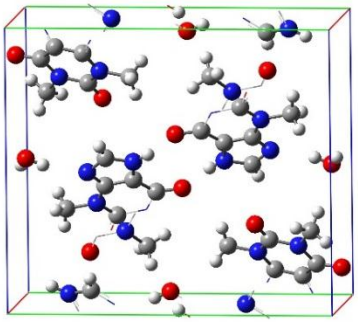

Figure 3.7 (f): The unit of TP-III.

From the unit cell, the complete single molecular structure of ACV-I, ACV-II, ACV-III, TP-I, TP-II, and TP-III were extracted via GaussView 5.0 software package with the help of Periodic Boundary Condition (PBC) and acted as the

host environment for DFT computational calculations. Figure 3.8 (a), (b), (c), (d), (e), and (f) show the complete single molecular structures of ACV-I, ACV-II, ACV-III, TP-I, TP-II, and TP-III. From the figures, it is observed that the single molecular systems of ACV-I, ACV-II, ACV-III, TP-II, and TP-III contained water molecules while TP-I is in an anhydrous state.

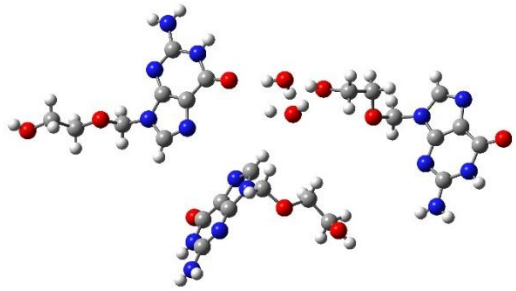

Figure 3.8 (a): The single molecular structure of ACV-I.

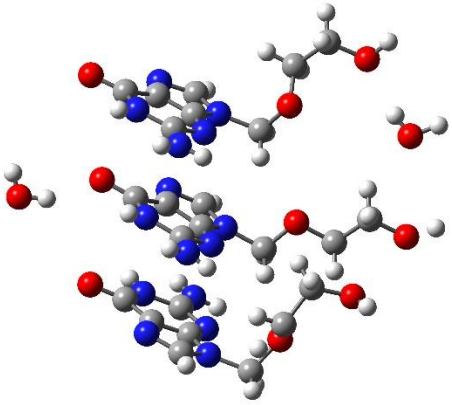

Figure 3.8 (b): The single molecular structure of ACV-II.

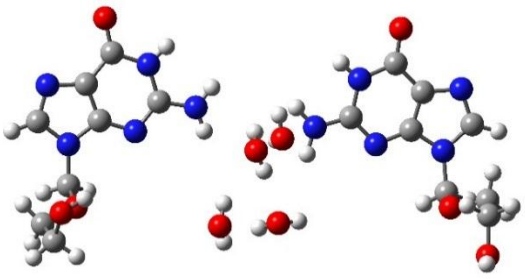

Figure 3.8 (c): The single molecular structure of ACV-III.

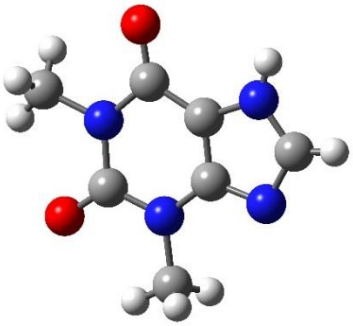

Figure 3.8 (d): The single molecular structure of TP-I.

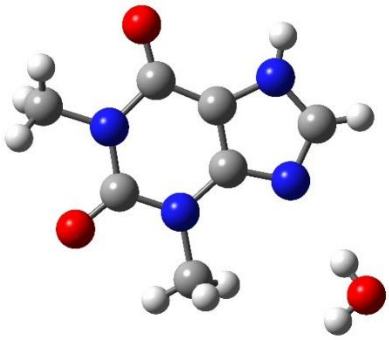

Figure 3.8 (e): The single molecular structure of TP-II.

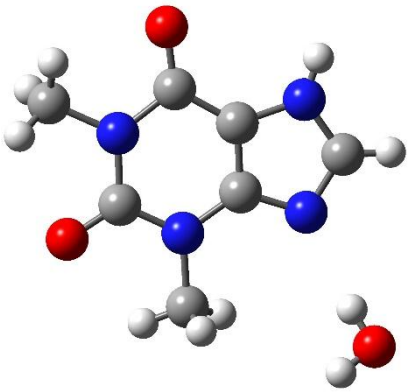

Figure 3.8 (f): The single molecular structure of TP-III.

3.4.3 Density Functional Theory (DFT) Computational Calculations

3.4.3.1 Geometry Optimization and Single Point Calculations

During the geometry optimization calculations, the molecular geometry structures of ACV-I, ACV-II, ACV-III, TP-I, TP-II, and TP-III were specified using *z*-matrix approaches (internal coordinates). In order to compute the total energy with tighter self-consistent field (SCF) convergence criteria, "SCF=tight" was set. The geometry optimization calculations for ACV-I, ACV-II, ACV-III, TP-I, TP-II, and TP-III were performed with the employment of DFT/B3LYP functional with different basis sets (i.e. 6-31G, 6-31G**, and 6-311G**). The equilibrium and stable optimized molecular geometry structures of ACV-I, ACV-II, ACV-III, TP-I, TP-II, and TP-III were obtained and compared with the single crystal X-ray diffraction experimental findings. After that, the reliable optimized geometry structures of ACV-I, ACV-II, ACV-III, TP-I, TP-II, and TP-III were used to performed fixed geometry single point calculations. The electronic properties (i.e. total energy, frontier molecular energy, dipole moment, MPA, NBO, and NLO) and vibrational frequencies (i.e. FT-IR) of ACV-I, ACV-II, ACV-III, TP-I, TP-II, and TP-III molecular system were successfully obtained. The computed HOMO-LUMO energy gaps and calculated FT-IR vibrational spectrum were later compared with UV-Vis spectroscopy and FT-IR spectroscopy experimental results.

3.4.3.2 HOMO and LUMO Surface Mapped Plots

With the help of GaussView 5.0 software package, the graphical interpretations of HOMO and LUMO surface mapped plots of ACV-I, ACV-II, ACV-III, TP-I, TP-II, and TP-III molecular system were plotted. Figure 3.9 shows the example of HOMO surface mapped plots of ACV-III molecule. The green colour lobe indicates the negative region while the red colour lobe represents the positive region. Noticed that all the HOMO and LUMO surface mapped plots in ACV-I, ACV-II, ACV-III, TP-I, TP-II, and TP-III molecular system had isosurface display values of 0.0004 a.u and plotted in "solid" display format.

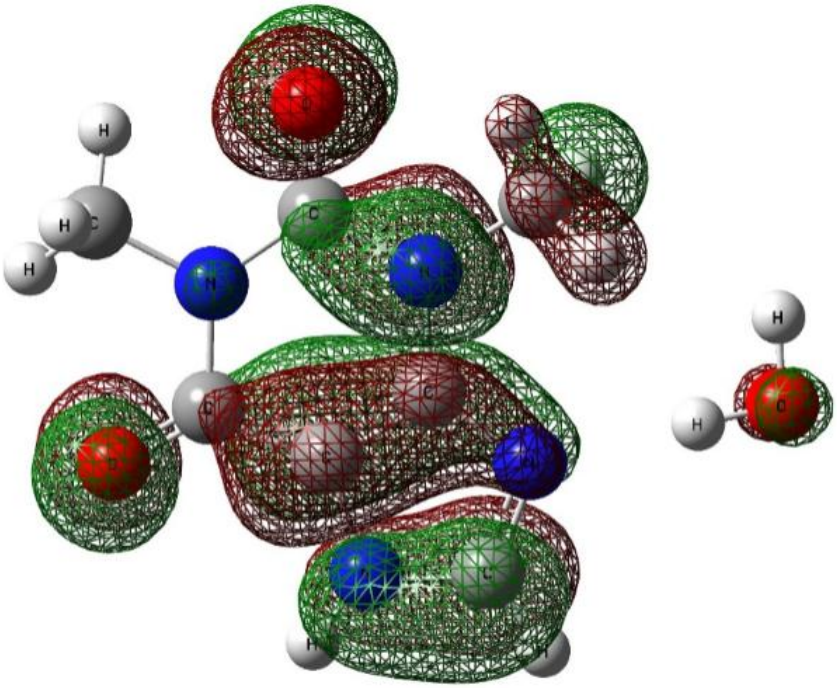

Figure 3.9: The HOMO surface mapped plot sample of TP-III molecular system.

3.4.3.3 Molecular Electrostatic Potential (MEP) Surface Mapped Plots

The molecular electrostatic potential (MEP) mapped plots of ACV-I, ACV-II, ACV-III, TP-I, TP-II, and TP-III molecular system were generated using GaussView 5.0 software package. In MEP, the electron density distributions of a system are presented using colouring scheme. Red colour mapping represents negative electrostatic potential region while blue colour mapping represents positive electrostatic potential region. The positivity of electrostatic potential increase in the colour sequences of red to yellow to green to blue. Figure 3.10 illustrates the MEP surface mapped plot example of the ACV-III molecular system. Noticed that the intensity of the colours depends on the ranges of isosurface display values. In this work, the default isosurface generated by GaussView 5.0 software package was directly used without any adjustment. Table 3.2 summarises the MEP isosurface details of ACV-I, ACV-II, ACV-III, TP-I, TP-II, and TP-III molecular system using different computational methods. Besides, in order to determine the global surface extrema points in ACV-I, ACV-II, ACV-III, TP-I, TP-II, and TP-III molecular system, qualitative analysis was carried out using the Multifwn software. The formatted checkpoint files (.fchk) generated from the Gaussian 09 software package were used as the main input sources for the calculations.

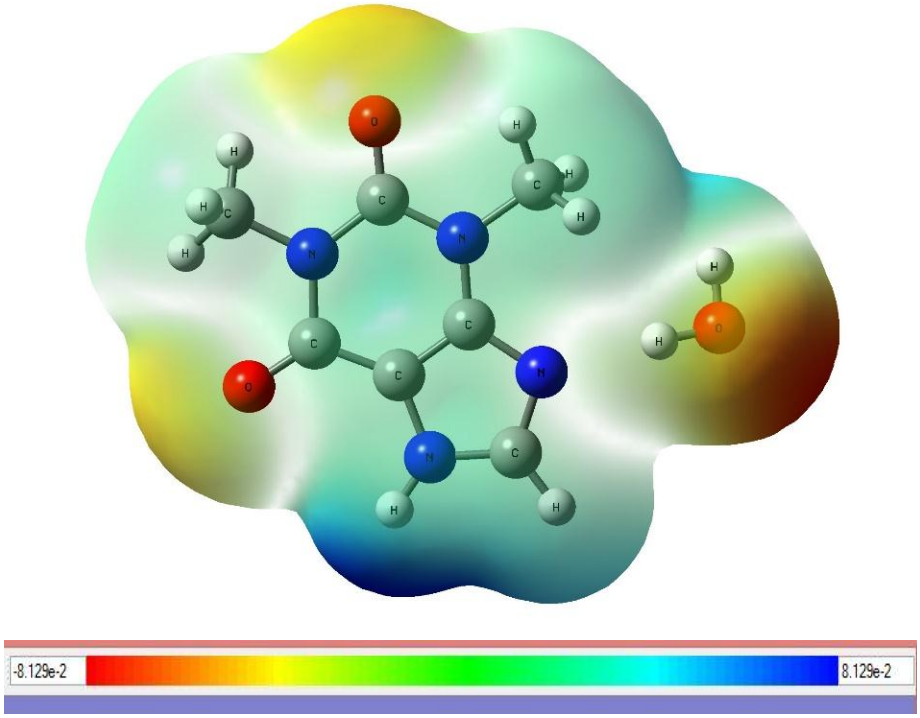

Figure 3.10: The MEP surface mapped plot sample of ACV-III molecular system.

Table 3.2: The MEP surface mapped plots isosurface display values of ACV-I, ACV-II, ACV-III, TP-I, TP-II, and TP-III molecular system.

	DFT/B3LYP/6-31G**	DFT/B3LYP/6-311G**
ACV-I	$-0.805e^{-2}$ to $0.805e^{-2}$ [a.u]	$-8.615e^{-2}$ to $8.615e^{-2}$ [a.u]
ACV-II	$-0.102e^{0}$ to $0.102e^{0}$ [a.u]	$-0.101e^{0}$ to $0.101e^{0}$ [a.u]
ACV-III	$-0.116e^{0}$ to $0.116e^{0}$ [a.u]	$-0.112e^{0}$ to $0.112e^{0}$ [a.u]
	DFT/B3LYP/6-31G	DFT/B3LYP/6-31G**
TP-I	$-7.346e^{-2}$ to $7.346e^{-2}$ [a.u]	$-7.282e^{-2}$ to $7.282e^{-2}$ [a.u]
TP-II	$-8.109e^{-2}$ to $8.109e^{-2}$ [a.u]	$-8.013e^{-2}$ to $8.013e^{-2}$ [a.u]
TP-III	$-8.129e^{-2}$ to $8.129e^{-2}$ [a.u]	$-7.477e^{-2}$ to $7.477e^{-2}$ [a.u]

3.4.3.4 Rotational Barrier Studies in ACV Molecules

Rotational energy refers to the kinetic energy obtained from the rotational activity of a system. The highest peak of rotational energy is defined as the rotational barrier. This barrier energy is informative as it separates the two energy minima of a system. For the rotational barrier studies in ACV molecules, the single ACV molecules were extracted from the optimized geometry structures of the ACV-I, ACV-II, and ACV-III molecular system. The side chains (i.e. N-C-O-C) were chosen to rotate from 0° to 360° as shown in Figure 3.11. With a rotational increment of 10° at every scanning cycle, there were a total of 36 steps in the Potential Energy Surface scans. Noted that all the computed relative energies and rotational barrier peaks for ACV molecules were obtained in this study.

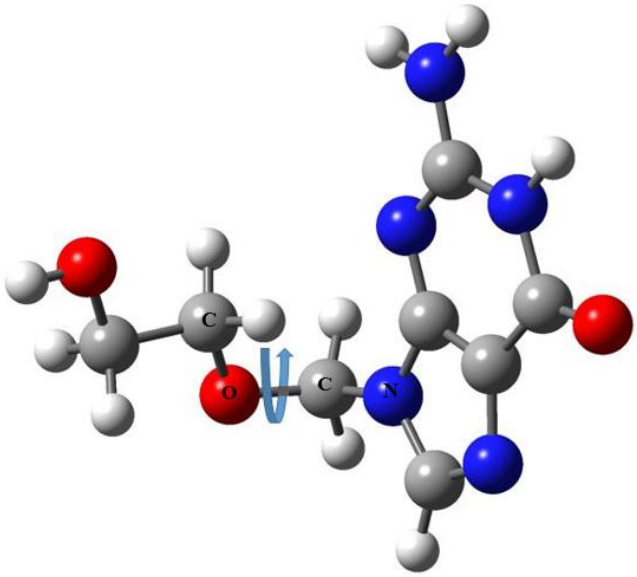

Figure 3.11: Single molecular of ACV with side chain rotation 0° to 360° .

3.4.3.5 Size Effect Studies of TP-I and TP-II Molecular System

In order to study and understand the molecular size effect in TP-I and TP-II molecular system, the nearest neighbouring molecules were added to surrounding the TP-I and TP-II molecular system. Periodic Boundary Condition (PBC) as provided in GaussView 5.0 software package was used to extend the unit cell of the TP-I and TP-II molecular system, thus the complete neighbouring molecules can be obtained. Again, geometry optimization and single point calculations were carried out to observed the impact of molecular size in DFT computational analysis. Figure 3.12 (a), (b), (c), (d), (e), and (f) visualise the molecular system of TP-I and TP-II with different molecular size effects.

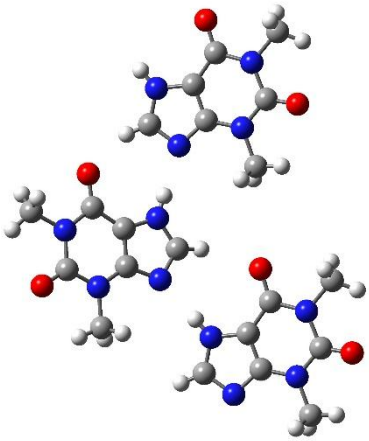

Figure 3.12 (a): The molecular size effect study on TP-I with three TP molecules.

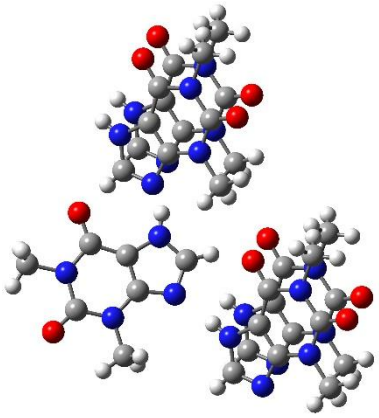

Figure 3.12 (b): The molecular size effect study on TP-I with five TP molecules.

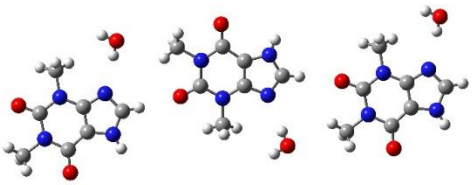

Figure 3.12 (c): The molecular size effect study on TP-II with three TP monohydrate molecules.

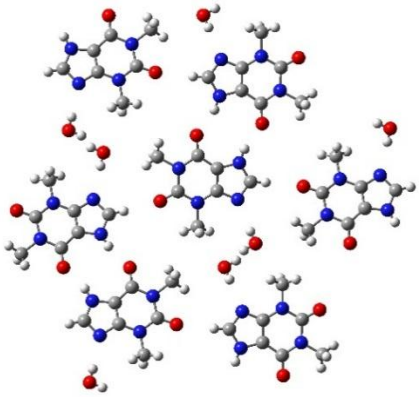

Figure 3.12 (e): The molecular size effect study on TP-II with seven TP monohydrate molecules.

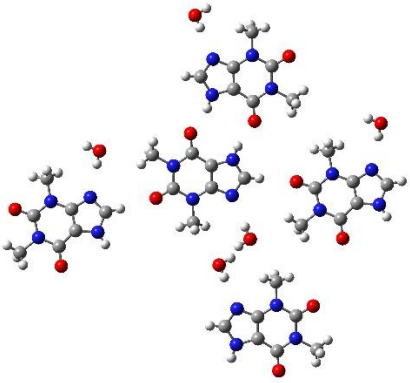

Figure 3.12 (d): The molecular size effect study on TP-II with five TP monohydrate molecules.

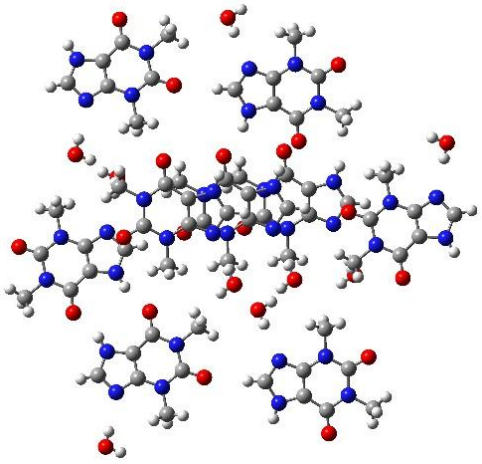

Figure 3.12 (f): The molecular size effect study on TP-II with nine TP monohydrate molecules.

CHAPTER 4

RESULTS AND DISCUSSIONS

Polymorphism Organic Compound 1: Acyclovir (ACV)

Acyclovir (ACV), as one of the family members of active pharmaceutical ingredients (APIs) organic drug compound, has been found to have many polymorphic forms. It is widely used for the treatment of Herpes Simplex Virus (HSV) and Varicella Zoster Virus (VZV) diseases due to its outstanding anti-viral characteristic. Previous literature surveys explicit that there is limited information about the quantum mechanics computational analysis on the electronic properties of hydrated acyclovir compound. Consequently, the geometry structures, electronic properties (i.e. FMOs, MEP, and NLO), and vibrational frequencies of hydrated ACV compounds are reported in this work. Three different hydrated polymorphic forms of ACVs (i.e. ACV-I, ACV-II, and ACV-III) are chosen. ACV-I is obtained from the crystallization experiment in the laboratory whereas ACV-II and ACV-III are obtained from the works done by Birnbaum *et al.* (1984) and Montha (2012). For ACV-I and ACV-II molecular system, both of them contain the same number of ACV and water molecules but different in the molecular structure conformations and arrangements. For ACV-III molecular system, it contains only two ACV molecules but has four water molecules. Three of them show unique molecular geometry structures

within each other. So that it is worth to study their electronic properties in order to identify their physicochemical characteristics. All the computational calculations are performed using DFT/B3LYP/6-31G** and DFT/B3LYP/6-311G** level of theories via Gaussian 09 quantum mechanics computational software package. Besides, several experimental works (i.e. single crystal X-ray diffraction, FT-IR, and UV-Vis spectroscopy) are carried out and act as comparative data with computational results for the purpose to ensure the reliability of the computational methods on ACV compound. Moreover, the rotational barrier study on ACV molecules also included in this work.

4.1: Acyclovir Hydrate (ACV-I) ($3[C_8H_{11}N_5O_3]\cdot 2[H_2O]$)

The crystallization from ACV drug powder with deionised water through slow evaporation method formed ACV hydrate crystal compound (ACV-I). From the single crystal X-ray diffraction experiment, the ACV-I crystal sample is found to be crystallized in a monoclinic space group of $P2_{1/n}$ with unit cell lattice constants of a = 10.765 Å, b = 11.287 Å, c = 25.455 Å, and β = 95.162°. Figure 4.1 (a) and (b) show the complete unit cell and single molecular crystal structure of the ACV-I compound. With chemical formula of $3[C_8H_{11}N_5O_3]\cdot 2[H_2O]$, the ACV-I single molecular system contains two water molecules (Water I and Water II) surrounded by three independent ACV molecules (Molecule A, B, and C). The single ACV-I molecular system is chosen as the host environment in the DFT computational studies. The numbering and labelling details are shown in Figure 4.1 (b). All the geometries and electronic properties of the ACV-I molecular system are determined and discussed.

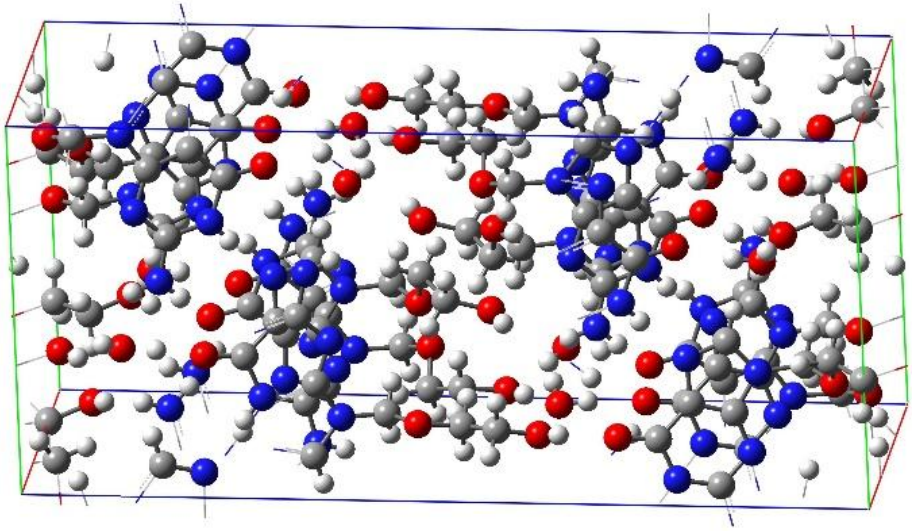

Figure 4.1 (a): The complete unit cell of ACV-I.

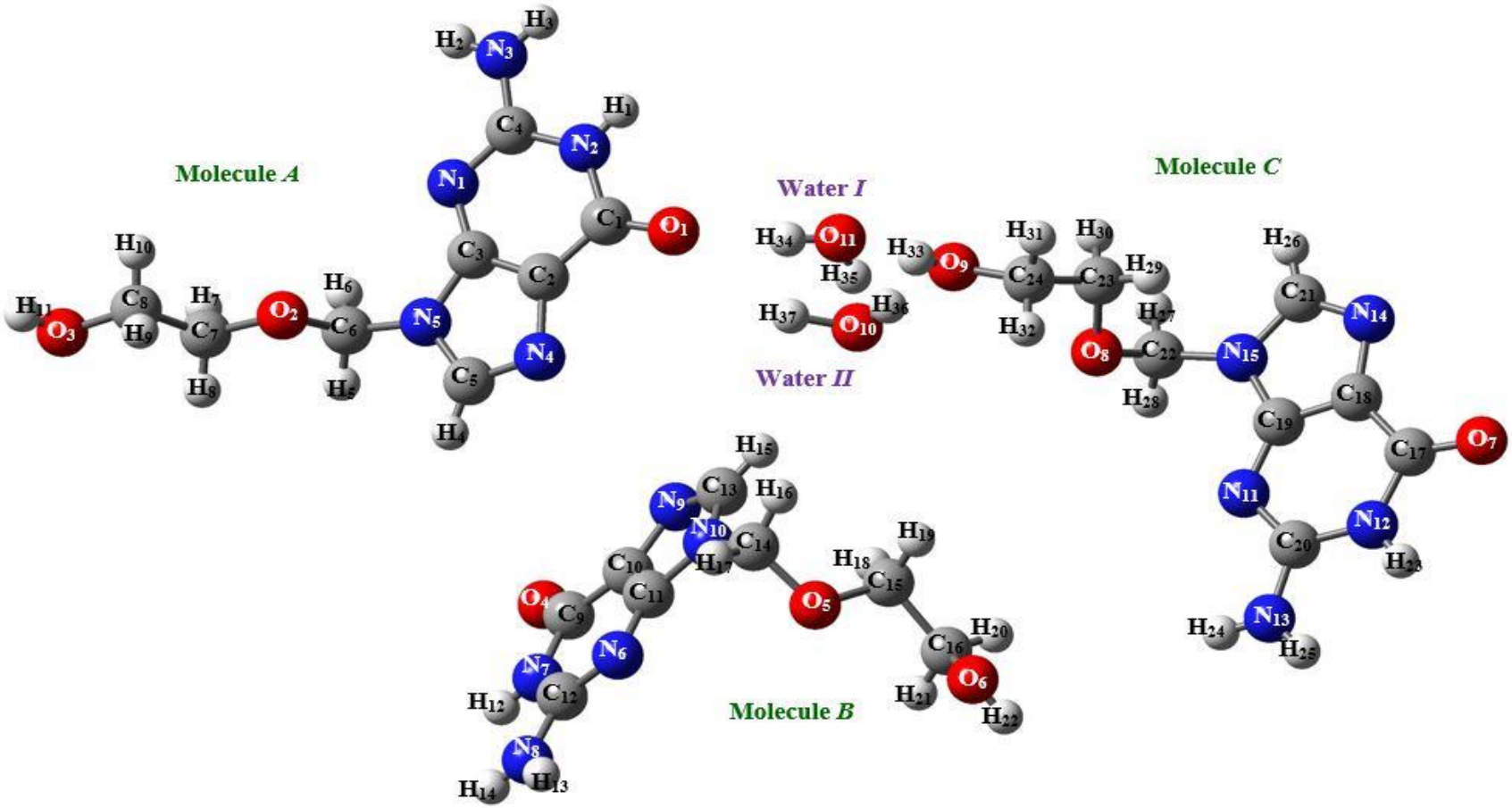

Figure 4.1 (b): Labelling and numbering details in ACV-I single molecular system.

4.1.1 Molecular Geometry Structural Analysis

The single molecular structure of the ACV-I compound contains C=O, C=C, C=N, C-O, C-C, C-N, C-H, N-H, and O-H types of bonds inside its molecular moiety. Figure 4.2 (a), (b), and (c) show some of the important geometrical peculiarities of ACV Molecule A, B, and C obtained from the single crystal X-ray diffraction experiment. From the figures, there are noticeable differences in the side chain orientations among Molecule A, B, and C. According to Newman projections principle (LibreTexts, 2019; *Alkane Conformation*, 2021), dihedral angle O_2-C_7-C_8-O_3 (-175.536 °) in Molecules A shows "staggered trans" orientation since it has closer dihedral angle to ±180.000°. On the other hands, with dihedral angles of -60.175° and -72.341°, dihedral angles of O_5-C_{15}-C_{16}-O_6 and O_8-C_{23}-C_{24}-O_9 in Molecule B and Molecule C show closer angle to ± 60.000 °. Hence, both of them pose "staggered gauche" orientations. Accompany with the difference in side chain arrangements, the C-C bonds (i.e. C_7-C_8, C_{15}-C_{16}, and C_{23}-C_{24}) in the side chains show deviations in geometry structures as compared among Molecule A, B, and C. For examples, with bond lengths of 1.492 Å and 1.480 Å, bond distances C_{15}-C_{16} (Molecule B) and C_{23}-C_{24} (Molecule C) show single C-C bond characteristic. However, bond distance C_7-C_8 with bond length of 1.434 Å, is found to be shorter than C_{15}-C_{16} and C_{23}-C_{24}. It is situated between the ranges of single C-C bond length and double C-C bond length (*Selected Bond Energies*, 2003; Wired Chemist, 2021). Besides, there is an observable difference in the linking edges (i.e. N_5-C_6, N_{10}-C_{14}, and N_{15}-C_{12}) between the guanine rings and side chains of ACV Molecule A, B, and C. For ACV Molecule A, bond distance and bond angle in

N_5-C_6 and N_5-C_6-O_2 are found to be 1.439 Å and 110.035°. For ACV Molecule B, it has N_{10}-C_{14} bond distance of 1.460 Å and N_{10}-C_{14}-O_5 bond angle of 111.933 °. For ACV Molecule C, bond distance N_{15}-C_{22} and bond angle N_{15}-C_{22}-O_8 obtained from the single crystal X-ray diffraction data are found to be 1.453 Å and 112.351°, respctively. All the N-C bonds (i.e. N_5-C_6, N_{10}-C_{14}, and N_{15}-C_{22}) explicit single N-C bond characteristics (*Selected Bond Energies*, 2003; Wired Chemist, 2021). Undoubtedly, these discrepancies indicate that three of the ACV Molecules A, B, and C have independent geometry identities. For the guanine moiety part, there is no significant difference among Molecule A, B, and C. Three of them show double bond (C=O) characteristic in bond distances O_1-C_1 (1.238 Å), O_4-C_9 (1.243 Å), and O_7-C_{17} (1.241 Å) (Peica, 2006). In Figure 4.2 (a), (b), and (c), it is found that all the aromatic C-C bond distances (i.e. C_1-C_2, C_2-C_3, C_9-C_{10}, C_{10}-C_{11}, C_{17}-C_{18}, and C_{18}-C_{19}) in the guanine moieties of ACV Molecules A, B, and C fall between the ranges of 1.374 Å to 1.421 Å. These indicate the presence of the resonance effect in the guanine rings of ACV molecules (Agrawal *et al.*, 2017; Bakkiyaraj, 2017). A similar trend of data is obtained from Álvarez Ros (2016) where the authors get 1.378 Å and 1.418 Å for the aromatic C-C bond distances in guanine molecule. Furthermore, the resonance effect also observable in bond distances N_2-C_4 (1.377 Å), C_4-N_3 (1.336 Å), N_5-C_3 (1.377 Å), N_7-C_{12} (1.362 Å), C_{12}-N_8 (1.339Å), N_{10}-C_{11} (1.374 Å), N_{12}-C_{20} (1.365 Å), C_{20}-N_{13} (1.337 Å), and N_{15}-C_{19} (1.372 Å). Since all of them have N-C bond lengths between single N-C bond (1.470 Å) and double N=C bond (1.290 Å) (Peica, 2006; Agrawal *et al.*, 2017). The pyrimidine rings of the guanine moieties in ACV Molecule A, B, and C do not explicit exactly hexagonal symmetry (120.000°) characteristic as shown in the benzene ring (Vidhya *et al.*,

2019). From the figures, the endocyclic bond angles for C_1-C_2-C_3, N_2-C_4-N_1, C_9-C_{10}-C_{11}, N_7-C_{12}-N_6, C_{17}-C_{18}-C_{19}, and N_{12}-C_{20}-N_{11} in Molecule A, B, and C are 119.023 °, 123.339 °, 119.049 °, 123.649 °, 118.672 °, and 122.943 °, respectively. These are due to the presence of nitrogen atoms in the pyrimidine ring caused the aromatic carbon atoms to exert an attraction force on the valence electron cloud of the nitrogen atoms (Agrawal *et al.*, 2017). Consequently, decrease the bond length in C-N bond distances. The unsymmetrical bond distances between C-C and C-N bonds affect the heterocyclic bond angles in the pyrimidine ring of guanine moieties. Moreover, three of the ACV Molecules A, B, and C explicit coplanar arrangements between the pyrimidine rings and imidazole rings of guanine moieties. As can be obtained from the figures, Molecule A shows -178.750° and -179.826° for dihedral angles N_1-C_3-N_5-C_5 and N_2-C_1-C_2-N_4. For Molecule B, N_6-C_{11}-N_{10}-C_{13} and N_7-C_9-C_{10}-N_9 have dihedral angles of 178.862° and 177.972°, whereas for Molecule C, dihedral angles of N_{12}-C_{17}-C_{18}-N_{14} and N_{11}-C_{19}-N_{15}-C_{21} are found to be -179.990° and -178.997°. Figure 4.2 (d) illustrates the hydrogen bonds in ACV-I molecular system. Noticed that the crystal packing of ACV-I molecular system is stabilised by N—H..O and O—H..O types of intermolecular hydrogen bond interactions (Sarojini *et al.*, 2012). In Table 4.1, all of the hydrogen bonds are categorised as moderate hydrogen bond since they have donor—acceptor bond distances of 2.669 Å to 3.167 Å and donor—hydrogen..acceptor angles of 138.000 ° to 164.800° (Pumpo, 2016).

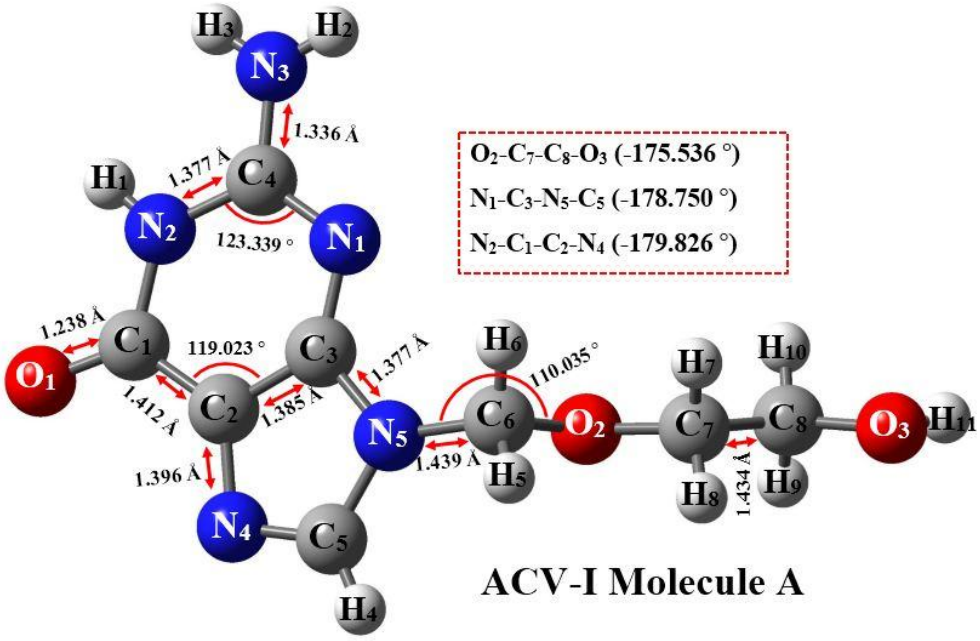

Figure 4.2 (a) Parts of the geometry parameters (i.e. bond distances, bond angles, and dihedral angles) of ACV-I Molecule A.

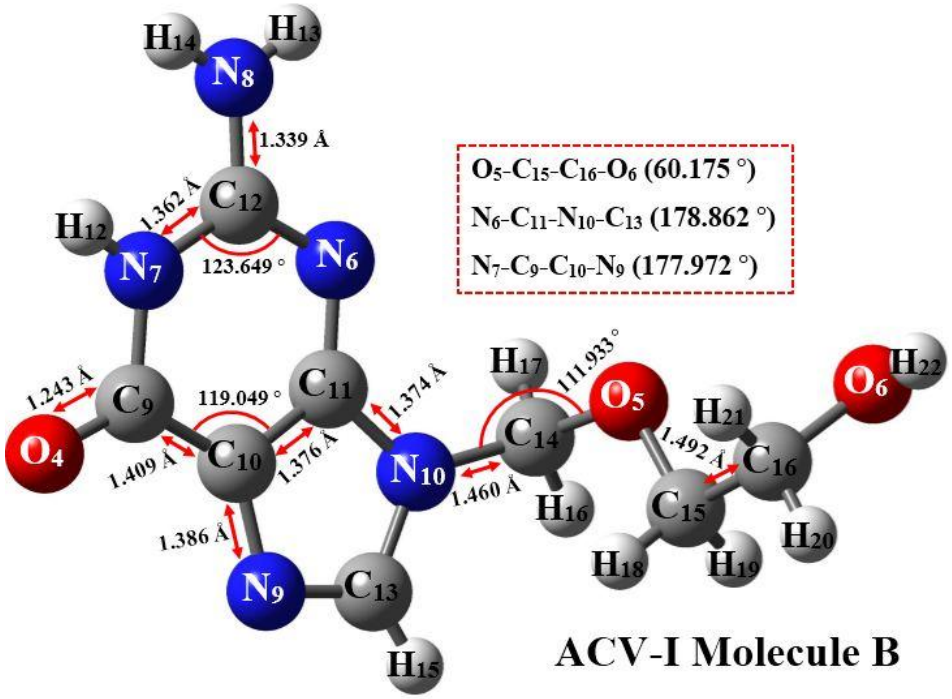

Figure 4.2 (b) Parts of the geometry parameters (i.e. bond distances, bond angles, and dihedral angles) of ACV-I Molecule B.

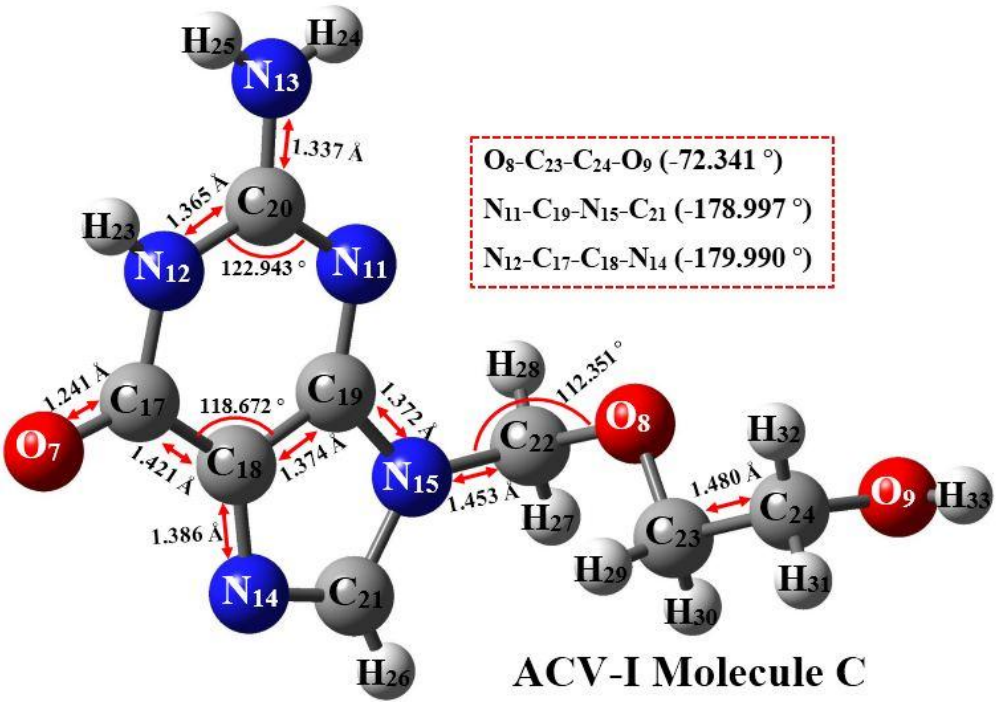

Figure 4.2 (c) Parts of the geometry parameters (i.e. bond distances, bond angles, and dihedral angles) of ACV-I Molecule C.

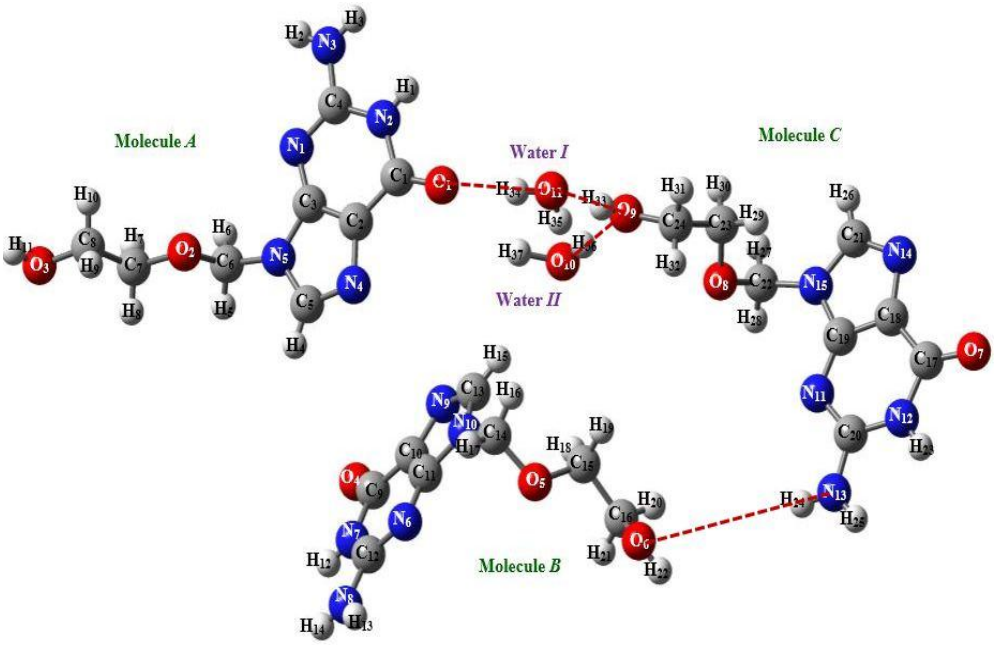

Figure 4.2 (d): The hydrogen bond interactions in ACV-I molecular system.

Table 4.1: Geometry parameters of intermolecular hydrogen bonds in ACV-I molecular system.

Donor---Hydrogen...Acceptor	Don--Hyd [Å]	Hyd--Acc [Å]	Don--Acc [Å]	D--H-----A
N_{13}---H_{24}…O_6	0.860	2.480	3.167	138.000°
O_9---H_{33}…O_{11}	0.820	1.870	2.669	164.200°
O_{10}---H_{36}…O_9	0.780	2.090	2.850	164.800°
O_{11}---H_{34}…O_1	0.850	1.940	2.739	156.500°

Table 4.2 (a), (b), and (c) summarise the experimental and computational geometry structures of the ACV-I single molecular system. As compared between the optimized and experimental geometry parameters (i.e. bond distances, bond angles, and dihedral angles), there are slight changes in the geometrical structures of ACV-I after geometry optimization calculations using DFT/B3LYP/6-31G** and DFT/B3LYP/6-311G** level of theories. In Table 4.2 (a), the largest deviations between experimental and computational data in ACV Molecule A can be observed from bond distance C_7-C_8, bond angle C_7-C_8-O_3, and dihedral angle N_1-C_3-N_5-C_6. DFT/B3LYP/6-31G** method shows percentage differences of 5.886%, 3.207%, and 0.319% in C_7-C_8, C_7-C_8-O_3, and N_1-C_3-N_5-C_6, while DFT/B3LYP/6-311G** method gets 5.668%, 3.121%, and 0.274%. Besides, Table 4.2 (b) reveals that ACV Molecule B has the largest optimized percentage differences in bond distance C_9-N_7, bond angle C_{15}-C_{16}-O_6, and dihedral angle N_6-C_{11}-N_{10}-C_{14}. For DFT/B3LYP/6-31G** method, the calculated percentage differences for C_9-N_7, C_{15}-C_{16}-O_6, and N_6-C_{11}-N_{10}-C_{14} are 2.877%, 3.630%, and 0.642%, whereas for DFT/B3LYP/6-311G** method are 2.920%, 3.466%, and 0.374%. Moreover, with percentage

differences of 3.222%, 3.034%, 1.929% (in DFT/B3LYP/6-31G** method) and 3.236%, 2.909%, 2.072% (in DFT/B3LYP/6-311G** method), ACV Molecule C shows the largest deviations in bond distance C_{17}-N_{12}, bond angle C_{19}-N_{15}-C_{22}, and dihedral angle N_{11}-C_{19}-N_{15}-C_{22}, as compared with experimental data. These differences are due to the reason that experimental data is obtained from the solid and bulk case, whereas computational data is presented under the gases phase (Sundaraganesan *et al.*, 2007; Kalaiarasi and Manivarman, 2017). With the maximum percentage differences of 5.886% and 5.668%, it can be concluded that both of the ACV-I optimized geometry structures using DFT/B3LYP/6-31G** and DFT/B3LYP/6-311G** computational methods show satisfactory agreement with experimental data. These give strong confidence in the ability of DFT computational methods (i.e. DFT/B3LYP/6-31G** and DFT/B3LYP/6-311G**) to accurately describe the ACVs molecular system (Kumar *et al.*, 2013).

Table 4.2 (a): Experimental and optimized geometry parameters of ACV Molecule A in ACV-I molecular system.

Molecule A	ACV-I		
	DFT/B3LYP/6-31G**	DFT/B3LYP/6-311G**	Experiment
Bond Distance (Å)			
O_1-C_1	1.231	1.225	1.238
C_1-N_2	1.427	1.429	1.385
N_2-C_4	1.376	1.374	1.377
N_1-C_3	1.354	1.351	1.339
C_3-C_2	1.396	1.394	1.385
C_4-N_3	1.360	1.359	1.336
C_2-N_4	1.382	1.381	1.396
C_3-N_5	1.374	1.373	1.377
N_5-C_6	1.439	1.438	1.439
C_6-O_2	1.411	1.411	1.381
O_2-C_7	1.420	1.421	1.431
C_7-C_8	1.519	1.516	1.434
C_8-O_3	1.423	1.424	1.387
Bond Angle (°)			
O_1-C_1-N_2	119.254	119.112	120.614
O_1-C_1-C_2	130.319	130.593	127.762
N_3-C_4-N_1	119.334	119.463	120.809
C_4-N_1-C_3	112.810	113.046	112.418
C_3-C_2-N_4	111.140	110.993	110.857
C_3-N_5-C_5	105.889	105.913	106.792
C_3-N_5-C_6	126.749	126.701	127.112
N_5-C_6-O_2	108.949	109.001	110.035
O_2-C_7-C_8	107.902	107.931	111.010
C_7-C_8-O_3	106.361	106.456	109.885
Dihedral Angle (°)			
O_1-C_1-C_2-C_3	-177.803	-177.803	-177.803
O_1-C_1-N_2-C_4	-179.791	-179.781	-179.800
N_3-C_4-N_1-C_3	-178.731	-178.731	-178.731
N_1-C_3-N_5-C_6	2.186	2.187	2.193
N_5-C_6-O_2-C_7	-172.690	-172.690	-172.690
O_2-C_7-C_8-O_3	-175.536	-175.536	-175.536

Table 4.2 (b): Experimental and optimized geometry parameters of ACV Molecule B in ACV-I molecular system.

Molecule B	ACV-I		
	DFT/B3LYP/6-31G**	DFT/B3LYP/6-311G**	Experiment
Bond Distance (Å)			
O_4-C_9	1.221	1.214	1.243
C_9-N_7	1.438	1.438	1.397
N_7-C_{12}	1.375	1.374	1.362
N_6-C_{11}	1.357	1.355	1.352
C_{11}-C_{10}	1.394	1.392	1.376
C_{12}-N_8	1.363	1.363	1.339
C_{10}-N_9	1.382	1.381	1.386
C_{11}-N_{10}	1.376	1.375	1.374
N_{10}-C_{14}	1.456	1.456	1.460
C_{14}-O_5	1.401	1.400	1.403
O_5-C_{15}	1.421	1.422	1.439
C_{15}-C_{16}	1.514	1.511	1.492
C_{16}-O_6	1.419	1.421	1.420
Bond Angle (°)			
O_4-C_9-N_7	119.688	119.826	119.806
O_4-C_9-C_{10}	130.588	130.523	128.458
N_8-C_{12}-N_6	119.127	119.229	119.537
C_{12}-N_6-C_{11}	112.745	113.020	112.256
C_{11}-C_{10}-N_9	111.101	110.987	110.287
C_{11}-N_{10}-C_{13}	105.655	105.650	106.018
C_{11}-N_{10}-C_{14}	126.491	126.464	126.084
N_{10}-C_{14}-O_5	113.903	113.990	111.933
O_5-C_{15}-C_{16}	109.288	109.423	109.896
C_{15}-C_{16}-O_6	108.724	108.909	112.819
Dihedral Angle (°)			
O_4-C_9-C_{10}-C_{11}	-179.106	-179.106	-179.106
O_4-C_9-N_7-C_{12}	179.034	179.033	179.024
N_8-C_{12}-N_6-C_{11}	178.145	178.145	178.145
N_6-C_{11}-N_{10}-C_{14}	3.765	3.755	3.741
N_{10}-C_{14}-O_5-C_{15}	76.682	76.682	76.682
O_5-C_{15}-C_{16}-O_6	-60.175	-60.175	-60.175

Table 4.2 (c): Experimental and optimized geometry parameters of ACV Molecule C in ACV-I molecular system.

Molecule C	ACV-I		
	DFT/B3LYP/6-31G**	DFT/B3LYP/6-311G**	Experiment
Bond Distance (Å)			
O_7-C_{17}	1.219	1.212	1.241
C_{17}-N_{12}	1.429	1.430	1.385
N_{12}-C_{20}	1.382	1.380	1.365
N_{11}-C_{19}	1.359	1.356	1.348
C_{19}-C_{18}	1.391	1.388	1.374
C_{20}-N_{13}	1.363	1.362	1.337
C_{18}-N_{14}	1.381	1.379	1.386
C_{19}-N_{15}	1.383	1.381	1.372
N_{15}-C_{22}	1.459	1.459	1.453
C_{22}-O_8	1.405	1.404	1.407
O_8-C_{23}	1.429	1.430	1.436
C_{23}-C_{24}	1.514	1.510	1.480
C_{24}-O_9	1.429	1.430	1.406
Bond Angle (°)			
O_7-C_{17}-N_{12}	123.203	123.359	120.685
O_7-C_{17}-C_{18}	126.926	126.816	127.732
N_{13}-C_{20}-N_{11}	118.840	118.949	119.560
C_{20}-N_{11}-C_{19}	113.047	113.304	112.361
C_{19}-C_{18}-N_{14}	111.532	111.449	110.831
C_{19}-N_{15}-C_{21}	105.391	105.436	105.836
C_{19}-N_{15}-C_{22}	130.357	130.199	126.519
N_{15}-C_{22}-O_8	114.156	113.818	112.351
O_8-C_{23}-C_{24}	112.238	112.303	109.967
C_{23}-C_{24}-O_9	109.678	109.714	109.753
Dihedral Angle (°)			
O_7-C_{17}-C_{18}-C_{19}	-179.707	-179.707	-179.707
O_7-C_{17}-N_{12}-C_{20}	-179.397	-179.399	-179.314
N_{13}-C_{20}-N_{11}-C_{19}	-179.427	-179.427	-179.427
N_{11}-C_{19}-N_{15}-C_{22}	1.525	1.527	1.496
N_{15}-C_{22}-O_8-C_{23}	66.490	66.490	66.490
O_8-C_{23}-C_{24}-O_9	-72.341	-72.341	-72.341

4.1.2 Total Energies and Frontier Molecular Orbital (FMO) Energies

Table 4.3 tabulates the computed total energies, HOMO energies, LUMO energies, and HOMO-LUMO energy gaps of ACV-I molecular system using DFT/B3LYP/6-31G** and DFT/B3LYP/6-311G** level of theories. From the table, noted that the optimized total energy of the ACV-I molecular system computed via DFT/B3LYP/6-31G** method is -70358.746 eV while for DFT/B3LYP/6-311G** method is -70376.691 eV. The computed total energy is important and directly related to the stability of a molecular system (Chavda *et al.*, 2016; Ali *et al.*, 2017; Chaturvedi *et al.*, 2018). Selsi *et al.* (2019) found that the optimized ground state total energy of anhydrous ACV molecular system using DFT/B3LYP/STO-3G* method is -21778.542 eV. Kumar *et al.* (2013) also get closer result (about -22067.085 eV) for anhydrous ACV molecule via DFT/B3LYP/6-311+G** method. These imply that ACV-I molecular system is more stable than anhydrous ACV molecular system since it has lower total energy. Besides, as can be obtained in Table 4.3, the HOMO energy and LUMO energy obtained using DFT/B3LYP/6-31G** method are -5.298 eV and -0.409 eV, respectively, whereas for DFT/B3LYP/6-311G** method are -5.509 eV and -0.607 eV. The frontier molecular energies (i.e. HOMO and LUMO) are the powerful guiding principle in the determination of molecular reactivity, electronic, and optical properties of ACV-I molecular system (Fahim and Shalaby, 2019; Tariq *et al.*, 2019; Tribak *et al.*, 2019). The HOMO energy describes the electron donating ability while the LUMO energy represents the electron accepting ability of the ACV-I molecular system (Fahim and Shalaby, 2019; Tribak *et al.*, 2019). Both of them show a direct relationship with

ionization energy (IE) and electron affinity (EA) of ACV-I molecule (Nabati and Mahkam, 2016; Asath *et al.*, 2017; Barakat *et al.*, 2018; Tribak *et al.*, 2019; Abdel-Rahman *et al.*, 2020). Consequently, the computed energy levels of HOMO and LUMO have significant usages in the determination of global reactivity descriptors of ACV-I molecular system. Based on the formulas state in Koopmans theorem (Barakat *et al.*, 2018; Demircioğlu *et al.*, 2019), the ionization energy (IE), electron affinity (EA), hardness (η), chemical potential (μ), softness (S), electronegativity (χ), and electrophilicity index (ω) of ACV-I molecular system for DFT/B3LYP/6-31G** method are 5.298 eV, 0.409 eV, 2.445, -2.854, 0.204, 2.854, and 1.662, respectively, while for DFT/B3LYP/6-311G** method are 5.509 eV, 0.607 eV, 2.451, -3.058, 0.204, 3.058, and 1.908, respectively. Furthermore, the HOMO and LUMO 3D surface mapped plots of ACV-I molecular system are presented in Figure 4.3 (a) and (b). The green colour lobe represents the negative phase, while the red colour lobe represents the positive region (Sachdeva *et al.*, 2018; Vidhya *et al.*, 2019). Noticed that both of DFT/B3LYP/6-31G** and DFT/B3LYP/6-311G** methods get similar HOMO and LUMO mapping results. In HOMO and LUMO surface mapped plots, atoms/molecules that are surrounded by a large number of HOMO electron densities will have stronger ability to donate electrons, while atoms/molecules that are covered by a huge amount of LUMO electron densities will show stronger ability to receive electrons (Balachandran *et al.*, 2013). Hence, the graphical interpretations of HOMO and LUMO help to visualise and predict the most reactive position of the ACV-I molecule in π electron system (Tribak *et al.*, 2019). As can be observed in Figure 4.3 (a) and (b), the electron density distributions for HOMO are mainly localised on the guanine ring of ACV

Molecule B, while the electron densities for LUMO are found to be distributed on the guanine ring of ACV Molecule A. Realized that there are absent of electron density distributions around the water molecules and the side chains for both HOMO and LUMO surface mapped plots. These indicate that the HOMO→ LUMO transition in ACV-I molecular system implies an electron density transfer from the guanine rings of Molecule B to the guanine ring of Molecule A (Targema *et al.*, 2013; Sachdeva *et al.*, 2018). Moreover, through the molecular coefficients analysis, it can be said that the transitions of electrons in ACV-I molecular system are mainly derived from π to π^*. Since both of the HOMO and LUMO orbitals are mainly composed from p_y type orbitals. In additions, the energy gap between HOMO and LUMO energies reveals the biological activity of ACV-I molecule (Fahim and Shalaby, 2019). It helps to predict the kinetic stability and chemical reactivity of ACV-I molecular system (Jasmine *et al.*, 2015; Abbaz *et al.*, 2019; Demircioğlu *et al.*, 2019). As refer to Table 4.3, the HOMO-LUMO energy gaps for ACV-I molecular system obtained via DFT/B3LYP/6-31G** and DFT/B3LYP/6-311G** methods fall between the ranges of 4.889 eV to 4.902 eV. Previous literature studies figured out that anhydrous ACV molecular system has HOMO-LUMO energy gap of 0.198 eV (Selsi *et al.*, 2019). Therefore, it can be said that ACV-I molecular system is less polarized, low chemical reactivity, high kinetic stability, and harder than anhydrous ACV molecule because ACV-I molecular system has larger HOMO-LUMO energy gap (Nabati and Mahkam, 2016; Demircioğlu *et al.*, 2019; Vidhya *et al.*, 2019). In order to validate the FMOs computational data, UV-Vis spectroscopy is employed. Noted that the absorption spectrum in the UV-Vis experiment occurred due to the transition of electron from the ground state to

the excitation state (Arivazhagan and James, 2017). Therefore, the experimental energy gap of ACV-I molecular system can be obtained from the peak of the absorption spectrum. With the absorption spectrum (λ) of 250 nm, the experimental energy gap for ACV-I molecular system is found to be 4.960 eV. Therefore, both the experimental and computed energy gaps show good agreement with each other.

Table 4.3: Total energies, HOMO energies, LUMO energies, and HOMO-LUMO energy gaps of ACV-I molecular system.

	ACV-I	
	DFT/B3LYP/6-31G**	DFT/B3LYP/6-311G**
Total Energy (eV)	-70358.746	-70376.691
HOMO (eV)	-5.298	-5.509
LUMO (eV)	-0.409	-0.607
HOMO-LUMO Energy Gap (eV)	4.889	4.902
Ionization Energy (IE) (eV)	5.298	5.509
Electron Affinity (EA) (eV)	0.409	0.607
Hardness (η)	2.445	2.451
Chemical Potential (μ)	-2.854	-3.058
Softness (S)	0.204	0.204
Electronegativity (χ)	2.854	3.058
Electrophilicity index (ω)	1.662	1.908

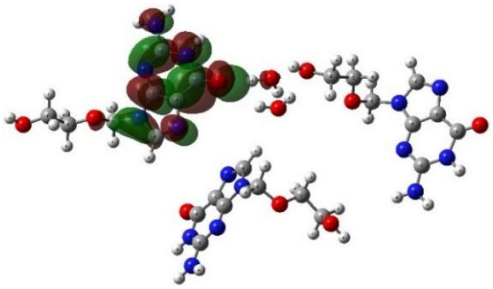

LUMO (−0.409 eV)

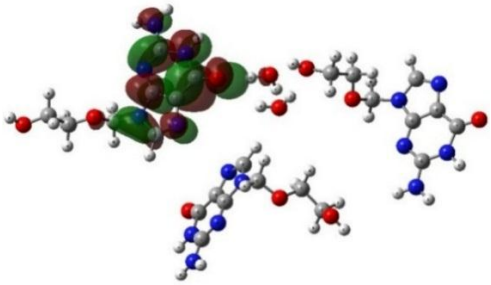

LUMO (−0.607 eV)

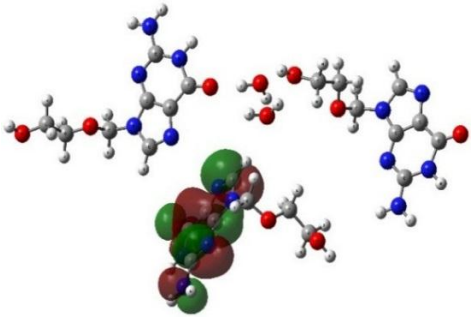

HOMO (-5.298 eV)

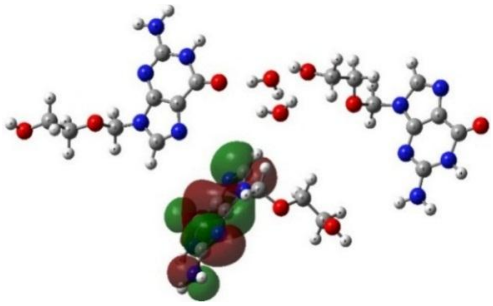

HOMO (-5.509 eV)

Figure 4.3 (a): LUMO and HOMO surface mapped plots of ACV-I molecular system using DFT/B3LYP/6-31G** method.

Figure 4.3 (b): LUMO and HOMO surface mapped plots of ACV-I molecular system using DFT/B3LYP/6-311G** method.

4.1.3 Mulliken Population Analysis (MPA)

Table 4.4 summarises all the effective Mulliken atomic charge distributions of ACV-I molecular system computed using DFT/B3LYP/6-31G** and DFT/B3LYP/6-311G** level of theories. Understanding the distributions of atomic charges in ACV-I molecular system via Mulliken population analysis (MPA) plays a significant role in quantum chemical calculations. It gives better knowledge about the reactive nature and electronic properties of the system because atomic charges strongly influence the dipole moment, polarizability, electronic structure, and reactivity of ACV-I molecule (Asath *et al.*, 2017;

Arivazhagan and James, 2017; Priya *et al.*, 2019). Besides, the polarity and magnitude of the charge values in MPA able to provide informative data about the atomic charge shift activities in the ACV-I molecular system. So that, Mulliken atomic charge analysis shows a direct relationship in the determination of chemical bonding in the ACV-I molecular system (Bharanidharan and Seevakan, 2018). It also estimates the ability of an atom contributes in hydrogen bonding interaction. Furthermore, the Mulliken atomic charges are also related to the vibrational properties of the ACV-I molecule and help in the measurement of hydrogen and carbon chemical shifts in NMR analysis (Bakkiyaraj, 2017; Bharanidharan and Seevakan, 2018). Figure 4.4 illustrates parts of the effective Mulliken atomic charges in ACV-I molecular system. From the histogram, both of the computational methods (i.e. 6-31G** and 6-311G** basis sets) show approximately same trend of MPA data but slightly different in charge values. For example, all the hydrogen atoms in the ACV-I molecule exhibit positive charge values while the oxygen and nitrogen atoms are all in negative charge distributions. From the computational results, it is obvious to notify that both of DFT/B3LYP/6-31G** and DFT/B3LYP/6-311G** methods show highest positive atomic charge value on carbon atom C_4 while the three nitrogen atoms (i.e. N_1, N_2, N_3) bonded with it elucidate higher negative atomic charges. These are because the presence of three electronegative nitrogen atoms as neighbouring bonded atoms intensively share the lone pair electrons of carbon atom C_4 (Sachdeva *et al.*, 2018; Lakshmi *et al.*, 2019). With the same reason, carbon atoms C_{12} and C_{20} are found to be the second and third highest positive atomic charges in ACV-I molecular system. On the other hands, the highest negative Mulliken atomic charge in ACV-I molecular system is found to be located on

oxygen atom O_{11} with charge values of -0.668 (6-31G**) and -0.537 (6-311G**). For the nitrogen atoms in the imidazole rings of ACV molecules, the presence of side chain bonding effect in atoms N_5, N_{10}, and N_{15} caused them to exhibit larger negative charge values than atoms N_4, N_9, and N_{14} (Alvarez-Ros and Palafox, 2014). Moreover, with atomic charge values of 0.214 (6-31G**) and 0.153 (6-311G**), carbon atom C_6 (ACV Molecule A) shows higher positive atomic charge than C_{14} (ACV Molecule B) and C_{22} (ACV Molecule C). This indicates that the C_6 atom is more reactive than C_{14} and C_{22}. Hence, the bond length of N_5-C_6 should be shorter than N_{10}-C_{14} and N_{15}-C_{22} which strongly supported by the single crystal X-ray diffraction data. As a group 14 element, carbon atoms can be either carry positive or negative atomic charge depending on their chelating atoms. According to Figure 4.4, there is a slightly conflict in the atomic charge polarity of carbon atoms C_2, C_{10}, and C_{18}. DFT/B3LYP/6-31G** method elucidates positive charge results, while DFT/B3LYP/6-311G** technique shows negative charge readings. It is more reasonable to obtain positive Mulliken atomic charges in atoms C_2, C_{10} and C_{18} due to the lone pair electron sharing activities with the bonded nitrogen atoms N_4, N_9, and N_{14}. So that, DFT/B3LYP/6-31G** method shows slightly better performance than the DFT/B3LYP/6-311G** method in the calculation of MPA for the ACV-I molecular system. The resonance effects in ACV-I molecular system can be observed from atoms C_1-C_2-C_3, C_9-C_{10}-C_{11}, and C_{17}-C_{18}-C_{19} since all of them poses positive Mulliken atomic charges. In additions, higher negative atomic charges in atoms N_3, N_8, N_{13}, O_1, O_9, O_{10}, and O_{11} together with larger positive atomic charges in atoms H_1, H_2, H_3, H_{11}, H_{12}, H_{13}, H_{14}, H_{22}, H_{23}, H_{24}, H_{25}, H_{33}, H_{34}, H_{35}, H_{36}, and H_7 suggest the presence of intra and intermolecular hydrogen

bonding interaction in ACV-I molecular system (Jasmine *et al.*, 2015).

Table 4.4: Computed Mulliken atomic charges analysis (MPA) of ACV-I molecular system using DFT/B3LYP/6-31G** and DFT/B3LYP/6-311G** methods.

ACV-I					
MPA					
Atoms	DFT/B3LYP/6-31G**	DFT/B3LYP/6-311G**	Atoms	DFT/B3LYP/6-31G**	DFT/B3LYP/6-311G**
O_1	-0.548	-0.403	H_{17}	0.138	0.135
C_1	0.575	0.453	O_5	-0.457	-0.344
C_2	0.136	-0.127	C_{15}	0.057	-0.027
C_3	0.538	0.394	H_{18}	0.100	0.108
N_1	-0.591	-0.421	H_{19}	0.099	0.100
C_4	0.752	0.600	C_{16}	0.040	-0.014
N_2	-0.619	-0.484	H_{20}	0.080	0.086
H_1	0.273	0.233	H_{21}	0.098	0.099
N_3	-0.661	-0.500	O_6	-0.527	-0.392
H_2	0.298	0.251	H_{22}	0.307	0.236
H_3	0.279	0.234	O_7	-0.502	-0.333
N_4	-0.485	-0.294	C_{17}	0.570	0.421
C_5	0.291	0.193	C_{18}	0.113	-0.153
N_5	-0.536	-0.411	C_{19}	0.524	0.383
H_4	0.130	0.119	N_{11}	-0.586	-0.413
C_6	0.214	0.153	C_{20}	0.742	0.590
H_5	0.109	0.109	N_{12}	-0.628	-0.486
H_6	0.122	0.118	H_{23}	0.266	0.225
O_2	-0.490	-0.367	N_{13}	-0.663	-0.503
C_7	0.070	-0.024	H_{24}	0.297	0.250
H_7	0.098	0.099	H_{25}	0.273	0.229

Table 4.4 Continued.

Atoms	DFT/B3LYP/6-31G**	DFT/B3LYP/6-311G**	Atoms	DFT/B3LYP/6-31G**	DFT/B3LYP/6-311G**
H_8	0.103	0.107	N_{14}	-0.487	-0.293
C_8	0.035	-0.016	C_{21}	0.260	0.151
H_9	0.101	0.102	N_{15}	-0.523	-0.415
H_{10}	0.097	0.099	H_{26}	0.113	0.110
O_3	-0.544	-0.408	C_{22}	0.182	0.123
H_{11}	0.313	0.245	H_{27}	0.105	0.114
O_4	-0.517	-0.348	H_{28}	0.143	0.143
C_9	0.555	0.408	O_8	-0.458	-0.340
C_{10}	0.129	-0.127	C_{23}	0.057	-0.028
C_{11}	0.524	0.381	H_{29}	0.107	0.119
N_6	-0.591	-0.419	H_{30}	0.096	0.093
C_{12}	0.743	0.591	C_{24}	0.036	-0.006
N_7	-0.623	-0.488	H_{31}	0.102	0.106
H_{12}	0.264	0.223	H_{32}	0.104	0.104
N_8	-0.664	-0.504	O_9	-0.563	-0.437
H_{13}	0.295	0.248	H_{33}	0.318	0.238
H_{14}	0.273	0.228	O_{10}	-0.641	-0.495
N_9	-0.487	-0.298	H_{34}	0.339	0.279
C_{13}	0.278	0.173	H_{35}	0.295	0.215
N_{10}	-0.521	-0.416	O_{11}	-0.668	-0.537
H_{15}	0.118	0.110	H_{36}	0.324	0.261
C_{14}	0.183	0.136	H_{37}	0.294	0.235
H_{16}	0.104	0.109			

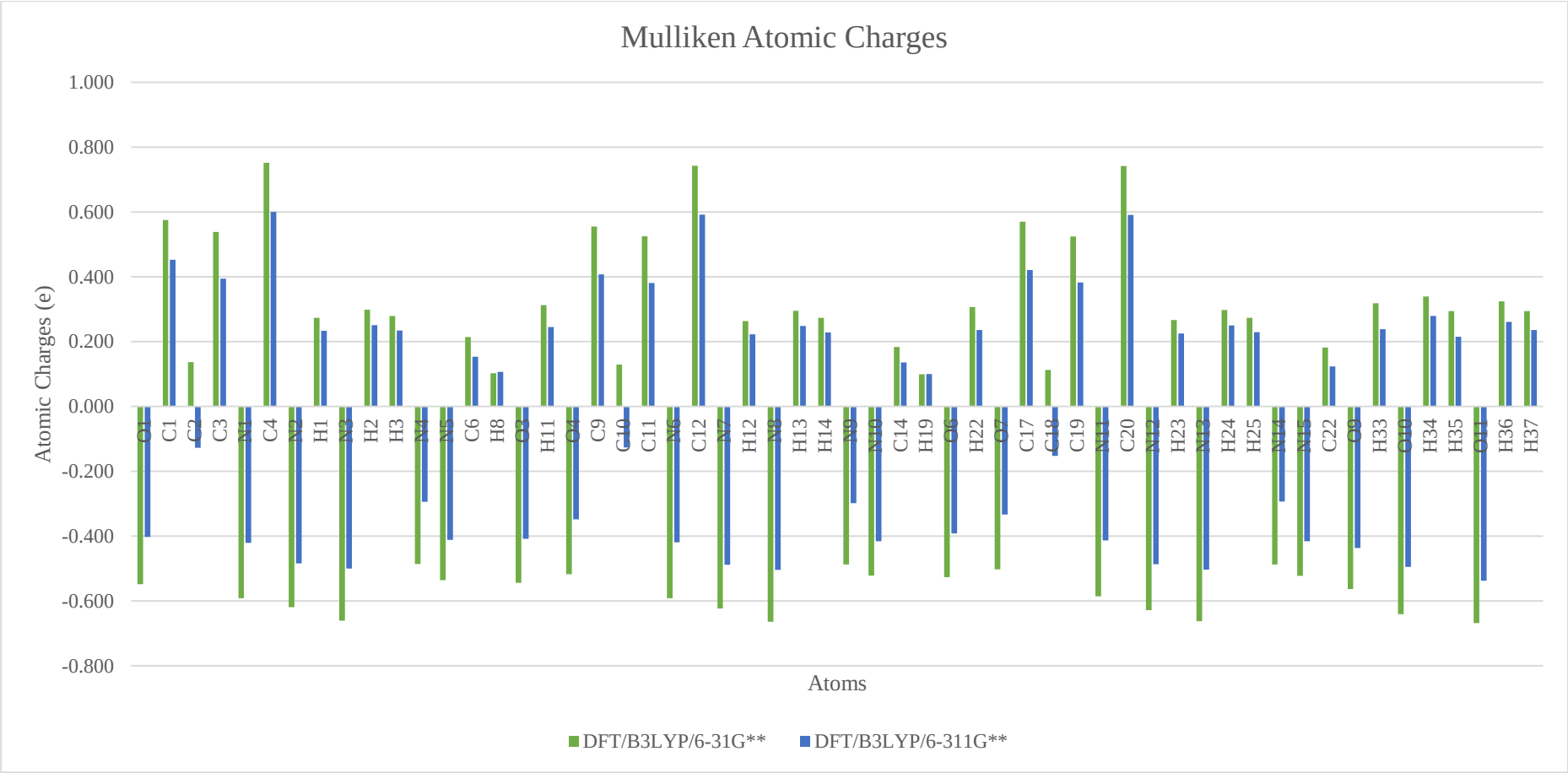

Figure 4.4: MPA analysis of ACV-I molecular system using DFT/B3LYP/6-31G** and DFT/B3LYP/6-311G** methods.

4.1.4 Molecular Electrostatic Potential (MEP)

Figure 4.5 (a) and (b) illustrate the molecular electrostatic potential (MEP) surface mapped plots of ACV-I molecular system calculated at DFT/B3LYP/6-31G** and DFT/B3LYP/6-311G** level of theories. The MEP is a powerful illustration tool used to predict and study the molecular behaviour and reactivity of ACV-I with other molecular species (Ahmad *et al.*, 2018). It elucidates the charge distributions of ACV-I molecule in three-dimensions (Sachdeva *et al.*, 2018) and provides informative data related to the electron densities structure of the ACV-I molecular system via colouring scheme (Erdemir *et al.*, 2020). Generally, the MEP surface mapping has colour code sequences of red > yellow > green > blue that represent the most negative electrostatic potential region to the least negative electrostatic potential region. In other words, the red colour mapped plot indicates electron rich region, while the blue colour mapped plot indicates electron deficient region (Sachdeva *et al.*, 2018). Therefore, MEP acts as a useful descriptor to determine and visualise the sites for electrophilic and nucleophilic reactions in ACV-I molecular system (Akbas *et al.*, 2018; Erdemir *et al.*, 2020). These find potent application in the studies of the biological recognition process and hydrogen bonding interaction in ACV-I molecule (Ali *et al.*, 2017; Sachdeva *et al.*, 2018). Besides, MEP also displays the molecular size, polarity, and shape of the ACV-I molecular system. As can be seen from the figures, both of the computational methods (i.e. 6-31G** and 6-311G** basis sets) produce approximately identical MEP results for the ACV-I molecular system. Noticed that the negative electrostatic potential regions (red colour) are mainly concentrated over oxygen atoms (O_1, O_4, O_6, O_7, O_{10}, O_{11}) and nitrogen

atoms (N_4, N_9, N_{12}) due to their high electronegativity characteristics and the presence of lone pair electrons (Barakat *et al.*, 2018). Conversely, it is figured out that the positive electrostatic potential regions are mainly focused around hydrogen atoms (H_1, H_3, H_{13}, H_{14}, H_{23}, H_{25}). These suggested that atoms O_1, O_4, O_6, O_7, O_{10}, O_{11}, N_4, N_9, and N_{12} will be the most probable sites for electrophilic attacks while atoms H_1, H_3, H_{13}, H_{14}, $H_{23,}$ and H_{25} are the sites preferred for nucleophilic reactions in ACV-I molecular system (Ali *et al.*, 2017; Ahmad *et al.*, 2018; Akbas *et al.*, 2018). Hence, reveals the possible regions where the intra and intermolecular interaction of the ACV-I molecular system can take place (Sridevi, 2012; Kabouchi *et al.*, 2017). Furthermore, all the carbon atoms in ACV-I molecular system pose colourless intermediate electropositive potential identities and behave as non-polar molecules. Moreover, with the help of the Multifwn software package, the global surface extrema points of the ACV-I molecular system are calculated and plotted in Figure 4.5 (a) and (b). From the figures, noted that the global surface minimum points for both computational methods are located around oxygen atom O_7 with values of -2.555 eV (6-31G**) and -2.510 eV (6-31G**). On the other hands, the global surface maximum points in ACV-I molecular system are found to be situated around hydrogen atom H_3 with values of 2.708 eV (6-31G**) and 2.703 eV (6-31G**).

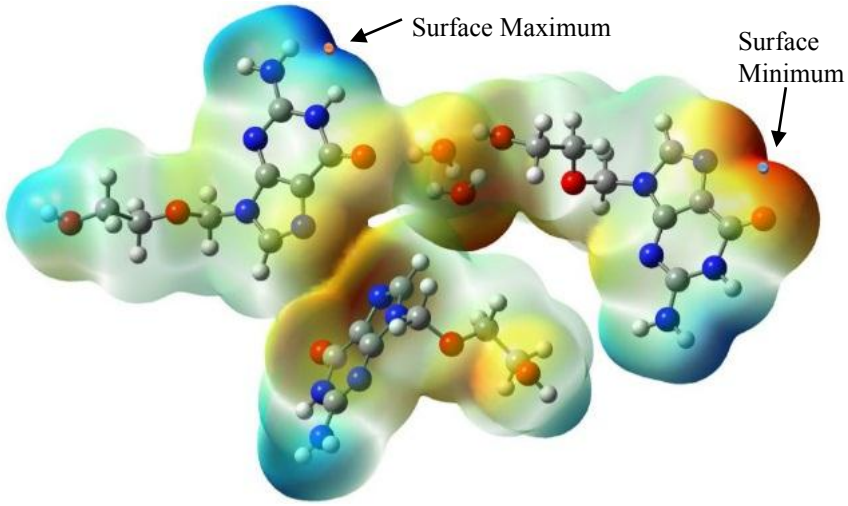

Surface Minimum (blue dot): -2.555 eV
Surface Maximum (red dot): 2.708 eV

Figure 4.5 (a): The MEP surface mapped plots of ACV-I molecular system using DFT/B3LYP/6-31G** method.

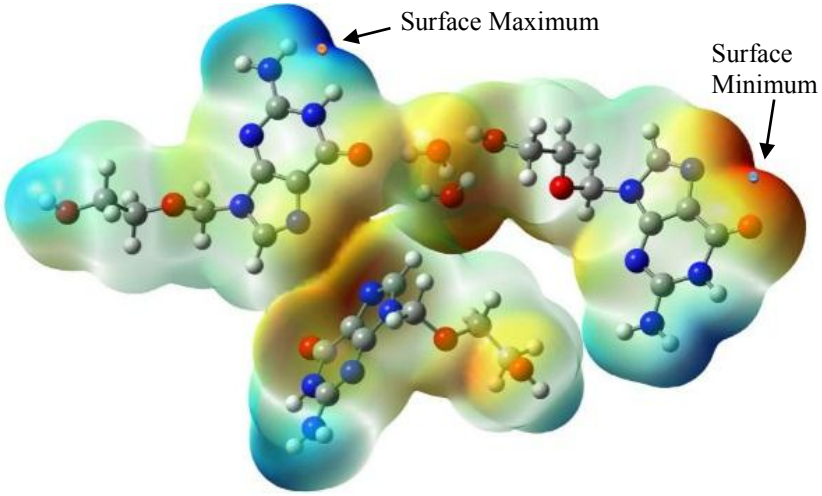

Surface Minimum (blue dot): -2.510 eV
Surface Maximum (red dot): 2.703 eV

Figure 4.5 (b): The MEP surface mapped plots of ACV-I molecular system using DFT/B3LYP/6-311G** method.

4.1.5 Non-Linear Optical (NLO) Properties

The determination and discovery of non-linear optical (NLO) behaviour in chemical substances has gathered huge attention in current research since an active NLO material shows fascinate applications in laser technologies, electrochemical sensors, data storage, and telecommunications industries (Abdel-Rahman *et al.*, 2020; Avci *et al.*, 2020). Recently, organic compounds gain high popularity as promising candidates for NLO applications because of the easy and flexible manipulation processes in organic crystal compounds (Valverde *et al.*, 2019). Besides, the presence of π electron conjugated system also leads organic compounds to exhibit better NLO properties than other chemical substances. So far, there is a lack of information addressing the NLO behaviour of hydrated ACV compounds. This triggered the interest to study and understand the NLO properties in the hydrated ACV molecular system. One of the easier and cost-effective way in the determination of NLO properties is through computational approach. With the employment of the DFT computational technique, the NLO behaviour of the ACV-I molecular system can be justified through dipole moment (μ) and first hyperpolarizability (β_{tot}) parameters. Both of them governed and have a direct relationship with the second harmonic generation (SHG) effect, which is a non-linear optical process that doubles the frequency of the incoming optical wave (Jiang et *al.*, 2014; Mohammed, 2017). Commonly, a qualified and active NLO material tends to show a higher value in both parameters (Abdel-Rahman *et al.*, 2020). Table 4.5 tabulates the computed dipole moment (μ) and first hyperpolarizability (β_{tot}) of ACV-I molecular system using DFT/B3LYP/6-31G** and DFT/B3LYP/6-

311G** methods. From the table, it is reported that the calculated dipole moment of ACV-I molecular system obtained from DFT/B3LYP/6-31G** method is 12.384 Debye, whereas for DFT/B3LYP/6-311G** method is 12.274 Debye. The dipole moment describes the molecular fundamental properties of ACV-I molecule and gives information about the non-bonded type dipole-dipole intermolecular interaction (Boukabcha *et al.*, 2015; Rahmani *et al.*, 2018). A larger value in dipole moment indicates stronger intermolecular interaction. Noticed that the vector direction of the dipole moment in the ACV-I molecular system depends on the centres of positive and negative charges. It is observed that both of the computational results (i.e. 6-31G** and 6-311G** basis sets) show major dipole moment contribution from Z-component (μ_z). Originally, the computed first hyperpolarizability results taken from Gaussian 09 software output data are recorded in atomic units (a.u). In order to simplify the NLO analysis process, conversion factor of 8.639 x 10^{-33} is used to shift the atomic units (a.u) to electrostatic units (e.s.u) (Arivazhagan and James, 2017; Abdel-Rahman *et al.*, 2020). Consequently, the converted first hyperpolarizabilities of ACV-I molecular system using DFT/B3LYP/6-31G** and DFT/B3LYP/6-311G** computational methods are found to be 5.141 x 10^{-29} e.s.u and 5.206 x 10^{-29} e.s.u. In this work, there is an absence of NLO experimental data for the ACV-I molecular system. Therefore, urea is chosen as the guiding and referencing data for the comparative purpose in the NLO study. With dipole moment (μ) of 1.373 Debye and first hyperpolarizability (β_{tot}) of 0.373 x 10^{-30} e.s.u (Joshi, 2016; Maache *et al.*, 2016; Abbaz *et al.*, 2019), urea is a standard prototype for active NLO materials. From the results, the computed dipole moment and first hyperpolarizability of ACV-I are at least 8.940 and 137.828

times greater than urea. So, it is figured out that ACV-I molecular system can be considered as one of the efficacious candidates for NLO materials.

Table 4.5: Computed dipole moment (μ) and first hyperpolarizability (β_{tot}) of ACV-I molecular system using DFT/B3LYP/6-31G** and DFT/B3LYP/6-311G** methods.

Parameters	DFT/B3LYP/6-31G**	DFT/B3LYP/6-311G**
μ_x	4.732	4.626
μ_y	6.984	6.865
μ_z	9.066	9.062
μ [Debye]	12.384	12.274
β_{xxx}	-1070.121	-1095.946
β_{xyy}	-420.977	-428.759
β_{xzz}	-96.487	-109.149
β_{yyy}	2649.474	2677.047
β_{xxy}	565.707	574.467
β_{yzz}	1395.703	1408.839
β_{zzz}	2318.833	2343.829
β_{xxz}	302.685	313.380
β_{yyz}	788.353	796.293
β_{tot} [a.u]	5950.453	6026.196
β_{tot} [e.s.u]	5.141×10^{-29}	5.206×10^{-29}

4.1.6 Fourier Transform Infrared (FT-IR) Spectroscopy

Fourier transform infrared (FT-IR) spectroscopy is one of the popular techniques highly employed by researchers in the molecular structure prediction of unknown material. It is able to provide significant information about the molecular structures, compositions, functional groups, intra, and inter molecular interactions (Rahmani *et al.*, 2018). The presence of different components in a molecular system affects the interaction between atoms. Therefore, the FT-IR method shows useful application in the differentiation between polymorphism compounds. Masuda *et al.* (2012) confirmed the existence of polymorphism in

ACV with tartaric acid since the authors get different FT-IR "biochemical fingerprint" spectrums for anhydrous ACV, tartaric acid, and ACV-tartaric acid compounds. Lutker *et al.* (2011) also discovered the discrepancies in FT-IR vibrational frequencies spectrums for five different polymorphic forms of ACV compounds. In this work, the computed FT-IR vibrational frequencies of the ACV-I molecular system are obtained using DFT/B3LYP/6-31G** and DFT/B3LYP/6-311G** level of theories. With a total atomic number of 87, ACV-I molecular system contains 255 fundamental vibrational modes that qualitatively mention the functional groups presented in the system. Figure 4.6 shows the experimental FT-IR "biochemical fingerprint" spectrum of the ACV-I molecular system obtained via FT-IR potassium bromine (KBr) diffuse reflectance method with ranges of 400 cm^{-1} to 4000 cm^{-1}. Table 4.6 tabulates some of the important computational and experimental vibrational frequencies of the ACV-I molecular system. From the table, it is noted that all the computed results show higher vibrational frequencies (unscaled) than experimental data. These phenomena occurred because of the ignorance of anharmonicity under gases phase condition during FT-IR computational calculation (Ali *et al.*, 2017; Ahmad *et al.*, 2018). Besides, basis sets deficiencies and electron correlation effects also the reasons that lead to the overestimation of theoretical FT-IR vibrational frequencies in the ACV-I molecular system (Narayan, 2012; Ibeji *et al.*, 2016; Suna *et al.*, 2016). To overcome this problem, direct scaling technique is introduced to minimize the deviations between experimental and computational FT-IR results (Sainz-Díaz *et al.*, 2010; Arivazhagan and James, 2017; Ahmad *et al.*, 2018). According to Computational Chemistry Comparison and Benchmark DataBase (CCCBDB, 2020), the proper scale factor close to

unity for DFT/B3LYP/6-31G** and DFT/B3LYP/6-311G** methods are 0.961 and 0.967. It is evident that both of the scaled computational FT-IR vibrational frequency results (i.e. 6-31G** and 6-311G** basis sets) correspond well with experimental data. For example, the O-H stretching vibrational modes from water molecules can be observed in band regions 3471 cm^{-1} to 3516 cm^{-1} (scaled 6-31G**), 3473 cm^{-1} to 3513 cm^{-1} (scaled 6-311G**), and 3472 cm^{-1} to 3524 cm^{-1} (experimental). It is figured out that the N-H stretching vibrational assignments of primary and secondary amides in the ACV-I molecular system occurred at band regions 3461 cm^{-1} (scaled 6-31G**), 3470 cm^{-1} (scaled 6-311G**), and 3441 cm^{-1} (experimental). Besides, band regions 3135 cm^{-1} (scaled 6-31G** and scaled 6-311G**) and 3186 cm^{-1} (experimental) are assigned to aromatic C-H stretching vibrational modes while frequency bands 2864 cm^{-1} (scaled 6-31G**), 2870 cm^{-1} (scaled 6-311G**), and 2855 cm^{-1} (experimental) correspond to H-C-H (CH_2) stretching vibrations from the side chains of ACV molecules. Conversely, the bending vibrational modes of aromatic C-H are observed in regions 1384 cm^{-1} (scaled 6-31G**), 1386 cm^{-1} (scaled 6-311G**), and 1388 cm^{-1} (experimental) whereas the C-H bending vibration assignments from the side chain of ACV molecules are located between regions 744 cm^{-1} to 859 cm^{-1} (scaled 6-31G**), 767 cm^{-1} to 851 cm^{-1} (scaled 6-311G**), and 750 cm^{-1} to 868 cm^{-1} (experimental). Moreover, a wide range of frequency bands corresponding to C-O stretching vibration from the side chains of ACV molecules can be obtained from 1010 cm^{-1} to 1209 cm^{-1} (scaled 6-31G**), 1011 cm^{-1} to 1212 cm^{-1} (scaled 6-311G**), and 1012 cm^{-1} to 1216 cm^{-1} (experimental). For the aromatic C=C bond in the guanine rings of ACV molecules, the stretching vibrational modes are found between ranges 1471 cm^{-1} to 1539 cm^{-1}

(scaled 6-31G**), 1469 cm^{-1} to 1540 cm^{-1} (scaled 6-311G**), and 1483 cm^{-1} to 1542 cm^{-1} (experimental). Furthermore, as can be obtained in Table 4.6, the aromatic C-N stretching vibrational assignments are found in the regions between 1302 cm^{-1} to 1346 cm^{-1} (scaled 6-31G**), 1307 cm^{-1} to 1346 cm^{-1} (scaled 6-311G**), and 1309 cm^{-1} to 1347 cm^{-1} (experimental). Noticed that there are no suspicious findings in the FT-IR results of ACV-I molecular system. All the computational and experimental FT-IR characteristic vibrational spectrums show satisfactory agreement with literature data (*Infrared Spectroscopy Table*, 2001; Bakkiyaraj, 2017; Susithra *et al.*, 2018; Demircioğlu *et al.*, 2019; Priya *et al.*, 2019; Vidhya *et al.*, 2019; LibreTexts, 2020) and matched with the geometry structure of ACV-I molecular system.

Table 4.6: Experimental and computational (unscaled and scaled) FT-IR vibrational frequencies of ACV-I molecular system.

Type of Vibration	DFT/B3LYP/6-31G**		DFT/B3LYP/6-311G**		Experiment
	Unscaled [cm^{-1}]	Scaled [cm^{-1}]	Unscaled [cm^{-1}]	Scaled [cm^{-1}]	[cm^{-1}]
O-H stretching vibration	3658	3516	3633	3513	3524
O-H stretching vibration	3612	3471	3592	3473	3472
N-H stretching vibration	3601	3461	3588	3470	3441
C-H stretching vibration	3262	3135	3242	3135	3186
C-H stretching vibration	2980	2864	2968	2870	2855
C=O stretching vibration	1788	1718	1768	1710	1718
C=C stretching vibration	1602	1539	1593	1540	1542
C=C stretching vibration	1531	1471	1519	1469	1483
C-H bending vibration	1440	1384	1433	1386	1388
C-N stretching vibration	1400	1346	1392	1346	1347
C-N stretching vibration	1355	1302	1351	1307	1309
C-O stretching vibration	1258	1209	1253	1212	1216
C-O stretching vibration	1154	1109	1139	1101	1106
C-O stretching vibration	1129	1085	1121	1084	1084
C-O stretching vibration	1077	1035	1074	1039	1032
C-O stretching vibration	1051	1010	1046	1011	1012
C-H bending vibration	894	859	880	851	868
C-H bending vibration	817	785	798	771	780
C-H bending vibration	774	744	794	767	750

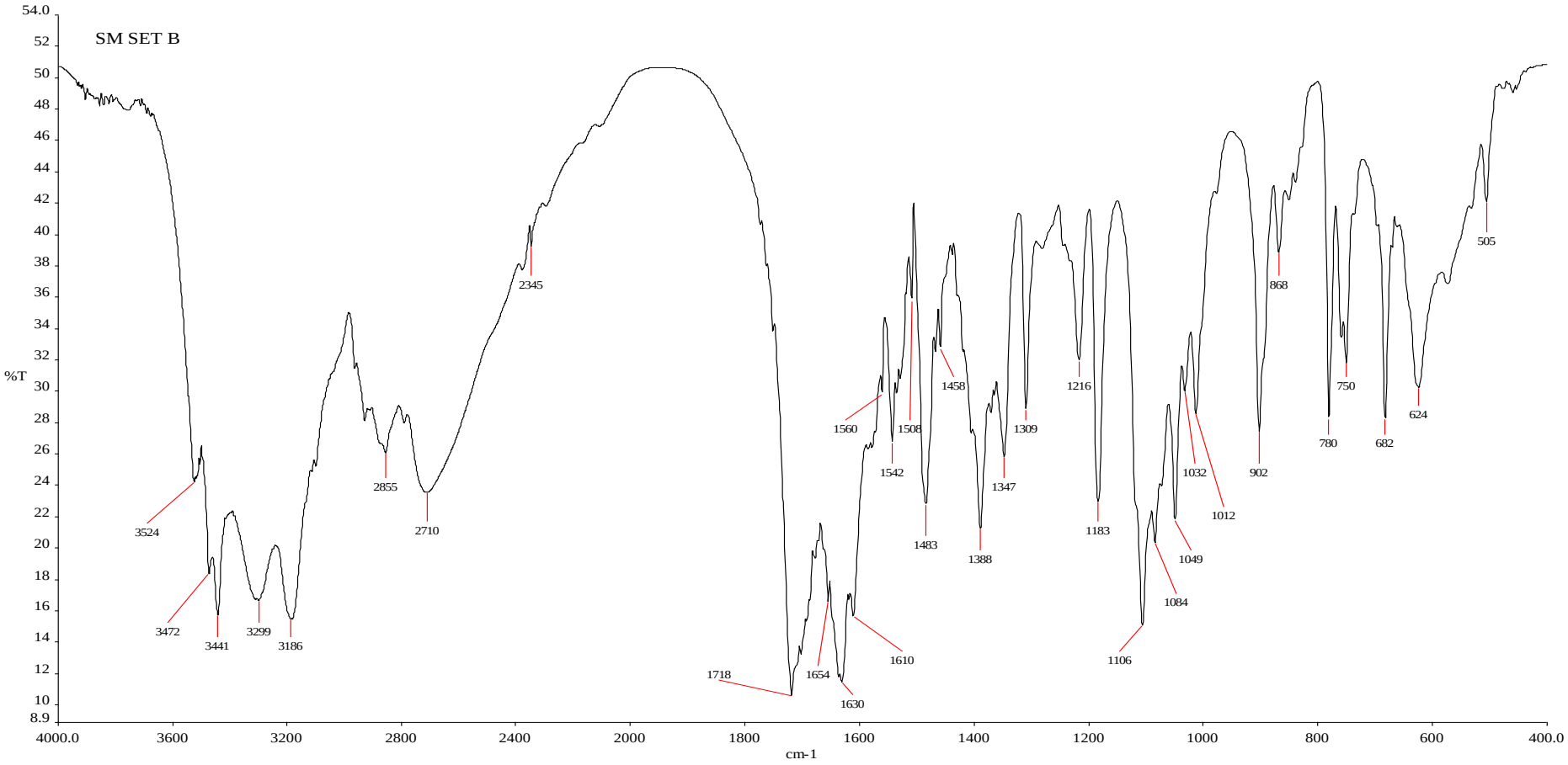

Figure 4.6: Experimental FT-IR vibrational spectrum of ACV-I molecular system.

4.1.7 Rotational Barrier Analysis

The conformation isomerism phenomena in the acyclovir molecule is not a recent new discovery. For example, Alvarez-Ros and Palafox (2014) discovered a total number of 78 possible stable conformers for ACV tautomer molecule (N1) through Potential Energy Surface (PES) scan in the dihedral angles of the side chain. Researchers figured out that at a given temperature, a molecule may have different conformations rather than in its minimum energy conformation due to thermal fluctuations (Abulyaissova, 2019). Therefore, it is crucial to understand the conformation preference in ACV Molecule A, B, and C. Since it influences the physical and dynamic properties of ACV molecules (Pereira *et al.*, 2014; Abulyaissova, 2019). According to Umar and Tijani (2015), it is a reliable way to study and predict the conformational preference and rotational barrier energy of a molecule using computational approach because the experimental conformational preference study is solvent dependent and restricted when deals with the conformers that have tiny change in energy. In this present work, the rotational barrier studies of ACV Molecule A, B, and C are calculated using the PES scanning technique at DFT/B3LYP/6-31G** and DFT/B3LYP/6-311G** level of theories. The PES scan is performed by rotating the dihedral angles of N_5-C_6-O_2-C_7 (Molecule A), N_{10}-C_{14}-O_5-C_{15} (Molecule B), and N_{15}-C_{22}-O_8-C_{23} (Molecule C) in interval step of 10° from 0° to 360° (36 steps of rotations). After one complete rotation cycle, all the computed relative energies, optimized total energies, and bond distances change correspondence with angles of rotation are obtained. Figure 4.7 (a), (b), and (c) show the PES diagrams of ACV Molecule A, B, and C. Noticed that both of DFT/B3LYP/6-31G** and DFT/B3LYP/6-

311G** methods show good agreement with each other. From the PES curves plotted in Figure 4.7 (a), ACV Molecule A shows two stable conformers (i.e. conformer IA and conformer IIA) at rotational angles of 90° and 270° (local minimum points). Conformer-IA has relative energies of 0.035 eV (6-31G**)/ 0.040 eV (6-311G**), C_6-O_2 bond distances of 1.413 Å (6-31G**)/1.412 Å (6-311G**), and optimized total energies of -22066.289 eV (6-31G**)/-22071.771 eV (6-311G**), while conformer-IIA shows relative energies of 0.020 eV (6-31G**)/0.026 eV (6-311G**), C_6-O_2 bond distances of 1.415 Å (6-31G** and 6-311G**), and optimized total energies of -22066.303 eV (6-31G**)/ -22071.785 eV (6-311G**). Besides, as can be obtained in Figure 4.7 (a), the most unstable conformer of ACV Molecule A (i.e. conformer-IIIA) is located at rotational angle of 170° (global maximum point) with relative energies of 0.443 eV (6-31G**)/0.437 eV (6-311G**), C_6-O_2 bond distances of 1.467 Å (6-31G** and 6-311G**), and optimized total energies of -22065.880 eV (6-31G**)/ -22071.375 eV (6-311G**). Furthermore, the PES curves plotted in Figure 4.7 (b) clearly noted that ACV Molecule B has two stable conformers (i.e. conformer-IB and conformer-IIB) at rotational angles of 110° and 180° (local minimum points). Noticed that conformer-IB has relative energies of 0.123 eV (6-31G**)/0.115 eV (6-311G**), C_{14}-O_5 bond distances of 1.404 Å (6-31G** and 6-311G**), and optimized total energies of -22066.214 eV (6-31G**)/ -22071.686 eV (6-311G**), whereas conformer-IIB shows relative energies of 0.075 eV (6-31G**)/0.073 eV (6-311G**), C_{14}-O_5 bond distances of 1.406 Å (6-31G**)/1.405 Å (6-311G**), and optimized total energies of -22066.261 eV (6-31G**)/-22071.727 eV (6-311G**). From the PES diagram, the most unstable conformer of ACV Molecule B (i.e. conformer-IIIB) is found at rotational angle

of 270° (global maximum point) with relative energies of 0.339 eV (6-31G**)/ 0.331 eV (6-311G**), C_{14}-O_5 bond distances of 1.440 Å (6-31G** and 6-311G**), and optimized total energies of -22065.997 eV (6-31G**)/-22071.469 eV (6-311G**). Moreover, based on the PES curves recorded in Figure 4.7 (c), ACV Molecule C poses two stable conformers (i.e. conformer-IC and conformer-IIC) at rotational angles of 110° and 200° (local minimum points). The computational results reveal that conformer-IC has relative energies of 0.125 eV (6-31G**)/0.113 eV (6-311G**), C_{22}-O_8 bond distances of 1.407 Å (6-31G**)/1.406 Å (6-311G**), and optimized total energies of -22066.141 eV (6-31G**)/-22071.624 eV (6-311G**). For conformer-IIC, it shows relative energies of 0.083 eV (6-31G**)/0.084 eV (6-311G**), C_{22}-O_8 bond distances of 1.408 Å (6-31G** and 6-311G**), and optimized total energies of -22065.863 eV (6-31G**)/-22071.653 eV (6-311G**). In additions, it is figured out that ACV Molecule C reaches its maximum unstable conformer state (i.e. conformer-IIIC) at rotational angle of 280 ° (global maximum point) with relative energies of 0.404 eV (6-31G**)/ 0.415 eV (6-311G**), C_{22}-O_8 bond distances of 1.451 Å (6-31G**)/1.453 Å (6-311G**), and optimized total energies of -22065.863 eV (6-31G**)/-22071.332 eV (6-311G**). As compared among the rotational barrier studies in ACV Molecule A, B, and C, three of them get different PES profiles. These are because the stability of conformational isomers strongly affected by the steric effects of aromatic and aliphatic substitutes, intermolecular hydrogen bonding, and degree of conjugation (Choudhary *et al.*, 2014). However, the computational data explicit that the increment in the bond distances of C_6-O_2 (Molecule A), C_{14}-O_5 (Molecule B), and C_{22}-O_8 (Molecule C) lead to higher relative energies in the conformers of

ACV Molecule A, B, and C. Noticed that the relative energy in rotational barrier study is an important parameter to determine the conformational preference in ACV Molecule A, B, and C (Guerdaoui *et al.*, 2014). Higher value of relative energy indicates harder rotational motion in the N-C-O-C dihedral angle.

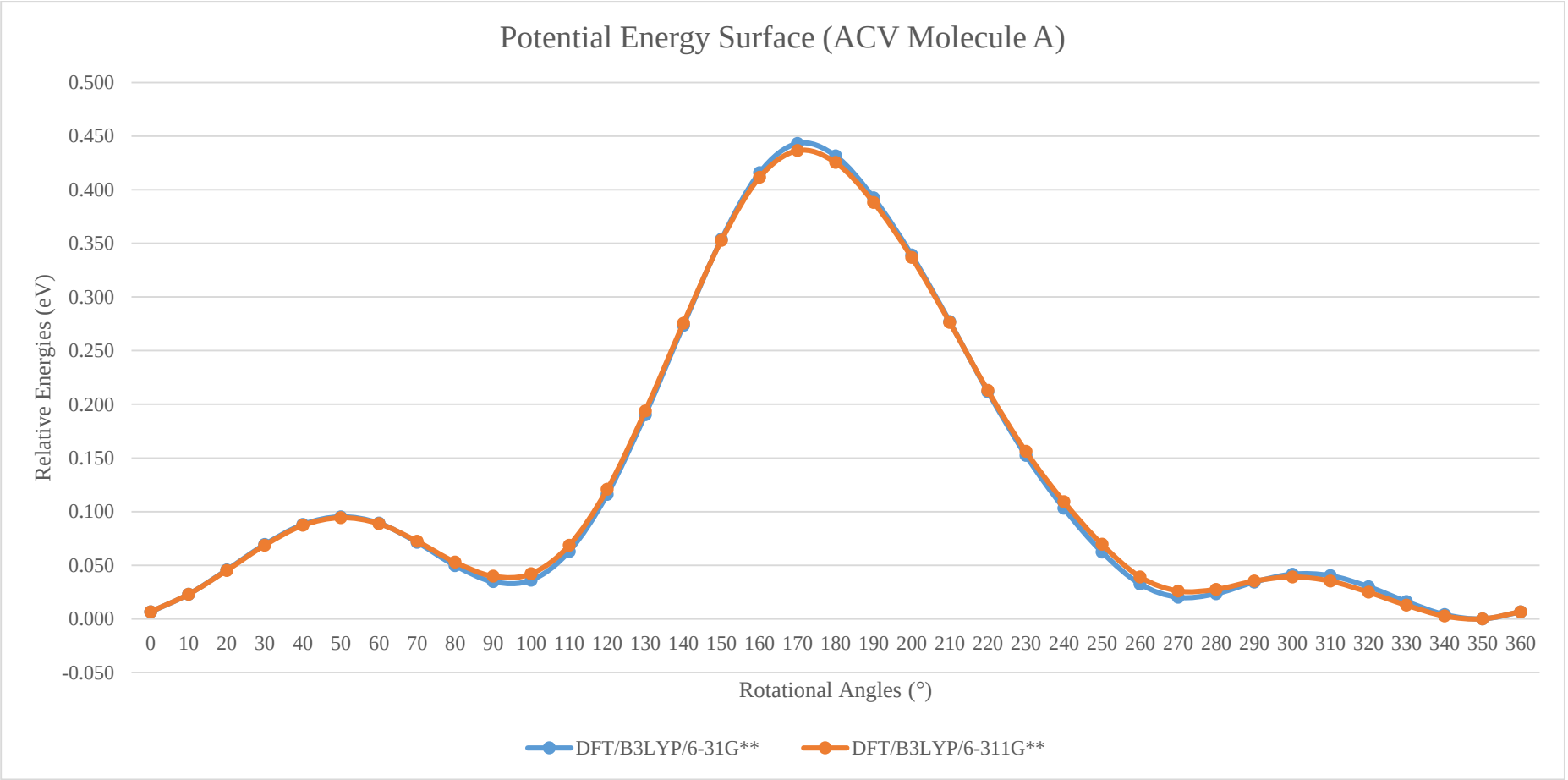

Figure 4.7 (a): Potential Energy Surface of ACV-I Molecule A using DFT/B3LYP/6-31G** and DFT/B3LYP/6-311G** methods.

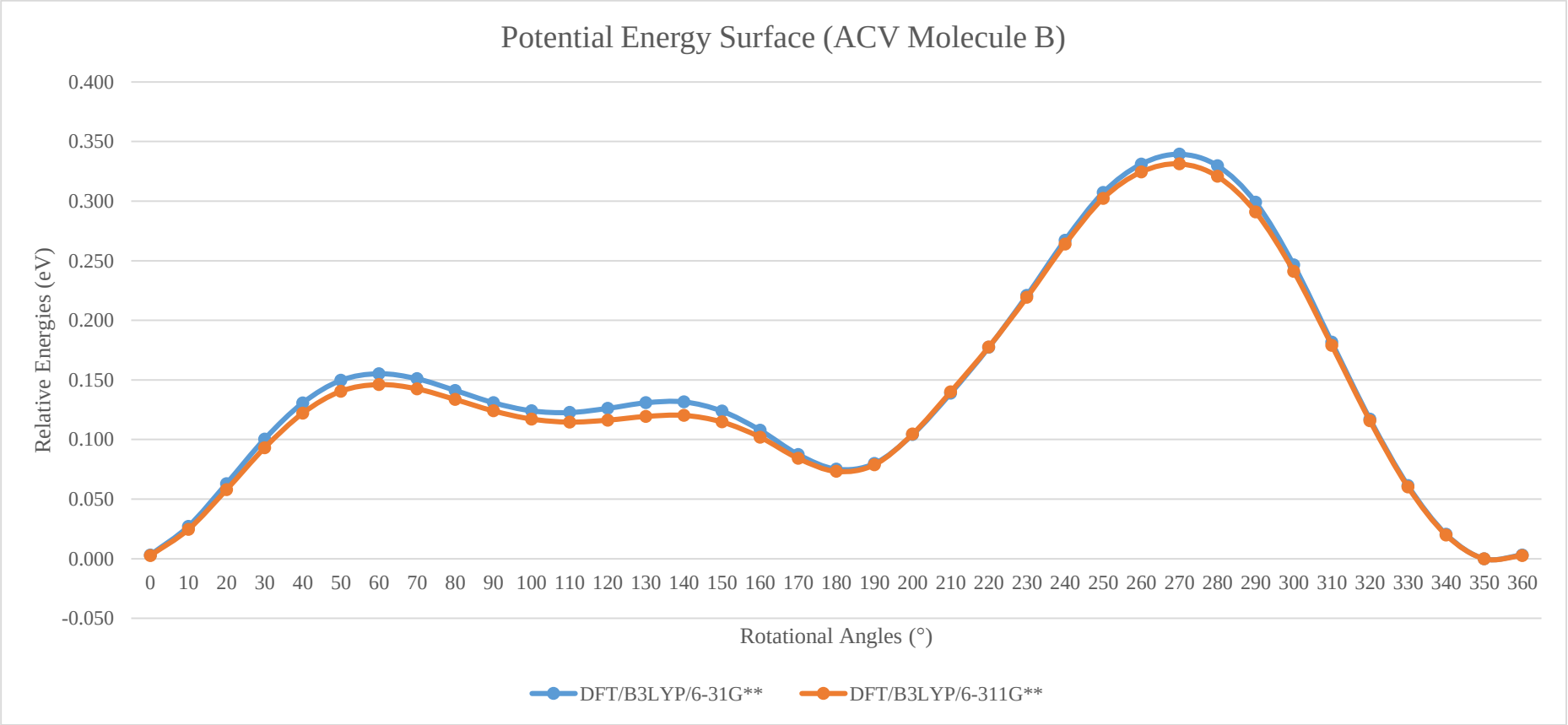

Figure 4.7 (b): Potential Energy Surface of ACV-I Molecule B using DFT/B3LYP/6-31G** and DFT/B3LYP/6-311G** methods.

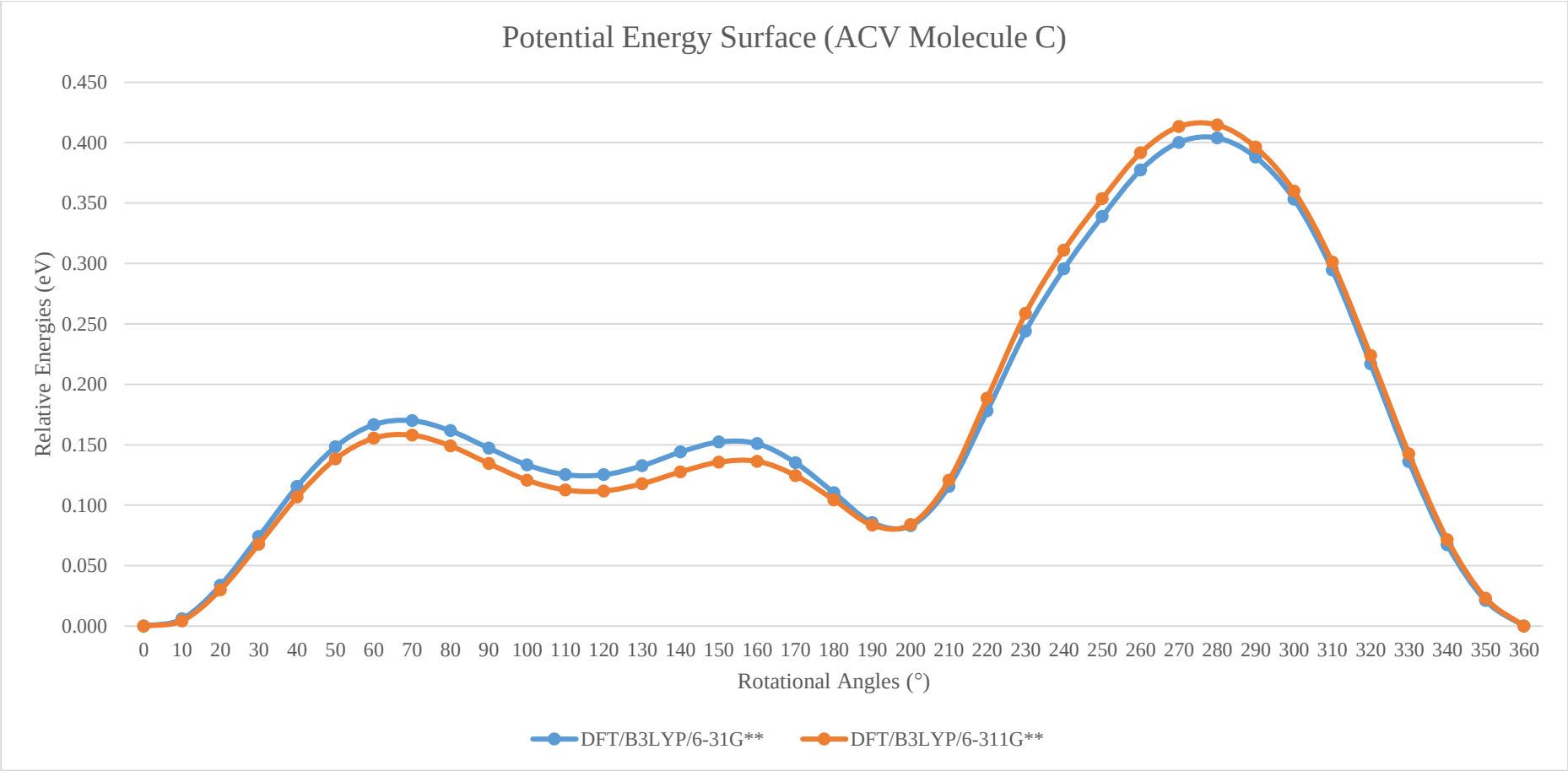

Figure 4.7 (c): Potential Energy Surface of ACV-I Molecule C using DFT/B3LYP/6-31G** and DFT/B3LYP/6-311G** methods.

Table 4.7 (a): Parts of the rotational barrier studies in ACV-I Molecule A using DFT/B3LYP/6-31G** and DFT/B3LYP/6-311G** methods.

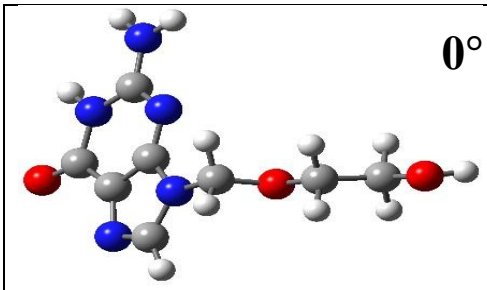	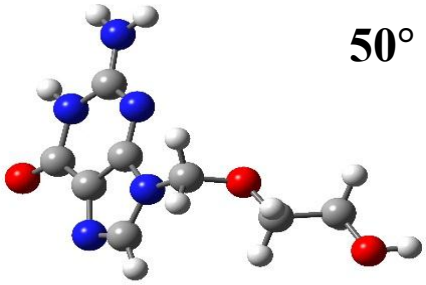
Relative Energy: 0.006 eV / 0.007 eV Optimized Total Energy: -22066.317 eV / -22071.804 eV C_6-O_2 Bond Distance: 1.411 Å / 1.411 Å	Relative Energy: 0.095 eV / 0.094 eV Optimized Total Energy: -22066.228 eV / -22071.717 eV C_6-O_2 Bond Distance: 1.419 Å / 1.419 Å
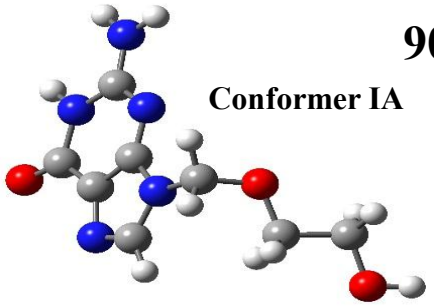	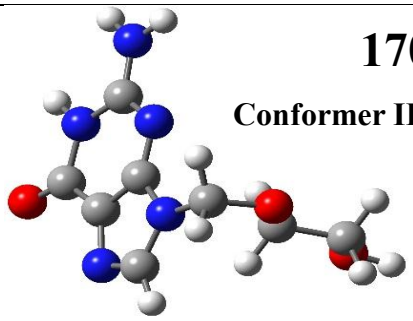
Relative Energy: 0.035 eV / 0.040 eV Optimized Total Energy: -22066.289 eV / -22071.771 eV C_6-O_2 Bond Distance: 1.413 Å / 1.412 Å	Relative Energy: 0.443 eV / 0.437 eV Optimized Total Energy: -22065.880 eV / -22071.375 eV C_6-O_2 Bond Distance: 1.467 Å / 1.467 Å
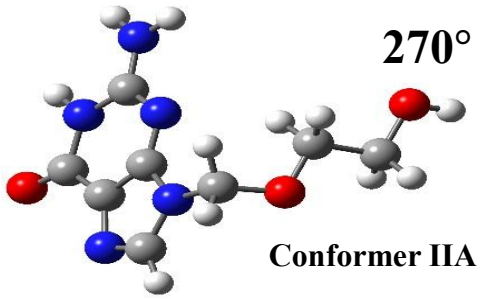	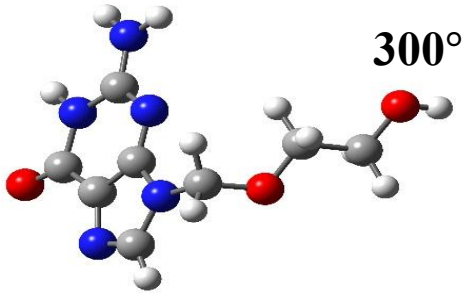
Relative Energy: 0.020 eV / 0.026 eV Optimized Total Energy: -22066.303 eV / -22071.785 eV C_6-O_2 Bond Distance: 1.415 Å / 1.415 Å	Relative Energy: 0.042 eV / 0.039 eV Optimized Total Energy: -22066.282 eV / -22071.772 eV C_6-O_2 Bond Distance: 1.417 Å / 1.416 Å

Table 4.7 (b): Parts of the rotational barrier studies in ACV-I Molecule B using DFT/B3LYP/6-31G** and DFT/B3LYP/6-311G** methods.

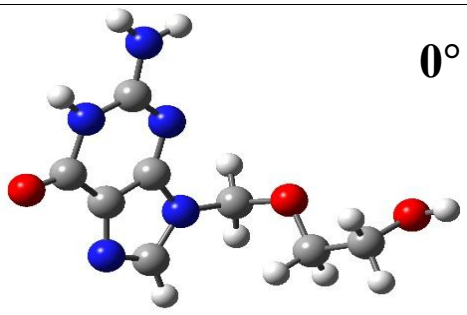	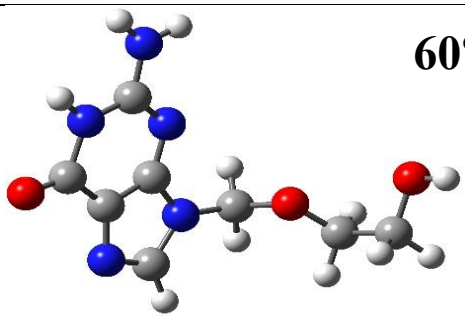
Relative Energy: 0.003 eV / 0.003 eV Optimized Total Energy: -22066.333 eV / -22071.798 eV C_{14}-O_5 Bond Distance: 1.400 Å / 1.399 Å	Relative Energy: 0.155 eV / 0.146 eV Optimized Total Energy: -22066.181 eV / -22071.654 eV C_{14}-O_5 Bond Distance: 1.409 Å / 1.409 Å
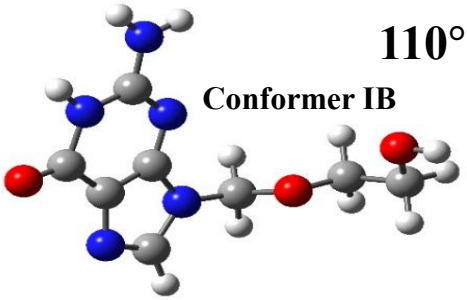	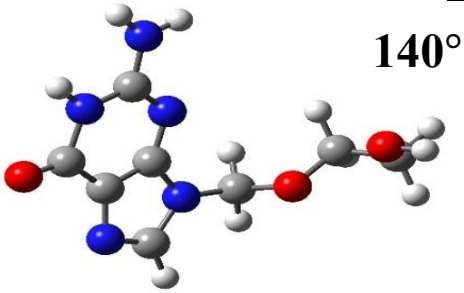
Relative Energy: 0.123 eV / 0.115 eV Optimized Total Energy: -22066.214 eV / -22071.686 eV C_{14}-O_5 Bond Distance: 1.404 Å / 1.404 Å	Relative Energy: 0.132 eV / 0.120 eV Optimized Total Energy: -22066.205 eV / -22071.680 eV C_{14}-O_5 Bond Distance: 1.407 Å / 1.406 Å
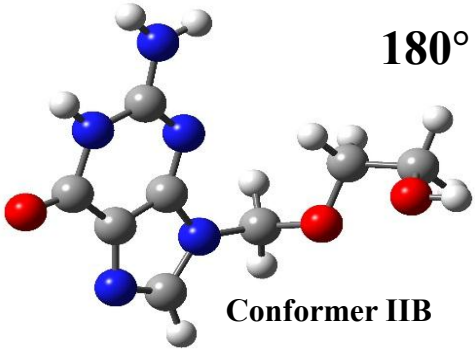	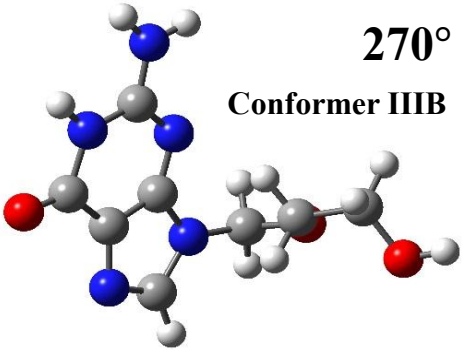
Relative Energy: 0.075 eV / 0.073eV Optimized Total Energy: -22066.261 eV / -22071.727 eV C_{14}-O_5 Bond Distance: 1.406 Å / 1.405 Å	Relative Energy: 0.339 eV / 0.331 eV Optimized Total Energy: -22065.997 eV / -22071.469 eV C_{14}-O_5 Bond Distance: 1.440 Å / 1.440 Å

Table 4.7 (c): Parts of the rotational barrier studies in ACV-I Molecule C using DFT/B3LYP/6-31G** and DFT/B3LYP/6-311G** methods.

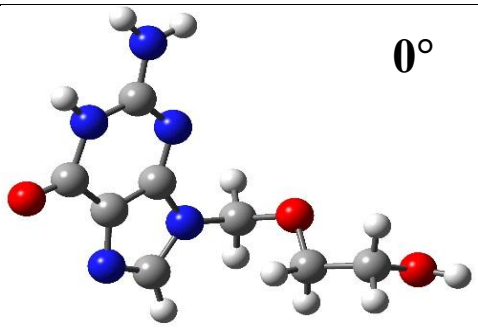	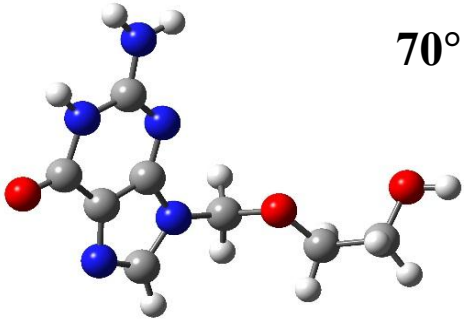
Relative Energy: 0.000 eV / 0.000 eV Optimized Total Energy: -22066.267 eV / -22071.737 eV C_{22}-O_8 Bond Distance: 1.403 Å / 1.402 Å	Relative Energy: 0.170 eV / 0.158 eV Optimized Total Energy: -22066.097 eV / -22071.579 eV C_{22}-O_8 Bond Distance: 1.413 Å / 1.413 Å
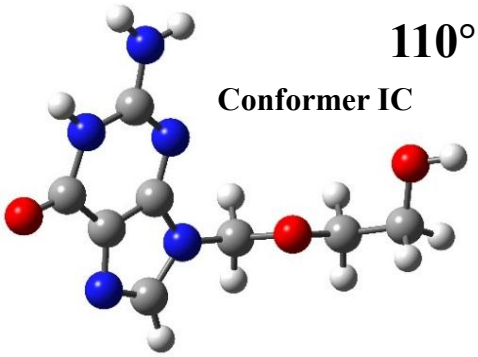	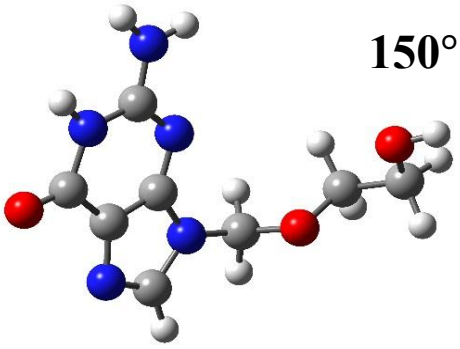
Relative Energy: 0.125 eV / 0.113 eV Optimized Total Energy: -22066.141 eV / -22071.624 eV C_{22}-O_8 Bond Distance: 1.407 Å / 1.406 Å	Relative Energy: 0.152 eV / 0.136 Optimized Total Energy: -22066.114 eV / -22071.601 eV C_{22}-O_8 Bond Distance: 1.411 Å / 1.411 Å
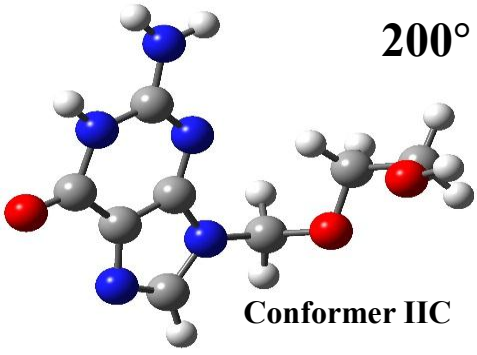	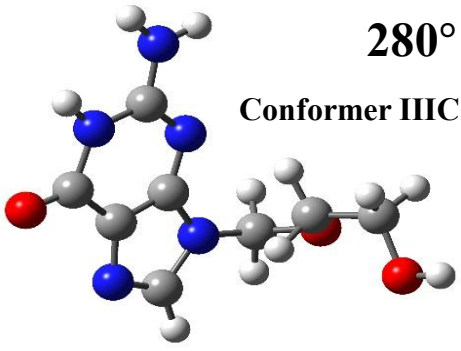
Relative Energy: 0.083 eV / 0.084 eV Optimized Total Energy: -22065.863 eV / -22071.653 eV C_{22}-O_8 Bond Distance: 1.408 Å / 1.408 Å	Relative Energy: 0.404 eV / 0.415 eV Optimized Total Energy: -22065.863 eV / -22071.322 eV C_{22}-O_8 Bond Distance: 1.451 Å / 1.453 Å

4.2: Acyclovir Hydrate (ACV-II) $3[C_8H_{11}N_5O_3]\cdot 2[H_2O]$

The crystallographic information file (CIF) for the ACV-II compound is obtained from the library database of Cambridge Crystallographic Data Centre (CCDC), with deposition number 1122548 and database identifier of CEHTAK10. Figure 4.8 (a) illustrates the complete unit cell of the ACV-II compound. According to Birnbaum *et al.* (1981) and Birnbaum *et al.* (1984), the ACV-II crystal fragment is reported to be crystallized in a monoclinic space group of $P2_{1/n}$ with unit cell lattice parameters of a = 25.459 Å, b = 11.282 Å, c = 10.768 Å, and β = 95.160°. Although ACV-II molecular system has an identical chemical formula of $3[C_8H_{11}N_5O_3]\cdot 2[H_2O]$ with the ACV-I compound, it shows distinctive molecular geometry structural from ACV-I molecular system. Figure 4.8 (b) represents the single molecular structural of ACV-II together with atomic labelling and numbering details. Noticed that three of the independent ACV molecules (Molecule A, B, and C) are situated in the centre and show stacking arrangements while the two water molecules (Water I and Water II) are located beside the ACV molecules. In this study, the perfect single ACV-II molecule is chosen as the main environment for DFT computational studies. The geometry and electronic properties of the ACV-II molecular system are discussed.

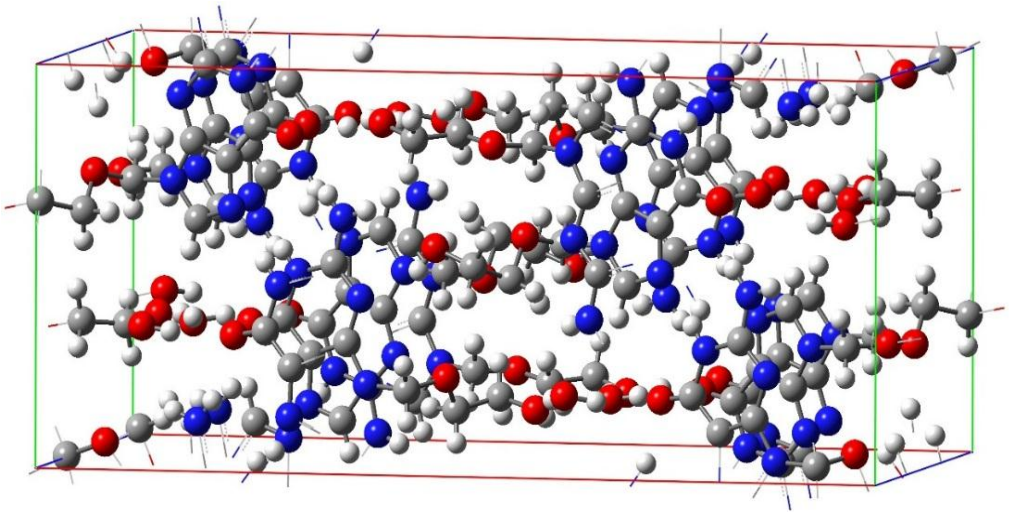

Figure 4.8 (a): The complete unit cell of ACV-II.

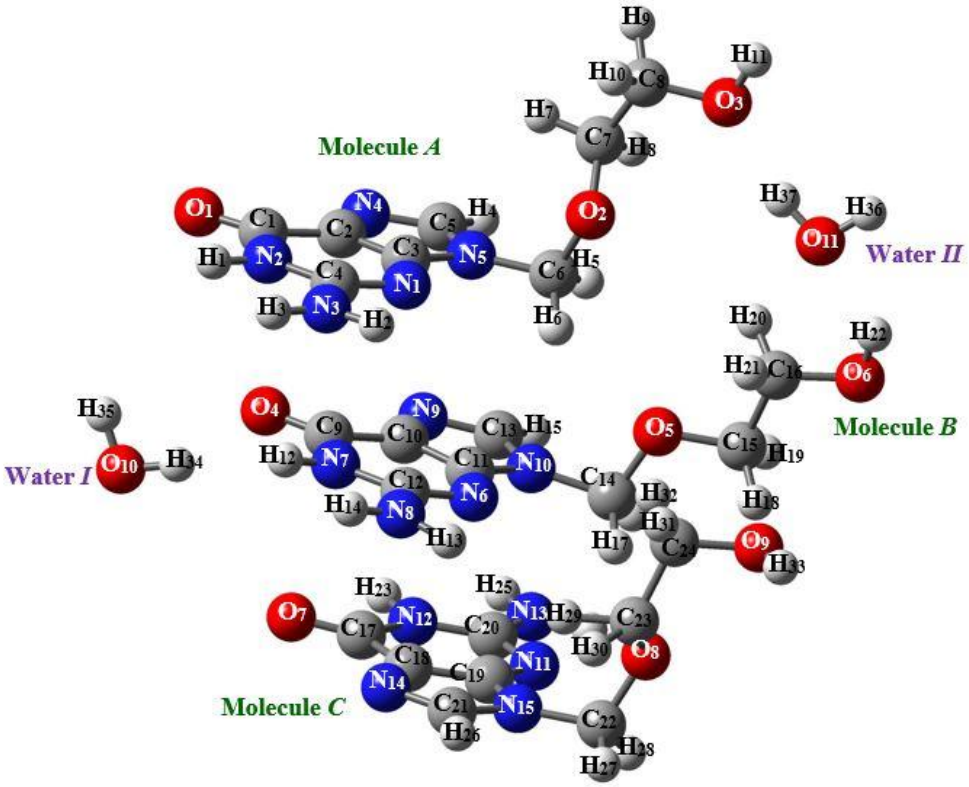

Figure 4.8 (b): Labelling and numbering details in ACV-II single molecular system.

4.2.1 Molecular Geometry Structural Analysis

For the sake of convenience, parts of the importance experimental geometry parameters of ACV Molecule A, B, and C are presented separately in Figure 4.9 (a), (b), and (c). From the diagrams, there are noticeable side chain orientation differences among Molecule A, B, and C. The side chain in Molecule B is observed to be fully extended while the side chains in Molecule A and Molecule C are found to be partially folded. Besides, the dihedral angles analysis in O_5-C_{15}-C_{16}-O_6 (-174.335 °), O_2-C_7-C_8-O_3 (73.507 °), and O_8-C_{23}-C_{24}-O_9 (-60.556 °) elucidate that Molecule B poses "staggered trans" side chain orientation, whereas Molecule A and Molecule C explicit "staggered gauche" side chain arrangements in ACV-II molecular system (LibreTexts, 2019; *Alkane Conformation*, 2021). The findings meet good agreement with outcome reported by Birnbaum *et al.* (1984). Accompany with the discrepancies in the side chain arrangements, there are observable geometrical parameter differences in the linking edges (i.e. N_5-C_6, N_{10}-C_{14}, and N_{15}-C_{12}) between the guanine rings and side chains of ACV Molecules. All of them (i.e. N_5-C_6, N_{10}-C_{14}, and N_{15}-C_{12}) pose single N-C bond characteristic. For Molecule A, it has N_5-C_6 bond distance of 1.469 Å and N_5-C_6-O_2 bond angle of 112.212°. For Molecule B, bond distance N_{10}-C_{14} and bond angle N_{10}-C_{14}-O_5 are found to be 1.444 Å and 109.257°. For Molecule C, it shows bond distance of 1.462 Å in N_{15}-C_{12} and bond angle of 111.520° in N_{15}-C_{22}-O_8. The diversity in the side chain orientations evidently indicates that ACV Molecule A, B, and C have independent geometry identities in ACV-II molecular system. Furthermore, there is no apparent deviation among the guanine moieties of ACV Molecules A, B, and C. For example, with bond

lengths of 1.239 Å, 1.241 Å, and 1.245 Å, ACV Molecules A, B, and C explicit double bond (C=O) characteristic in bond distances O_1-C_1, O_4-C_9, and O_7-C_{17} (Peica, 2006). As can be obtained in Figure 4.9 (a), (b), and (c), the aromatic C-C bonds (i.e. C_1-C_2, C_2-C_3, C_9-C_{10}, C_{10}-C_{11}, C_{17}-C_{18}, and C_{18}-C_{19}) and C-N bonds (i.e. N_2-C_4, C_4-N_3, N_5-C_3, N_7-C_{12}, C_{12}-N_8, N_{10}-C_{11}, N_{12}-C_{20}, C_{20}-N_{13}, and N_{15}-C_{19}) in the guanine moieties of ACV Molecule A, B, and C show bond distances ranging from 1.375 Å to 1.419 Å and 1.335 Å to 1.379 Å. These findings imply the presence of resonance effects in the guanine rings of ACV molecules since all of them have bond distances lie between single C-C, C-N bond lengths and double C=C, C=N bond lengths (Peica, 2006; Agrawal *et al.*, 2017; Bakkiyaraj, 2017). Moreover, as a six-member aromatic ring, it is figured out that the pyrimidine rings of ACV Molecule A, B, and C show slightly distortions in bond angles C_1-C_2-C_3 (119.095°), N_2-C_4-N_1 (123.587°), C_9-C_{10}-C_{11} (118.364°), N_7-C_{12}-N_6 (123.401°), C_{17}-C_{18}-C_{19} (118.588°), and N_{12}-C_{20}-N_{11} (123.202°). All of them do not explicit hexagonal symmetry characteristic of 120.000° due to the uneven attraction interactions between aromatic carbon atoms and nitrogen atoms (Agrawal *et al.*, 2017). In additions, it is noted that three of the ACV Molecule A, B, and C with dihedral angles of 179.217° (N_1-C_3-N_5-C_5), 179.340 ° (N_2-C_1-C_2-N_4), -178.246 ° (N_6-C_{11}-N_{10}-C_{13}), 179.779 ° (N_7-C_9-C_{10}-N_9), 177.997 ° (N_{12}-C_{17}-C_{18}-N_{14}), and 178.984 ° (N_{11}-C_{19}-N_{15}-C_{21}) show coplanar arrangements between the pyrimidine rings and imidazole rings of guanine moieties.

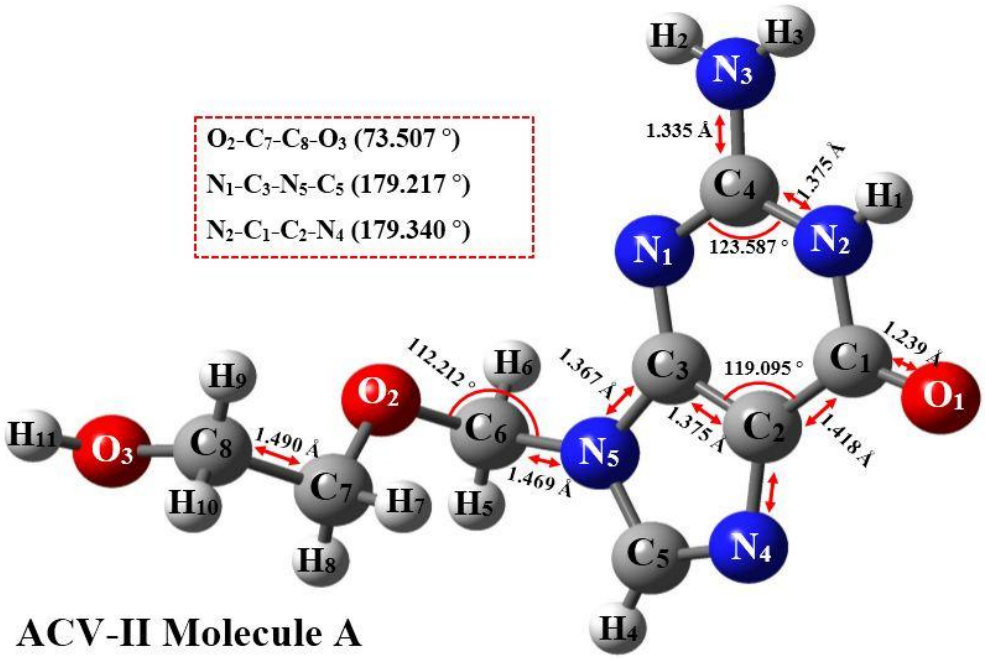

Figure 4.9 (a): Parts of the geometry parameters (i.e. bond distances, bond angles, and dihedral angles) of ACV-II Molecule A.

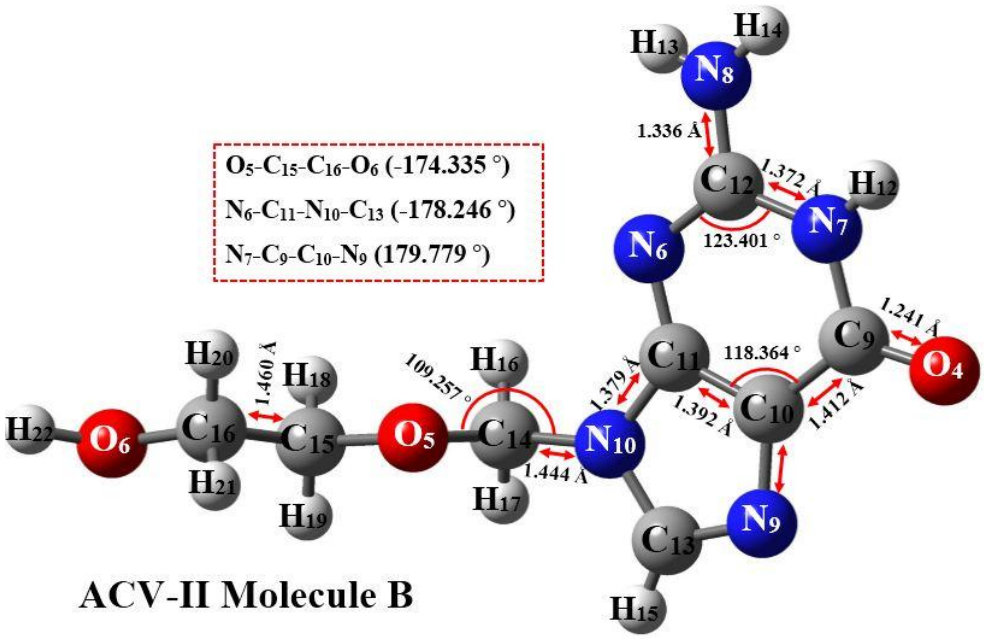

Figure 4.9 (b): Parts of the geometry parameters (i.e. bond distances, bond angles, and dihedral angles) of ACV-II Molecule B.

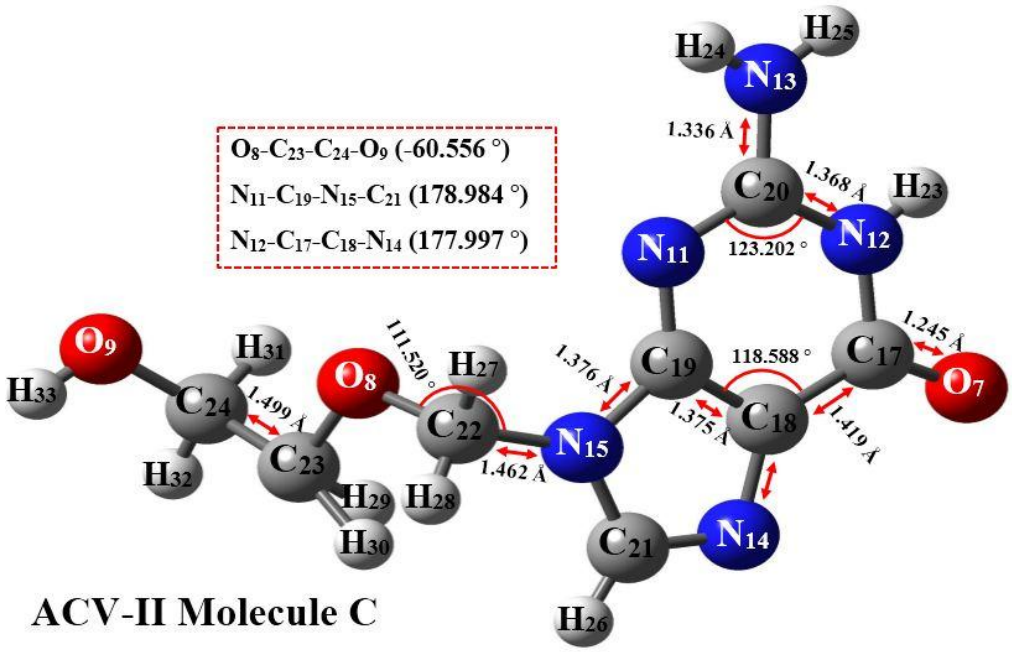

Figure 4.9 (c): Parts of the geometry parameters (i.e. bond distances, bond angles, and dihedral angles) of ACV-II Molecule C.

Table 4.8 (a), (b), and (c) tabulate the experimental and computational geometry parameters (i.e. bond distances, bond angles, and dihedral angles) of the ACV-II single molecular system. Based on the tables, it is observable that both of the optimized geometry structures of the ACV-II molecular system computed using DFT/B3LYP/6-31G** and DFT/B3LYP/6-311G** methods show slightly different with experimental data. In Table 4.8 (a), noticed that the largest percentage differences between experimental and optimized geometry structures of ACV Molecule A fall on bond distance C_1-N_1, bond angle O_1-C_1-C_2, and dihedral angle N_1-C_3-N_5-C_6. The DFT/B3LYP/6-31G** technique shows percentage differences of 3.573%, 2.003%, and 0.107% in C_1-N_1, O_1-C_1-C_2, and N_1-C_3-N_5-C_6, while the DFT/B3LYP/6-311G** method gets percentage values of 3.643%, 1.949%, and 0.053%. Besides, the data in Table 4.8 (b) clearly noted that ACV Molecule B has the highest optimized geometry deviations in bond

distance C_{15}-C_{16}, bond angle O_5-C_{15}-C_{16}, and dihedral angle N_6-C_{11}-N_{10}-C_{14} if compared with experimental data. For DFT/B3LYP/6-31G** method, the percentage differences in C_{15}-C_{16}, O_5-C_{15}-C_{16}, and N_6-C_{11}-N_{10}-C_{14} are found to be 3.410%, 5.699%, and 1.656%, respectively, whereas for DFT/B3LYP/6-311G** method are 3.202%, 5.495%, and 1.715%, respectively. Furthermore, with values of 3.843%, 5.808%, 0.122% (DFT/B3LYP/6-31G** method) and 3.923%, 5.899%, 0.097% (DFT/B3LYP/6-311G** method), ACV Molecule C shows the largest bond distance, bond angle, and dihedral angle percentage differences in C_{17}-N_{12}, O_8-C_{23}-C_{24}, and N_{11}-C_{19}-N_{15}-C_{22} as recorded in Table 4.8 (c). The disparities are resulted due to experimental data is obtained under the solid and bulk case, while computational results are calculated under the gases phase (Sundaraganesan *et al.*, 2007; Kalaiarasi and Manivarman, 2017). Overall, with the highest percentage differences of 5.808% and 5.899%, it can be said that both of the optimized ACV-II molecular geometry structures obtained from DFT/B3LYP/6-31G** and DFT/B3LYP/6-311G** level of theories show satisfactory agreement with experimental data.

Table 4.8 (a): Experimental and optimized geometry parameters of ACV Molecule A in ACV-II molecular system.

Molecule A	ACV-II		
	B3LYP/6-31G**	B3LYP/6-311G**	Experiment
Bond Distance (Å)			
O_1-C_1	1.216	1.209	1.239
C_1-N_2	1.441	1.442	1.391
N_2-C_4	1.372	1.370	1.375
N_1-C_3	1.361	1.359	1.353
C_3-C_2	1.393	1.390	1.375
C_4-N_3	1.369	1.369	1.335
C_2-N_4	1.380	1.378	1.387
C_3-N_5	1.378	1.377	1.367
N_5-C_6	1.454	1.454	1.469
C_6-O_2	1.417	1.417	1.391
O_2-C_7	1.420	1.421	1.428
C_7-C_8	1.508	1.505	1.490
C_8-O_3	1.426	1.428	1.419
Bond Angle (°)			
O_1-C_1-N_2	119.529	119.664	120.015
O_1-C_1-C_2	130.964	130.895	128.392
N_3-C_4-N_1	118.963	119.087	119.355
C_4-N_1-C_3	112.693	112.943	112.227
C_3-C_2-N_4	111.183	111.106	110.401
C_3-N_5-C_5	105.465	105.482	105.944
C_3-N_5-C_6	127.782	127.641	126.275
N_5-C_6-O_2	112.551	112.472	112.212
O_2-C_7-C_8	110.854	110.973	109.855
C_7-C_8-O_3	111.103	111.336	109.383
Dihedral Angle (°)			
O_1-C_1-C_2-C_3	179.881	179.881	179.881
O_1-C_1-N_2-C_4	179.387	179.388	179.403
N_3-C_4-N_1-C_3	179.585	179.586	179.586
N_1-C_3-N_5-C_6	-1.868	-1.871	-1.870
N_5-C_6-O_2-C_7	-66.292	-66.292	-66.292
O_2-C_7-C_8-O_3	73.507	73.507	73.507

Table 4.8 (b): Experimental and optimized geometry parameters of ACV Molecule B in ACV-II molecular system.

Molecule B	ACV-II		
	B3LYP/6-31G**	B3LYP/6-311G**	Experiment
Bond Distance (Å)			
O_4-C_9	1.222	1.216	1.241
C_9-N_7	1.419	1.419	1.383
N_7-C_{12}	1.375	1.373	1.372
N_6-C_{11}	1.357	1.355	1.339
C_{11}-C_{10}	1.391	1.389	1.392
C_{12}-N_8	1.361	1.361	1.336
C_{10}-N_9	1.381	1.379	1.385
C_{11}-N_{10}	1.379	1.378	1.379
N_{10}-C_{14}	1.443	1.443	1.444
C_{14}-O_5	1.407	1.406	1.395
O_5-C_{15}	1.429	1.430	1.424
C_{15}-C_{16}	1.510	1.507	1.460
C_{16}-O_6	1.410	1.411	1.391
Bond Angle (°)			
O_4-C_9-N_7	122.236	122.122	120.029
O_4-C_9-C_{10}	127.197	127.462	127.732
N_8-C_{12}-N_6	119.385	119.507	120.656
C_{12}-N_6-C_{11}	113.022	113.199	112.324
C_{11}-C_{10}-N_9	111.545	111.434	110.735
C_{11}-N_{10}-C_{13}	105.762	105.765	106.721
C_{11}-N_{10}-C_{14}	129.808	129.812	126.865
N_{10}-C_{14}-O_5	107.039	107.150	109.257
O_5-C_{15}-C_{16}	104.246	104.471	110.546
C_{15}-C_{16}-O_6	110.454	110.428	109.890
Dihedral Angle (°)			
O_4-C_9-C_{10}-C_{11}	-178.061	-178.061	-178.061
O_4-C_9-N_7-C_{12}	-179.024	-179.018	-179.028
N_8-C_{12}-N_6-C_{11}	-178.372	-178.372	-178.372
N_6-C_{11}-N_{10}-C_{14}	3.438	3.440	3.382
N_{10}-C_{14}-O_5-C_{15}	-173.340	-173.340	-173.340
O_5-C_{15}-C_{16}-O_6	-174.335	-174.335	-174.335

Table 4.8 (c): Experimental and optimized geometry parameters of ACV Molecule C in ACV-II molecular system.

Molecule C	ACV-II		
	B3LYP/6-31G**	B3LYP/6-311G**	Experiment
Bond Distance (Å)			
O_7-C_{17}	1.217	1.210	1.245
C_{17}-N_{12}	1.442	1.443	1.388
N_{12}-C_{20}	1.366	1.364	1.368
N_{11}-C_{19}	1.356	1.353	1.348
C_{19}-C_{18}	1.394	1.392	1.375
C_{20}-N_{13}	1.362	1.362	1.336
C_{18}-N_{14}	1.383	1.382	1.385
C_{19}-N_{15}	1.378	1.377	1.376
N_{15}-C_{22}	1.459	1.459	1.462
C_{22}-O_8	1.400	1.399	1.408
O_8-C_{23}	1.429	1.429	1.435
C_{23}-C_{24}	1.502	1.500	1.499
C_{24}-O_9	1.426	1.427	1.421
Bond Angle (°)			
O_7-C_{17}-N_{12}	117.974	118.229	120.096
O_7-C_{17}-C_{18}	132.705	132.538	128.234
N_{13}-C_{20}-N_{11}	119.011	119.080	119.668
C_{20}-N_{11}-C_{19}	112.509	112.784	112.289
C_{19}-C_{18}-N_{14}	110.772	110.683	110.899
C_{19}-N_{15}-C_{21}	105.561	105.555	106.171
C_{19}-N_{15}-C_{22}	125.243	125.330	125.622
N_{15}-C_{22}-O_8	113.244	113.447	111.520
O_8-C_{23}-C_{24}	115.792	115.892	109.436
C_{23}-C_{24}-O_9	111.692	111.733	113.215
Dihedral Angle (°)			
O_7-C_{17}-C_{18}-C_{19}	-178.360	-178.360	-178.360
O_7-C_{17}-N_{12}-C_{20}	178.523	178.524	178.489
N_{13}-C_{20}-N_{11}-C_{19}	177.514	177.514	177.514
N_{11}-C_{19}-N_{15}-C_{22}	4.108	4.107	4.103
N_{15}-C_{22}-O_8-C_{23}	76.852	76.852	76.852
O_8-C_{23}-C_{24}-O_9	-60.555	-60.556	-60.556

4.2.2 Total Energies and Frontier Molecular Orbital (FMO) Energies

Table 4.9 tabulates the computed total energies, frontier molecular orbital (FMO) energies, and global descriptors (i.e. IE, EA, η, μ, S, χ, and ω) of the ACV-II molecular system. As can be observed in Table 4.9, the total energy of the ACV-II molecular system computed via DFT/B3LYP/6-31G** method is -70355.920 eV, whereas for DFT/B3LYP/6-311G** technique is -70373.840 eV. The findings indicate that ACV-II molecular system is slightly less stable than the ACV-I molecule (Chavda *et al.*, 2016; Ali *et al.*, 2017; Chaturvedi *et al.*, 2018). Besides, Table 4.9 clearly noted that the HOMO energy and LUMO energy obtained using DFT/B3LYP/6-31G** method are -5.248 eV and -0.236 eV, while for DFT/B3LYP/6-311G** method are -5.478 eV and -0.566 eV. Based on the computed HOMO and LUMO energies, the global descriptors of the ACV-II molecular system are obtained through the formulas stated in Koopmans theorem. For DFT/B3LYP/6-31G** method, the calculated ionization energy (IE), electron affinity (EA), hardness (η), chemical potential (μ), softness (S), electronegativity (χ), and electrophilicity index (ω) of ACV-II molecule are found to be 5.248 eV, 0.236 eV, 2.506, -2.742, 0.200, 2.742, and 1.504, respectively, while for DFT/B3LYP/6-311G** method are 5.478 eV, 0.566 eV, 2.456, -3.022, 0.204, 3.022, and 1.863, respectively. Furthermore, with ranges of 4.912 eV to 5.012 eV, it is figured out that the computed HOMO-LUMO energy gaps of the ACV-II molecular system show closer results with the ACV-I molecular system. Figure 4.10 (a) and (b) show the HOMO and LUMO 3D surface mapped plots of ACV-II molecular system using DFT/B3LYP/6-31G** and DFT/B3LYP/6-311G** level of calculations. Noticed that both of the

computational methods (i.e. 6-31G** and 6-311G** basis sets) generated approximately identical mapping results. The electron density distributions for HOMO are mainly focused on the guanine moieties of ACV Molecule A and B, while the electron densities distributions for LUMO are mainly localised on the guanine moieties of ACV Molecule B and C. From the figures, it is observed that neither the side chains nor the water molecules participate in the HOMO and LUMO surface mapped plots. These imply that the transitions of electrons from HOMO→ LUMO in the ACV-II molecular system are mainly taking place from the guanine rings of ACV Molecule A and B to guanine rings of ACV Molecule B and C (Targema *et al.*, 2013; Sachdeva *et al.*, 2018). Furthermore, the molecular coefficients analysis clearly reveals that both of the HOMO and LUMO orbitals are mainly composed from p_y type, thus proposed $\pi \rightarrow \pi^*$ type of electronic transition in ACV-II molecular system.

Table 4.9: Total energies, HOMO energies, LUMO energies, and HOMO-LUMO energy gaps of ACV-II molecular system.

	ACV-II	
	DFT/B3LYP/6-31G**	DFT/B3LYP/6-311G**
Total Energy (eV)	-70355.920	-70373.840
HOMO (eV)	-5.248	-5.478
LUMO (eV)	-0.236	-0.566
HOMO-LUMO Energy Gap (eV)	5.012	4.912
Ionization Energy (IE) [eV]	5.248	5.478
Electron Affinity (EA) [eV]	0.236	0.566
Hardness (η)	2.506	2.456
Chemical Potential (μ)	-2.742	-3.022
Softness (S)	0.200	0.204
Electronegativity (χ)	2.742	3.022
Electrophilicity index (ω)	1.504	1.863

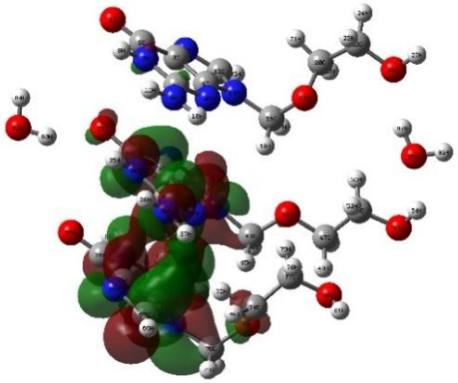

LUMO (−0.236 eV)

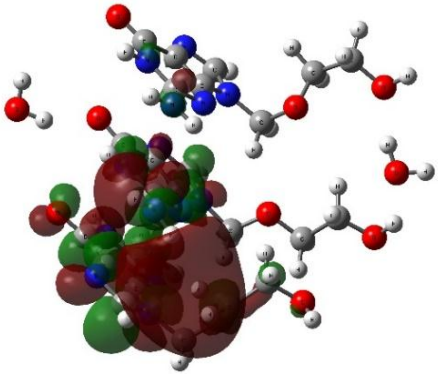

LUMO (−0.566 eV)

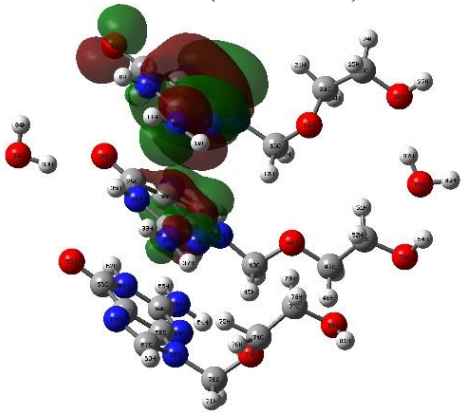

HOMO (-5.248 eV)

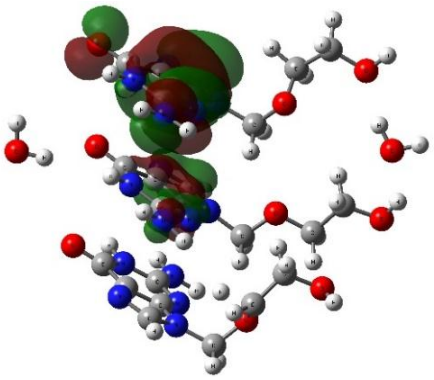

HOMO (-5.478 eV)

Figure 4.10 (a): LUMO and HOMO surface mapped plots of ACV-II molecular system using DFT/B3LYP/6-31G** method.

Figure 4.10 (b): LUMO and HOMO surface mapped plots of ACV-II molecular system using DFT/B3LYP/6-311G** method.

4.2.3 Mulliken Population Analysis (MPA)

Table 4.10 and Figure 4.11 show the effective Mulliken atomic charge distributions of ACV-II molecular system obtained through DFT/B3LYP/6-31G** and DFT/B3LYP/6-311G** level of calculations. As expected, all the hydrogen atoms in ACV-II molecular system show electron donor characteristics and have positive atomic charge distributions ranging from 0.053 to 0.344 (Alam

and Park, 2018; N.Sudha *et al.*, 2020). It is observable that hydrogen atoms bonded with oxygen atoms and nitrogen atoms tend to show larger positive atomic charge distributions than those linked with carbon atoms. The reason is oxygen and nitrogen atoms are more electronegative than carbon atoms which caused stronger charge shift activities in the ACV-II molecule. For oxygen and nitrogen atoms, all of them explicit electron acceptor traits as they pose negative atomic charges with ranges of -0.319 to -0.666 and -0.282 to -0.677. From the MPA data, noted that oxygen atoms O_1, O_4, and O_7 show higher negative atomic charge distributions in ACV-II molecule, while the carbon atoms bonded with them (i.e. C_1, C_9, and C_{17}) explicit larger positive atomic charges than atoms C_6, C_7, C_8, C_{14}, C_{15}, C_{16}, C_{22}, C_{23}, and C_{24}. These indicate the presence of polarized C=O bonds in the ACV-II molecular system (Lakshmi *et al.*, 2019). From the MPA analysis, the highest positive Mulliken atomic charge distribution in the ACV-II molecule is located on atom C_{12}, followed by atoms C_{20} and C_4. These are due to the reason that carbon atoms C_{12}, C_{20}, and C_4 bonded with three electronegative nitrogen atoms (i.e. N_1, N_2, N_3, N_6, N_7, N_8, N_{11}, N_{12}, and N_{13}) that caused them to undergo intensive charge shift activities from less electronegative carbon atoms to high electronegative nitrogen atoms. Besides, with atomic charge readings of -0.677 (6-31G**) and -0.520 (6-311G**), nitrogen atom N_3 is assigned to be the largest negative atomic charge distribution in the ACV-II molecular system. These findings show disparity with the ACV-I molecule where it obtained the highest negative Mulliken atomic charge in oxygen atom (i.e. O_{11}) rather than nitrogen atom. Furthermore, larger negative atomic charges in atoms O_3, O_4, O_6, O_9, N_3, N_8, and N_{13} accompany with higher positive atomic charges in H_1, H_2, H_3, H_{11}, H_{12}, H_{13}, H_{14}, H_{22}, H_{23}, H_{24}, H_{25}, H_{33},

H_{34}, H_{35}, H_{36}, and H_7 suggest the presence of O-H-O, O-H-N, and N-H-N types of intra and intermolecular hydrogen bonding interaction in ACV-II molecular system (Jasmine *et al.*, 2015).

Table 4.10: Computed Mulliken atomic charges analysis (MPA) of ACV-II molecular system using DFT/B3LYP/6-31G** and DFT/B3LYP/6-311G** method.

ACV-II					
MPA					
Atoms	DFT/B3LYP/6-31G**	DFT/B3LYP/6-311G**	Atoms	DFT/B3LYP/6-31G**	DFT/B3LYP/6-311G**
O_1	-0.504	-0.331	H_{17}	0.150	0.162
C_1	0.582	0.427	O_5	-0.511	-0.396
C_2	0.146	-0.101	C_{15}	0.040	-0.035
C_3	0.502	0.332	H_{18}	0.127	0.128
N_1	-0.594	-0.413	H_{19}	0.084	0.094
C_4	0.734	0.577	C_{16}	0.082	0.013
N_2	-0.625	-0.485	H_{20}	0.067	0.071
H_1	0.265	0.223	H_{21}	0.103	0.100
N_3	-0.677	-0.520	O_6	-0.571	-0.424
H_2	0.291	0.244	H_{22}	0.315	0.234
H_3	0.271	0.228	O_7	-0.496	-0.319
N_4	-0.487	-0.288	C_{17}	0.572	0.419
C_5	0.277	0.169	C_{18}	0.132	-0.129
N_5	-0.520	-0.405	C_{19}	0.536	0.390
H_4	0.109	0.100	N_{11}	-0.615	-0.432
C_6	0.183	0.125	C_{20}	0.755	0.592
H_5	0.114	0.121	N_{12}	-0.614	-0.474
H_6	0.152	0.154	H_{23}	0.284	0.242
O_2	-0.478	-0.364	N_{13}	-0.665	-0.502
C_7	0.060	-0.028	H_{24}	0.294	0.248
H_7	0.111	0.123	H_{25}	0.284	0.238

Table 4.10 Continued.

Atoms	DFT/B3LYP/6-31G**	DFT/B3LYP/6-311G**	Atoms	DFT/B3LYP/6-31G**	DFT/B3LYP/6-311G**
H_8	0.094	0.092	N_{14}	-0.496	-0.296
C_8	0.030	-0.007	C_{21}	0.248	0.126
H_9	0.096	0.098	N_{15}	-0.514	-0.402
H_{10}	0.115	0.114	H_{26}	0.105	0.106
O_3	-0.538	-0.424	C_{22}	0.164	0.115
H_{11}	0.319	0.254	H_{27}	0.109	0.117
O_4	-0.541	-0.389	H_{28}	0.147	0.142
C_9	0.626	0.485	O_8	-0.451	-0.333
C_{10}	0.126	-0.145	C_{23}	0.057	-0.033
C_{11}	0.532	0.375	H_{29}	0.053	0.065
N_6	-0.613	-0.437	H_{30}	0.099	0.086
C_{12}	0.797	0.638	C_{24}	0.024	-0.031
N_7	-0.624	-0.470	H_{31}	0.080	0.092
H_{12}	0.270	0.226	H_{32}	0.151	0.157
N_8	-0.667	-0.500	O_9	-0.518	-0.378
H_{13}	0.283	0.233	H_{33}	0.305	0.233
H_{14}	0.273	0.224	O_{10}	-0.666	-0.522
N_9	-0.492	-0.282	H_{34}	0.337	0.266
C_{13}	0.254	0.131	H_{35}	0.288	0.220
N_{10}	-0.525	-0.386	O_{11}	-0.641	-0.505
H_{15}	0.105	0.094	H_{36}	0.294	0.229
C_{14}	0.214	0.145	H_{37}	0.344	0.282
H_{16}	0.082	0.084			

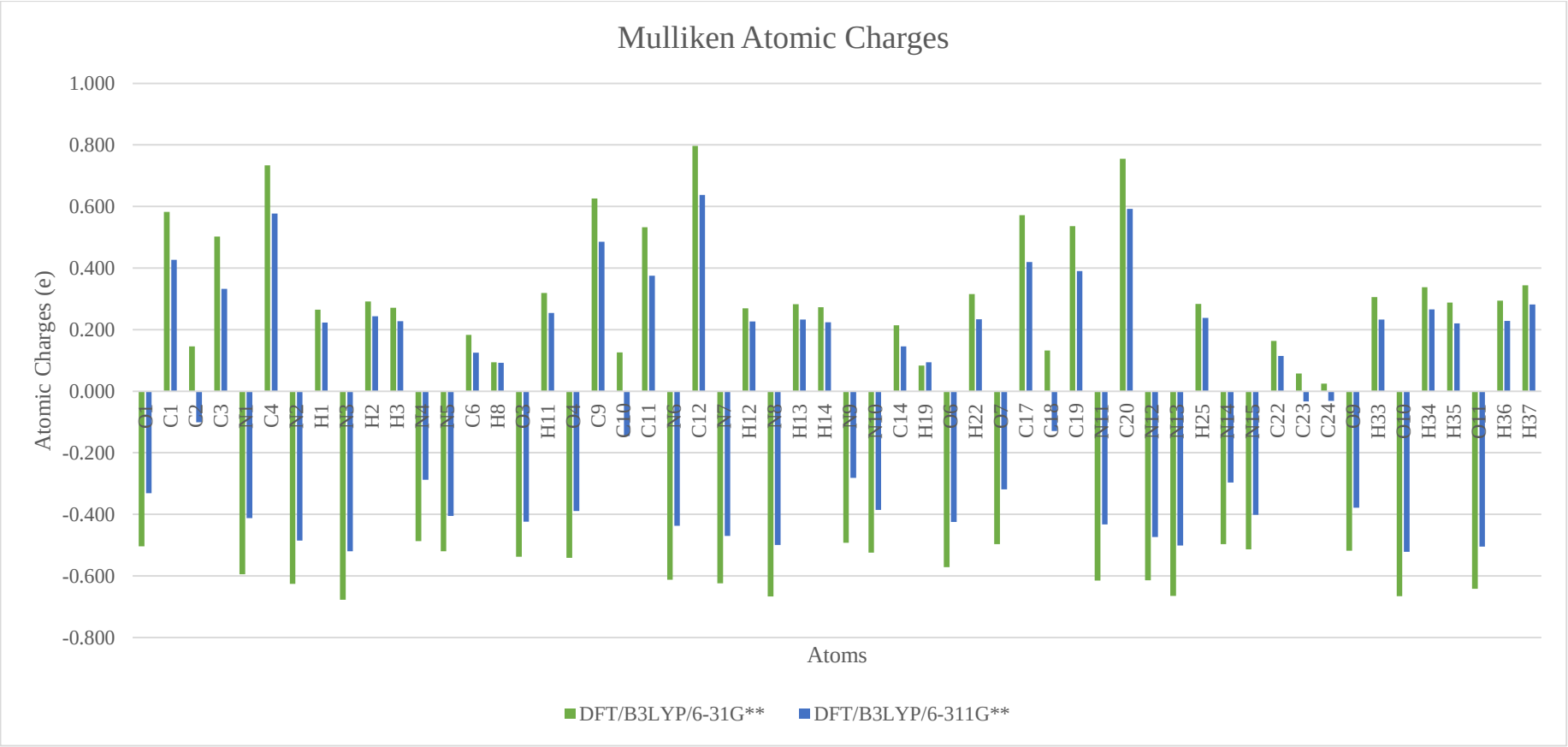

Figure 4.11: MPA analysis of ACV-II molecular system using DFT/B3LYP/6-31G** and DFT/B3LYP/6-311G** methods.

4.2.4 Molecular Electrostatic Potential (MEP)

Figure 4.12 (a) and (b) show the 3D molecular electrostatic potential (MEP) surface mapped plots of ACV-II molecular system obtained via DFT/B3LYP/6-31G** and DFT/B3LYP/6-311G** level of calculations. Both of the computational methods show satisfactory agreement with each other. From the MEP results, noticed that areas around electronegative oxygen atoms (O_1, O_4, O_7, O_{10}) and nitrogen atoms (N_4, N_9) pose strong negative electrostatic potential characteristics (red colour mapping). Besides, regions concentered around electropositive hydrogen atoms (H_1, H_3, H_{12}, H_{14}) exhibit high positive electrostatic potential features (blue colour mapping). These findings imply that atoms O_1, O_4, O_7, O_{10}, N_4, and N_9 will be the most probable sites for electrophilic reactions, while atoms H_1, H_3, H_{12}, and H_{14} will be the most preferred sites for nucleophilic reactions in ACV-II molecular system (Alam and Park, 2018). Consequently, gives an ideal about the possible regions where the intra and intermolecular interactions may occur in ACV-II molecular system (Sridevi, 2012; Kabouchi *et al.*, 2017). Similar to ACV-I molecular system, the carbon atoms in the ACV-II molecule explicit neutral electrostatic potentials (colourless mapping) and will not consider as the reactive sites for both electrophilic and nucleophilic reactions. Furthermore, Figure 4.12 (a) and (b) also illustrate the global surface extrema points of the ACV-II molecular system computed from the Multifwn software package. Noticed that the global surface maximum points for both DFT/B3LYP/6-31G** and DFT/B3LYP/6-311G** level of calculations are situated around hydrogen atom H_{14} with values of 2.571 eV and 2.646 eV. Moreover, the global surface minimum points in ACV-II molecule are found to

be located around oxygen atom O_{10} with values of -3.060 eV, respectively for DFT/B3LYP/6-31G** and DFT/B3LYP/6-311G** computational methods. These findings show large deviation with the ACV-I molecular system where the global surface minimum point of the ACV-I molecule tends to locate nearby the oxygen atom in the guanine rings rather than the water molecule.

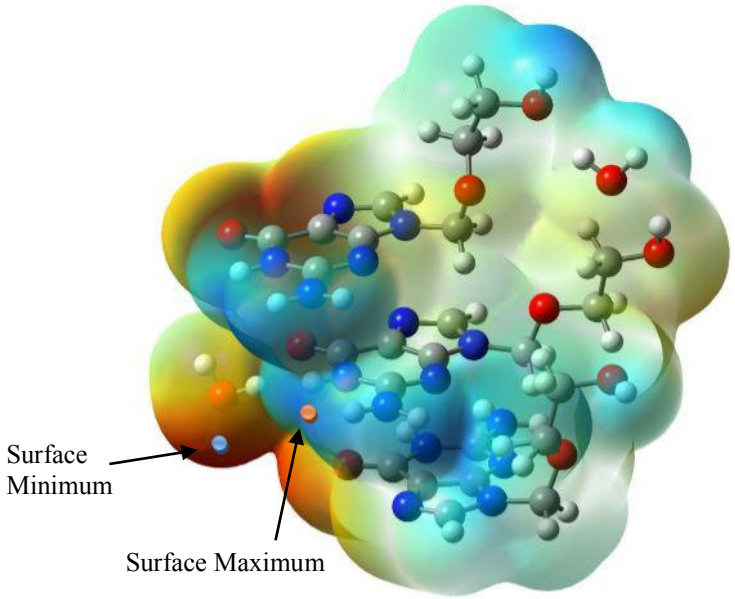

Surface Minimum (blue dot) - -3.060 eV
Surface Maximum (red dot) – 2.571 eV

Figure 4.12 (a): The MEP surface mapped plots of ACV-II molecular system using DFT/B3LYP/6-31G** method.

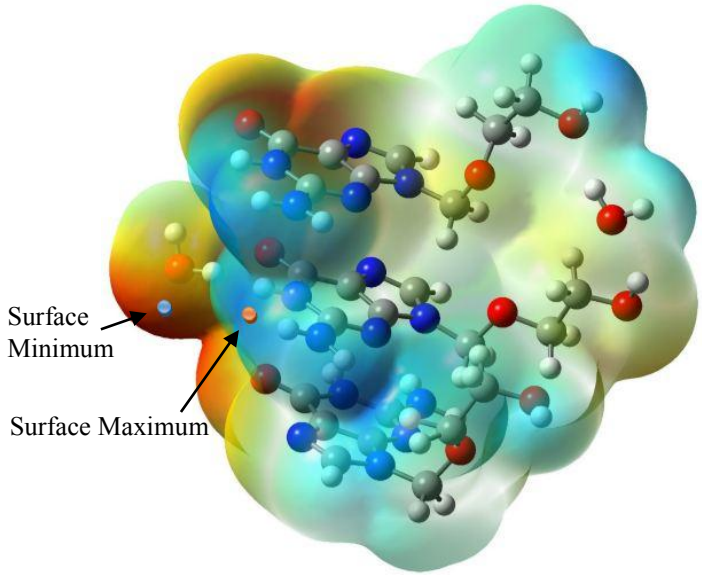

Surface Minimum (blue dot) - -3.060 eV
Surface Maximum (red dot) – 2.646 eV

Figure 4.12 (b): The MEP surface mapped plots of ACV-II molecular system using DFT/B3LYP/6-311G** method.

4.2.5 Non-Linear Optical (NLO) Properties

Table 4.11 summarises the computed dipole moment (μ) and first hyperpolarizability (β_{tot}) of ACV-II molecular system using DFT/B3LYP/6-31G** and DFT/B3LYP/6-311G** level of calculations. Even though ACV-I and ACV-II molecules contain identical number of same type atoms (i.e. O, C, H, N), both of them explicit different computing results in the NLO study. This is because the NLO properties in organic molecules are mainly affected by its molecular geometry structure, coordination environment, charge mobility, and delocalisation effect in the π conjugated system (Joshi, 2016; Lokhande *et al.*, 2019; Avci *et al.*, 2020). As can be observed in Table 4.11, the calculated dipole moment using DFT/B3LYP/6-31G** method is 14.822 Debye, while for DFT/B3LYP/6-311G** technique is 14.600 Debye. Both of the computational results elucidate that the major dipole moment contribution in ACV-II molecular system are come from Z -direction (μ_z). Besides, the computed first hyperpolarizabilities of the ACV-II molecular system are found to be 6.690 x 10^{-29} e.s.u and 6.837 x 10^{-29} e.s.u, respectively for DFT/B3LYP/6-31G** and DFT/B3LYP/6-311G** level of theories. It is worth mentioning that ACV-II molecular system shows better NLO active nature than the ACV-I molecular system. The computed dipole moment and first hyperpolarizability of the ACV-II molecular system are at least 10.634 and 179.357 times larger than urea.

Table 4.11: Computed dipole moment (μ) and first hyperpolarizability (β_{tot}) of ACV-II molecular system using DFT/B3LYP/6-31G** and DFT/B3LYP/6-311G** methods.

Parameters	DFT/B3LYP/6-31G**	DFT/B3LYP/6-311G**
μ_x	-3.610	-3.545
μ_y	5.029	4.983
μ_z	13.467	13.258
μ [Debye]	14.822	14.600
β_{xxx}	-943.648	-948.581
β_{xyy}	-37.925	-41.774
β_{xzz}	-657.699	-662.565
β_{yyy}	2424.549	2461.549
β_{xxy}	577.940	588.245
β_{yzz}	736.131	755.405
β_{zzz}	-4251.241	-4366.929
β_{xxz}	-1313.545	-1331.607
β_{yyz}	-1015.497	-1041.071
β_{tot} [a.u]	7743.682	7914.163
β_{tot} [e.s.u]	6.690 x 10^{-29}	6.837 x 10^{-29}

4.2.6 Fourier Transform Infrared (FT-IR) Spectroscopy

Table 4.12 summarises parts of the computational FT-IR vibrational frequencies of the ACV-II molecular system obtained using DFT/B3LYP/6-31G** and DFT/B3LYP/6-311G** level of theories. With a total atomic number of 87, ACV-II molecular system contains 255 fundamental vibrational modes that

quantitatively represent the functional groups appearing in the system. From the table, noticed that all the computed FT-IR results (unscaled) tend to overestimate before the employment of the direct scaling technique. This is caused by the ignorance of anharmonicity under the gases phase during FT-IR computational calculation (Ali *et al.*, 2017; Ahmad *et al.*, 2018). In order to ratify the computational results, scale factors of 0.961 (DFT/B3LYP/6-31G** method) and 0.967 (DFT/B3LYP/6-311G** method) are used to shift the overall vibrational frequencies to become more comparable with literature data (CCCBDB, 2020). As a result, all the scaled FT-IR vibrational frequencies obtained using DFT/B3LYP/6-31G** and DFT/B3LYP/6-311G** computational methods show high conformity with the geometry structure of the ACV-II molecular system. As an example, the O-H stretching vibrational modes from the water molecules can be observed between band regions 3497 cm^{-1} to 3526 cm^{-1} (scaled 6-31G**) and 3506 cm^{-1} to 3552 cm^{-1} (scaled 6-311G**). Besides, band regions 3456 cm^{-1} (scaled 6-31G**) and 3471 cm^{-1} (scaled 6-311G**) represent the N-H stretching vibrational assignments of primary and secondary amides in the ACV-II molecular system. In Table 4.12, it is figured out that band regions 3068 cm^{-1} (scaled 6-31G**) and 3127 cm^{-1} (scaled 6-311G**) are assigned for aromatic C-H stretching vibrational modes, while band regions 2876 cm^{-1} (scaled 6-31G**) and 2883 cm^{-1} (scaled 6-311G**) are correspondence to C-H stretching vibrations from the side chains of ACV molecules. On the other hands, the aromatic C-H bending vibrational modes are observed in regions 1386 cm^{-1} (scaled 6-31G**) and 1395 cm^{-1} (scaled 6-311G**) whereas the side chains C-H bending vibrational modes are located between regions 770 cm^{-1} to 829 cm^{-1} (scaled 6-31G**) and 768 cm^{-1} to

833 cm^{-1} (scaled 6-311G**). Furthermore, noticed that band regions 1466 cm^{-1} to 1531 cm^{-1} (scaled 6-31G**) and 1469 cm^{-1} to 1537 cm^{-1} (scaled 6-311G**) are found to be the aromatic C=C stretching vibrational modes in the guanine rings of ACV molecules. Moreover, the C=O stretching vibrational modes in the ACV-II molecule appeared at band regions of 1735 cm^{-1} (scaled 6-31G**) and 1727 cm^{-1} (scaled 6-311G**). As listed in Table 4.12, the stretching vibrational assignments for aromatic C-N lie between band regions of 1311 cm^{-1} to 1351 cm^{-1} (scaled 6-31G**) and 1313 cm^{-1} to 1351 cm^{-1} (scaled 6-311G**). In additions, the C-O stretching vibrational modes from the sides chains of ACV molecules are found at band regions 1022 cm^{-1} to 1205 cm^{-1} (scaled 6-31G**) and 1023 cm^{-1} to 1214 cm^{-1} (scaled 6-311G**). In a conclusion, there is no suspicious finding in the computational FT-IR results of the ACV-II molecular system. Hence, give confidence in the usage of the DFT computational approach in the study of FT-IR vibrational spectrum in ACV compounds.

Table 4.12: Computational (unscaled and scaled) FT-IR vibrational frequencies of ACV-II molecular system.

	DFT/B3LYP/6-31G**		DFT/B3LYP/6-311G**	
	Unscaled [cm^{-1}]	Scaled [cm^{-1}]	Unscaled [cm^{-1}]	Scaled [cm^{-1}]
O-H stretching vibration	3669	3526	3673	3552
O-H stretching vibration	3639	3497	3626	3506
N-H stretching vibration	3597	3456	3589	3471
C-H stretching vibration	3192	3068	3233	3127
C-H stretching vibration	2993	2876	2981	2883
C=O stretching vibration	1805	1735	1786	1727
C=C stretching vibration	1593	1531	1590	1537
C=C stretching vibration	1526	1466	1519	1469
C-H bending vibration	1443	1386	1443	1395
C-N stretching vibration	1406	1351	1397	1351
C-N stretching vibration	1365	1311	1358	1313
C-O stretching vibration	1254	1205	1256	1214
C-O stretching vibration	1136	1091	1137	1100
C-O stretching vibration	1124	1080	1125	1088
C-O stretching vibration	1075	1033	1072	1037
C-O stretching vibration	1064	1022	1057	1023
C-H bending vibration	863	829	862	833
C-H bending vibration	813	781	815	788
C-H bending vibration	801	770	794	768

4.2.7 Rotational Barrier Analysis

In order to understand and determine the conformational stabilities and behaviours of ACV Molecule A, B, and C in ACV-II molecular system, rotational barrier studies are carried out via Potential Energy Surface (PES) scanning calculations in dihedral angles N_5-C_6-O_2-C_7 (Molecule A), N_{10}-C_{14}-O_5-C_{15} (Molecule B), and N_{15}-C_{22}-O_8-C_{23} (Molecule C). Noticed that each of the

dihedral angles undergo a total number of 36 steps rotation starting from 0° to 360°. The changes in computed relative energies, optimized total energies, and bond distances according to the angles of rotation are obtained after one complete cycle of the PES scan. Figure 4.13 (a), (b), and (c) show the PES diagrams of ACV Molecule A, B, and C plotted from the changes in relative energies corresponding with rotational angles. In Figure 4.13 (a), it is figured out that ACV Molecule A has two stable conformers (i.e. conformer-AI and conformer-AII) at rotational angles of 170° and 240°. Based on the computed results, the relative energies, C_6-O_2 bond distances, and optimized total energies for conformer-AI are 0.133 eV (6-31G**)/0.132 eV (6-311G**), 1.417 Å (6-31G** and 6-311G**), and -22066.182 eV (6-31G**)/-22071.652 eV (6-311G**), while for conformer-AII are found to be 0.143 eV (6-31G**)/0.134 eV (6-311G**), 1.414 Å (6-31G**)/1.413 Å (6-311G**), and -22066.172 eV (6-31G**)/-22071.650 eV (6-311G**). Besides, with highest relative energies of 0.442 eV (6-31G**)/0.439 eV (6-311G**), farthest C_6-O_2 bond distances of 1.459 Å (6-31G**)/1.460 Å (6-311G**), and largest optimized total energies of -22065.874 eV (6-31G**)/-22071.344 eV (6-311G**), the most unstable conformer of ACV Molecule A (conformer-AIII) is found at rotational angle of 90°. For ACV Molecule B, the PES curves plotted in Figure 4.13 (b) clearly noted that there are two stable conformers (i.e. conformer-BI and conformer-BII) located at rotational angles of 90° and 270°. Conformer-BI has computed relative energies of 0.056 eV (6-31G**)/0.061 eV (6-311G**), C_{14}-O_5 bond distances of 1.416 Å (6-31G**)/1.415 Å (6-311G**), and optimized total energies of -22066.140 eV (6-31G**)/-22071.626 eV (6-311G**), whereas conformer-BII shows computed relative energies of 0.013 eV (6-31G**)/0.017 eV (6-311G**),

C_{14}-O_5 bond distances of 1.415 Å (6-31G** and 6-311G**), and optimized total energies of -22066.183 eV (6-31G**)/-22071.670 eV (6-311G**). Furthermore, it is noticed that ACV Molecule B reaches its maximum unstable conformer (conformer-BIII) state at the rotational angle of 170°. The computed results reveal that conformer-BIII consist highest relative energies of 0.447 eV (6-31G**)/0.440 eV (6-311G**), longest C_{14}-O_5 bond distances of 1.469 Å (6-31G** and 6-311G**), and largest optimized total energies of -22065.749 eV (6-31G**)/-22071.247 eV (6-311G**). Moreover, the PES curves plotted in Figure 4.13 (c) pointed out that ACV molecule C has two possible stable conformers (i.e. conformer-CI and conformer-CII) at rotational angles of 110° and 220 °. For conformer-CI, it shows relative energies of 0.123 eV (6-31G**)/0.118 eV (6-311G**), C_{22}-O_8 bond distances of 1.401 Å (6-31G** and 6-311G**), and optimized total energies of -22063.517 eV (6-31G**)/ -22069.017 eV (6-311G**). For conformer-CII, the computed relative energies, C_{22}-O_8 bond distances, and optimized total energies are calculated to be 0.082 eV (6-31G**)/0.084 eV (6-311G**), 1.409 Å (6-31G**)/1.408 Å (6-311G**), and -22063.558 eV (6-31G**)/-22069.051 eV (6-311G**). In additions, accompany with largest relative energies of 0.454 eV (6-31G**)/0.441 eV (6-311G**), farthest C_{22}-O_8 bond distances of 1.454 Å (6-31G** and 6-311G**), and highest optimized total energies of -22063.186 eV (6-31G**)/-22068.694 eV (6-311G**), it is realized that ACV Molecule C poses maximum unstable conformer (conformer-CIII) state at the rotational angle of 270°. Overall, it is noted that the elongation in C-O bond distances (i.e. C_6-O_2, C_{14}-O_5, and C_{22}-O_8) leads to higher relative energy and lower stability in ACV Molecule A, B, and C conformers.

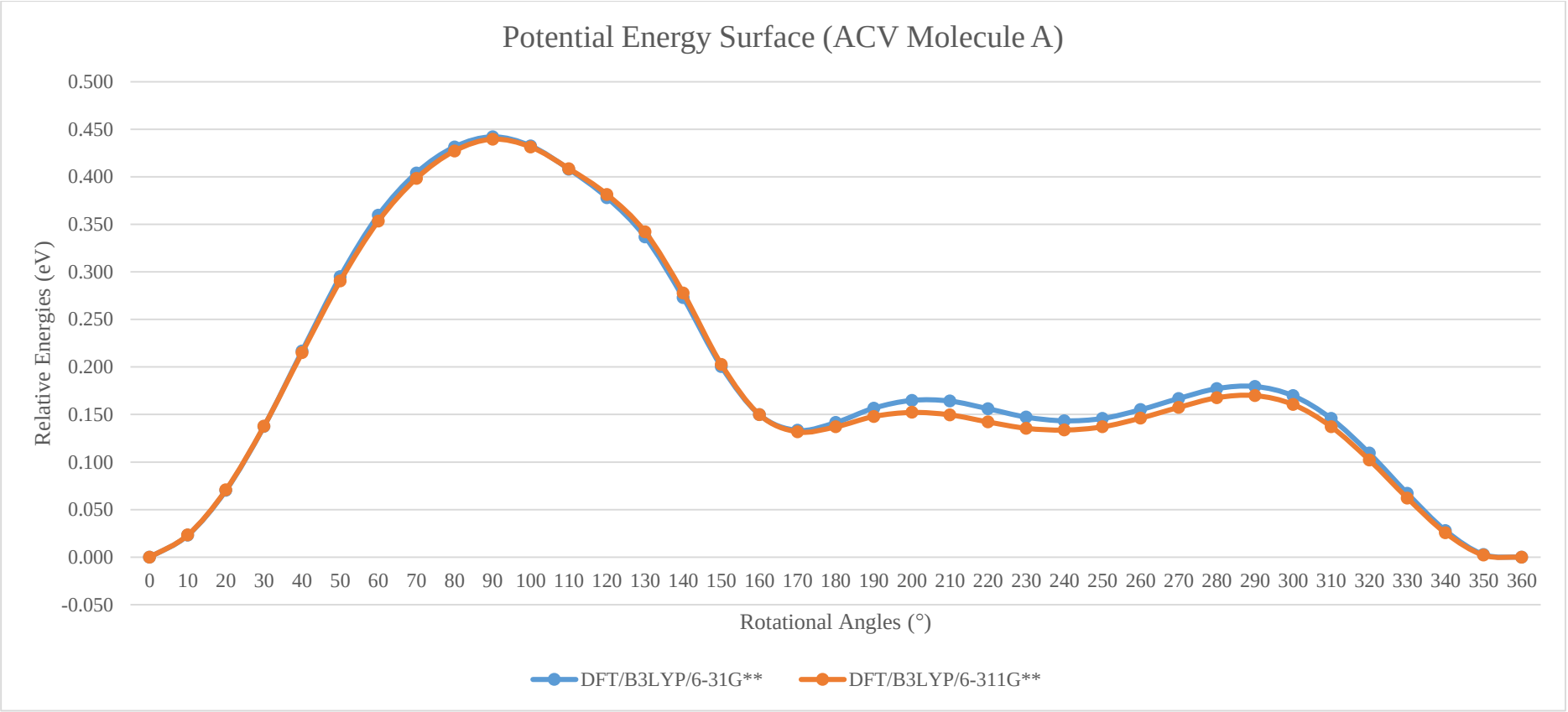

Figure 4.13 (a): Potential Energy Surface of ACV-II Molecule A using DFT/B3LYP/6-31G** and DFT/B3LYP/6-311G** methods.

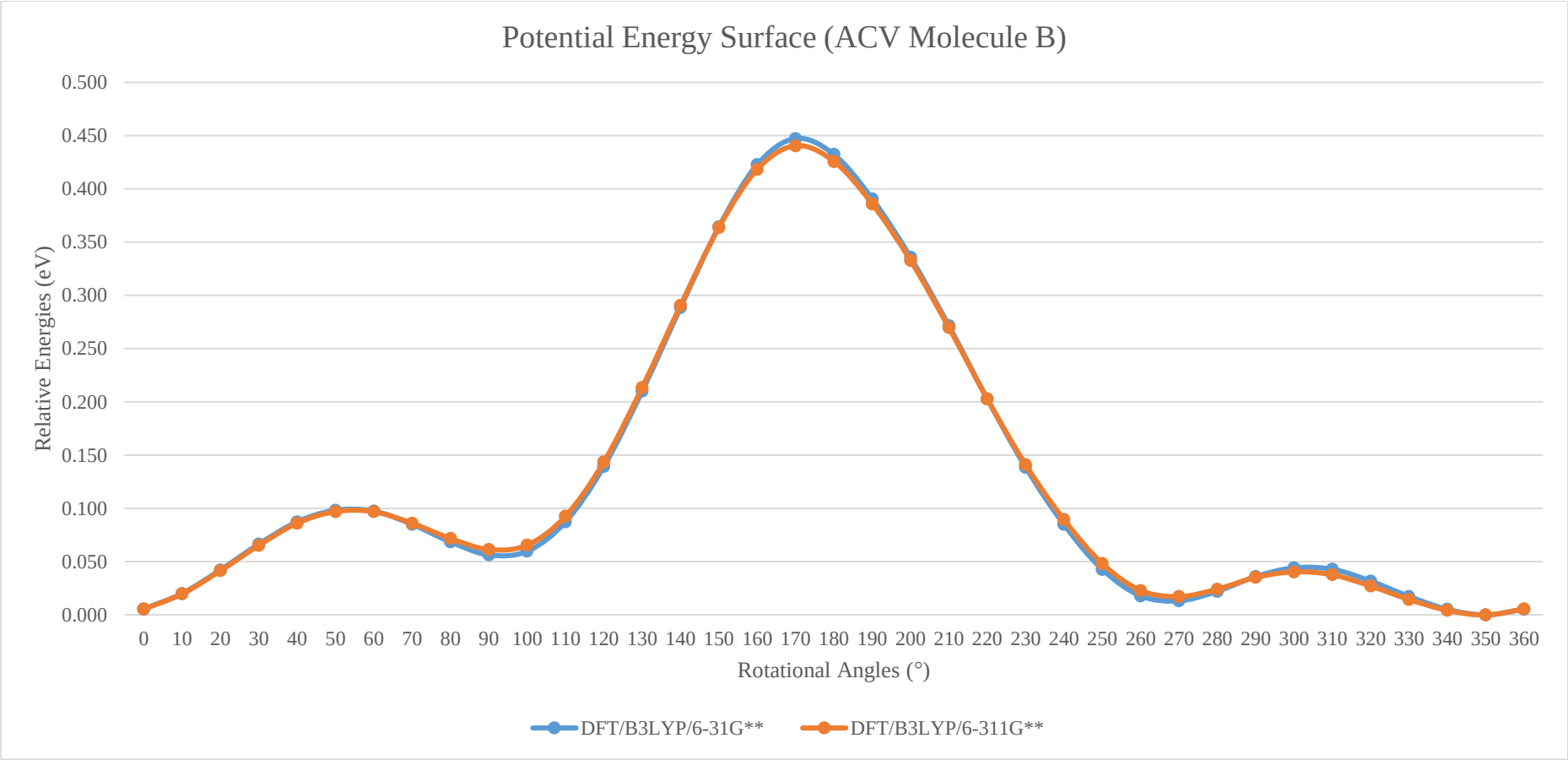

Figure 4.13 (b): Potential Energy Surface of ACV-II Molecule B using DFT/B3LYP/6-31G** and DFT/B3LYP/6-311G** methods.

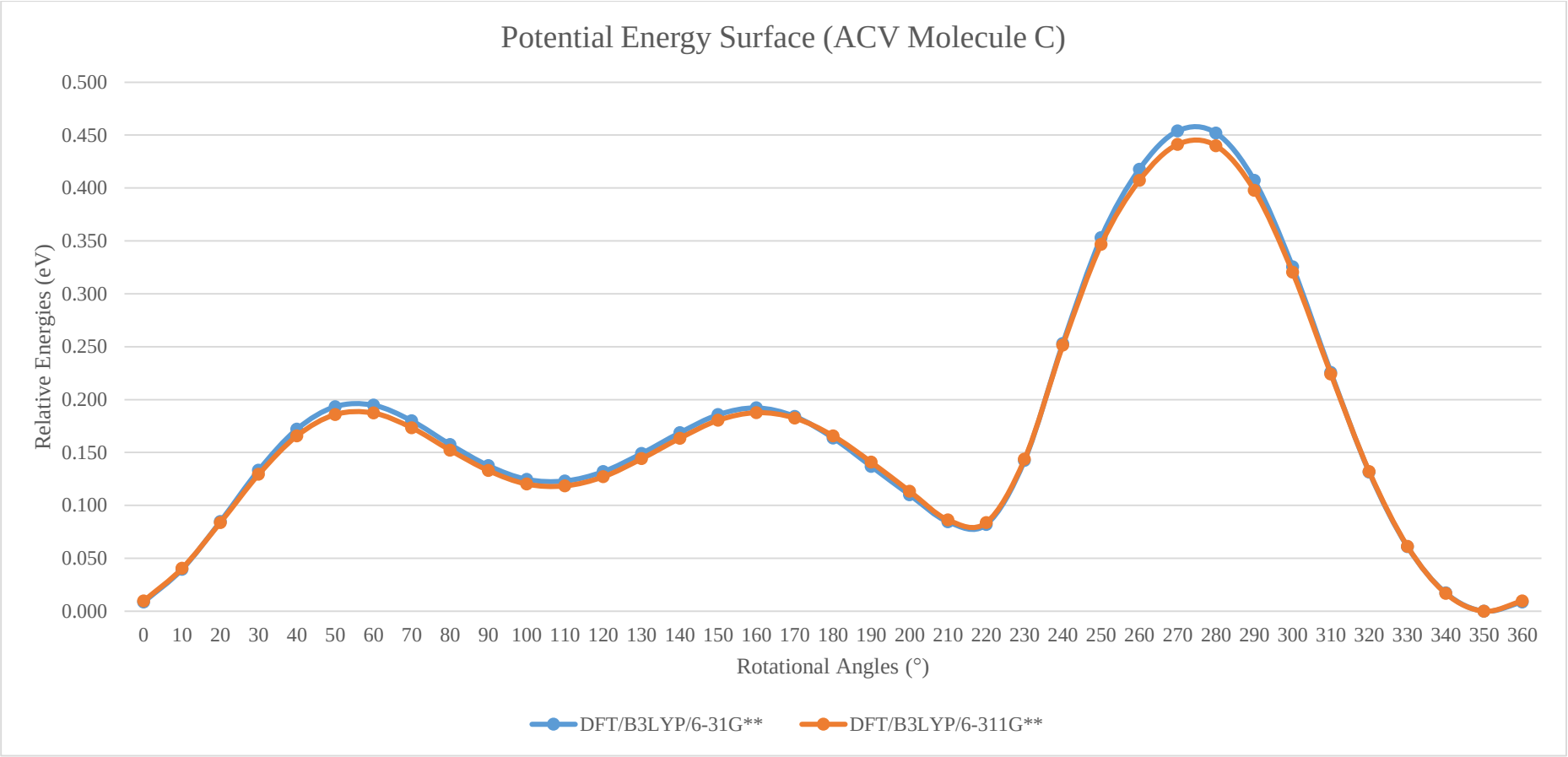

Figure 4.13 (c): Potential Energy Surface of ACV-II Molecule C using DFT/B3LYP/6-31G** and DFT/B3LYP/6-311G** methods.

Table 4.13 (a): Parts of the rotational barrier studies in ACV-II Molecule A using DFT/B3LYP/6-31G** and DFT/B3LYP/6-311G** methods.

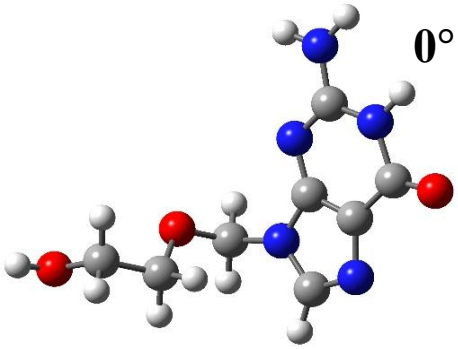	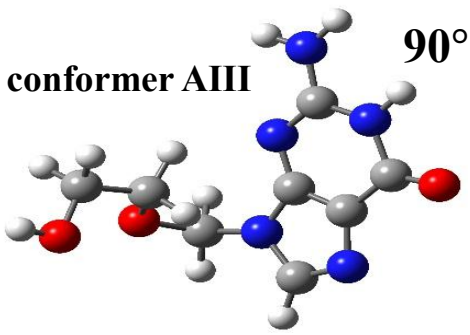
Relative Energy: 0.000 eV / 0.000 eV Optimized Total Energy: -22066.316 eV / -22071.784 eV C_6-O_2 Bond Distance: 1.408 Å / 1.408 Å	Relative Energy: 0.442 eV / 0.439 eV Optimized Total Energy: -22065.874 eV / -22071.344 eV C_6-O_2 Bond Distance: 1.459 Å / 1.460 Å
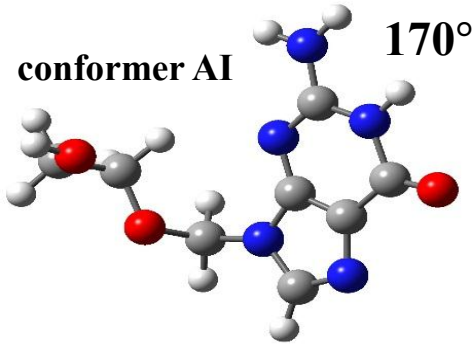	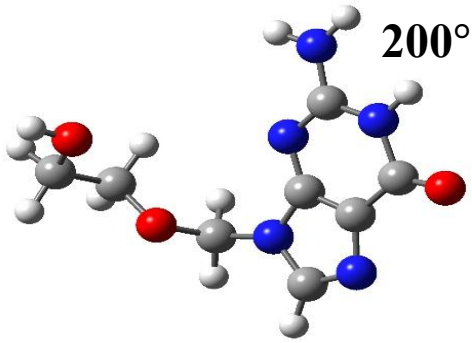
Relative Energy: 0.133 eV / 0.132 eV Optimized Total Energy: -22066.182 eV / -22071.652 eV C_6-O_2 Bond Distance: 1.417 Å / 1.417 Å	Relative Energy: 0.165 eV / 0.152 eV Optimized Total Energy: -22066.151 eV / -22071.632 eV C_6-O_2 Bond Distance: 1.418 Å / 1.418 Å
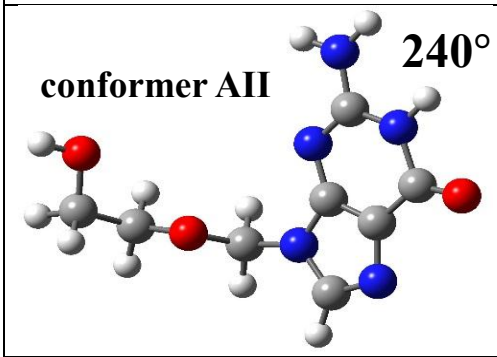	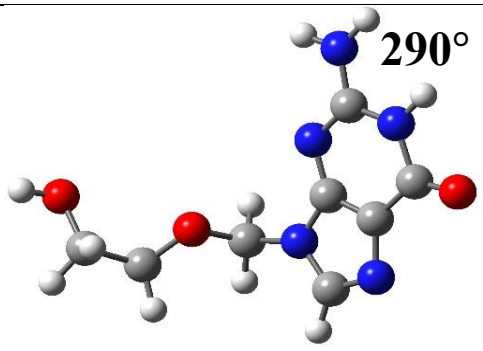
Relative Energy: 0.143 eV / 0.134 eV Optimized Total Energy: -22066.172 eV / -22071.650 eV C_6-O_2 Bond Distance: 1.414 Å / 1.413 Å	Relative Energy: 0.180 eV / 0.170 eV Optimized Total Energy: -22066.136 eV / -22071.614 eV C_6-O_2 Bond Distance: 1.420 Å / 1.419 Å

Table 4.13 (b): Parts of the rotational barrier studies in ACV-II Molecule B using DFT/B3LYP/6-31G** and DFT/B3LYP/6-311G** methods.

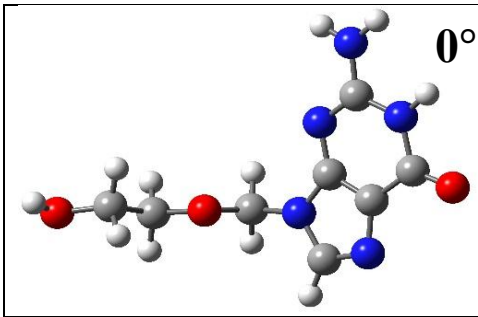	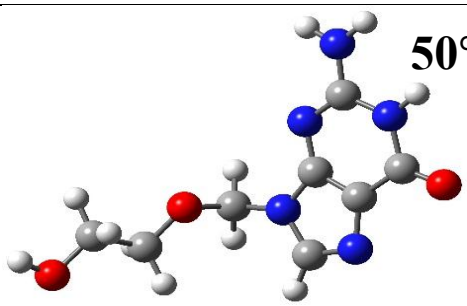
Relative Energy: 0.006 eV / 0.006 eV Optimized Total Energy: -22066.191 eV / -22071.681 eV C_{14}-O_5 Bond Distance: 1.413 Å / 1.413 Å	Relative Energy: 0.098 eV / 0.097 eV Optimized Total Energy: -22066.098 eV / -22071.590 eV C_{14}-O_5 Bond Distance: 1.421 Å / 1.421 Å
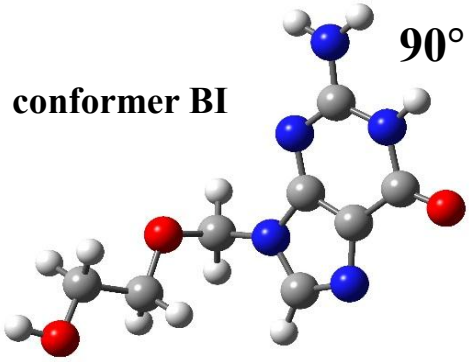	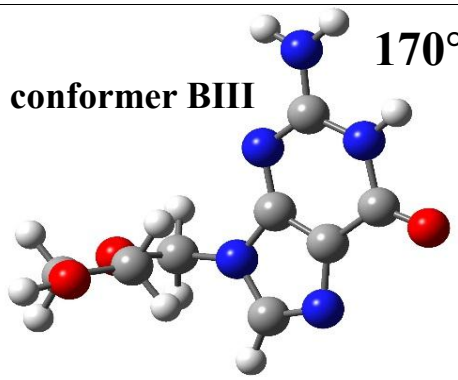
Relative Energy: 0.056 eV / 0.061 eV Optimized Total Energy: -22066.140 eV / -22071.626 eV C_{14}-O_5 Bond Distance: 1.416 Å / 1.415 Å	Relative Energy: 0.447 eV / 0.440 eV Optimized Total Energy: -22065.749 eV / -22071.247 eV C_{14}-O_5 Bond Distance: 1.469 Å / 1.469 Å
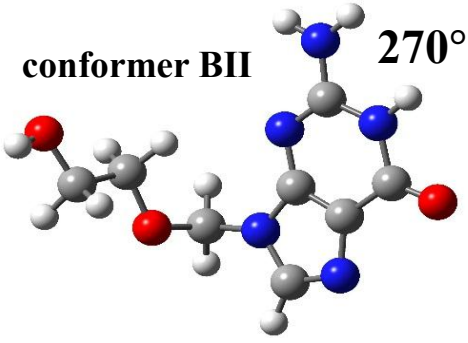	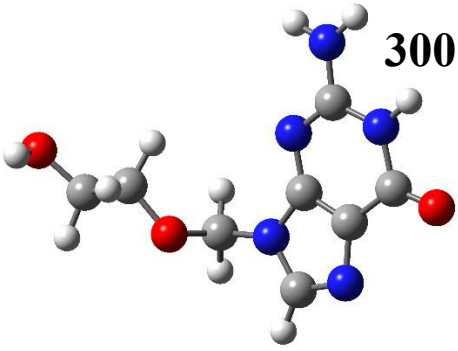
Relative Energy: 0.013 eV / 0.017 eV Optimized Total Energy: -22066.183 eV / -22071.670 eV C_{14}-O_5 Bond Distance: 1.415 Å / 1.415 Å	Relative Energy: 0.044 eV / 0.041 eV Optimized Total Energy: -22066.152 eV / -22071.647 eV C_{14}-O_5 Bond Distance: 1.419 Å / 1.418 Å

Table 4.13 (c): Parts of the rotational barrier studies in ACV-II Molecule C using DFT/B3LYP/6-31G** and DFT/B3LYP/6-311G** methods.

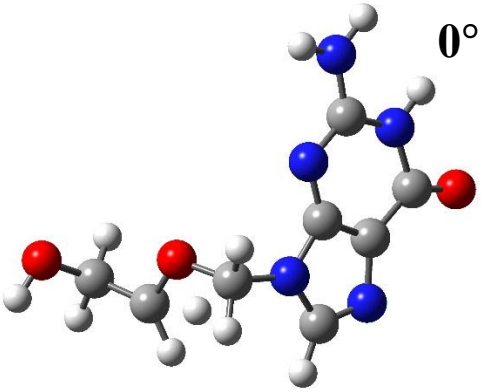	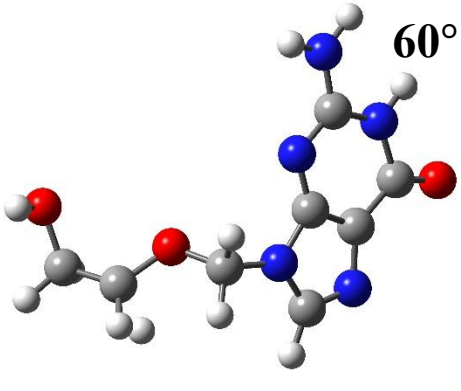
Relative Energy: 0.009 eV / 0.010 eV Optimized Total Energy: -22063.631 eV / -22069.126 eV C_{22}-O_8 Bond Distance: 1.398 Å / 1.398 Å	Relative Energy: 0.195 eV / 0.187 eV Optimized Total Energy: -22063.445 eV / -22068.948 eV C_{22}-O_8 Bond Distance: 1.409 Å / 1.409 Å
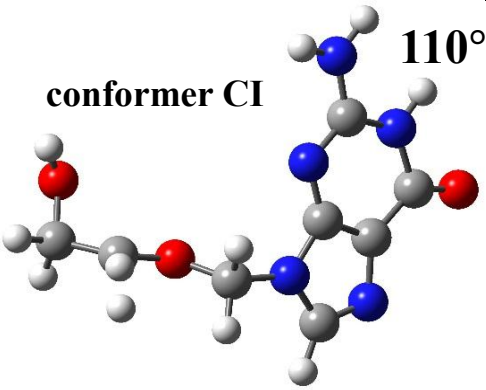	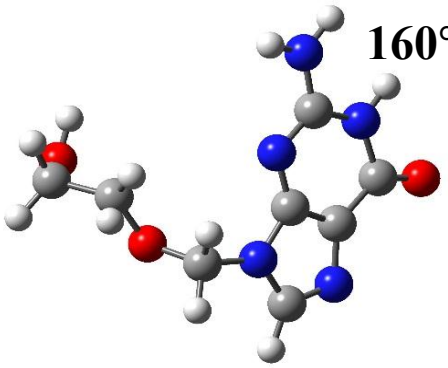
Relative Energy: 0.123 eV / 0.118 eV Optimized Total Energy: -22063.517 eV / -22069.017 eV C_{22}-O_8 Bond Distance: 1.401 Å / 1.401 Å	Relative Energy: 0.192 eV / 0.188 eV Optimized Total Energy: -22063.448 eV / -22068.948 eV C_{22}-O_8 Bond Distance: 1.408 Å / 1.407 Å
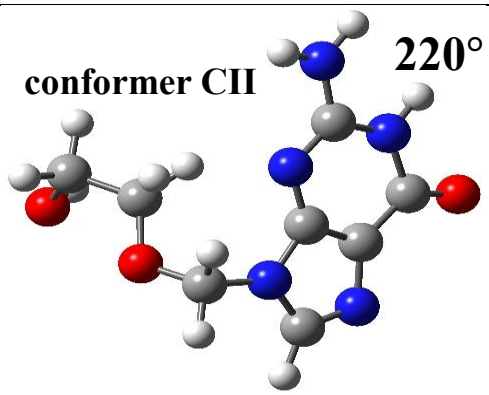	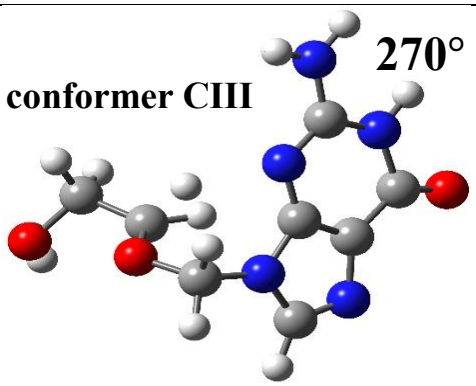
Relative Energy: 0.082 eV / 0.084 eV Optimized Total Energy: -22063.558 eV / -22069.051 eV C_{22}-O_8 Bond Distance: 1.409 Å / 1.408 Å	Relative Energy: 0.454 eV / 0.441 eV Optimized Total Energy: -22063.186 eV / -22068.694 eV C_{22}-O_8 Bond Distance: 1.454 Å / 1.454 Å

4.3: Acyclovir Hydrate (ACV-III) $2[C_8H_{11}N_5O_3]\cdot 4[H_2O]$

The crystallographic information file (CIF) of the ACV-III compound is provided by Montha (2012). With the help of the GaussView 5.0 software package, the complete single molecular structure of ACV-III is extracted from the unit cell and used as the host environment for DFT computational studies. Figure 4.14 (a) and (b) show the complete unit cell and single molecular crystal structures of the ACV-III molecular system together with numbering and labelling details. According to Montha (2012), ACV-III compound is crystallized in the triclinic space group of $P\bar{1}$ with unit cell lattice parameters of a = 6.900 Å, b = 11.417 Å, c = 15.081 Å, $\alpha = 82.595°$, $\beta = 82.395°$, and $\gamma = 89.368°$. With chemical formula of $2[C_8H_{11}N_5O_3]\cdot 4[H_2O]$, the perfect single molecular structure of ACV-III contains four water molecules (Water I, II, III, and IV) surrounded by two independent ACV molecules (Molecule A and B). In this work, the geometry and electronic properties of the ACV-III molecular system are discussed.

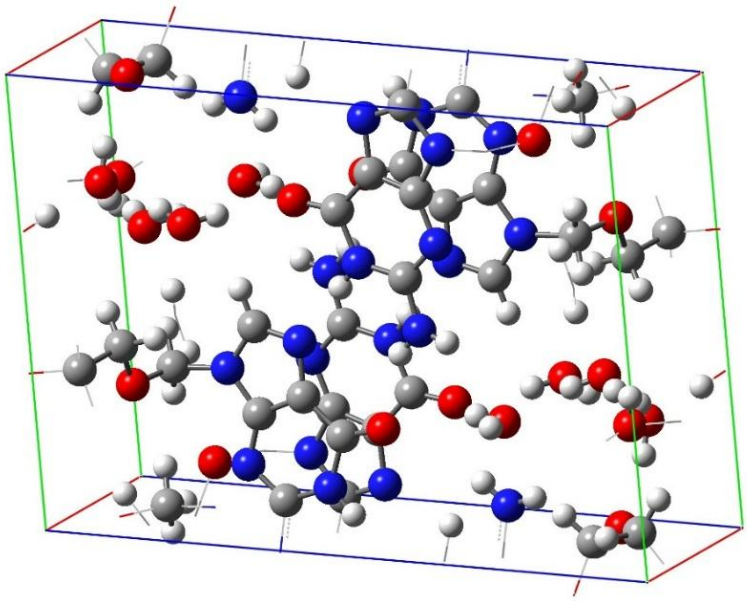

Figure 4.14 (a): The complete unit cell of ACV-III.

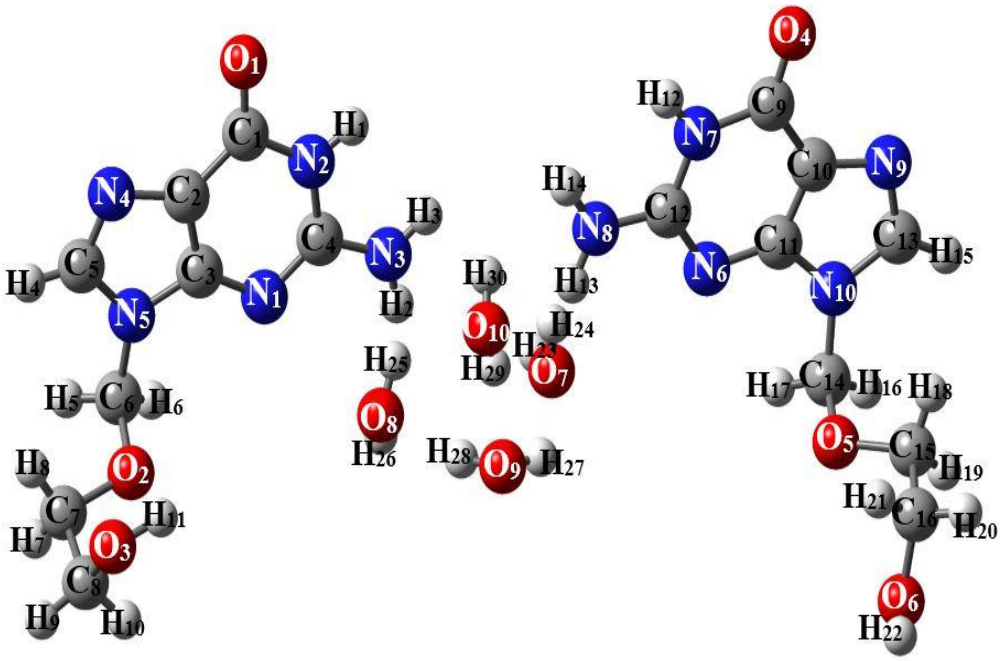

Figure 4.14 (b): Labelling and numbering details in ACV-III single molecular system.

4.3.1 Molecular Geometry Structural Analysis

Figure 4.15 (a) and (b) show parts of the significant experimental geometrical data of ACV Molecule A and B in the ACV-III single molecular system. From the diagrams, it is observed that both of the ACV Molecule A and B show closer geometry parameters with each other. For example, it is noted that both of the side chains in ACV Molecule A and B possess "staggered gauche" orientations since they have dihedral angles of 69.333 ° and 72.435 ° in O_2-C_7-C_8-O_3 (Molecule A) and O_5-C_{15}-C_{16}-O_6 (Molecule B). The findings are supported well by Lutker *et al.* (2011). Besides, with bond lengths of 1.423 Å, 1.427 Å, 1.415 Å, and 1.432 Å, bond distances C_8-O_3, C_7-O_2, C_{16}-O_6, and C_{15}-O_5 from the side chains of ACV Molecule A and B explicit single (C-O) bond characteristic (Peica, 2006). For the connection edges between the guanine moieties and side chains of ACV molecules, it is observed that bond distances N_5-C_6 (Molecule A) and N_{10}-C_{14} (Molecule B) have values of 1.456 Å and 1.458 Å, which elucidate single (N-C) bond identity. Noted that ACV Molecule A has bond angle N_5-C_6-O_2 of 112.170 °, whereas ACV Molecule B shows bond angle of 111.859° in N_{10}-C_{14}-O_5. As refer to the pyrimidine rings of ACV Molecule A and B, there are unsymmetrical bond distances between the C-C and C-N bonds. In ACV Molecule A, bond distances in C_4-N_2 (1.371 Å) and C_1-N_2 (1.387 Å) show shorter bond lengths than C_1- C_2 (1.416 Å). A similar situation is observed from ACV Molecule B where the bond distance in C_9-C_{10} (1.420 Å) is larger than C_9-N_7 (1.394 Å) and C_{12}-N_7 (1.367 Å). As a result, with endocyclic bond angles of 118.571 ° (C_1-C_2-C_3), 123.896 ° (N_2-C_4-N_1), 118.903 ° (C_9-C_{10}-C_{11}), and 123.947 ° (N_7-C_{12}-N_6), both of the ACV Molecule A and B show slightly

distortion in their heterocyclic pyrimidine rings. Moreover, there is present of resonance effect in the guanine moieties of ACV molecule A and B since all the C-N bonds (i.e. C_4-N_2, C_4-N_3, C_3-N_5, C_{12}-N_7, C_{12}-N_8, and C_{11}-N_{10}) and C-C bonds (i.e. C_1-C_2, C_2-C_3, C_9-C_{10}, and C_{10}-C_{11}) in the guanine moieties show bond distances ranges of 1.338 Å to 1.375 Å and 1.382 Å to 1.420 Å. All of them have bond lengths situated between single C-C, C-N bonds and double C=C, C=N bonds (Peica, 2006; Agrawal *et al.*, 2017; Bakkiyaraj, 2017). In additions, dihedral angles in N_1-C_3-N_5-C_5 (179.842 °), N_2-C_1-C_2-N_4 (-178.450 °), N_6-C_{11}-N_{10}-C_{13} (-179.620°), and N_7-C_9-C_{10}-N_9 (-178.258°) as shown in Figure 4.15 (a) and (b) indicate that ACV Molecule A and B have coplanar arrangements between the pyrimidine rings and imidazole rings of the guanine moieties.

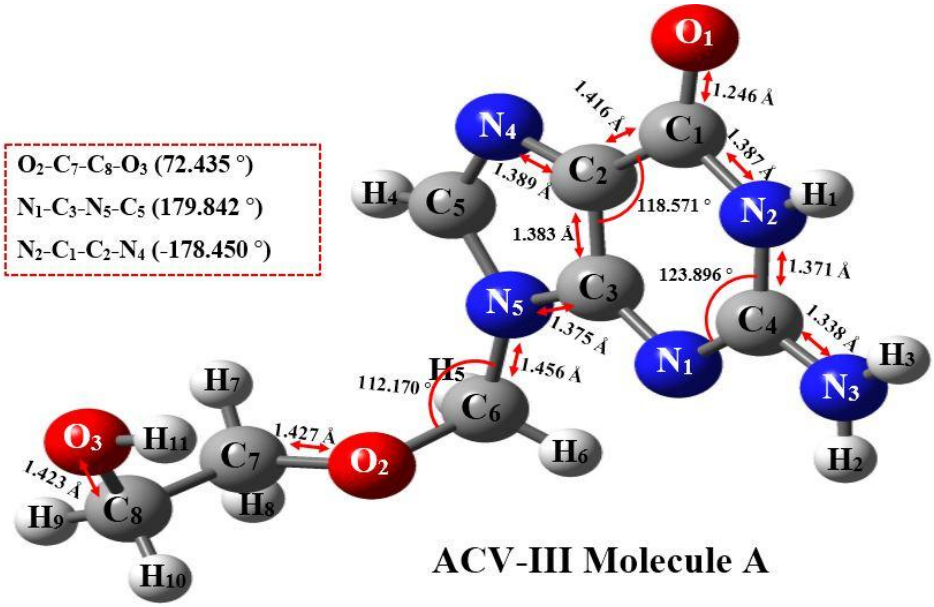

Figure 4.15 (a): Parts of the geometry parameters (i.e. bond distances, bond angles, and dihedral angles) of ACV-III Molecule A.

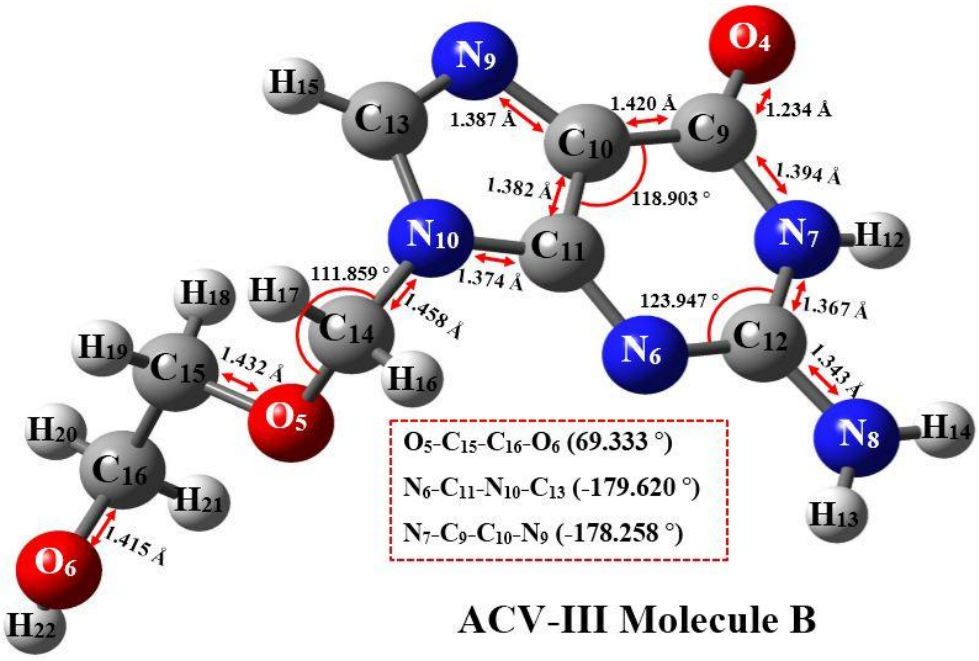

Figure 4.15 (b): Parts of the geometry parameters (i.e. bond distances, bond angles, and dihedral angles) of ACV-III Molecule B.

Table 4.14 (a) and (b) show the experimental and optimized geometry parameters (i.e. bond distances, bond angles, and dihedral angles) of the ACV-III single molecular system. From the tables, there have slight changes in the geometry structure of the ACV-III molecular system after the geometry optimization calculation process. As recorded in Table 4.14 (a), it is noted that bond distance C_1-N_2, bond angle O_1-C_1-C_2, and dihedral angle N_1-C_3-N_5-C_6 in ACV Molecule A explicit highest percentage differences between experimental and computational data. For DFT/B3LYP/6-31G** method, the largest percentage differences in bond distance C_1-N_2, bond angle O_1-C_1-C_2, and dihedral angle N_1-C_3-N_5-C_6 are calculated to be 3.686%, 2.812%, and 0.867%, whereas for DFT/B3LYP/6-311G** method are found to be 3.765%, 2.812%, and 0.674%. Besides, Table 4.14 (b) clearly indicates that the largest deviations

between experimental and optimized geometry structure of ACV Molecule B are located on bond distance C_9-N_7, bond angle O_4-C_9-C_{10}, and dihedral angle N_6-C_{11}-N_{10}-C_{14}. For DFT/B3LYP/6-31G** method, the highest percentage differences in bond distance C_9-N_7, bond angle O_4-C_9-C_{10}, and dihedral angle N_6-C_{11}-N_{10}-C_{14} are calculated to be 3.657%, 3.939%, and 1.068%, respectively, while for DFT/B3LYP/6-311G** method are 3.754%, 5.958%, and 1.387%, respectively. The variations are due to the fact that experimental data is collected under the solid and bulk case, while the computational calculation is performed under the gases phase (Sundaraganesan *et al.*, 2007; Kalaiarasi and Manivarman, 2017). In overall, both of the DFT/B3LYP/6-31G** and DFT/B3LYP/6-311G** methods show good agreement with experimental data since the discrepancies between computed and experimental results are less than 5.958%. Again, confirm the usability of DFT/B3LYP/6-31G** and DFT/B3LYP/6-311G** computational methods in the geometry optimization study of ACV compounds (Kumar *et al.*, 2013).

Table 4.14 (a): Experimental and optimized geometry parameters of ACV Molecule A in ACV-III molecular system.

Molecule A	ACV-III		
	DFT/B3LYP/6-31G**	DFT/B3LYP/6-311G**	Experiment
Bond Distance (Å)			
O_1-C_1	1.219	1.213	1.246
C_1-N_2	1.438	1.439	1.387
N_2-C_4	1.376	1.374	1.371
N_1-C_3	1.355	1.353	1.348
C_3-C_2	1.395	1.393	1.383
C_4-N_3	1.358	1.357	1.338
C_2-N_4	1.383	1.382	1.389
C_3-N_5	1.378	1.376	1.375
N_5-C_6	1.451	1.451	1.456
C_6-O_2	1.407	1.407	1.402
O_2-C_7	1.428	1.430	1.427
C_7-C_8	1.519	1.516	1.492
C_8-O_3	1.417	1.418	1.423
Bond Angle (°)			
O_1-C_1-N_2	119.037	119.143	120.147
O_1-C_1-C_2	131.559	131.559	127.961
N_3-C_4-N_1	119.830	119.891	119.681
C_4-N_1-C_3	112.590	112.858	111.881
C_3-C_2-N_4	110.973	110.855	110.549
C_3-N_5-C_5	105.763	105.759	106.188
C_3-N_5-C_6	126.144	126.056	125.306
N_5-C_6-O_2	113.045	113.109	112.170
O_2-C_7-C_8	106.860	107.021	109.923
C_7-C_8-O_3	112.062	112.147	112.747
Dihedral Angle (°)			
O_1-C_1-C_2-C_3	177.545	177.545	177.545
O_1-C_1-N_2-C_4	-179.133	-179.139	-179.147
N_3-C_4-N_1-C_3	179.691	179.691	179.691
N_1-C_3-N_5-C_6	-1.047	-1.045	-1.038
N_5-C_6-O_2-C_7	101.564	101.564	101.564
O_2-C_7-C_8-O_3	72.435	72.435	72.435

Table 4.14 (b): Experimental and optimized geometry parameters of ACV Molecule B in ACV-III molecular system.

Molecule B	ACV-III		
	DFT/B3LYP/6-31G**	DFT/B3LYP/6-311G**	Experiment
Bond Distance (Å)			
O_4-C_9	1.217	1.210	1.234
C_9-N_7	1.445	1.447	1.394
N_7-C_{12}	1.368	1.365	1.367
N_6-C_{11}	1.360	1.357	1.351
C_{11}-C_{10}	1.397	1.395	1.382
C_{12}-N_8	1.368	1.367	1.343
C_{10}-N_9	1.382	1.380	1.387
C_{11}-N_{10}	1.376	1.374	1.374
N_{10}-C_{14}	1.459	1.459	1.458
C_{14}-O_5	1.397	1.396	1.406
O_5-C_{15}	1.424	1.425	1.432
C_{15}-C_{16}	1.513	1.510	1.496
C_{16}-O_6	1.422	1.423	1.415
Bond Angle (°)			
O_4-C_9-N_7	117.630	117.711	120.170
O_4-C_9-C_{10}	133.246	133.270	128.196
N_8-C_{12}-N_6	119.278	119.345	119.499
C_{12}-N_6-C_{11}	112.347	112.613	112.311
C_{11}-C_{10}-N_9	110.890	110.764	110.619
C_{11}-N_{10}-C_{13}	105.667	105.659	106.001
C_{11}-N_{10}-C_{14}	125.974	125.881	126.258
N_{10}-C_{14}-O_5	114.190	114.257	111.859
O_5-C_{15}-C_{16}	108.978	109.106	109.520
C_{15}-C_{16}-O_6	108.087	108.248	109.638
Dihedral Angle (°)			
O_4-C_9-C_{10}-C_{11}	177.264	177.264	177.264
O_4-C_9-N_7-C_{12}	-178.838	-178.842	-178.801
N_8-C_{12}-N_6-C_{11}	-178.347	-178.347	-178.347
N_6-C_{11}-N_{10}-C_{14}	-7.135	-7.112	-7.212
N_{10}-C_{14}-O_5-C_{15}	-73.034	-73.034	-73.034
O_5-C_{15}-C_{16}-O_6	69.333	69.333	69.333

4.3.2 Total Energies and Frontier Molecular Orbital (FMO) Energies

Table 4.15 tabulates the total energies, frontier molecular orbital (FMO) energies, and global descriptors of the ACV-III molecular system computed using DFT/B3LYP/6-31G** and DFT/B3LYP/6-311G** level of calculations. From the table, noticed that the optimized total energy of the ACV-III molecular system computed via DFT/B3LYP/6-31G** method is -52451.747 eV, whereas for DFT/B3LYP/6-311G** method is -52465.782 eV. The findings denoted that ACV-III molecular system is the most unstable hydrated ACV polymorphic form among ACV-I and ACV-II molecular system since it has larger computed total energies (Chavda *et al.*, 2016; Ali *et al.*, 2017; Chaturvedi *et al.*, 2018). Besides, the energy levels of HOMO and LUMO obtained from DFT/B3LYP/6-31G** method are -5.379 eV and -0.834 eV, respectively, while for DFT/B3LYP/6-311G** method are -5.611 eV and -1.562 eV. Noticed that the energetic behaviours of HOMO and LUMO show useful applications in the determination of global reactivity descriptors of the ACV-III molecular system. Based on the equations stated in Koopmans theorem, the calculated ionization energy (IE), electron affinity (EA), hardness (η), chemical potential (μ), softness (S), electronegativity (χ), and electrophilicity index (ω) of ACV-III molecule obtained through DFT/B3LYP/6-31G** method are 5.379 eV, 0.834 eV, 2.273, -3.107, 0.220, 3.107, and 2.124, respectively. For DFT/B3LYP/6-311G** method, the IE, EA, η, μ, S, χ, and ω as recorded in Table 4.15 are found to be 5.611 eV, 1.562 eV, 2.025, -3.587, 0.247, 3.587, and 3.178, respectively. Furthermore, with HOMO-LUMO energy gaps of 4.049 eV to 4.545 eV, ACV-III molecular system is more polarized, high chemical reactivity, low

kinetic stability, and softer than ACV-I and ACV-II molecular system. Figure 4.16 (a) and (b) illustrate the HOMO and LUMO 3D surface mapped plots of ACV-III molecular system using DFT/B3LYP/6-31G** and DFT/B3LYP/6-311G** level of theories. Both of the computational methods (i.e. 6-31G** and 6-311G** basis sets) show identical HOMO surface mapped plots but slightly different in the polarity of LUMO surface mapped plots. As can be observed in Figure 4.16 (a) and (b), the electron density distributions for HOMO are mainly localised on the guanine moiety of ACV Molecule A. For LUMO, majority of electron densities are distributed on the water molecules. The findings indicate that the electronic transition of HOMO→ LUMO in the ACV-III molecular system implies an electron density transfer from the guanine rings of Molecule A to the water molecules (Targema *et al.*, 2013; Sachdeva *et al.*, 2018). Moreover, according to the molecular coefficients analysis, it is figured out that the HOMO and LUMO orbitals of the ACV-III molecular system are mainly composed from p_y type orbitals. Hence, suggested the $\pi \rightarrow \pi^*$ type of electronic transition in ACV-III molecule.

Table 4.15: Total energies, HOMO energies, LUMO energies, and HOMO-LUMO energy gaps of ACV-III molecular system.

	ACV-III	
	DFT/B3LYP/6-31G**	DFT/B3LYP/6-311G**
Total Energy (eV)	-52451.747	-52465.782
HOMO (eV)	-5.379	-5.611
LUMO (eV)	-0.834	-1.562
HOMO-LUMO Energy Gap (eV)	4.545	4.049
Ionization Energy (IE) [eV]	5.379	5.611
Electron Affinity (EA) [eV]	0.834	1.562
Hardness (η)	2.273	2.025
Chemical Potential (μ)	-3.107	-3.587
Softness (S)	0.220	0.247
Electronegativity (χ)	3.107	3.587
Electrophilicity index (ω)	2.124	3.178

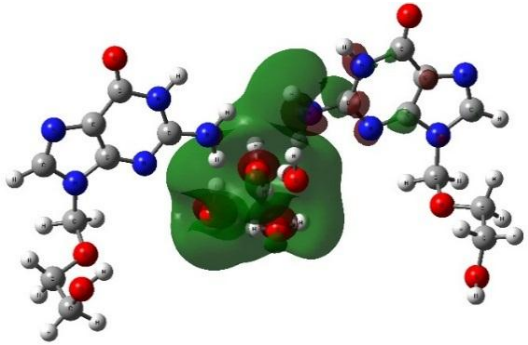

LUMO (−0.834 eV)

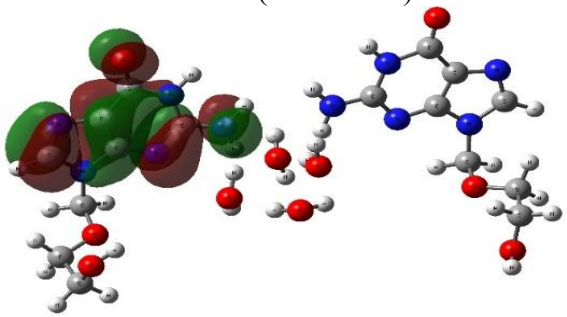

HOMO (-5.379 eV)

Figure 4.16 (a): LUMO and HOMO surface mapped plots of ACV-III molecular system using DFT/B3LYP/6-31G** method.

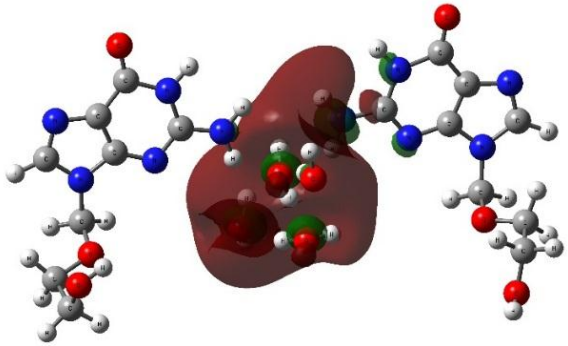

LUMO (−1.562 eV)

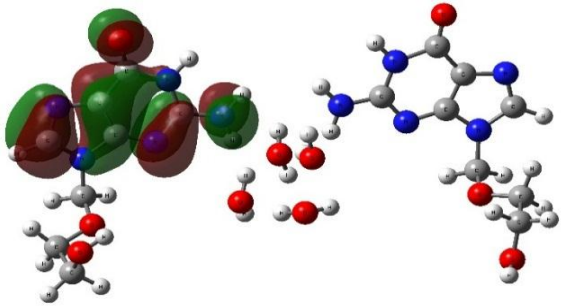

HOMO (-5.611 eV)

Figure 4.16 (b): LUMO and HOMO surface mapped plots of ACV-III molecular system using DFT/B3LYP/6-311G** method.

4.3.3 Mulliken Population Analysis (MPA)

Table 4.16 and Figure 4.17 represent the computed Mulliken atomic charge distributions of the ACV-III molecular system obtained through DFT/B3LYP/6-31G** and DFT/B3LYP/6-311G** level of calculations. Based on the computational data, the highest Mulliken atomic charge in the ACV-III molecule is located on atom C_{12} with values of 0.758 (6-31G**) and 0.603 (6-311G**). This is because carbon atom C_{12} undergoes rigorous electron withdrawing activity from the three electronegative nitrogen atoms N_1, N_2, and N_3 (Sachdeva *et al.*, 2018; Lakshmi *et al.*, 2019). With charge readings of -0.684 (6-31G**) and -0.504 (6-311G**), nitrogen atom N_3 from the amine group is assigned to be the largest negative Mulliken atomic charge in the ACV-III molecular system. From the MPA analysis, it is observed that hydrogen atom H_2 from the amine group is more electron deficient than atom H_3. Atom H_2 has positive atomic charges of 0.324 (6-31G**) and 0.255 (6-311G**) while atom H_3 shows charge readings of 0.254 (6-31G**) and 0.204 (6-311G**). This rigorous loss of electrons in atom H_2 may be caused by the formation of the hydrogen bond with water molecules (D, 2012). The higher negative Mulliken atomic charges in atoms O_1 and O_4 accompany with larger positive Mulliken atomic charges in atoms C_1 and C_9 explained the C=O double bond feature in the ACV-III molecular system (Lakshmi *et al.*, 2019). As a result, high electronegative atoms O_1 and O_4 tend to pull atoms C_1 and C_9 toward themselves and so do for atoms N_3 and N_8 on atoms C_4 and C_{12} (D, 2012). Hence, leading to the distortion of bond angles in the pyrimidine rings of the ACV-III molecular system. According to Alvarez-Ros and Palafox (2014), the study of atomic charges on atoms N_4 and

N_9 in ACV molecules is potent because they are strongly related to the performance of anti-tumour platinum drugs. Basically, the platinum atom prefers the sites at nitrogen atoms N_4 and N_9 rather than other oxygen atoms in ACV molecules. Besides, they are also the most open positions to attack in DNA. In Table 4.16, noticed that the computed Mulliken atomic charges for N_4 and N_9 using DFT/B3LYP/6-31G** method are -0.491 and -0.487, respectively, while for DFT/B3LYP/6-311G** technique are -0.298 and -0.294, respectively. Furthermore, there is also a point of interest to identify the atomic charges of atoms N_2 and N_7 in ACV molecules. Both of them act as the formal metal binding sites when dealing with the deprotonation of weak acid ACV. The calculated Mulliken atomic charges of N_2 and N_7 in the ACV-III molecular system obtain via DFT/B3LYP/6-31G** method are found to be -0.623 and -0.621, respectively, whereas for DFT/B3LYP/6-311G** technique are -0.493 and -0.491, respectively. Moreover, as can be observed in Table 4.16 and Figure 4.17, larger negative Mulliken atomic charges in O_3, O_6, O_7, O_8, O_9, O_{10}, N_3, and N_8 together with higher positive Mulliken atomic charges in H_1, H_2, H_3, H_{11}, H_{12}, H_{13}, H_{14}, H_{22}, H_{23}, H_{24}, H_{25}, H_{26}, H_{27}, H_{28}, H_{29}, and H_{30} suggest the presence of intra and intermolecular hydrogen bonding interaction in ACV-III molecular system (Jasmine *et al.*, 2015).

Table 4.16: Computed Mulliken atomic charges analysis (MPA) of ACV-III molecular system using DFT/B3LYP/6-31G** and DFT/B3LYP/6-311G** methods.

ACV-III					
MPA					
Atoms	DFT/B3LYP/6-31G**	DFT/B3LYP/6-311G**	Atoms	DFT/B3LYP/6-31G**	DFT/B3LYP/6-311G**
O_1	-0.510	-0.340	N_7	-0.621	-0.491
C_1	0.562	0.415	H_{12}	0.268	0.227
C_2	0.123	-0.132	N_8	-0.673	-0.503
C_3	0.518	0.373	H_{13}	0.269	0.211
N_1	-0.594	-0.419	H_{14}	0.272	0.226
C_4	0.746	0.588	N_9	-0.487	-0.294
N_2	-0.623	-0.493	C_{13}	0.263	0.156
H_1	0.263	0.222	N_{10}	-0.520	-0.414
N_3	-0.684	-0.504	H_{15}	0.120	0.116
H_2	0.324	0.255	C_{14}	0.187	0.137
H_3	0.254	0.204	H_{16}	0.101	0.107
N_4	-0.491	-0.298	H_{17}	0.134	0.131
C_5	0.268	0.165	O_5	-0.460	-0.347
N_5	-0.514	-0.406	C_{15}	0.053	-0.032
H_4	0.112	0.109	H_{18}	0.102	0.112
C_6	0.185	0.140	H_{19}	0.102	0.101
H_5	0.100	0.104	C_{16}	0.040	-0.009
H_6	0.140	0.133	H_{20}	0.089	0.094
O_2	-0.482	-0.374	H_{21}	0.106	0.107
C_7	0.047	-0.027	O_6	-0.534	-0.401
H_7	0.084	0.093	H_{22}	0.311	0.242
H_8	0.102	0.100	O_7	-0.648	-0.493
C_8	0.040	-0.021	H_{23}	0.320	0.245
H_9	0.108	0.108	H_{24}	0.282	0.216
H_{10}	0.102	0.106	O_8	-0.582	-0.465
O_3	-0.535	-0.397	H_{25}	0.320	0.256
H_{11}	0.318	0.246	H_{26}	0.334	0.275
O_4	-0.500	-0.330	O_9	-0.633	-0.507
C_9	0.563	0.420	H_{27}	0.314	0.256
C_{10}	0.131	-0.122	H_{28}	0.341	0.278
C_{11}	0.521	0.375	O_{10}	-0.641	-0.512
N_6	-0.603	-0.432	H_{29}	0.348	0.293
C_{12}	0.758	0.603	H_{30}	0.287	0.221

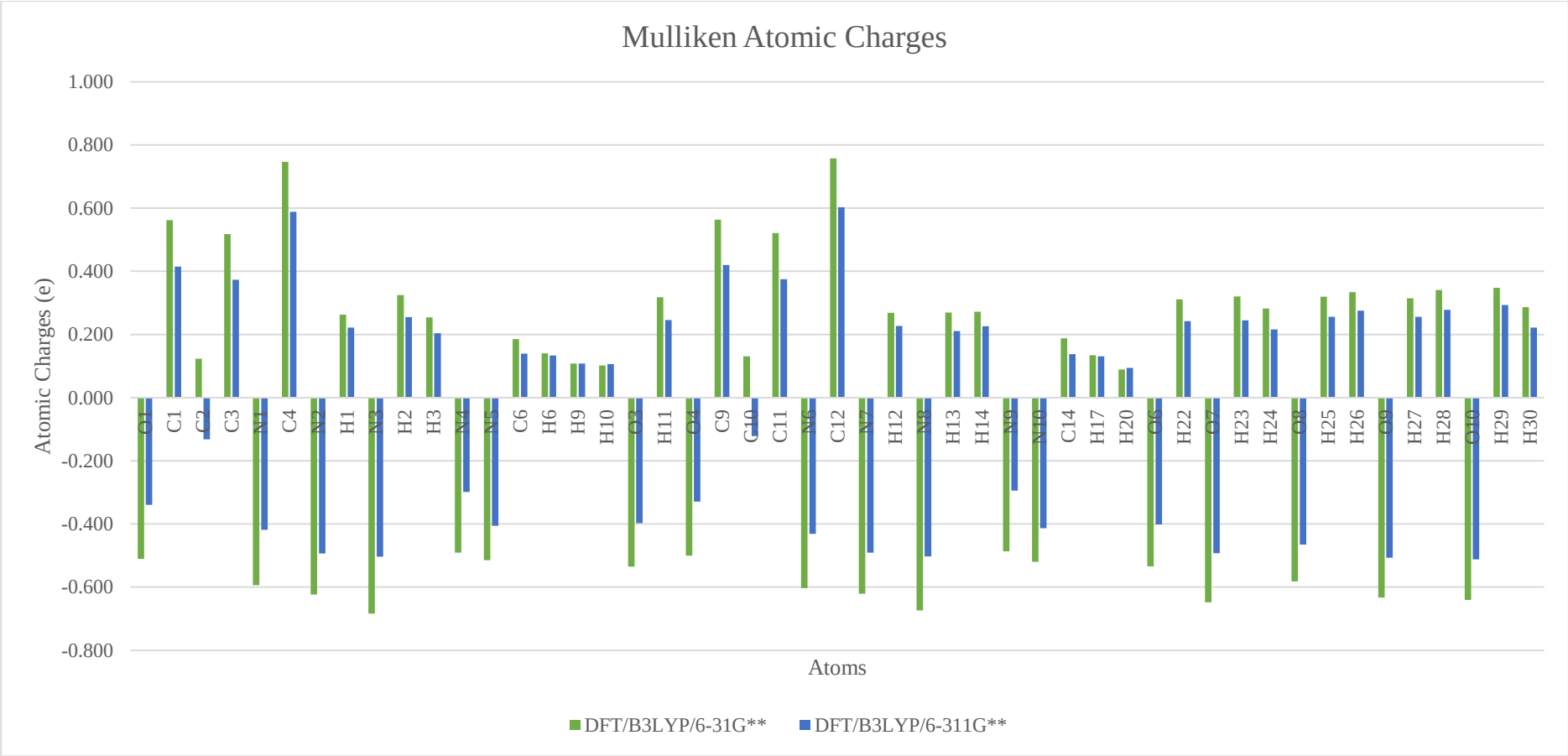

Figure 4.17: MPA analysis of ACV-III molecular system using DFT/B3LYP/6-31G** and DFT/B3LYP/6-311G** methods.

4.3.4 Molecular Electrostatic Potential (MEP)

Figure 4.18 (a) and (b) show the 3D molecular electrostatic potential (MEP) surface mapped plots of ACV-III molecular system calculated using DFT/B3LYP/6-31G** and DFT/B3LYP/6-311G** level of theories. Based on the figures, both of the computational methods (i.e. 6-31G** and 6-311G** basis sets) show identical MEP mapping results for the ACV-III molecular system. Noticed that regions located around atoms O_1, O_3, O_4, O_7, N_4, and N_9 show negative electrostatic potentials (yellowish red colour mapping), suggested the sites for electrophilic attacks in ACV-III molecule. Conversely, areas situated around atoms H_3, H_{13}, H_{14}, H_{25}, H_{26}, H_{29}, and H_{30} elucidate positive electrostatic potentials (blues colour mapping), proposed the sites for nucleophilic reactions. All of these sites provide informative data about the possible regions where the intra and intermolecular reactions may take place in the ACV-III molecular system. It is worth to mention that only the ACV-III molecule itself explicit high positive electrostatic potential regions (deep blue mapping) in water molecules as compared with ACV-I and ACV-II molecular system. Besides, by using the Multifwn software package, the global surface extrema points (i.e. minimum and maximum) of the ACV-III molecular system are successfully obtained and plotted in Figure 4.18 (a) and (b). The red dot represents the maximum point while the blue dot represents the minimum point. From the diagrams, it is figured out that the global surface maximum points for both DFT/B3LYP/6-31G** and DFT/B3LYP/6-311G** methods are located around hydrogen atom H_{25} with values of 3.585 eV and 3.514 eV. On the other hands, the global surface minimum points of the ACV-III molecular system are found to be situated around

oxygen atom O_1 with values of -2.394 eV and -2.349 eV, respectively for DFT/B3LYP/6-31G** and DFT/B3LYP/6-311G** level of theories.

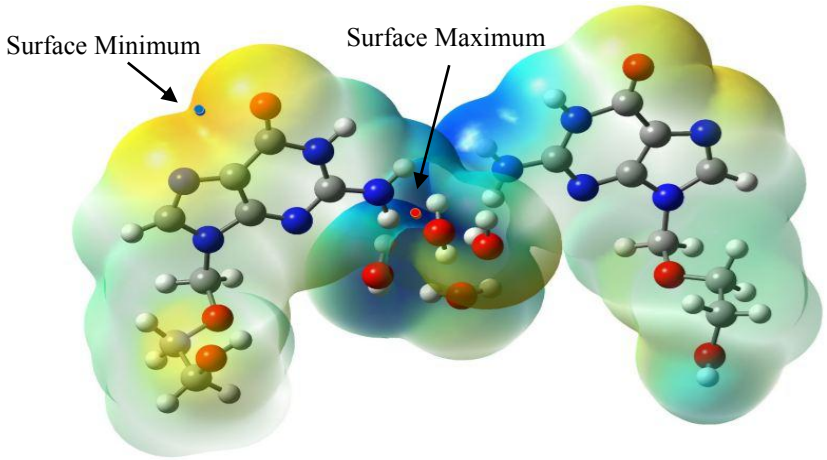

Surface Minimum (blue dot) - -2.394 eV
Surface Maximum (red dot) – 3.585 eV

Figure 4.18 (a): The MEP surface mapped plots of ACV-III molecular system using DFT/B3LYP/6-31G** method.

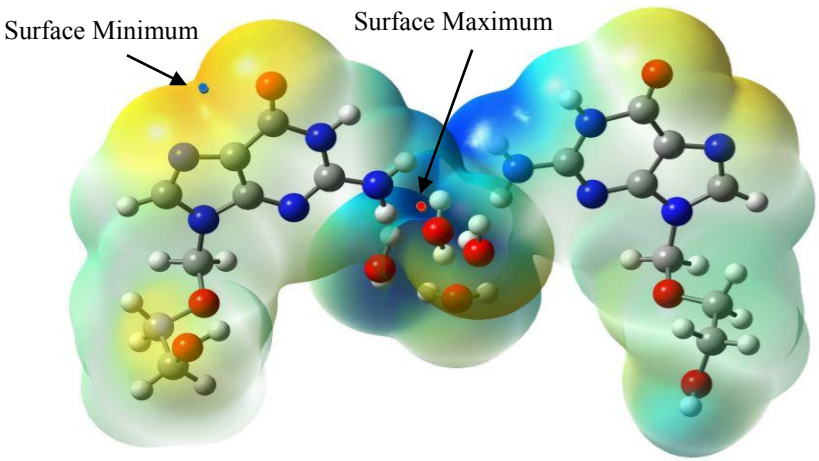

Surface Minimum (blue dot) - -2.349 eV
Surface Maximum (red dot) – 3.514 eV

Figure 4.18 (b): The MEP surface mapped plots of ACV-III molecular system using DFT/B3LYP/6-311G** method.

4.3.5 Non-Linear Optical (NLO) Properties

In order to identify the NLO behaviour of the ACV-III molecular system, theoretical investigation based on dipole moment (μ) and first hyperpolarizability (β_{tot}) parameters are carried out using Gaussian 09 software package with the employment of DFT/B3LYP/6-31G** and DFT/B3LYP/6-311G** level of theories. As can be observed in Table 4.17, the calculated dipole moments obtained via DFT/B3LYP/6-31G** method is 13.803 Debye, while for DFT/B3LYP/6-311G** method is 13.626 Debye. Besides, the computed first hyperpolarizabilities of the ACV-III molecular system show magnitudes of 5.756 x 10^{-29} e.s.u and 5.840 x 10^{-29} e.s.u, respectively for DFT/B3LYP/6-31G** and DFT/B3LYP/6-311G** methods. From the NLO analysis, ACV-III molecular system has approximately 10.053 and 154.316 times larger than urea in terms of dipole moment and first hyperpolarizability values. Therefore, the ACV-III molecular system can be regarded as a potential candidate for active NLO materials. As compared among the three different hydrated ACV molecules in this research study, the NLO behaviours increased in the sequences of ACV-I < ACV-III < ACV-II molecular system.

Table 4.17: Computed dipole moment (μ) and first hyperpolarizability (β_{tot}) of ACV-III molecular system using DFT/B3LYP/6-31G** and DFT/B3LYP/6-311G** methods.

Parameters	DFT/B3LYP/6-31G**	DFT/B3LYP/6-311G**
μ_x	-2.432	-2.414
μ_y	8.347	8.152
μ_z	10.720	10.648
μ [Debye]	13.803	13.626
β_{xxx}	3677.725	3692.490
β_{xyy}	860.101	875.983
β_{xzz}	420.858	443.545
β_{yyy}	-481.075	-492.373
β_{xxy}	-445.763	-455.119
β_{yzz}	326.208	314.608
β_{zzz}	-2792.999	-2860.128
β_{xxz}	-661.207	-656.729
β_{yyz}	-955.098	-975.765
β_{tot} [a.u]	6662.677	6760.512
β_{tot} [e.s.u]	5.756×10^{-29}	5.840×10^{-29}

4.3.6 Fourier Transform Infrared (FT-IR) Spectroscopy

Table 4.18 tabulates parts of the theoretical FT-IR vibrational frequencies of the ACV-III molecular system computed via DFT/B3LYP/6-31G** and DFT/B3LYP/6-311G** level of calculations. Different from ACV-I and ACV-II molecules, the ACV-III molecular system with a total atomic number of 66, has 192 fundamental vibrational modes that quantitatively explicit the functional groups presented in the system. Initially, it is observed that all the FT-IR vibrational spectrums (unscaled) in ACV-III molecular system obtained via DFT/B3LYP/6-31G** and DFT/B3LYP/6-311G** methods show higher results

than literature data (*Infrared Spectroscopy Table*, 2001; Bakkiyaraj, 2017; Susithra *et al.*, 2018; Demircioğlu *et al.*, 2019; Priya *et al.*, 2019; Vidhya *et al.*, 2019; LibreTexts, 2020). This is due to the fact that computational calculation in FT-IR always ignores the anharmonicity of the real case system (Ali *et al.*, 2017; Ahmad *et al.*, 2018). To overcome this problem, scale factors of 0.961 (6-31G**) and 0.967 (6-311G**) are employed to shift the overall computed FT-IR results to become more consistent with the literature values. As a result, all the scaled computational FT-IR vibrational spectrums obtained from DFT/B3LYP/6-31G** and DFT/B3LYP/6-311G** methods show satisfactory agreement with the geometry structure of the ACV-III molecular system. Hence, enhance the reliability of the computational data. For example, the O-H stretching vibrational modes from water molecules can be observed at band regions 3506 cm^{-1} to 3553 cm^{-1} (scaled 6-31G**) and 3516 cm^{-1} to 3589 cm^{-1} (scaled 6-311G**). Besides, band regions 3462 cm^{-1} (scaled 6-31G**) and 3471 cm^{-1} (scaled 6-311G**) show N-H stretching vibration behaviours of primary and secondary amides in the ACV-III molecular system. Based on the computational data, band regions 3033 cm^{-1} (scaled 6-31G**) and 3039 cm^{-1} (scaled 6-311G**) are assigned to the stretching vibrational modes of aromatic C-H while band regions 2867 cm^{-1} (scaled 6-31G**) and 2886 cm^{-1} (scaled 6-311G**) are correspondence to the C-H stretching vibrational modes from the side chains of ACV molecules. Conversely, it is figured out that the aromatic C-H bending vibrational modes from the guanine rings of ACV molecules appeared at frequencies 1401 cm^{-1} (scaled 6-31G** and 6-311G**) whereas the bending vibration behaviours of side chains C-H are located at band regions 778 cm^{-1} to 819 cm^{-1} (scaled 6-31G**) and 768 cm^{-1} to 823 cm^{-1} (scaled 6-311G**). Furthermore, the stretching

vibrational assignments for aromatic C=C in ACV-III molecular system are found to be situated between regions 1468 cm^{-1} to 1533 cm^{-1} (scaled 6-31G**) and 1466 cm^{-1} to 1536 cm^{-1} (scaled 6-311G**). In Table 4.18, it is noted that band regions 1321 cm^{-1} to 1334 cm^{-1} (scaled 6-31G**) and 1321 cm^{-1} to 1337 cm^{-1} (scaled 6-311G**) elucidate aromatic C-N stretching vibrational characteristics. Moreover, the C=O stretching vibrational modes from the pyrimidine rings of ACV-III molecule can be observed via band regions 1755 cm^{-1} (scaled 6-31G**) and 1748 cm^{-1} (scaled 6-311G**). In additions, the C-O stretching vibrational modes from the side chains of ACV molecules are located between band regions 1016 cm^{-1} to 1209 cm^{-1} (scaled 6-31G**) and 1016 cm^{-1} to 1211 cm^{-1} (scaled 6-311G**).

Table 4.18: Experimental and computational (unscaled and scaled) FT-IR vibrational frequencies of ACV-III molecular system.

	DFT/B3LYP/6-31G**		DFT/B3LYP/6-311G**	
	Unscaled [cm^{-1}]	Scaled [cm^{-1}]	Unscaled [cm^{-1}]	Scaled [cm^{-1}]
O-H stretching vibration	3697	3553	3711	3589
O-H stretching vibration	3648	3506	3636	3516
N-H stretching vibration	3603	3462	3589	3471
H-C-H stretching vibration	3156	3033	3143	3039
H-C-H stretching vibration	2984	2867	2985	2886
C=O stretching vibration	1826	1755	1807	1748
C=C stretching vibration	1595	1533	1589	1536
C=C stretching vibration	1528	1468	1516	1466
H-C-H bending vibration	1458	1401	1449	1401
C-N stretching vibration	1388	1334	1382	1337
C-N stretching vibration	1374	1321	1366	1321
C-O-C stretching vibration	1258	1209	1252	1211
C-O stretching vibration	1137	1093	1136	1099
C-O stretching vibration	1126	1082	1125	1088
C-O stretching vibration	1072	1030	1067	1032
C-O stretching vibration	1057	1016	1050	1016
C-H bending vibration	853	819	851	823
C-H bending vibration	819	787	822	795
C-H bending vibration	810	778	794	768

4.3.7 Rotational Barrier Analysis

The rotational barrier studies in ACV Molecule A and B are carried out theoretically using the Potential Energy Surface (PES) scanning method at DFT/B3LYP/6-31G** and DFT/B3LYP/6-311G** level of theories. During the PES scanning calculations, dihedral angles N_5-C_6-O_2-C_7 (Molecule A) and N_{10}-C_{14}-O_5-C_{15} (Molecule B) are rotated from 0° to 360° with interval steps of 10°. All the changes in relative energies, optimized total energies, and C-O bond distances upon PES rotational calculations are obtained. Figure 4.19 (a) and (b) show the PES profiles of ACV Molecule A and B plotted from the changes in

relative energies corresponding with angles of rotation. Noticed that both DFT/B3LYP/6-31G** and DFT/B3LYP/6-311G** computational methods show satisfactory agreement in the PES plots of ACV Molecule A and B. As can be observed in Figure 4.19 (a), ACV Molecule A show the most stable conformer (i.e. conformer-AI) state at the rotational angle of 180° (global minimum point), while the maximum unstable conformer (i.e. conformer-AII) form is observed at the rotational angle of 260 ° (global maximum point). According to the computational results, conformer AI shows zero relative energies, lowest optimized total energies of -22066.460 eV (6-31G**)/-22071.934 eV (6-311G**), and shortest C_6-O_2 bond distances of 1.405 Å (6-31G**)/1.404 Å (6-311G**). For conformer-AII, it has largest relative energies of 0.260 eV (6-31G**)/ 0.251 eV (6-311G**), highest optimized total energies of -22066.199 eV (6-31G**)/-22071.683 eV (6-311G**), and farthest C_6-O_2 bond distances of 1.436 Å (6-31G**)/1.437 Å (6-311G**). Besides, the PES curves plotted in Figure 4.19 (a) clearly noted that ACV Molecule A poses three possible conformers (i.e. conformer-AIII, conformer-AIV, and conformer-AV) at rotational angles of 0°, 80°, and 330° (local minimum points). Noticed that conformer-AIII has relative energies of 0.075 eV (6-31G**)/0.069 eV (6-311G**), C_6-O_2 bond distances of 1.407 Å (6-31G** and 6-311G**), and optimized total energies of -22066.385 eV (6-31G**)/-22071.865 eV (6-311G**), while conformer-AIV shows relative energies of 0.076 eV (6-31G**)/0.069 eV (6-311G**), C_6-O_2 bond distances of 1.407 Å (6-31G** and 6-311G**), and optimized total energies of -22066.383 eV (6-31G**)/ -22071.865 eV (6-311G**). For conformer-AV, the computational data reveals that it explicit relative energies of 0.028 eV (6-31G**)/0.026 eV (6-311G**),

C_6-O_2 bond distances of 1.405 Å (6-31G**)/1.404 Å (6-311G**), and optimized total energies of -22066.432 eV (6-31G**)/-22071.908 eV (6-311G**). Furthermore, based on the PES curves illustrated in Figure 4.19 (b), it is figured out that ACV Molecule B has two possible conformers (i.e. conformer-BI and conformer-BII) at rotational angles of 170° and 250°. Noted that the computed relative energies, optimized total energies, and C_{14}-O_5 bond distances for conformer-BI are found to be 0.065 eV (6-31G**)/0.064 eV (6-311G**), -22066.283 eV (6-31G**)/-22071.754 eV (6-311G**), and 1.403 Å (6-31G**)/1.402 Å (6-311G**), whereas for conformer-BII are 0.126 eV (6-31G**)/0.119 eV (6-311G**), -22066.222 eV (6-31G**)/-22071.699 eV (6-311G**), and 1.403 Å (6-31G** and 6-311G**). Moreover, with largest relative energies of 0.297 eV (6-31G**)/0.291 eV (6-311G**), highest optimized total energies of -22066.051 eV (6-31G**)/-22071.527 eV (6-311G**), and longest C_{14}-O_5 bond distances of 1.434 Å (6-31G** and 6-311G**), ACV Molecule B show maximum unstable conformer (i.e. conformer-BIII) state at rotational angle of 80°. Both of the rotational barrier studies in ACV Molecule A and B denoted that the increment in C-O bond distances (i.e. C_6-O_2 and C_{14}-O_5) will lead to higher relative energies in the system. Consequently, the rotational motion in the N-C-O-C dihedral angle will become harder and restricted.

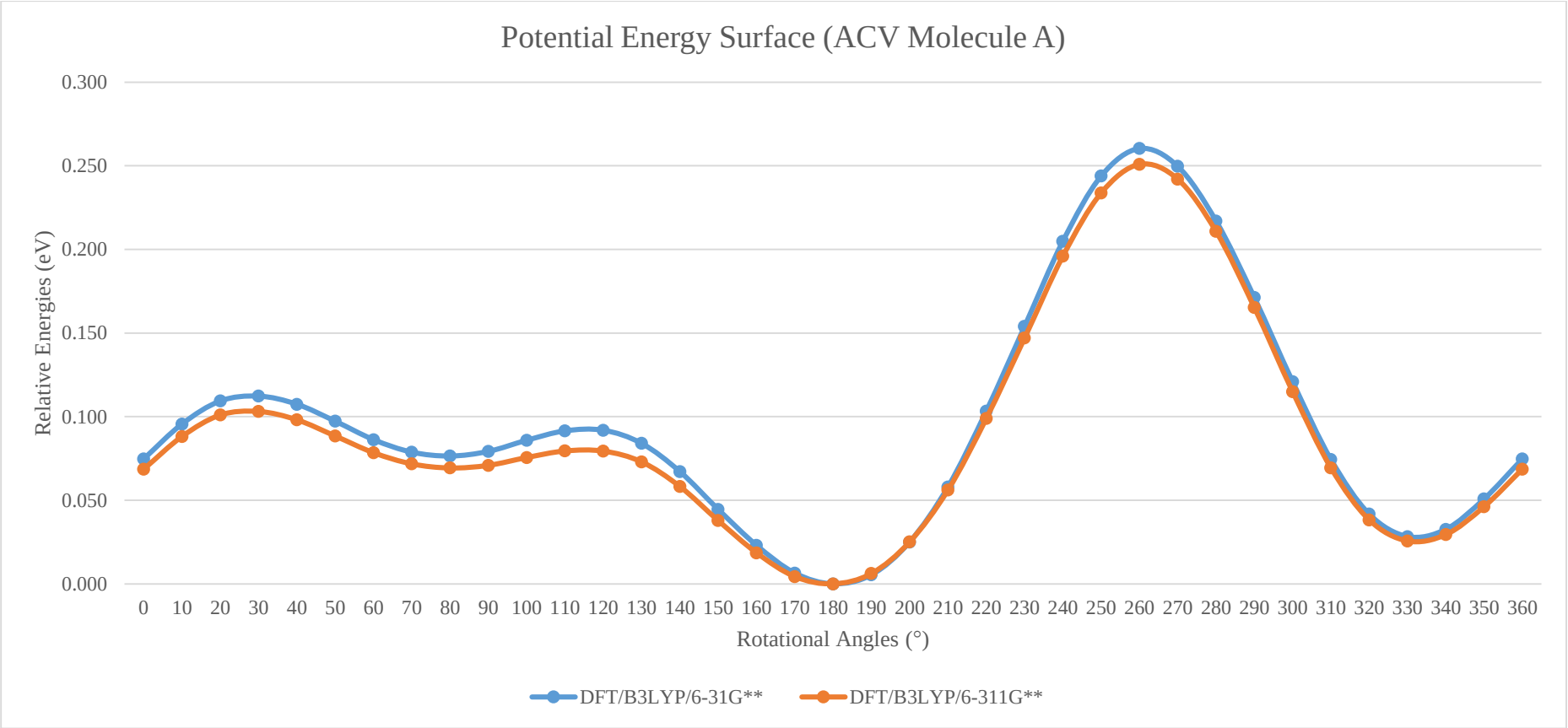

Figure 4.19 (a): Potential Energy Surface of ACV-III Molecule A using DFT/B3LYP/6-31G** and DFT/B3LYP/6-311G** methods.

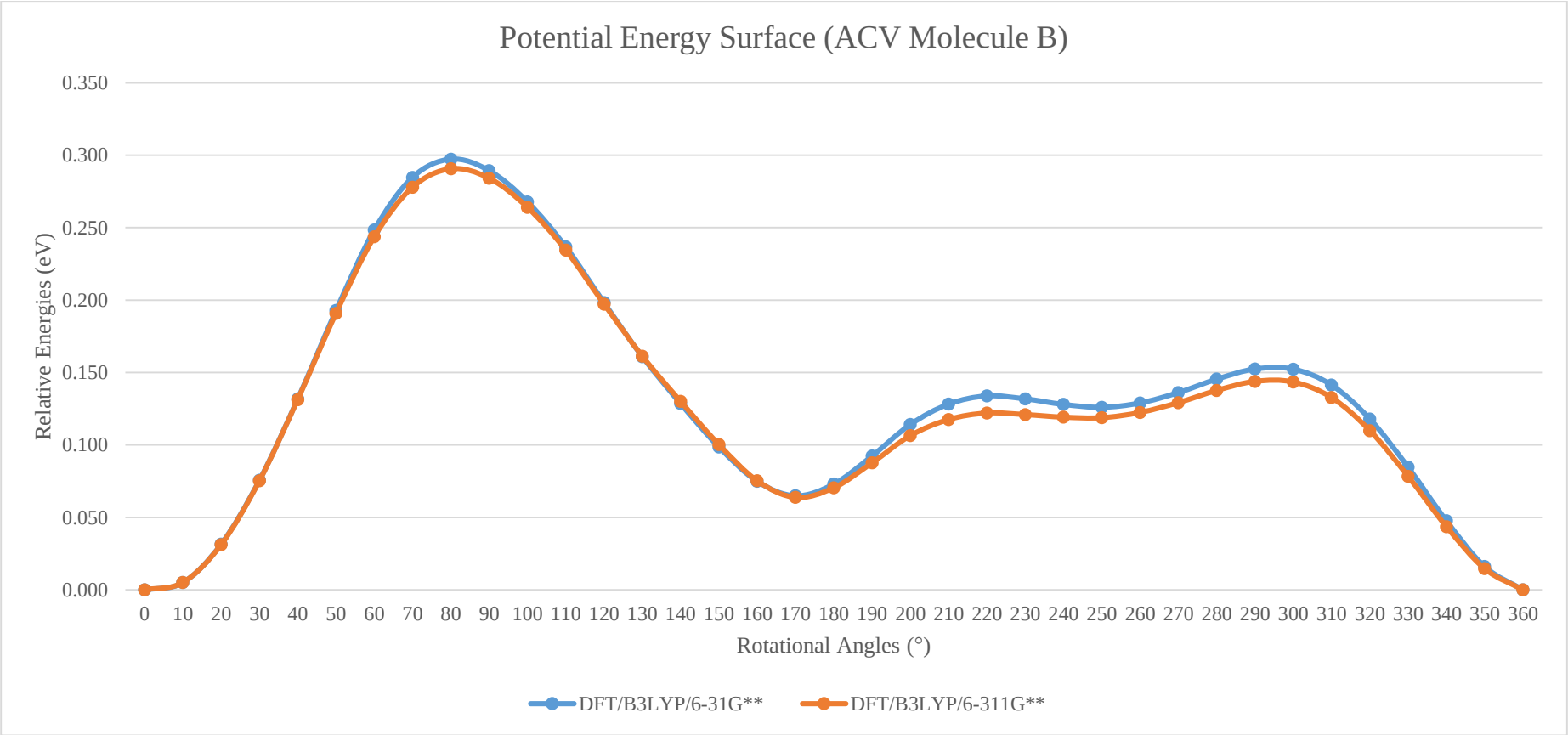

Figure 4.19 (b): Potential Energy Surface of ACV-III Molecule B using DFT/B3LYP/6-31G** and DFT/B3LYP/6-311G** methods.

Table 4.19 (a): Parts of the rotational barrier studies in ACV-III Molecule A using DFT/B3LYP/6-31G** and DFT/B3LYP/6-311G** methods.

0° **conformer AIII** 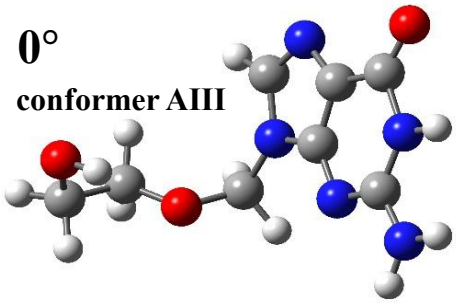	**30°** 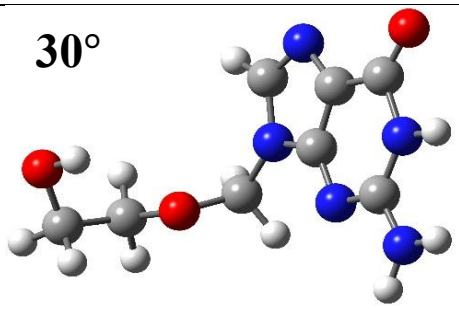
Relative Energy: 0.075 eV / 0.069 eV Optimized Total Energy: -22066.385 eV / -22071.865 eV C_6-O_2 Bond Distance: 1.407 Å / 1.407 Å	Relative Energy: 0.112 eV / 0.103 eV Optimized Total Energy: -22066.348 eV / -22071.831 eV C_6-O_2 Bond Distance: 1.411 Å / 1.411 Å
80° **conformer AIV** 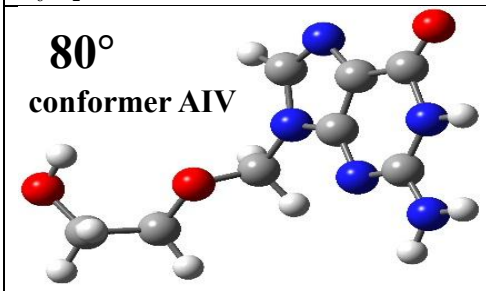	**120°** 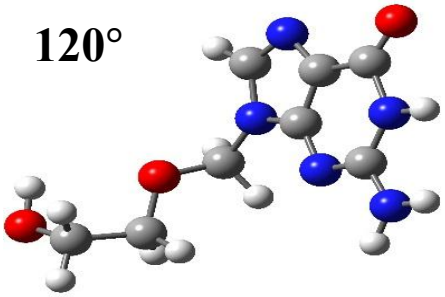
Relative Energy: 0.076 eV / 0.069 eV Optimized Total Energy: -22066.383 eV / -22071.865 eV C_6-O_2 Bond Distance: 1.407 Å / 1.407 Å	Relative Energy: 0.092 eV / 0.079 eV Optimized Total Energy: -22066.368 eV / -22071.855eV C_6-O_2 Bond Distance: 1.410 Å / 1.410 Å
180° **conformer AI** 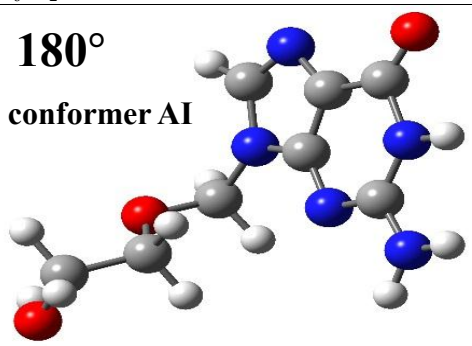	**260°** **conformer AII** 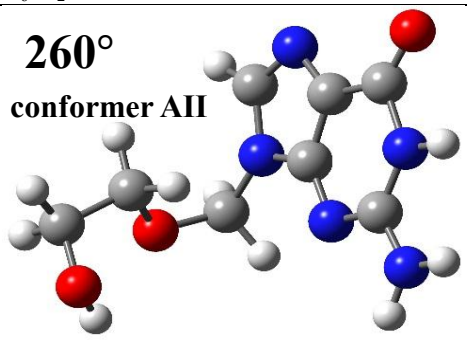
Relative Energy: 0.000 eV / 0.000 eV Optimized Total Energy: -22066.460 eV / -22071.934 eV C_6-O_2 Bond Distance: 1.405 Å / 1.404 Å	Relative Energy: 0.260 eV / 0.251 eV Optimized Total Energy: -22066.199 eV / -22071.683 eV C_6-O_2 Bond Distance: 1.436 Å / 1.437 Å
330° **conformer AV** 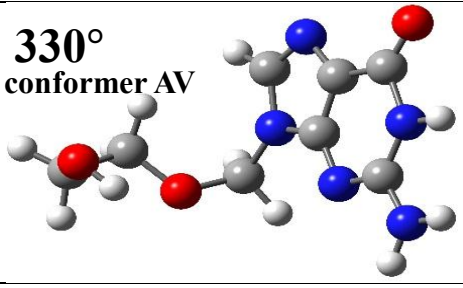	
Relative Energy: 0.028 eV / 0.026 eV Optimized Total Energy: -22066.432 eV / -22071.908 eV C_6-O_2 Bond Distance: 1.405 Å / 1.404 Å	

Table 4.19 (b): Parts of the rotational barrier studies in ACV-III Molecule B using DFT/B3LYP/6-31G** and DFT/B3LYP/6-311G** methods.

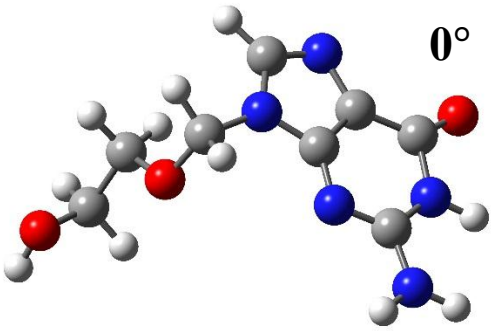 **0°**	**conformer BIII** **80°** 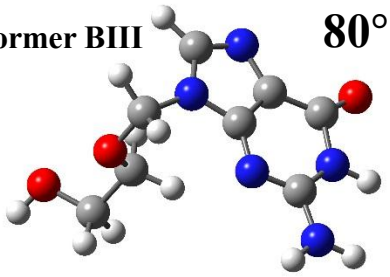
Relative Energy: 0.000 eV / 0.000 eV Optimized Total Energy: -22066.348 eV / -22071.818 eV C_{14}-O_5 Bond Distance: 1.398 Å / 1.397 Å	Relative Energy: 0.297 eV / 0.291 eV Optimized Total Energy: -22066.051 eV / -22071.527 eV C_{14}-O_5 Bond Distance: 1.434 Å / 1.434 Å
conformer BI **170°** 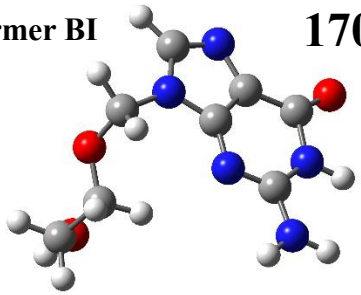	**220°** 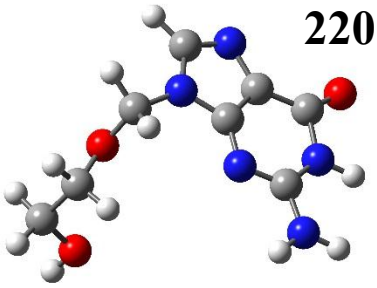
Relative Energy: 0.065 eV / 0.064 eV Optimized Total Energy: -22066.283 eV / -22071.754 eV C_{14}-O_5 Bond Distance: 1.403 Å / 1.402 Å	Relative Energy: 0.134 eV / 0.122 eV Optimized Total Energy: -22066.214 eV / -22071.696 eV C_{14}-O_5 Bond Distance: 1.406 Å / 1.405 Å
conformer BII **250°** 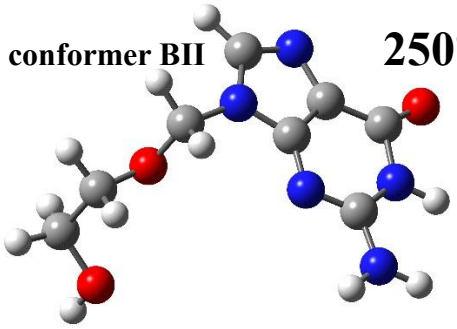	**290°** 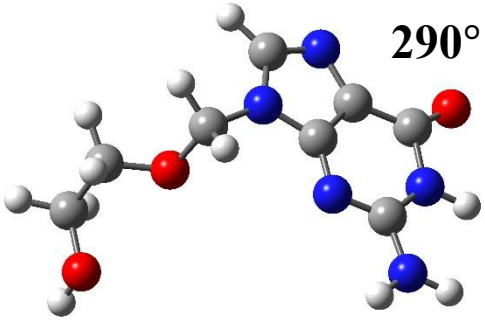
Relative Energy: 0.126 eV / 0.119 eV Optimized Total Energy: -22066.222 eV / -22071.699 eV C_{14}-O_5 Bond Distance: 1.403 Å / 1.403 Å	Relative Energy: 0.152 eV / 0.144 eV Optimized Total Energy: -22066.196 eV / -22071.674 eV C_{14}-O_5 Bond Distance: 1.407 Å / 1.406 Å

Polymorphism Organic Compound 2: Theophylline

Theophylline (TP) is categorised as active pharmaceutical ingredients (APIs) organic drug compound that tends to form polymorphism easily. It acts as a useful bronchodilator agent and has potent applications in the treatment of asthma and chronic obstructive pulmonary disease (COPD). Previous literature studies reveal that there are plenty of different polymorphic forms discovered by researchers. However, to the best of our knowledge, there is still limited information about the quantum computational studies on the electronic structures of the TP compound and its polymorphism. In this work, the geometry structures, electronic properties (i.e. FMOs, MEP, NBO and NLO), and vibrational frequencies of pure TP and TP monohydrate compounds are obtained using DFT/B3LYP/6-31G and DFT/B3LYP/6-31G** level of theories. Besides, the optimized geometry structures, computed HOMO-LUMO energy gaps, and calculated FT-IR spectrums are compared with experimental data (i.e. single crystal X-ray diffraction, UV-Vis spectroscopy, and FT-IR experiments) to validate the reliability of the computational results and confirm the usability of the computational methods on TP compounds. Furthermore, in order to figure out the effect of neighbouring molecules, the size effect study is included in this work.

4.4: Pure Theophylline Compound (TP-I) ($C_7H_8N_4O_2$)

From the single crystal X-ray diffraction experiment, the TP-I crystal sample is found to be crystallized in an orthorhombic space group of P_{na21} with lattice parameters of a = 24.493 Å, b = 3.8124 Å, c = 8.456 Å and α/ β/ γ = 90.000°. It is realized that TP-I is a pure theophylline compound ($C_7H_8N_4O_2$) without any other substitute inside its crystal structure as shown in Figure 4.20 (a). Figure 4.20 (b) shows the detailed labelling and numbering scheme for TP-I single molecular system. It acts as the main host environment in the DFT computational studies. Literature surveys based on the Cambridge Crystallographic Data Centre (CCDC) library found that the crystal structure of TP-I shows high similarity with the finding of Ebisuzaki *et al.* (1997), although both of the TP crystals are obtained using different crystallization methods. Preliminary tests show that the geometry and electronic properties between TP-I and Ebisuzaki *et al.* (1997) molecular system are closer to each other as listed in Table 4.20 (a) and (b). Therefore, the DFT computational studies on the geometry and electronic structures of the TP-I molecular system also means the re-investigation on the TP molecule obtained by Ebisuzaki *et al.* (1997). The crystallographic information file (CIF) of Ebisuzaki *et al.* (1997) can be obtained from the CCDC website with deposition number 128707 and database identifier of BAPLOT01.

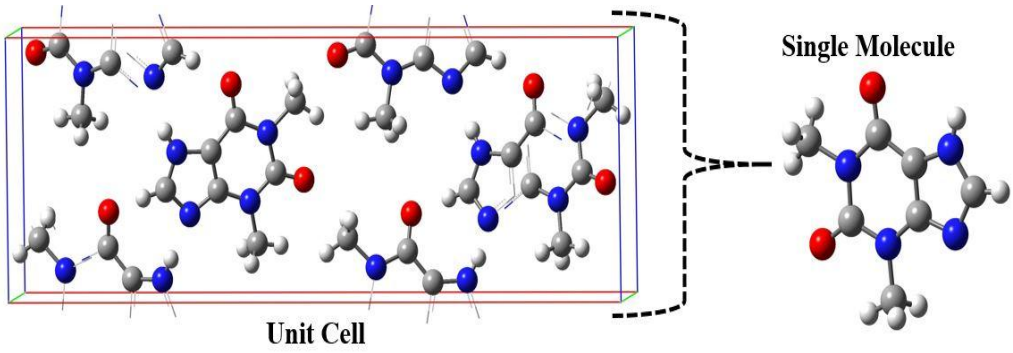

Figure 4.20 (a): The complete unit cell and single molecule for TP-I.

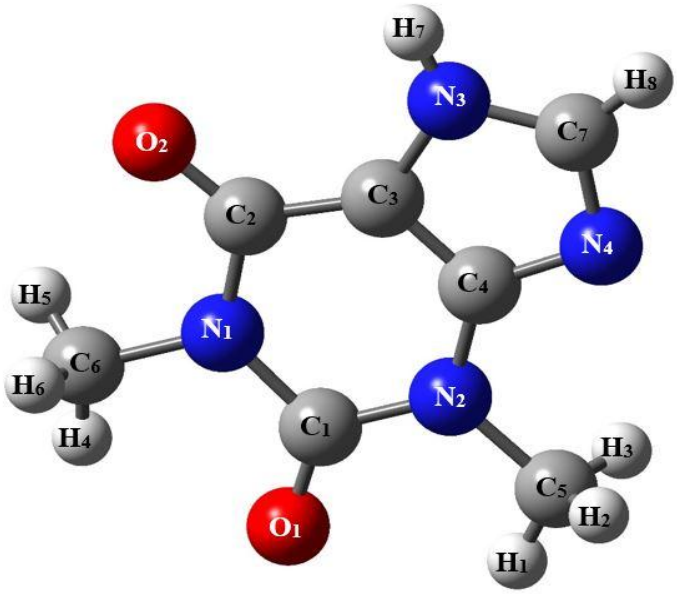

Figure 4.20 (b): Labelling and numbering details in TP-I single molecule.

Table 4.20 (a): Comparison between the experimental (single crystal X-ray diffraction) geometry parameters of TP-I with Ebisuzaki *et al.* (1997) molecular system.

$C_7H_8N_4O_2$		
Atoms	TP-I	Ebisuzaki *et al.*, (1997)
Bond Distance [Å]		
O_1-C_1	1.198	1.221
C_1-N_2	1.368	1.359
N_2-C_4	1.365	1.384
C_4-C_3	1.36	1.350
N_1-C_6	1.469	1.488
C_2-O_2	1.221	1.213
C_4-N_4	1.350	1.350
N_4-C_7	1.334	1.317
C_7-N_3	1.314	1.326
N_2-C_5	1.465	1.469
Bond Angle [°]		
O_1-C_1-N_1	120.74	120.123
C_1-N_1-C_6	115.89	117.083
C_1-N_1-C_2	126.516	126.626
O_2-C_2-N_1	121.586	122.021
C_5-N_2-C_4	121.129	120.174
C_2-C_3-C_4	123.38	124.81
C_4-N_4-C_7	103.672	104.224
C_4-C_3-N_3	104.884	105.344
Dihedral Angle [°]		
O_1-C_1-N_1-C_6	0.014	2.257
O_2-C_2-N_1-C_1	-178.984	179.956
C_1-N_2-C_4-C_3	-3.129	2.201
C_5-N_2-C_4-C_3	179.272	-179.064
N_2-C_4-N_4-C_7	179.851	179.586
O_2-C_2-C_3-N_3	2.156	-1.644

Table 4.20 (b): Comparison between the computed electronic properties of TP-I with Ebisuzaki *et al.* (1997) molecular system using DFT/B3LYP/6-31G and DFT/B3LYP/6-31G** method.

	TP-I		Ebisuzaki *et al.*, (1997)	
	DFT/B3LYP/6-31G	DFT/B3LYP/6-31G**	DFT/B3LYP/6-31G	DFT/B3LYP/6-31G**
Total Energy [eV]	-17438.443	-17444.539	-17438.433	-17444.527
HOMO [eV]	-6.283	-6.083	-6.284	-6.084
LUMO [eV]	-1.282	-0.961	-1.285	-0.966
HOMO-LUMO Energy Gap [eV]	5.002	5.121	5.000	5.118
Dipole Moment [Debye]	3.642	3.481	3.622	3.462

4.4.1 Molecular Geometry Structural Analysis

Figure 4.21 shows some of the experimental geometry parameters of the TP-I single molecular system. The TP-I molecule under investigation contains C=O, C=C, C=N, C-C, C-N, N-H, and C-H bonds in its molecular moieties. O_1-C_1 and C_2-O_2 show double bond characteristic since both of them have bond distances of approximately 1.200 Å (*Selected Bond Energies*, 2003; Wired Chemist, 2021). Besides, N_1-C_6 and N_2-C_5, with bond distances of 1.469 Å and 1.465 Å, show single bond characteristic (i.e. 1.47 Å) (*Selected Bond Energies*, 2003; Wired Chemist, 2021). These findings strongly supported by the study made by Marta *et al.* (2010) where the authors obtained double bonded C=O (1.200 Å and 1.210 Å) and single bonded N-C (1.470 Å and 1.480 Å) for theophylline molecular system using DFT/B3LYP/6-311+G** level of theory. In additions, from the

experimental geometry structure, the pyrimidine ring of TP-I does not show exactly hexagon identity (120.000°) but has slightly distortion in it since the bond angles of C_1-N_1-C_2 and C_2-C_3-C_4 are 126.516° and 123.380°. Noticed that the bond distance of C_4-C_3 in the pyrimidine ring of TP-I molecular structure lies between the normal bond distance of C-C single bond (1.54 Å) and C=C double bond (1.33 Å) (*Selected Bond Energies*, 2003; Suna *et al.*, 2016; Wired Chemist, 2021). Bond distances C_4-N_4 and N_4-C_7 in the imidazole ring of TP-I also lie between the normal bond length of C=N double (1.290 Å) and C-N single (1.470 Å) bonds. Therefore suggest the appearance of π electron delocalisation over the pyrimidine and imidazole ring of the TP-I molecular system (Peica, 2006). The planarity of the TP-I molecular system can be determined by referring to the dihedral angle between the pyrimidine ring and the imidazole ring of the theophylline compound. A molecular system is said to be planar when the dihedral angles have the reading of 0.000°, 180.000°, and 360.000° (Suna, Hota and Misra, 2016). The negative sign in the dihedral angle indicated anti-clockwise rotation. In Figure 4.21, the dihedral angle of O_1-C_1-N_1-C_6 (0.014°), O_2-C_2-N_1-C_1 (-178.984°), and C_5-N_2-C_4-C_3 (179.272°) show slightly distortion from planarity in the pyrimidine ring of the TP-I molecular system. Furthermore, with value of 179.851 °, dihedral angle at N_2-C_4-N_4-C_7 indicates that the pyrimidine ring is in-plane with the imidazole ring, but is slightly distorted.

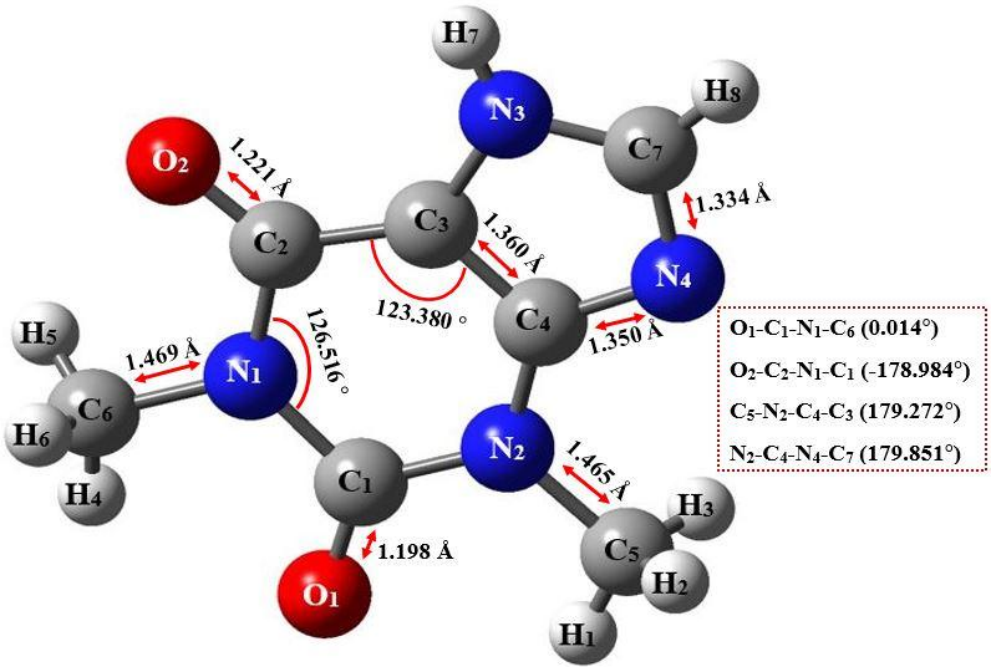

Figure 4.21: Parts of the geometry parameters (i.e. bond distances, bond angles, and dihedral angles) of TP-I molecular system.

Table 4.21 tabulates the experimental and optimized geometry structure of the TP-I single molecular system. In order to assess the reliability of the employment of DFT/B3LYP/6-31G and DFT/B3LYP/6-31G** methods in the computational studies of TP-I molecular system, the optimized geometry structure of TP-I is compared with the experimental geometry results obtained from the single crystal X-ray diffraction technique. As can be observed in Table 4.21, the geometry parameters (i.e. bond distances, bond angles, and dihedral angles) are slightly changed after the geometry optimization calculation. However, both of the TP-I optimized geometry structures using DFT/B3LYP/6-31G and DFT/B3LYP/6-31G** level of calculations show satisfactory agreement with the experimental data. As can be observed from the table, both of the computational methods have the largest percentage differences in bond distance

C_7-N_3, bond angle C_1-N_1-C_6, and dihedral angle C_1-N_2-C_4-C_3 as compared with experimental data. For DFT/B3LYP/6-31G method, the highest percentage differences in bond distance C_7-N_3, bond angle C_1-N_1-C_6, and dihedral angle C_1-N_2-C_4-C_3 are 4.414%, 1.049%, and 1.023%, respectively, while for DFT/B3LYP/6-31G** method are 3.425%, 1.011%, and 0.543%, respectively. The disparities are due to the fact that the experimental data is collected under the bulk and solid phase in which the inter and intra molecular interactions between neighbouring molecules are present. Conversely, the computational calculation is performed under the gases phase (Karthika *et al.*, 2012; Novena *et al.*, 2016; Kabouchi *et al.*, 2017; Novena *et al.*, 2017).

Table 4.21: The experimental and optimized geometry parameters for TP-I molecular system.

$C_7H_8N_4O_2$ (TP-I)			
Atoms	DFT/B3LYP/6-31G	DFT/B3LYP/6-31G**	Experiment
Bond Distance [Å]			
O_1-C_1	1.248	1.223	1.198
C_1-N_2	1.401	1.397	1.368
N_2-C_4	1.376	1.375	1.365
C_4-C_3	1.383	1.378	1.360
N_1-C_6	1.476	1.468	1.469
C_2-O_2	1.252	1.226	1.221
C_4-N_4	1.379	1.364	1.350
N_4-C_7	1.342	1.328	1.334
C_7-N_3	1.372	1.359	1.314
N_2-C_5	1.471	1.462	1.465
Bond Angle [°]			
O_1-C_1-N_1	121.633	121.738	120.740
C_1-N_1-C_6	117.106	117.062	115.890
C_1-N_1-C_2	126.665	127.151	126.516
O_2-C_2-N_1	121.91	122.161	121.586
C_5-N_2-C_4	120.508	120.353	121.129
C_2-C_3-C_4	123.443	123.656	123.380
C_4-N_4-C_7	104.299	103.821	103.672
C_4-C_3-N_3	105.148	104.794	104.884
Dihedral Angle [°]			
O_1-C_1-N_1-C_6	0.014	0.014	0.014
O_2-C_2-N_1-C_1	-178.98	-178.98	-178.984
C_1-N_2-C_4-C_3	-3.097	-3.112	-3.129
C_5-N_2-C_4-C_3	179.248	179.237	179.272
N_2-C_4-N_4-C_7	179.796	179.796	179.851
O_2-C_2-C_3-N_3	2.158	2.157	2.156

4.4.2 Total Energies and Frontier Molecular Orbital (FMO) Energies

Table 4.22 presents the computed total energies and frontier molecular orbital energies (i.e. HOMO, LUMO, and HOMO-LUMO energy gap) of the TP-I molecular system using DFT/B3LYP/6-31G and DFT/B3LYP/6-31G** methods. As can be observed in Table 4.22, the optimized ground state total energies of the TP-I molecular system using both DFT/B3LYP/6-31G and DFT/B3LYP/6-31G** methods are -17438.443 eV and -17444.539 eV. These findings show good agreement with Che *et al.* (2009) where the authors get -17445.235 eV total energy for pure TP molecular system via DFT/B3LYP/6-31+G** level of theory. The computed total energy is important since it can predict and identify the most stable polymorphic form of theophylline compound. The more negative the value of total energy, the more stable the compound (Kumer *et al.*, 2019). In Table 4.22, the energy levels of HOMO and LUMO for the TP-I molecular system using DFT/B3LYP/6-31G method are -6.283 eV and -1.282 eV, respectively, whereas for DFT/B3LYP/6-31G** method are -6.083 eV and -0.961 eV, respectively. Both of the methods (i.e. 6-31G and 6-31G** basis sets) show that the HOMO-LUMO energy gaps of the TP-I molecular system are situated between the ranges of 5.002 eV to 5.121 eV. The computed HOMO-LUMO energy gaps show closer finding with Salihović *et al.* (2014). The frontier molecular orbitals energies (i.e. HOMO energy, LUMO energy, and HOMO-LUMO energy gap) are helpful in the prediction and determination of the chemical reactivity and kinetic stability of the TP-I molecular system (Holmes-Hampton *et al.*, 2014; Subhapriya, 2014). For example, TP-I molecular system is more polarized, high chemical reactivity, low kinetic stability, and softer than

theophyillinium chloride monohydrate (TCM) ($C_7H_8N_4O_2Cl \cdot H_2O$) molecule since TP-I has a lower HOMO-LUMO energy gap than TCM (5.576 eV) (Novena *et al.,* 2017). A molecular system with a narrow HOMO-LUMO energy gap will exhibit a significant degree of intramolecular charge transfer (ICT) from electron donating groups to electron accepting group via π conjugated path (Sridevi, 2012). Figure 4.22 (a) and (b) illustrate the 3D contour surface mapped plots of HOMO and LUMO for TP-I molecular system using DFT/B3LYP/6-31G and DFT/B3LYP/6-31G** methods. Clearly noted that both of the computational methods give approximately identical results. The green colour lobe representing the negative region while the red colour lobe indicates the positive region (Kabouchi *et al.*, 2017; Rajalakshmi and Nayak, 2017). In Figure 4.22 (a) and (b), majority of the electron density in both HOMO and LUMO orbitals are distributed over the pyrimidine ring and imidazole ring of the TP-I molecular system. HOMO represents the donating ability of electron while LUMO represents the accepting ability of electron. Basically, the atom that occupied with large surface of HOMO electron density distribution has stronger ability to donate electron while for LUMO, it is the opposite of HOMO (Balachandran *et al.*, 2013). Consequently, the HOMO→ LUMO transition implies electron density transfer between the pyrimidine ring and the imidazole ring of the TP-I molecular system (Sridevi, 2012; Nyakung'U, 2015). Besides, the molecular orbital coefficients analysis reveal that the HOMO and LUMO orbitals are mainly composed from p_y type orbitals. So that the transition of electrons are mainly from π to π^*. Furthermore, the HOMO energy and LUMO energy are important parameters in the determination of global reactivity descriptors. According to Koopmans theorem, the ionization energy (IE),

electron affinity (EA), hardness (η), chemical potential (μ), softness (S), electronegativity (χ), and electrophilicity index (ω) of TP-I molecular system can be calculated using the formulas stated in Chapter 2 (Equation 2.32 - Equation 2.38). Table 4.22 also tabulates the calculated global reactivity descriptors. For DFT/B3LYP/6-31G method, the calculated IE, EA, η, μ, S, χ, and ω of TP-I molecular system are 6.283 eV, 1.282 eV, 2.501, -3.783, 0.200, 3.783, and 2.861, while for DFT/B3LYP/6-31G** method are 6.083 eV, 0.961 eV, 2.561, -3.522, 0.195, 3.522, and 2.422. Moreover, to confirm and verify the suitability of the selected DFT computational methods (i.e. B3LYP/6-31G and B3LYP/6-31G**) in the study of FMOs, UV-Vis spectroscopy experiment was carried out to determine the experimental energy gap of TP-I molecular system (Raja *et al.*, 2014; Hu *et al.*, 2016; Rahmani *et al.*, 2018). The absorption process in UV-Vis spectroscopy is based on the excitation of electrons from a lower energy state to a higher energy state (Subhapriya, 2014). In this work, the absorption spectrum (λ) obtained from the UV-Vis spectroscopy technique is 271 nm, thus the experimental energy gap is 4.580 eV. Both the experimental and computed energy gaps show satisfactory agreement with each other.

Table 4.22: Total energies, HOMO energies, LUMO energies and HOMO-LUMO energy gaps, and global descriptors of TP-I molecular system.

	$C_7H_8N_4O_2$ (TP-I)	
	DFT/B3LYP/6-31G	DFT/B3LYP/6-31G**
Total Energy [eV]	-17438.443	-17444.539
HOMO [eV]	-6.283	-6.083
LUMO [eV]	-1.282	-0.961
HOMO-LUMO Energy Gap [eV]	5.002	5.121
Ionization Energy (IE) [eV]	6.283	6.083
Electron Affinity (EA) [eV]	1.282	0.961
Hardness (η)	2.501	2.561
Chemical Potential (μ)	-3.783	-3.522
Softness (S)	0.200	0.195
Electronegativity (χ)	3.783	3.522
Electrophilicity index (ω)	2.861	2.422

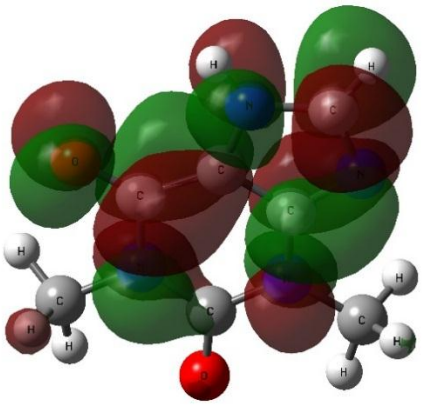

LUMO (-1.282 eV)

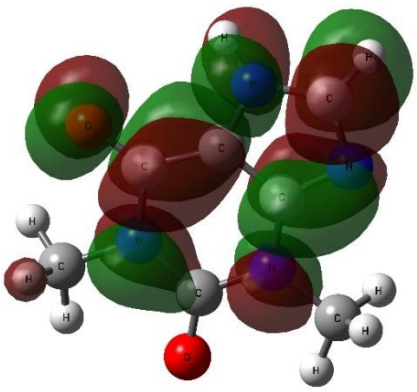

LUMO (-0.961 eV)

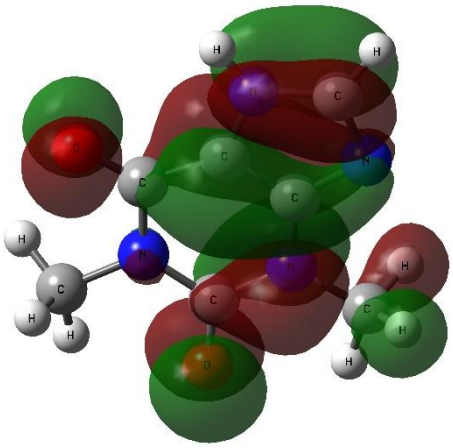

HOMO (-6.283 eV)

Figure 4.22 (a): LUMO and HOMO surface mapped plots of TP-I molecular system using DFT/B3LYP/6-31G method.

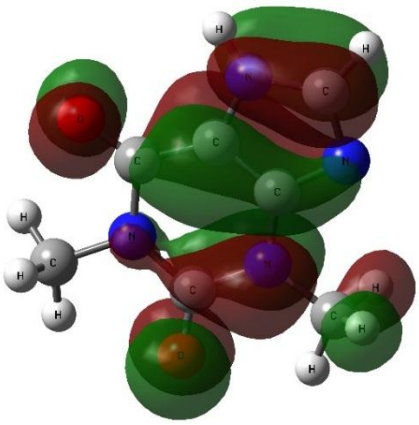

HOMO (-6.083 eV)

Figure 4.22 (b): LUMO and HOMO surface mapped plots of TP-I molecular system using DFT/B3LYP/6-31G** method.

4.4.3 Mulliken Population Analysis (MPA)

Table 4.23 tabulates the Mulliken atomic charges distribution of the TP-I molecular system using DFT/B3LYP/6-31G and DFT/B3LYP/6-31G** level of calculations. Mulliken atomic charge has potent application in quantum

chemical calculations since it is directly related to the chemical bonds and the vibrational modes of the TP-I molecular system (Sharmi, 2015; Novena *et al.*, 2016). It influences the dipole moment, polarizability, electronic structures, and properties of a molecular system (Sharmi, 2015; Novena *et al.*, 2016; Akman, 2017; Novena *et al.*, 2017). The Mulliken atomic charge analysis is able to provide significant information about the charge shift activities (donate or receive) in TP-I molecular system (Jawaher *et al.*, 2018b). Besides, it also determines the ability and contribution of an atom in hydrogen bond interactions (Gandhi *et al.*, 2019). The Mulliken atomic charges for the TP-I molecular system are plotted in Figure 4.23. From the figure, both of the computational methods show similar trends but slightly different in atomic charge values. For example, all the calculated Mulliken atomic charges in oxygen atoms and nitrogen atoms show negative charge values, whereas all hydrogen atoms are in positive atomic charge distributions. Clearly noted that in Figure 4.23, both of the DFT/B3LYP/6-31G and DFT/B3LYP/6-31G** methods show the highest positive atomic charge value on carbon atom C_1, while the atoms bonded with it (i.e. O_1, N_1, and N_2) have higher negative atomic charge readings. The result indicate the charge shift activities from less electronegativity atom C_1 to high electronegativity atoms O_1, N_1, and N_2 (Hunt, 2008). Carbon atom as a group 14 element, can carry either positive or negative atomic charge depending on its neighbouring atoms. Noticed that carbon atoms C_5 and C_6 exhibit negative atomic charge values due to the electron withdrawing character of nitrogen atoms N_1 and N_2 (Novena *et al.*, 2016; Akman, 2017; Novena *et al.*, 2017). Besides, the three carbon atoms C_2, C_3, and C_4 linked in the pyrimidine ring of the TP-I molecular system contain positive atomic charges, indicate the presence

of resonance effect. Higher negative atomic charges in atoms O_1, O_2, N_1, N_2, N_3, and N_4 together with largest positive atomic charges in hydrogen atom H_7 suggest the presence of intra and intermolecular hydrogen bonding interaction in the TP-I molecular system (Meenatchi *et al.*, 2015; Novena *et al.*, 2017).

Table 4.23: Computed Mulliken atomic charges analysis (MPA) of TP-I molecular system using DFT/B3LYP/6-31G and DFT/B3LYP/6-31G** method.

$C_7H_8N_4O_2$ (TP-I)					
MPA					
Atoms	DFT/B3LYP/6-31G	DFT/B3LYP/6-31G**	Atoms	DFT/B3LYP/6-31G	DFT/B3LYP/6-31G**
O_1	-0.451	-0.525	C_6	-0.234	-0.171
C_1	0.729	0.785	H_4	0.196	0.154
N_1	-0.670	-0.587	H_5	0.180	0.141
C_2	0.560	0.633	H_6	0.172	0.134
C_3	0.310	0.215	O_2	-0.454	-0.535
C_4	0.334	0.480	N_3	-0.730	-0.581
N_2	-0.676	-0.605	C_7	0.275	0.292
C_5	-0.238	-0.181	N_4	-0.396	-0.506
H_1	0.201	0.161	H_7	0.353	0.289
H_2	0.176	0.138	H_8	0.187	0.133
H_3	0.175	0.137			

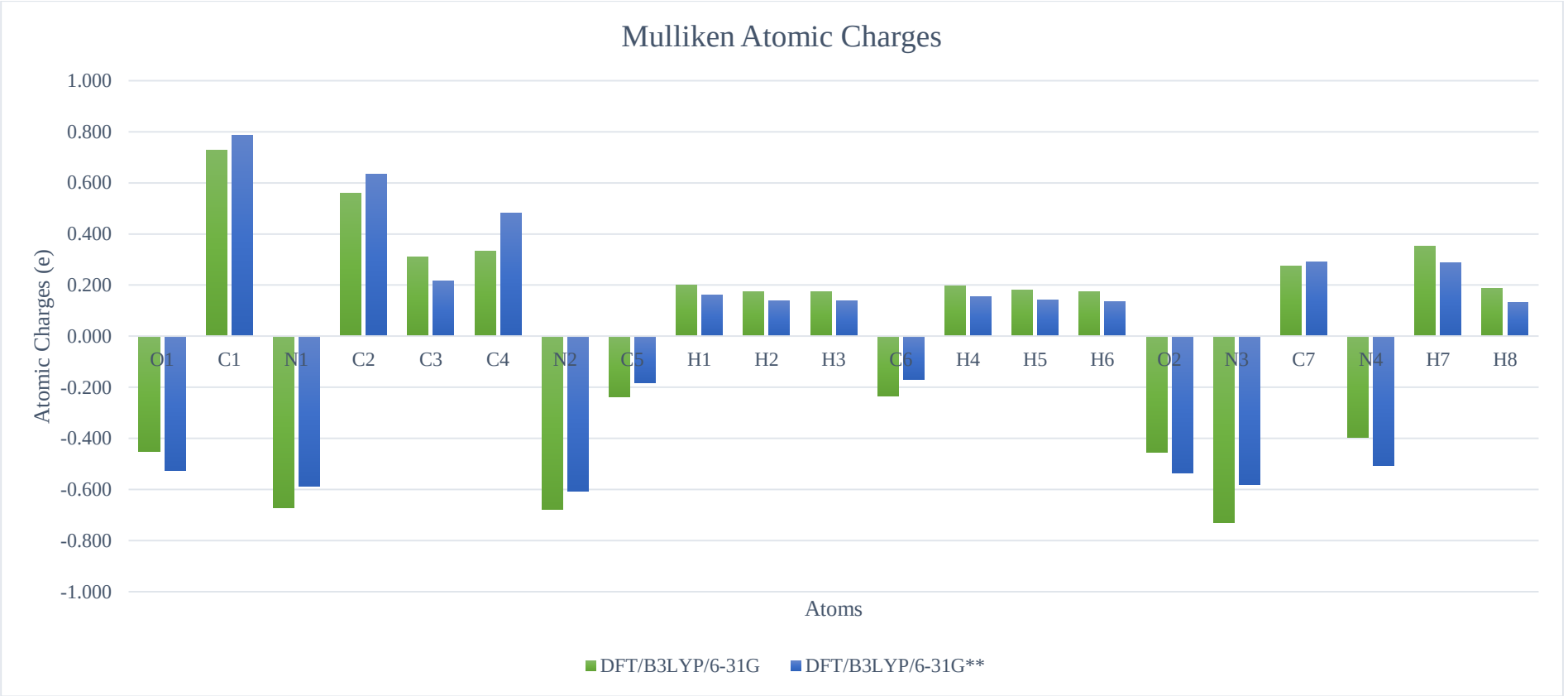

Figure 4.23: MPA analysis of TP-I molecular system using DFT/B3LYP/6-31G and DFT/B3LYP/6-31G** methods.

4.4.4 Molecular Electrostatic Potential (MEP)

In the present study, the 3D molecular electrostatic potential (MEP) surface plots of TP-I molecular system using DFT/B3LYP/6-31G and DFT/B3LYP/6-31G** methods are illustrated in Figure 4.24 (a) and (b). The MEP surface plot contains informative information about the nuclear and electronic charge distributions of the TP-I molecular system (Saranya *et al.*, 2018). Hence, it is able to visualise the sites for electrophilic and nucleophilic reactions via colouring scheme and have potent usages in the study of the biological recognition process and hydrogen bonding interaction in the TP-I molecular system (Kabouchi *et al.*, 2017; Rahmani *et al.*, 2018; shodhganga, 2021). Besides, the MEP also simultaneously displays the polarity, molecular size, and shape of the TP-I molecular system. In Figure 4.24 (a) and (b), both of the computational methods show approximately identical MEP surface plots for the TP-I molecular system. The red-yellowish negative electrostatic potential regions are mainly focused around oxygen atoms (O_1, O_2) and nitrogen atom (N_4) due to their high electronegativity characteristics and the presence of lone pairs (Nagabalasubramanian, 2012). On the other hands, the deep blue positive electrostatic potential region is found to be located on hydrogen atom (H_7) due to the electrons withdrawing characteristic from the N_3 nitrogen atom (Prasana *et al.*, 2019). These suggested that O_1, O_2, and N_4 will be the sites for the electrophilic attack, while H_7 is preferred for nucleophilic reaction in TP-I molecular system. Hence, reveals the possible regions where the intra and intermolecular interaction of the TP-I molecular system can take place (Sridevi, 2012; Kabouchi *et al.*, 2017). Besides, noticed that all the carbon atoms in TP-I

molecular system show intermediate electropositive electrostatic potential (colourless) and behave as non-polar molecules. Furthermore, the global extrema points of the TP-I molecular system are calculated using Multifwn software and mapped on Figure 4.24 (a) and (b). Both of the computational calculations obtain surface minimum point around oxygen atom (O_1) with values of -1.762 eV and -1.523 eV, respectively for DFT/B3LYP/6-31G and DFT/B3LYP/6-31G** methods. The surface maximum points for both DFT/B3LYP/6-31G and DFT/B3LYP/6-31G** theories are located on hydrogen atom (H_7) with values of 2.488 eV and 2.364 eV.

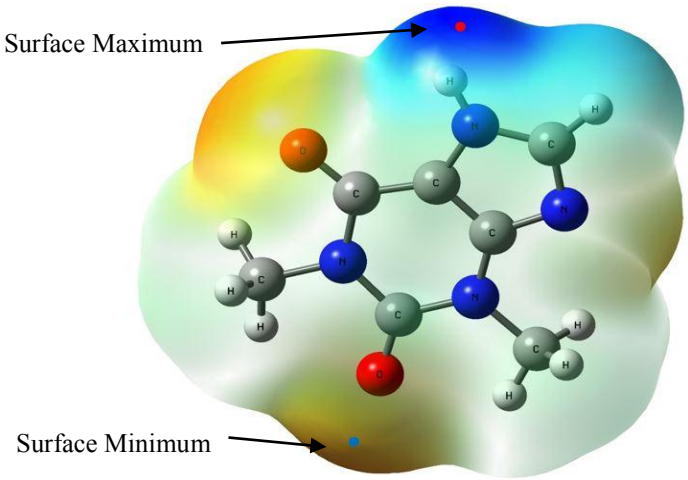

Surface Minimum (blue dot) - -1.762 eV
Surface Maximum (red dot) – 2.488 eV

Figure 4.24 (a): MEP surface mapped plots of TP-I molecular system using DFT/B3LYP/6-31G method.

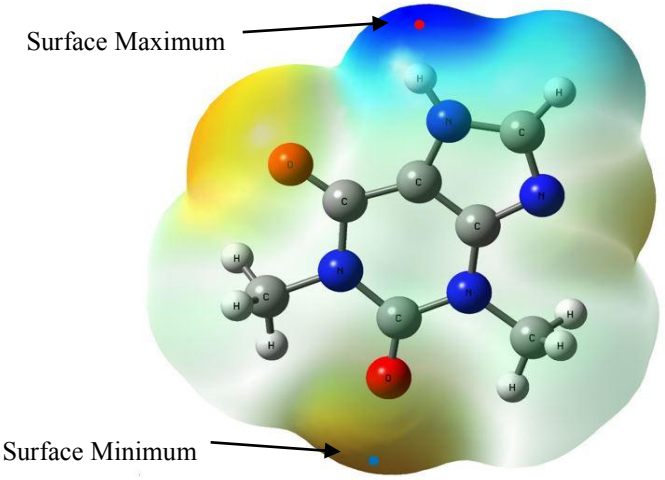

Surface Minimum (blue dot) - -1.523 eV
Surface Maximum (red dot) – 2.364 eV

Figure 4.24 (b): MEP surface mapped plots of TP-I molecular system using DFT/B3LYP/6-31G** method.

4.4.5 Natural Bond Orbital (NBO) Analysis

Table 4.24 (a) and (b) tabulate the NBO analysis of the TP-I molecular system using DFT/B3LYP/6-31G and DFT/B3LYP/6-31G** method. Natural bond orbital (NBO) analysis is a useful method to understand the charge transfer mechanism and conjugative interaction in the TP-I molecular system (Sridevi, 2012; Bahgat and Fraihat, 2015; Dheivamalar *et al.*, 2016; shodhganga, 2021). It is able to give a strong perception about the intra and intermolecular bonding interaction among the bonds in the TP-I molecular system. From the computed NBO data, the significant types of intramolecular interactions in the TP-I molecular system using both DFT/B3LYP/6-31G and DFT/B3LYP/6-31G** methods are mainly contributed by $\sigma \rightarrow \sigma^*$, $\pi \rightarrow \pi^*$ and LP $\rightarrow \pi^*$. Through the second-order perturbation theory Fock matrix calculation, the intensiveness of the interactions between electron donors and electron acceptors can be determined. Noticed that stronger stabilisation energy ($E(2)$) could signify the intensive charge transfer interactions between electron donors and electron acceptors. Consequently, lead to a greater extent of conjugation in the molecular system (Sridevi, 2012; Maache *et al.*, 2016; shodhganga, 2021). From the tables, both of the computational methods (i.e. 6-31G and 6-31G** basis sets) elucidate that the intramolecular interactions are formed by the orbitals overlap between π (C_3-C_4) with π^* (C_2-O_2), π (C_3-C_4) with π^* (C_7-N_4), and π (C_7-N_4) with π^* (C_3-C_4). Hence, causing high stabilisation to the TP-I molecular system (Sridevi, 2012; Dubey *et al.*, 2018). For DFT/B3LYP/6-31G method, the computed stabilisation energies for π (C_3-C_4) $\rightarrow \pi^*$ (C_2-O_2), π (C_3-C_4) $\rightarrow \pi^*$ (C_7-N_4), and π (C_7-N_4) $\rightarrow \pi^*$ (C_3-C_4) are 1.288 eV, 0.611 eV, and 1.045 eV, while for

DFT/B3LYP/6-31G** method are 1.234 eV, 0.580 eV, and 1.102 eV. These indicate strong delocalisation ($\pi \rightarrow \pi^*$) in the pyrimidine ring and imidazole ring of the TP-I molecular system (Novena e*t al.*, 2016). Furthermore, it can be observed that orbitals LP (N_1) $\rightarrow \pi^*$ (O_1-C_1), LP (N_1) $\rightarrow \pi^*$ (C_2-O_2), LP (N_2) $\rightarrow \pi^*$ (O_1-C_1), LP (N_2) $\rightarrow \pi^*$ (C_3-C_4), LP (N_3) $\rightarrow \pi^*$ (C_3-C_4), and LP (N_3) $\rightarrow \pi^*$ (C_7-N_4) are considered as stronger interactions and have the dominant role in the stabilisation of TP-I molecular system (Dubey *et al.*, 2018). As recorded in Table 4.24 (a) and (b), the computed stabilisation energies using DFT/B3LYP/6-31G level of theory for LP (N_1) $\rightarrow \pi^*$ (O_1-C_1) is 2.689 eV, LP (N_1) $\rightarrow \pi^*$ (C_2-O_2) is 2.535 eV, LP (N_2) $\rightarrow \pi^*$ (O_1-C_1) is 2.774 eV, LP (N_2) $\rightarrow \pi^*$ (C_3-C_4) is 2.112 eV, LP (N_3) $\rightarrow \pi^*$ (C_3-C_4) is 1.396 eV, and LP (N_3) $\rightarrow \pi^*$ (C_7-N_4) is 2.309 eV, whereas the computed stabilisation energies using DFT/B3LYP/6-31G** method for LP (N_1) $\rightarrow \pi^*$ (O_1-C_1) is 2.520 eV, LP (N_1) $\rightarrow \pi^*$ (C_2-O_2) is 2.361 eV, LP (N_2) $\rightarrow \pi^*$ (O_1-C_1) is 2.593 eV, LP (N_2) $\rightarrow \pi^*$ (C_3-C_4) is 2.051 eV, LP (N_3) $\rightarrow \pi^*$ (C_3-C_4) is 1.351 eV, and LP (N_3) $\rightarrow \pi^*$ (C_7-N_4) is 2.409 eV.

Table 4.24 (a): Donor-acceptor interactions and second-order perturbation energies of TP-I molecular system using DFT/B3LYP/6-31G method.

Donor (i)	ED (e)	Acceptor (j)	ED (e)	E(2) [kcal/mol]	E(2) [eV]	E(j) - E(i) [a.u]	F (i,j) [a.u]
σ (N_1-C_2)	1.984	σ* (C_3-N_3)	0.023	4.550	0.197	1.210	0.066
σ (C_2-C_3)	1.977	σ* (C_3-C_4)	0.032	4.820	0.209	1.290	0.071
π (C_2-O_2)	1.979	π* (C_3-C_4)	0.435	5.890	0.255	0.360	0.046
π (C_3-C_4)	1.732	π* (C_2-O_2)	0.370	29.700	1.288	0.270	0.083
π (C_3-C_4)	1.732	π* (C_7-N_4)	0.397	14.090	0.611	0.260	0.056
σ (C_3-N_3)	1.982	σ* (C_4-N_2)	0.040	4.310	0.187	1.260	0.066
σ (C_4-N_4)	1.979	σ* (C_7-H_8)	0.015	4.080	0.177	1.270	0.064
σ (N_3-C_7)	1.99	σ* (C_2-C_3)	0.055	4.860	0.211	1.350	0.073
σ (C_7-N_4)	1.983	σ* (C_4-N_2)	0.040	7.610	0.330	1.280	0.089
π (C_7-N_4)	1.842	π* (C_3-C_4)	0.435	24.090	1.045	0.320	0.084
LP (N_1)	1.617	π* (O_1-C_1)	0.408	62.010	2.689	0.240	0.109
LP (N_1)	1.617	π* (C_2-O_2)	0.370	58.470	2.535	0.250	0.108
LP (N_2)	1.624	π* (O_1-C_1)	0.408	63.970	2.774	0.240	0.112
LP (N_2)	1.624	π* (C_3-C_4)	0.435	48.710	2.112	0.270	0.103
LP (N_3)	1.574	π* (C_3-C_4)	0.435	32.200	1.396	0.290	0.086
LP (N_3)	1.574	π* (C_7-N_4)	0.397	53.250	2.309	0.260	0.105

Table 4.24 (b): Donor-acceptor interactions and second-order perturbation energies of TP-I molecular system using DFT/B3LYP/6-31G** method.

Donor (i)	ED (e)	Acceptor (j)	ED (e)	E(2) [kcal/mol]	E(2) [eV]	E(j) - E(i) [a.u]	F (i,j) [a.u]
σ (C_1-N_2)	1.983	σ* (C_4-N_4)	0.018	4.060	0.176	1.290	0.065
σ (N_1-C_2)	1.984	σ* (C_3-N_3)	0.022	4.520	0.196	1.240	0.067
π (C_2-O_2)	1.981	π* (C_3-C_4)	0.425	4.980	0.216	0.380	0.043
π (C_3-C_4)	1.734	π* (C_2-O_2)	0.351	28.460	1.234	0.290	0.083
π (C_3-C_4)	1.734	π* (C_7-N_4)	0.400	13.370	0.580	0.270	0.055
σ (C_3-N_3)	1.981	σ* (C_4-N_2)	0.041	4.570	0.198	1.280	0.069
σ (C_4-N_4)	1.978	σ* (C_7-H_8)	0.018	4.720	0.205	1.260	0.069
σ (N_3-C_7)	1.989	σ* (C_2-C_3)	0.060	5.090	0.221	1.340	0.075
σ (C_7-N_4)	1.981	σ* (C_4-N_2)	0.041	8.540	0.370	1.300	0.094
π (C_7-N_4)	1.838	π* (C_3-C_4)	0.425	25.420	1.102	0.330	0.088
LP (N_1)	1.628	π* (O_1-C_1)	0.387	58.110	2.520	0.260	0.110
LP (N_1)	1.628	π* (C_2-O_2)	0.351	54.440	2.361	0.270	0.109
LP (N_2)	1.635	π* (O_1-C_1)	0.387	59.800	2.593	0.270	0.113
LP (N_2)	1.635	π* (C_3-C_4)	0.425	47.290	2.051	0.280	0.104
LP (N_3)	1.572	π* (C_3-C_4)	0.425	31.160	1.351	0.300	0.086
LP (N_3)	1.572	π* (C_7-N_4)	0.400	55.550	2.409	0.270	0.110

4.4.6 Non-Linear Optical (NLO) Properties

The recent study of non-linear optical (NLO) properties in organic compounds have gained extensive attention in current research since an active NLO material has several applications in optical signal processing, data storage, switching, photonic, laser technologies, and telecommunications industries (Sridevi, 2012; Jawaher *et al.*, 2018; Abbaz *et al.*, 2019; Varghese *et al.*, 2019). Generally, an organic compound will have π electron conjugated system that leads to a push-pull conjugated structure and shows better NLO properties (Dubey *et al.*, 2018). The computational approach in the study of NLO properties in chemical compounds is an inexpensive and yet effective way to analyse the suitability of that particular compound to become an active NLO material (Dubey *et al.*, 2018). Previous literature surveys reveal that the NLO properties of pure theophylline compound have not been reported yet. So that, in order to identify the NLO properties of the TP-I molecular system, urea is employed and act as the reference molecule to compare and determine the NLO status of the TP-I molecular system (Sridevi, 2012; Dubey *et al.*, 2018; Abbaz *et al.*, 2019). Urea is a famous and well-known active NLO material with dipole moment (μ) of 1.373 Debye and first hyperpolarizability (β_{tot}) of 0.373 x 10^{-30} e.s.u (Maache *et al.*, 2016; Abbaz *et al.*, 2019). Table 4.25 summarises the computed dipole moment (μ) and first hyperpolarizability (β_{tot}) of TP-I molecular system using DFT/B3LYP/6-31G and DFT/B3LYP/6-31G** level of theories. The dipole moment vector direction for TP-I molecular system depends on the centres of positive and negative charge (Narayan, 2012). In Table 4.25, the computed dipole moment (μ) for TP-I molecular system using DFT/B3LYP/6-31G method

is 3.642 Debye, whereas for DFT/B3LYP/6-31G** method is 3.481 Debye. Both of them show maximum dipole moment contribution from Z-direction (μ_z). Polarizability refers as the quantity created from the induced dipole moment of a molecular system by an external electric field that gives the perturbation knock on the electron density (Narayan, 2012; Sridevi, 2012). From Gaussian 09 software output data, the first polarizability of the TP-I molecular system is computed in atomic units (a.u). For the convenient in data comparison between urea and TP-I molecular system, the computed first hyperpolarizability results are converting into electrostatic units (e.s.u) which 1.000 a.u = 8.639 x 10^{-33} e.s.u (Maache *et al.*, 2016; Dubey *et al.*, 2018; Abbaz *et al.*, 2019). Noticed that in Table 4.25, the computed first hyperpolarizability (β_{tot}) of TP-I molecular system are 7.598 x 10^{-30} e.s.u and 7.378 x 10^{-30} e.s.u, respectively for DFT/B3LYP/6-31G and DFT/B3LYP/6-31G** methods. As compare with urea, the dipole moment and first hyperpolarizability of TP-I molecular system are at least 2.535 and 19.767 times larger than urea. Hence, TP-I molecular system can be considered as good NLO materials (Boukabcha *et al.*, 2015; Maache *et al.*, 2016; Rahmani *et al.*, 2018; Abbaz *et al.*, 2019).

Table 4.25: Computed dipole moment (μ) and first hyperpolarizability (β_{tot}) of TP-I molecular system using DFT/B3LYP/6-31G and DFT/B3LYP/6-31G** methods.

Parameters	DFT/B3LYP/6-31G	DFT/B3LYP/6-31G**
μ_x	-1.547	-1.479
μ_y	0.088	0.079
μ_z	3.296	3.150
μ [Debye]	3.642	3.481
β_{xxx}	17.757	18.331
β_{xyy}	10.846	10.742
β_{xzz}	-41.230	-35.747
β_{yyy}	-14.413	-14.069
β_{xxy}	-7.109	-6.691
β_{yzz}	6.916	6.453
β_{zzz}	-403.998	-396.624
β_{xxz}	-261.392	-248.931
β_{yyz}	-213.842	-208.322
β_{tot} [a.u]	879.444	854.023
β_{tot} [e.s.u]	7.598×10^{-30}	7.378×10^{-30}

4.4.7 Fourier Transform Infrared (FT-IR) Spectroscopy

Fourier transform infrared spectroscopy (FT-IR) is a non-destructive method used to determine the interactions between atoms at the molecular level based on the vibrational spectrum generated between the bonded atoms (Bhattacharyya, 2015). It is able to identify the types of functional groups present in a molecular system (Suna, Hota and Misra, 2016). Besides, FT-IR provides a faster way in the differentiation between polymorphism compounds by comparing to their "biochemical fingerprint" generated through the FT-IR technique. In this study,

the FT-IR vibrational frequencies of the TP-I molecular system are computed using DFT/B3LYP/6-31G and DFT/B3LYP/6-31G** methods. TP-I molecular system with a total atoms number of 21, has 57 fundamental vibrational modes that qualitatively represented the existence of different functional groups in the TP-I molecule. In order to rationalise the theoretical data, the experimental FT-IR vibrational spectrum of the TP-I molecular system is obtained using the potassium bromine (KBr) diffuse reflectance method in the ranges of 400 cm^{-1} to 4000 cm^{-1} as shown in Figure 4.25. Table 4.26 summarises the experimental and computational FT-IR vibrational frequency spectra of the TP-I molecular system. Clearly noticed that all the calculated vibrational frequencies (unscaled) results have larger values than experimental data. This is due to the reason that computational calculation is carried out under the gases phase condition. So, it ignores the anharmonicity in the real case system (Marta *et al.*, 2010; Nagabalasubramanian, 2012; Narayan, 2012; Novena *et al.*, 2016; Novena *et al.*, 2017). Furthermore, the electron correlation effects and basis set deficiencies during the computational calculation are the major causes as well for the overestimation of the vibrational frequencies in the TP-I molecular system (Nagabalasubramanian, 2012; Narayan, 2012; Suna *et al.*, 2016). Nevertheless, the shortcoming in the larger deviation between experimental and computational FT-IR results can be overcome by direct scaling technique via the employment of proper scale factor (Che *et al.*, 2009; Marta *et al.*, 2010; Narayan, 2012; Sasaki *et al.*, 2016). From Computational Chemistry Comparison and Benchmark DataBase (CCCBDB, 2020), the scale factors for DFT/B3LYP/6-31G and DFT/B3LYP/6-31G** techniques are 0.962 and 0.961, respectively. In Table 4.26, both of the scaled computational FT-IR vibrational frequency results (i.e.

6-31G and 6-31G** basis sets) show a high level of conformity with experimental data. For example, band regions 3536 cm^{-1} (scaled 6-31G), 3523 cm^{-1} (scaled 6-31G**), and 3447 cm^{-1} (Experiment) are assigned to N-H stretching vibrational mode in the imidazole ring of TP-I molecular system. Conversely, the N-H bending vibrational mode occurs in frequency bands 1483 cm^{-1} (scaled 6-31G and Experiment) and 1450 cm^{-1} (6-31G**). The C=O stretching vibration mode could be observed in the ranges between 1576 cm^{-1} to 1665 cm^{-1} (scaled 6-31G), 1586 cm^{-1} to 1727 cm^{-1} (scaled 6-31G**), and 1610 cm^{-1} to 1717 cm^{-1} (Experiment). Moreover, a wide range of frequency bands corresponding to C-N stretching vibration can be obtained from 1040 cm^{-1} to 1378 cm^{-1} (scaled 6-31G), 1024 cm^{-1} to 1372 cm^{-1} (scaled 6-31G**), and 1049 cm^{-1} to 1284 cm^{-1} (Experiment). For the C=C bond in the pyrimidine ring of TP-I molecular system, the stretching vibrational mode is observed in band regions 1528 cm^{-1} (scaled 6-31G), 1534 cm^{-1} (scaled 6-31G**), and 1568 cm^{-1} (Experiment), whereas the bending vibration mode can be obtained between regions 715 cm^{-1} to 744 cm^{-1} (scaled 6-31G), 707 cm^{-1} to 712 cm^{-1} (scaled 6-31G**), and 682 cm^{-1} to 743 cm^{-1} (Experiment). Noted that both of the computational and experimental FT-IR characteristic vibrational spectrum results strongly support the structure of the TP-I molecular system and show good agreement with literature data (*Infrared Spectroscopy Table*, 2001; Che *et al.*, 2009; Nagabalasubramanian, 2012; Sarma and Saikia, 2014; Novena *et al.*, 2016; Sasaki *et al.*, 2016; LibreTexts, 2020).

Table 4.26: Experimental and computational (unscaled and scaled) FT-IR vibrational frequencies of TP-I molecular system.

Type of Vibration	DFT/B3LYP/6-31G		DFT/B3LYP/6-31G**		Experiment [cm^{-1}]
	Unscaled [cm^{-1}]	Scaled [cm^{-1}]	Unscaled [cm^{-1}]	Scaled [cm^{-1}]	
N-H stretching vibration	3675	3536	3666	3523	3447
C-H stretching vibration	3209	3087	3204	3079	3058
C-H stretching vibration	3085	2968	3076	2956	2986
C-H stretching vibration	3079	2962	3069	2949	2825
C=O stretching vibration	1731	1665	1798	1727	1717
C=O stretching vibration	1687	1623	1760	1691	1669
C=O stretching vibration	1638	1576	1650	1586	1610
C=C stretching vibration	1588	1528	1596	1534	1568
N-H bending vibration	1541	1483	1508	1450	1483
C-H bending vibration	1491	1435	1488	1430	1447
C-N stretching vibration	1433	1378	1428	1372	1284
C-N stretching vibration	1262	1214	1266	1216	1224
C-N stretching vibration	1218	1172	1221	1174	1188
C-N stretching vibration	1141	1097	1125	1081	1107
C-N stretching vibration	1081	1040	1065	1024	1049
C-H bending vibration	851	818	836	803	785
C=C bending vibration	774	744	741	712	743
C=C bending vibration	743	715	736	707	682

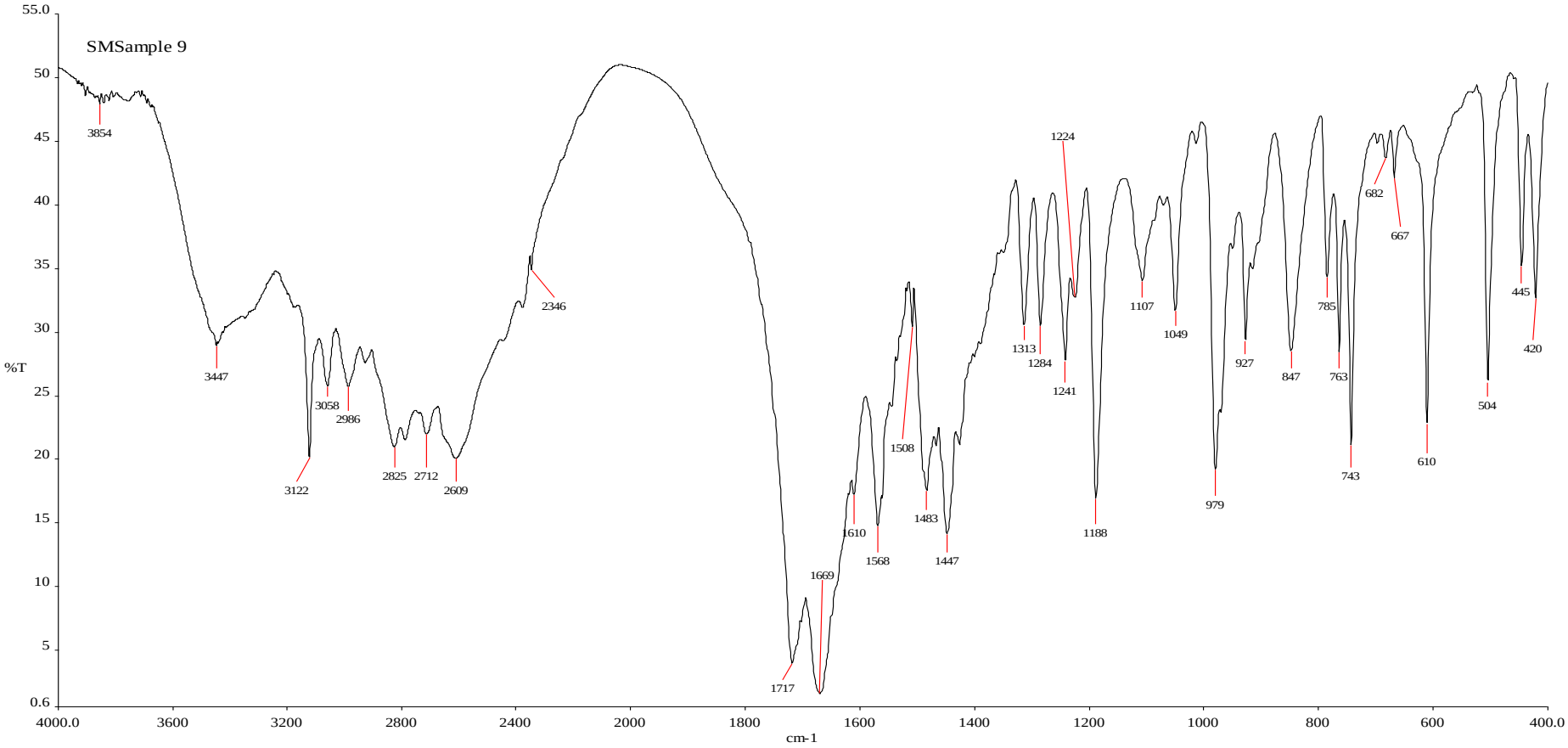

Figure 4.25: Experimental FT-IR vibrational spectrum of TP-I molecular system.

4.4.8 Size Effect Study

In the real case system, the TP-I crystal sample contains numerous identical TP-I molecules that repeatedly situated with each other in the solid state crystal lattice. The existence of the intra and intermolecular interactions between neighbouring molecules strongly influence the geometry and electronic structures of the system. Even though the employment of a single TP-I molecule ($C_7H_8N_4O_2$) in the DFT computational studies has successfully obtained reasonable and reliable computational data for the geometrical and electronic properties of pure theophylline compound, there is still valuable to investigate the molecular size effect during DFT computational analysis. In this work, additional theophylline molecules are added to the nearby single TP-I molecule as shown in Figure 4.26 (a) and (b). The 3[TP-I] molecular system (Figure 4.26 (a)) contains three theophylline molecules, while the 5[TP-I] molecular system (Figure 4.26 (b)) contains five theophylline molecules. Both of the 3[TP-I] and 5[TP-I] molecular system are fully optimized using DFT/B3LYP/6-31G and DFT/B3LYP/6-31G** level of theories. The optimized geometry structures and computed electronic properties for 3[TP-I] and 5[TP-I] molecular system are presented in this study.

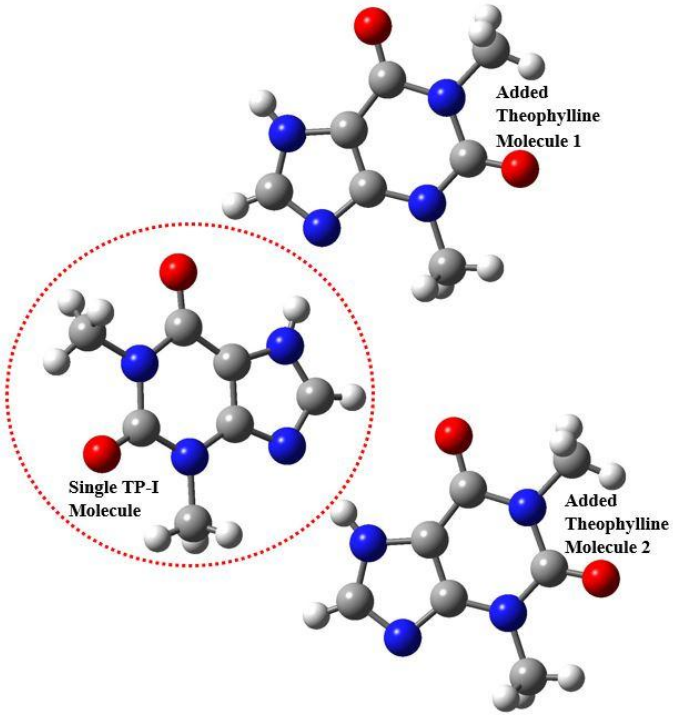

Figure 4.26 (a): Molecular structure of 3[TP-I] molecular system involved in the size effect study.

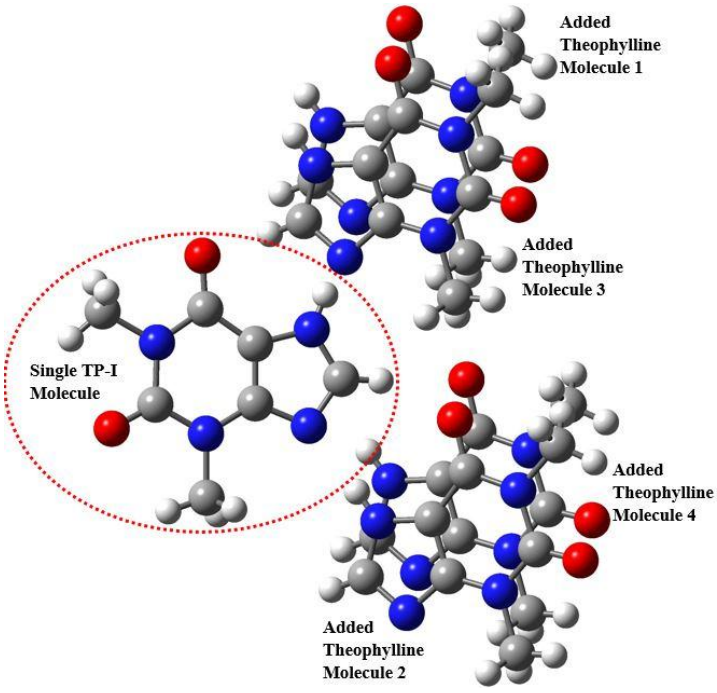

Figure 4.26 (b): Molecular structure of 5[TP-I] molecular system involved in the size effect study.

Table 4.27 (a) and (b) summarise the optimized geometry parameters (i.e. bond distances, bond angles, and dihedral angles) of TP-I molecule obtained from TP-I, 3[TP-I], and 5[TP-I] molecular system. Undoubtedly, both of the computational methods (i.e. 6-31G basis set and 6-31G** basis set) used in 3[TP-I] and 5[TP-I] molecular system generate closer molecular geometrical findings with experimental data. The tables clearly noted that the increment in the molecular size during geometry optimization calculation evidently reduced the discrepancies of geometry parameters between computational and experimental data. Figure 4.27 (a) and (b) demonstrate the bond distances of the TP-I molecule taken from the experimental, optimized TP-I, 3[TP-I], and 5[TP-I] molecular system. For the single TP-I molecular system, the optimized bond distance percentage differences of O_1-C_1, C_1-N_2, C_4-N_4, and C_7-N_3 computed using DFT/B3LYP/6-31G method are 4.174%, 2.412%, 2.148%, and 4.414%, respectively, whereas for DFT/B3LYP/6-31G** method are calculated to be 2.087%, 2.120%, 1.037%, and 3.425%, respectively. Conversely, the optimized bond distances of O_1-C_1, C_1-N_2, C_4-N_4, and C_7-N_3 in the 5[TP-I] molecular system significantly decrease in length and show closer findings with the single crystal X-ray diffraction data. For DFT/B3LYP/6-31G method, the optimized bond distance percentage differences of O_1-C_1, C_1-N_2, C_4-N_4, and C_7-N_3 are decreased to 4.007%, 1.901%, 1.407%, and 2.816%, respectively, while for DFT/B3LYP/6-31G** method are reduced to 1.920%, 1.608%, 0.370%, and 1.979%, respectively. Besides, the 5[TP-I] molecular system also exhibit smaller bond angle percentage differences (i.e. O_1-C_1-N_1, C_1-N_1-C_6, C_1-N_1-C_2, and O_2-C_2-N_1) than the single TP-I molecular system if compared with experimental data. The existence of neighbouring molecules restricts the movement of

molecules and atoms, thus the pushing and pulling forces (i.e. intra and intermolecular interactions) between molecules and atoms are taking account in the geometry optimization calculation.

Table 4.27 (a): Optimized geometry structures of TP-I, 3[TP-I] and 5[TP-I] molecular system based on size effect study using DFT/B3LYP/6-31G method.

DFT/B3LYP/6-31G			
Atoms	TP-I	3[TP-I]	5[TP-I]
Bond Distance [Å]			
O_1-C_1	1.248	1.248	1.246
C_1-N_2	1.401	1.396	1.394
N_2-C_4	1.376	1.375	1.376
C_4-C_3	1.383	1.385	1.387
N_1-C_6	1.476	1.476	1.476
C_2-O_2	1.252	1.256	1.262
C_4-N_4	1.379	1.370	1.369
N_4-C_7	1.342	1.351	1.356
C_7-N_3	1.372	1.355	1.351
N_2-C_5	1.471	1.468	1.468
Bond Angle [°]			
O_1-C_1-N_1	121.633	121.434	120.932
C_1-N_1-C_6	117.106	116.914	116.927
C_1-N_1-C_2	126.665	126.817	126.516
O_2-C_2-N_1	121.910	121.514	121.335
C_5-N_2-C_4	120.508	121.117	121.215
C_2-C_3-C_4	123.443	122.775	122.797
C_4-N_4-C_7	104.299	104.629	104.476
C_4-C_3-N_3	105.148	105.445	105.364
Dihedral Angle [°]			
O_1-C_1-N_1-C_6	0.014	0.014	0.014
O_2-C_2-N_1-C_1	-178.984	-178.984	-178.984
C_1-N_2-C_4-C_3	-3.097	-3.087	-3.067
C_5-N_2-C_4-C_3	179.248	179.250	179.271
N_2-C_4-N_4-C_7	179.796	179.785	179.809
O_2-C_2-C_3-N_3	2.158	2.154	2.155

Table 4.27 (b): Optimized geometry structures of TP-I, 3[TP-I] and 5[TP-I] molecular system based on size effect study using DFT/B3LYP/6-31G** method.

DFT/B3LYP/6-31G**			
Atoms	TP-I	3[TP-I]	5[TP-I]
Bond Distance [Å]			
O_1-C_1	1.223	1.222	1.221
C_1-N_2	1.397	1.391	1.390
N_2-C_4	1.375	1.374	1.374
C_4-C_3	1.378	1.379	1.381
N_1-C_6	1.468	1.468	1.468
C_2-O_2	1.226	1.229	1.235
C_4-N_4	1.364	1.356	1.355
N_4-C_7	1.328	1.335	1.340
C_7-N_3	1.359	1.344	1.340
N_2-C_5	1.462	1.460	1.460
Bond Angle [°]			
O_1-C_1-N_1	121.738	121.434	121.014
C_1-N_1-C_6	117.062	116.862	116.878
C_1-N_1-C_2	127.151	127.338	127.064
O_2-C_2-N_1	122.161	121.792	121.549
C_5-N_2-C_4	120.353	120.997	121.075
C_2-C_3-C_4	123.656	122.934	122.906
C_4-N_4-C_7	103.821	104.174	104.073
C_4-C_3-N_3	104.794	105.178	105.099
Dihedral Angle [°]			
O_1-C_1-N_1-C_6	0.014	0.014	0.014
O_2-C_2-N_1-C_1	-178.984	-178.984	-178.984
C_1-N_2-C_4-C_3	-3.112	-3.098	-3.083
C_5-N_2-C_4-C_3	179.237	179.233	179.250
N_2-C_4-N_4-C_7	179.796	179.781	179.798
O_2-C_2-C_3-N_3	2.157	2.154	2.154

Figure 4.27 (a): Bond distances for experimental, computed TP-I, 3[TP-I] and 5[TP-I] molecular system using DFT/B3LYP/6-31G method.

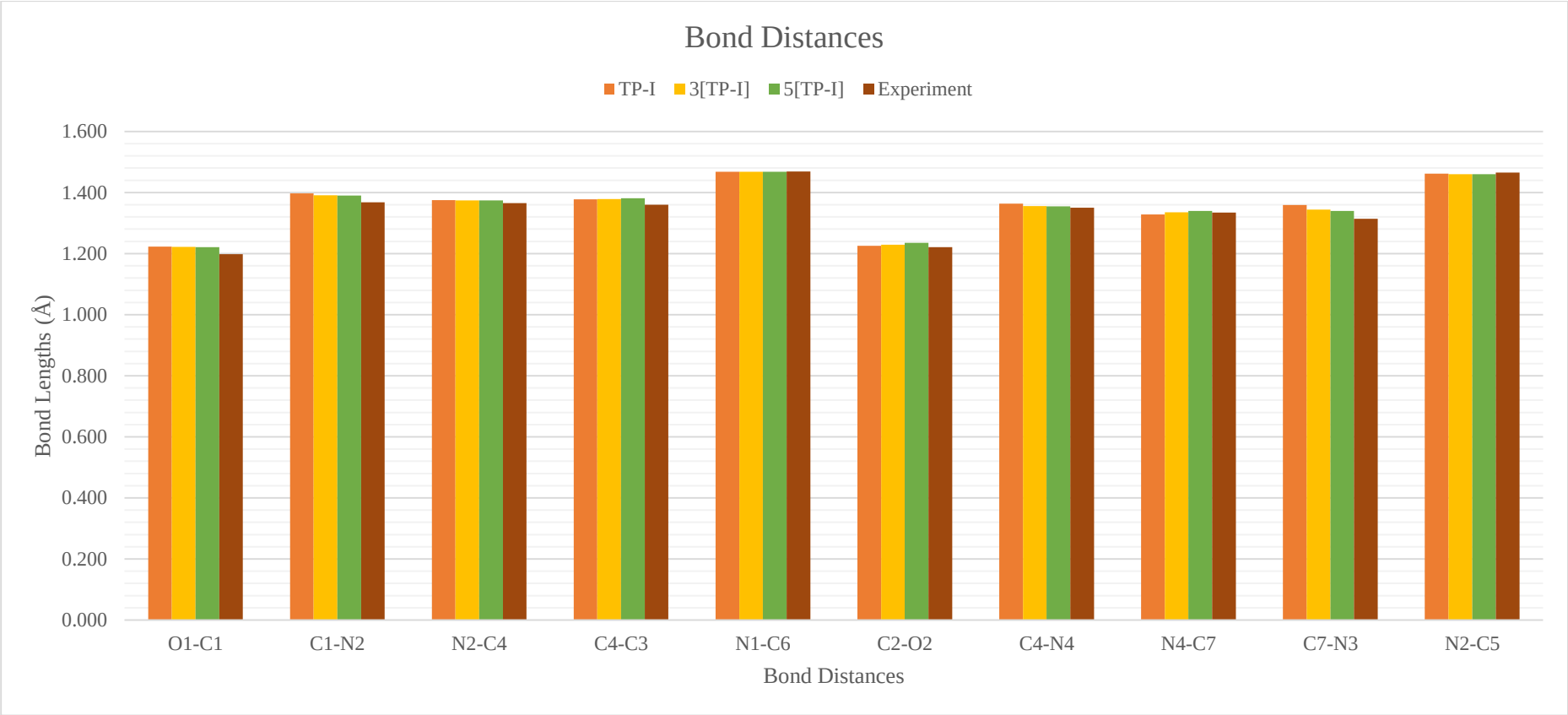

Figure 4.27 (b): Bond distances for experimental, computed TP-I, 3[TP-I] and 5[TP-I] molecular system using DFT/B3LYP/6-31G** method.

Table 4.27 (c) and (d) tabulate the calculated size effect electronic structures of TP-I, 3[TP-I] and 5[TP-I] molecular system using DFT/B3LYP/6-31G and DFT/B3LYP/6-31G** methods. From the computed total energies, it is denoted that the addition of theophylline molecules into the TP-I molecular system ((i.e. 3[TP-I] and 5[TP-I]) significantly increase the stability of the system. The findings supported well by Karki and Adhikari (2014) where the authors get a more stable H-graphene structure with the increment in the size of H-graphene clusters. The optimized total energies for 3[TP-I] and 5[TP-I] molecular system using DFT/B3LYP/6-31G method are -52308.550 eV and -87177.916 eV, respectively, while for DFT/B3LYP/6-31G** method are -52327.040 eV and 87209.021 eV, respectively. Besides, as can be observed from the tables, the HOMO-LUMO energy gaps decrease with the increment of the molecular size in the TP-I system. A similar situation is obtained by Shukla and Leszczynski (2006) during their computation study in carbon nanostructures. This is because the presents of neighbouring molecules increase the overlapping between orbitals and the delocalisation of electrons in a system. So that the energy levels will progressively become closer (Jain, 2005). With values of 4.702 eV (6-31G basis set) and 4.788 eV (6-31G** basis set), 5[TP-I] show closer energy gap with UV-Vis experimental results (4.580 eV) as compared with TP-I and 3[TP-I] molecular system. Moreover, similar to TP-I molecular system, 3[TP-I] and 5[TP-I] molecular system show maximum dipole moment contribution from Z-direction (μ_z). The computed dipole moments for 3[TP-I] and 5[TP-I] molecular system using DFT/B3LYP/6-31G method are 4.893 Debye and 10.012 Debye, respectively, while for DFT/B3LYP/6-31G** method are 4.608 Debye and 9.792 Debye, respectively. The differences in the dipole moments may due to the

asymmetry of the molecular structures during the computational calculation. From the size effect study, the increment of molecular sizes during DFT computational analysis of course will generate high accuracy output results that show good accordance with experimental data. However, at the same times, the computational power, time and cost also increase substantially (Hasnip *et al.*, 2014; Kirste, 2016).

Table 4.27 (c): Computed electronic properties of TP-I, 3[TP-I] and 5[TP-I] molecular system based on size effect study using DFT/B3LYP/6-31G level of theory.

	DFT/B3LYP/6-31G		
	TP-I	3[TP-I]	5[TP-I]
Total Energy [eV]	-17438.443	-52308.550	-87177.916
HOMO [eV]	-6.283	-6.145	-6.169
LUMO [eV]	-1.282	-1.377	-1.468
HOMO-LUMO Energy Gap (eV)	5.002	4.767	4.702
Dipole Moment [Debye]	3.642	4.893	10.012

Table 4.27 (d): Computed electronic properties of TP-I, 3[TP-I] and 5[TP-I] molecular system based on size effect study using DFT/B3LYP/6-31G** level of theory.

	DFT/B3LYP/6-31G**		
	TP-I	3[TP-I]	5[TP-I]
Total Energy [eV]	-17444.539	-52327.040	-87209.021
HOMO [eV]	-6.083	-6.003	-6.002
LUMO [eV]	-0.961	-1.202	-1.213
HOMO-LUMO Energy Gap (eV)	5.122	4.801	4.788
Dipole Moment [Debye]	3.481	4.608	9.792

4.5: Theophylline Monohydrate Compound (TP-II) ($C_7H_8N_4O_2 \cdot H_2O$)

The polymorphism in TP monohydrate is not a recent new discovery but has been reported by researchers many years ago. Sutor (1958) discovered the first TP monohydrate form in 1958. The authors realized that the TP monohydrate crystal is crystallized in a monoclinic space group of $P2_1$ with lattice parameters of a = 13.300 Å, b = 15.300 Å, c = 4.500 Å, and β = 99.500°. Later, another crystal structure form of TP monohydrate is reported by Sun *et al.* (2002). It is crystallized in a monoclinic space group of $P2_{1/n}$ and has lattice constants of a = 4.468 Å, b = 15.355 Å, c = 13.123 Å, and β = 97.792°. From the X-ray diffraction result, Sun *et al.* (2002) found that the TP monohydrate crystal structure contains two disorder sites (50:50 occupancy) in the hydrogen atoms. One is at the water molecule and another one is at the methyl group that is linked with the pyrimidine ring of the TP molecule. In this present work, a new polymorphic form of TP monohydrate is found in TP-II and TP-III crystal samples. Both of TP-II and TP-III do not contain any disorder sites in their TP monohydrate crystal structure, which makes them different from Sun *et al.* (2002) findings. Figure 4.28 (a) illustrates the complete unit cell and full single molecular structure of TP-II and TP-III compounds. With chemical formula of $C_7H_8N_4O_2 \cdot H_2O$, both of them contain one theophylline molecule and one water molecule in their single molecular system. Even though the crystallization procedures for TP-II and TP-III crystals are different but the end products obtained show high similarity with each other. Table 4.28 (a) and (b) summarise the crystal space groups, lattice constants, and geometry parameters of the TP-II and TP-III molecular system. From the tables, both of them are crystallized in

the monoclinic space group of $P2_{1/n}$. The TP-II compound has lattice parameters of a = 4.489 Å, b = 15.408 Å, c = 13.287 Å, and β = 98.591°, whereas the TP-III compound shows lattice constants of a = 4.499 Å, b = 15.451 Å, c = 13.329 Å, and β = 98.581°. As compared between the geometry parametrs (i.e. bond distances, bond angles, and dihedral angles) of the TP-II and TP-III molecular system, noted that both of them have approximately identical geometry structures. So that, TP-II compound is chosen as the main computational study target in this work. Figure 4.28 (b) provides the details labelling and numbering scheme of the TP-II single molecular system that act as the local environment for the entire DFT computational calculations. The geometry structures, electronic properties, and vibrational spectrums of TP-II (TP monohydrate) molecular system are discussed.

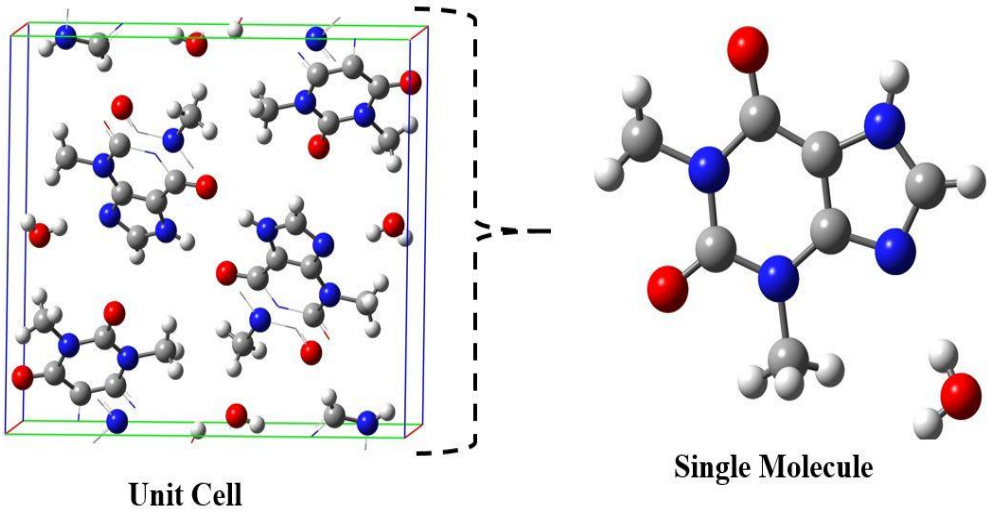

Figure 4.28 (a): The complete unit cell and single molecule of TP-II and TP-III.

Table 4.28 (a): Lattice parameters of TP-II and TP-III molecular system.

TP-II	TP-III
$C_7H_8N_4O_2 \cdot H_2O$	$C_7H_8N_4O_2 \cdot H_2O$
Monoclinic, $P2_{1/n}$	Monoclinic, $P2_{1/n}$
a = 4.499 Å, b = 15.451 Å, c = 13.329 Å	a = 4.489 Å, b = 15.408 Å, c = 13.287 Å
α = 90.000°, β = 98.581°, γ = 90.000°	α = 90.000°, β = 98.591°, γ = 90.000°

Table 4.28 (b): Comparison between the experimental (single crystal X-ray diffraction) geometry parameters of TP-II with TP-III molecular system.

$C_7H_8N_4O_2 \cdot H_2O$		
Atoms	TP-II	TP-III
Bond Distance [Å]		
O_1-C_1	1.222	1.220
C_1-N_2	1.373	1.368
N_2-C_4	1.375	1.371
C_4-C_3	1.369	1.367
N_1-C_6	1.478	1.471
C_2-O_2	1.236	1.234
C_4-N_4	1.364	1.358
N_4-C_7	1.334	1.330
C_7-N_3	1.342	1.340
N_2-C_5	1.465	1.458
N_4-O_3	2.925	2.918
C_7-O_3	3.789	3.777
Bond Angle [°]		
O_1-C_1-N_1	120.755	120.613
C_1-N_1-C_6	116.342	116.449
C_1-N_1-C_2	126.006	125.933
O_2-C_2-N_1	120.435	120.298
C_5-N_2-C_4	121.222	121.238
C_2-C_3-C_4	122.943	122.789
C_4-N_4-C_7	103.308	103.590
C_4-C_3-N_3	105.180	105.261
H_9-O_3-H_{10}	99.644	98.379
Dihedral Angle [°]		
O_1-C_1-N_1-C_6	-4.567	-4.822
O_2-C_2-N_1-C_1	-179.755	-179.800
C_5-N_2-C_4-C_3	-178.829	-178.809
N_2-C_4-N_4-C_7	179.946	179.930
O_2-C_2-C_3-N_3	-0.879	-0.952

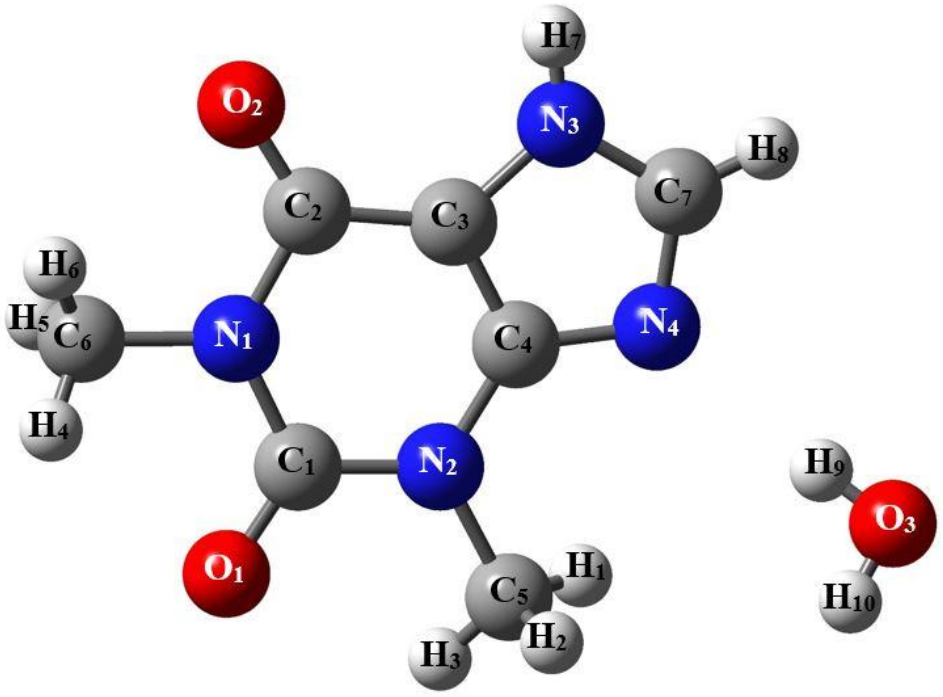

Figure 4.28 (b): Labelling and numbering details in TP-II single molecule.

4.5.1 Molecular Geometry Structural Analysis

Figure 4.29 illustrates parts of the experimental geometry parameters of the TP-II single molecular system obtained from the single crystal X-ray diffraction experiment. Similar to TP-I molecular system, it contains C=O, C=C, C=N, C-C, C-N, N-H, and C-H bonds in its TP molecular moieties. The presence of the water molecule in the TP-II molecular system makes it has an extra O-H type of bonding in its molecular structure. There is no doubt that the presence of the water molecule had slightly change the overall geometry structures of the TP-II molecular system as compared with the TP-I molecule. Consequently, may alter the electronic and physicochemical properties of TP-II molecule from TP-I molecule (Suma and Aruldhas, 2019). As can be observed in Figure 4.29, O_1-C_1

and C_2-O_2 with values of 1.222 Å and 1.236 Å, remain their double bond characteristic in the TP-II molecule although the bond lengths are slightly enlarged than the TP-I molecule (Benhalima *et al.*, 2018). With bond lengths of 1.478 Å and 1.465 Å, bond distances N_1-C_6 and N_2-C_5 fall within a reasonable range of the single N-C bond length (1.470 Å). Besides, the aromatic (i.e. pyrimidine ring and imidazole ring) conjugated characteristic in the TP-II molecular system can be observed from bond distances C_4-C_3 (1.369 Å), C_1-N_2 (1.373 Å), C_4-N_4 (1.364 Å), and N_4-C_7 (1.334 Å), since all of them have bond length values situated between the single C-C, C-N bonds and double C=C, C=N bonds (*Selected Bond Energies*, 2003; Wired Chemist, 2021). Noticed that the bond distance in H_9-O_3 (0.832 Å) is slightly shorter than H_{10}-O_3 (0.841 Å). This is due to the presents of N_4—H_9…O_3 hydrogen bond interaction, which affects the stiffness of the bond (Narayan, 2012; Suma and Aruldhas, 2019). For the same reason, it is found that the bond angle H_9-O_3-H_{10} in the water molecule has an angle of 99.644°, which is different from the normal tetrahedron structure of H_2O (109.000° to 104.5.000°) (Khan, 2021). It is worth to mention that with the donor-acceptor distance of 2.925 Å and donor—hydrogen..acceptor angle of 168.340°, the strength of the hydrogen bond in N_4—H_9…O_3 is defined as moderate type (Pumpo, 2016). Moreover, it is observed that the pyrimidine ring of the TP-II molecular system exhibits a more hexagonal shape than the TP-I molecule since the bond angles of C_1-N_1-C_2 (126.006°) and C_2-C_3-C_4 (122.943°) have a closer angle to 120.000°. In Figure 4.29, dihedral angle N_2-C_4-N_4-C_7 with value of 179.946°, shows planarity between the pyrimidine ring and imidazole ring of the TP molecule.

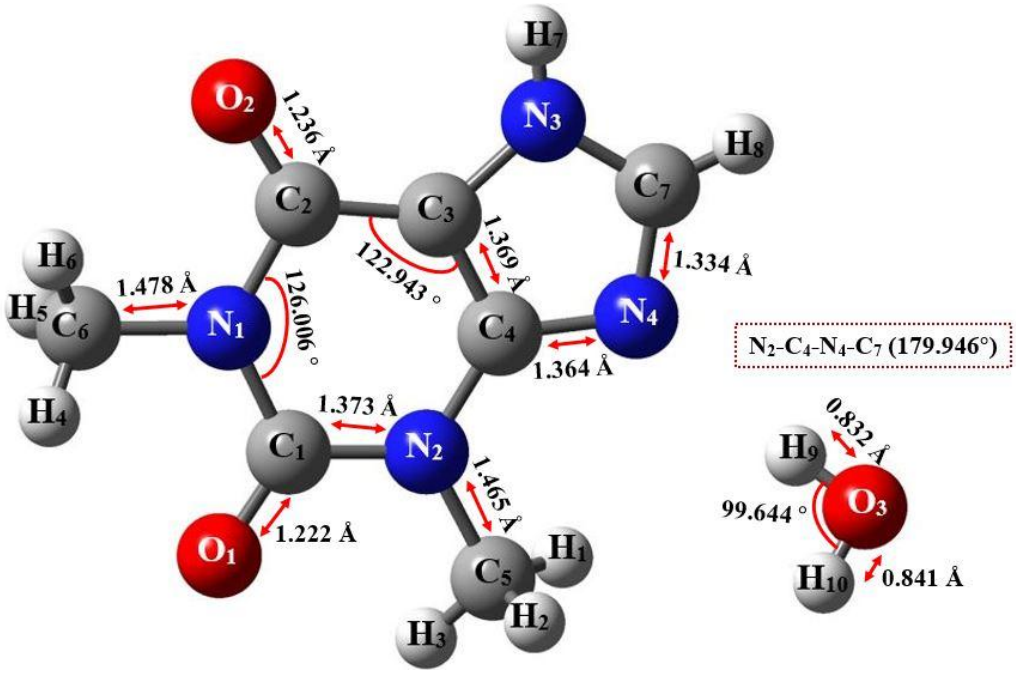

Figure 4.29: Parts of the geometry parameters (i.e. bond distances, bond angles, and dihedral angles) of TP-II molecular system.

Table 4.29 summarises the experimental and optimized geometry structures of the TP-II single molecular system. Both of the computational geometry structures show satisfactory agreement with experimental data. As can be obtained in Table 4.29, both of the DFT/B3LYP/6-31G and DFT/B3LYP/6-31G** computational methods show the largest fluctuation in bond distance C_1-N_2, bond angle O_2-C_2-N_1, and dihedral angle O_2-C_2-C_3-N_3. For DFT/B3LYP/6-31G method, the highest percentage differences in bond distance C_1-N_2, bond angle O_2-C_2-N_1, and dihedral angle O_2-C_2-C_3-N_3 are 2.112% (0.029 Å), 1.710% (2.059 °), and 3.072% (0.027 °), respectively, whereas for DFT/B3LYP/6-31G** method are 1.821% (0.025 Å), 1.988% (2.394°), and 3.185% (0.028°), respectively. The small variation between computational and experimental results is mainly caused by the differences in the environment during the data collection process. The computational calculation is carried out

under gases condition, while the experimental data is obtained from the solid bulk case (Karthika *et al.*, 2012; Novena *et al.*, 2016; Pumpo, 2016; Kabouchi *et al.*, 2017; Novena *et al.*, 2017). Noticed that both of the TP-II optimized geometry structures show high suitability for further computational analysis since the discrepancies between theoretical and computational results are not more than 4.000%.

Table 4.29: The experimental and optimized geometry parameters of TP-II molecular system.

$C_7H_8N_4O_2{\cdot}H_2O$ (TP-II)			
Atoms	DFT/B3LYP/6-31G	DFT/B3LYP/6-31G**	Experiment
Bond Distance [Å]			
O_1-C_1	1.246	1.221	1.222
C_1-N_2	1.402	1.398	1.373
N_2-C_4	1.373	1.373	1.375
C_4-C_3	1.382	1.377	1.369
N_1-C_6	1.476	1.468	1.478
C_2-O_2	1.251	1.225	1.236
C_4-N_4	1.378	1.364	1.364
N_4-C_7	1.344	1.330	1.334
C_7-N_3	1.367	1.355	1.342
N_2-C_5	1.470	1.462	1.465
N_4-O_3	2.904	2.975	2.925
C_7-O_3	3.775	3.845	3.789
Bond Angle [°]			
O_1-C_1-N_1	121.801	121.763	120.755
C_1-N_1-C_6	116.354	116.137	116.342
C_1-N_1-C_2	126.553	126.989	126.006
O_2-C_2-N_1	122.494	122.829	120.435
C_5-N_2-C_4	121.376	121.336	121.222
C_2-C_3-C_4	123.553	123.849	122.943
C_4-N_4-C_7	104.901	104.350	103.308
C_4-C_3-N_3	105.209	104.917	105.180
H_9-O_3-H_{10}	99.644	99.644	99.644
Dihedral Angle [°]			
O_1-C_1-N_1-C_6	-4.567	-4.567	-4.567
O_2-C_2-N_1-C_1	-179.755	-179.755	-179.755
C_5-N_2-C_4-C_3	-178.856	-178.871	-178.829
N_2-C_4-N_4-C_7	179.903	179.885	179.946
O_2-C_2-C_3-N_3	0.906	0.907	0.879

4.5.2 Total Energies and Frontier Molecular Orbital (FMO) Energies

Table 4.30 summarises the total energies, frontier molecular orbital energies, and global descriptors of the TP-II molecular system using DFT/B3LYP/6-31G and DFT/B3LYP/6-31G** methods. The optimized total energies using both DFT/B3LYP/6-31G and DFT/B3LYP/6-31G** level of theories are -19517.293 eV and -19524.267 eV. These elucidate that TP-II molecular system is more stable than the TP-I molecule since it has more negative total energy than the TP-I molecular system (KUMER *et al.*, 2019). In Table 4.30, the HOMO energy and LUMO energy obtained using DFT/B3LYP/6-31G level of theory are -6.662 eV and -1.633 eV, respectively, while for DFT/B3LYP/6-31G** method are -6.403 eV and -1.256eV, respectively. Noted that the HOMO and LUMO energies are important parameters used for the measurement of global descriptors via Koopmans theorem (Shoba, 2021). From the table, the ionization energy (IE), electron affinity (EA), hardness (η), chemical potential (μ), softness (S), electronegativity (χ), and electrophilicity index (ω) of the TP-II molecular system are 6.662 eV, 1.633 eV, 2.515, -4.148, 0.199, 4.148, and 3.421, respectively for DFT/B3LYP/6-31G method. For DFT/B3LYP/6-31G** method, the IE, EA, η, μ, S, χ, and ω are calculated to be 6.403 eV, 1.256 eV, 2.574, -3.830, 0.194, 3.830, and 2.849, respectively. Besides, the computed HOMO-LUMO energy gaps for TP-II molecular system are found in the range between 5.029 eV to 5.147 eV, which show nearly identical findings with the TP-I molecular system. As compared among the HOMO-LUMO energy gaps in TP-I, TP-II, theophyllinium chloride monohydrate (TCM) (Novena *et al.*, 2017), Theophyllinium nitrate (TN) (Novena *et al.*, 2016) and Theophylline –InP

diamantine (TInP) (Al Shaabani *et al.*, 2016), the softness, polarity, and chemical reactivity of the molecular system decrease in the sequence arrangement of TInP > TN > TP-I > TP-II > TCM, with the increase in HOMO-LUMO energy gap. Moreover, Figure 4.30 (a) and (b) show the HOMO-LUMO 3D surface mapped plots of the TP-II molecular system using DFT/B3LYP/6-31G and DFT/B3LYP/6-31G** level of calculations. Both of the methods produce approximately identical results. As can be observed in Figure 4.30 (a) and (b), majority of the electron densities are localised around the pyrimidine ring and imidazole ring of the TP-II molecular system. Noticed that there are no electron density distributions around the water molecule. This implies that the presence of water molecule in TP-II molecular system has no obvious impact on the HOMO-LUMO energy gap since the transition of electrons from HOMO→ LUMO are mainly occur between the pyrimidine ring and imidazole ring of the TP-II molecular system. Hence, explains the phenomena of having closer HOMO-LUMO energy gaps between pure TP and TP monohydrate compounds. Furthermore, the molecular orbital coefficients analysis explicit that the HOMO and LUMO orbitals are mainly composed of p_y type orbitals, indicates $\pi \rightarrow \pi^*$ type electronic transition in TP-II molecular system. Again, with the UV-Vis spectrum absorption peak of 271 nm, the experimental energy gap (4.580 eV) of TP-II molecular system show satisfactory agreement with computed results (Tariq *et al.*, 2019).

Table 4.30: Total energies, HOMO energies, LUMO energies, HOMO-LUMO energy gaps, and global descriptors of TP-II molecular system.

	$C_7H_8N_4O_2 \cdot H_2O$ (TP-II)	
	DFT/B3LYP/6-31G	DFT/B3LYP/6-31G**
Total Energy [eV]	-19517.293	-19524.267
HOMO [eV]	-6.662	-6.403
LUMO [eV]	-1.633	-1.256
HOMO-LUMO Energy Gap [eV]	5.029	5.147
Ionization Energy (IE) [eV]	6.662	6.403
Electron Affinity (EA) [eV]	1.633	1.256
Hardness (η)	2.515	2.574
Chemical Potential (μ)	-4.148	-3.830
Softness (S)	0.199	0.194
Electronegativity (χ)	4.148	3.830
Electrophilicity index (ω)	3.421	2.849

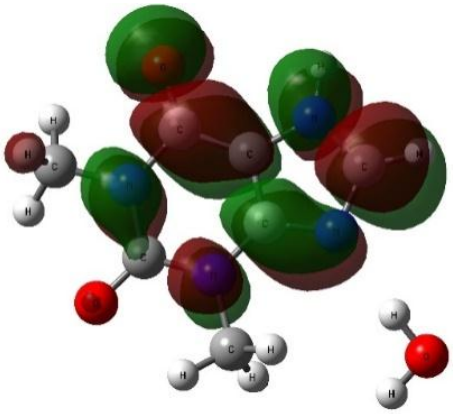

LUMO (-1.633 eV)

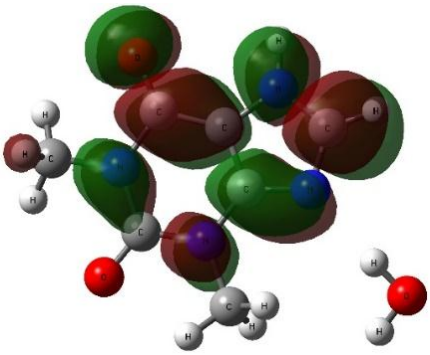

LUMO (-1.256 eV)

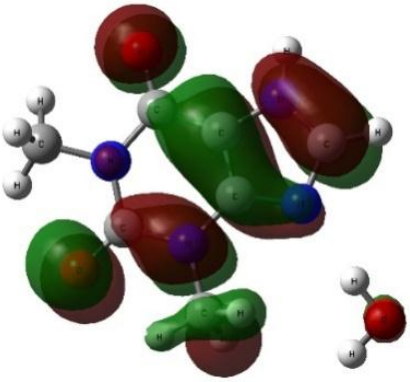

HOMO (-6.662 eV)

Figure 4.30 (a): LUMO and HOMO surface mapped plots of TP-II molecular system using DFT/B3LYP/6-31G method.

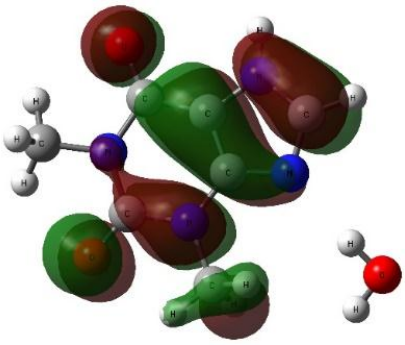

HOMO (-6.403 eV)

Figure 4.30 (b): LUMO and HOMO surface mapped plots of TP-II molecular system using DFT/B3LYP/6-31G** method.

4.5.3 Mulliken Population Analysis (MPA)

Table 4.31 and Figure 4.31 present the Mulliken atomic charges distribution of the TP-II molecular system obtained from DFT/B3LYP/6-31G and DFT/B3LYP/6-31G** level of calculations. Both of the computational methods show good agreement with each other. From the figure, noticed that the polarity

of the atomic charges in O, N, C, and H show a similar trend with the findings in TP-I molecular system. For example, all the oxygen and nitrogen atoms in TP-II molecular system show negative atomic charge values, while hydrogen atoms are all in positive atomic charge readings. The carbon atoms (C_1, C_2, C_3, C_4, and C_7) involve in the aromatic rings (i.e. pyrimidine ring and imidazole ring) show positive atomic charges, while carbon atoms (C_5 and C_6) which come from the methyl group, have negative atomic charge values. In Figure 4.31, the highest positive atomic charge is located in carbon atom C_1 due to the intensive electron withdrawing activity from the electronegative atoms O_1, N_1, and N_2. With the C=O double bond feature, carbon atom C_2 shows the second highest positive atomic charge reading (Benhalima *et al.*, 2018). Besides, oxygen atom O_3 show the highest negative atomic charge distribution in both computational methods (i.e. DFT/B3LYP/6-31G and DFT/B3LYP/6-31G**). From the computational results, clearly noted that hydrogen atom H_9 that bonded with O_3 atom elucidates higher positive charge distribution than H_{10} atoms. Furthermore, as compared with the TP-I molecular system, nitrogen atom N_4 show larger negative atomic charge distribution in the TP-II molecule. These proofs the existence of hydrogen bonding interaction between TP molecule with water molecule via N_4—H_9..O_{10} (Kanagathara *et al.*, 2013; Zaini *et al.*, 2018; Suma and Aruldhas, 2019). Moreover, noticed that in Table 4.31 and Figure 4.31, the atoms N_4, C_4, C_7, H_1, H_2, and H_8 located nearby the water molecule show drastic changes in the magnitude of the atomic charges if compared with the TP-I molecule (Table 4.23 and Figure 4.23). These indicate that the presence of water molecule alters the charge distribution in the TP-II molecular system which may also influence the electronic structure, dipole moment, and properties of the

TP-II molecular system as compared with TP-I molecule (Sharmi, 2015; Novena, Kumar *et al.*, 2016; Akman, 2017; Novena *et al.*, 2017). From the MPA analysis, it is suggested that O_1, O_2, O_3, N_1, N_2, N_3, and N_4 may have intra and intermolecular interaction with H_7, H_9, and H_{10} since all of them have considerable high negative and positive atomic charge distributions in TP-II molecular system (Kanagathara *et al.*, 2013; Meenatchi *et al.*, 2015; Novena *et al.*, 2017).

Table 4.31: Computed Mulliken atomic charges analysis (MPA) of TP-II molecular system using DFT/B3LYP/6-31G and DFT/B3LYP/6-31G** method.

$C_7H_8N_4O_2 \cdot H_2O$ (TP-II)					
MPA					
Atoms	DFT/B3LYP/6-31G	DFT/B3LYP/6-31G**	Atoms	DFT/B3LYP/6-31G	DFT/B3LYP/6-31G**
O_1	-0.445	-0.521	H_4	0.192	0.150
C_1	0.733	0.791	H_5	0.174	0.136
N_1	-0.672	-0.59	H_6	0.193	0.152
C_2	0.566	0.638	O_2	-0.446	-0.529
C_3	0.295	0.201	N_3	-0.729	-0.578
C_4	0.400	0.525	C_7	0.309	0.311
N_2	-0.677	-0.609	N_4	-0.469	-0.546
C_5	-0.25	-0.190	H_7	0.360	0.295
H_1	0.173	0.137	H_8	0.208	0.150
H_2	0.207	0.165	O_3	-0.762	-0.657
H_3	0.175	0.137	H_9	0.381	0.327
C_6	-0.237	-0.175	H_{10}	0.322	0.283

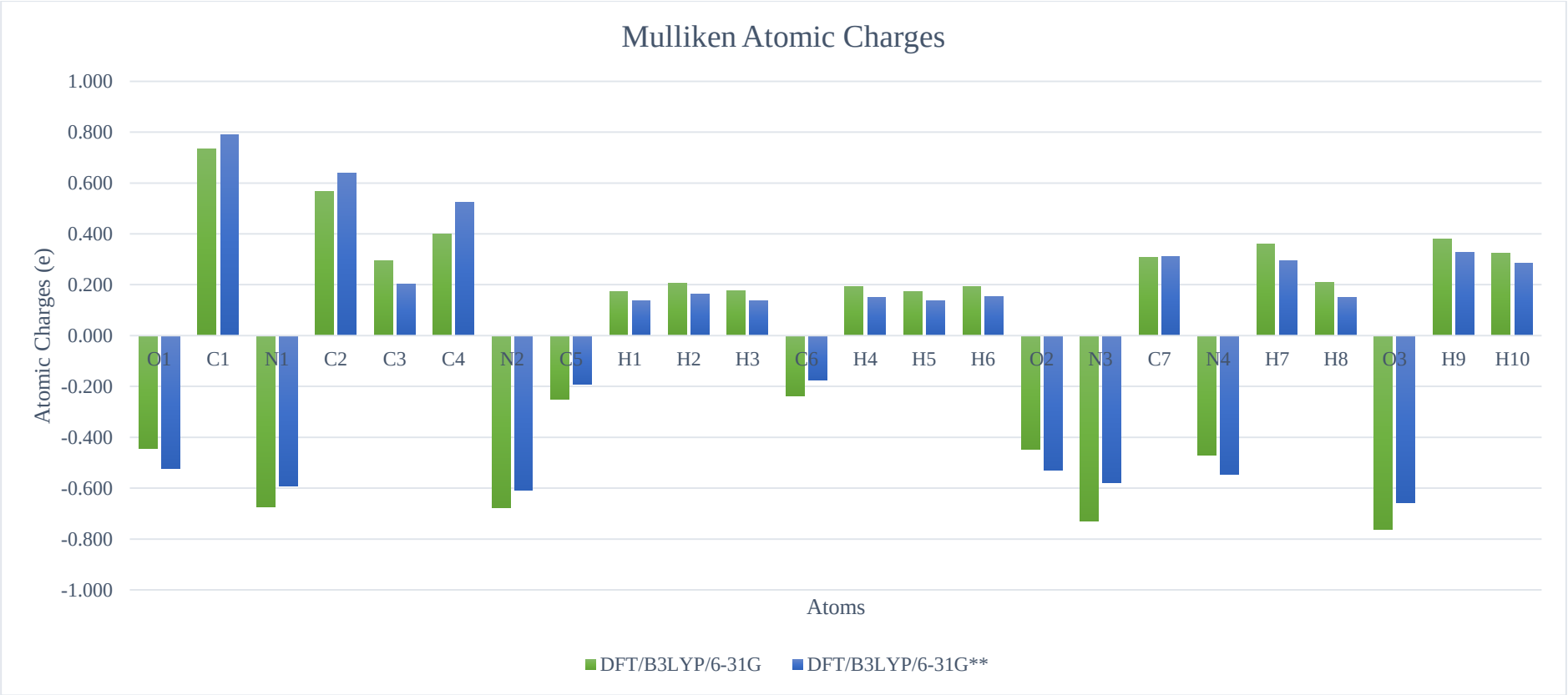

Figure 4.31: MPA analysis of TP-II molecular system using DFT/B3LYP/6-31G and DFT/B3LYP/6-31G** methods.

4.5.4 Molecular Electrostatic Potential (MEP)

Figure 4.32 (a) and (b) illustrate the 3D molecular electrostatic potential (MEP) surface mapped plots of TP-II molecular system using DFT/B3LYP/6-31G and DFT/B3LYP/6-31G** level of calculations. From the diagrams, both of the computational methods show identical results where the negative (red/ yellow) electrostatic potential regions are focused around electronegative oxygen atoms (O_1, O_2, and O_3), then suggested the sites for electrophilic attack (Benhalima *et al.*, 2018; Tribak *et al.*, 2019). Besides, the positive (blue) electrostatic potential regions are found to be located around electropositive hydrogen atoms (H_7 and H_8), thus proposed the sites for nucleophilic attack (Shoba, 2021). Those regions are important since they give the picture of the possible regions where the intra and intermolecular reaction may take place in the TP-II molecular system (Sridevi, 2012; Kabouchi *et al.*, 2017). Noticed that the nitrogen atom (N_4) in the TP-II molecular system show green colour electrostatic potential (neutral) and do not consider as one of the sites for the electrophilic reaction as found in the TP-I molecular system (Figure 4.24 (a) and (b)). This is due to the hydrogen bonding interaction between theophylline molecule and water molecule through N_4---H_9--O_3. By using Multifwn software, the global extrema points (i.e. maximum and minimum) of the TP-II molecular system are mapped on the MEP surface plots. The surface maximum points for both DFT/B3LYP/6-31G and DFT/B3LYP/6-31G** methods are located on hydrogen atom (H_7) with values of 2.725 eV and 2.559 eV. For the surface minimum points, TP-II molecular system shows distinctive results as compared with the TP-I molecular system. The calculated surface minimum points are found on oxygen atom (O_3) with

values of -2.476 eV and -1.975 eV, respectively for DFT/B3LYP/6-31G and DFT/B3LYP/6-31G** theories.

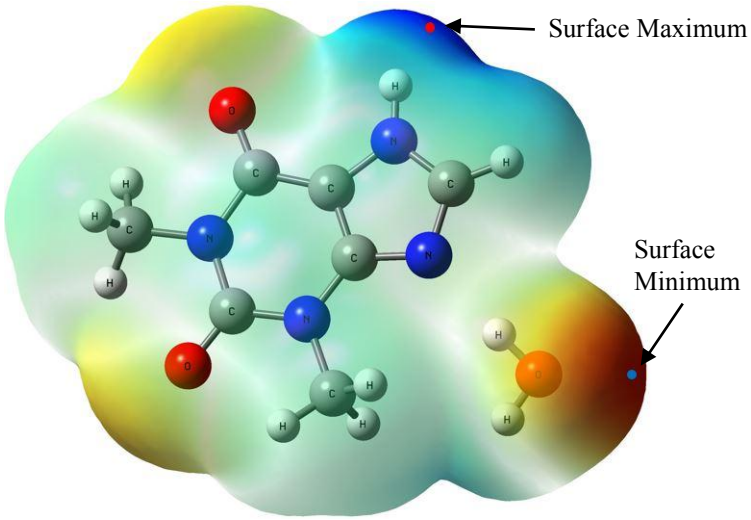

Surface Minimum (blue dot) - -2.476 eV
Surface Maximum (red dot) – 2.725 eV

Figure 4.32 (a): The MEP surface mapped plots of TP-II molecular system using DFT/B3LYP/6-31G method.

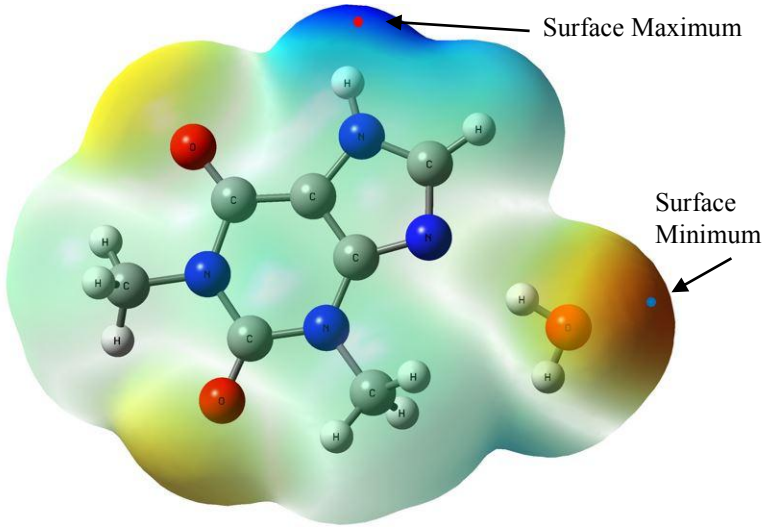

Surface Minimum (blue dot) - -1.975 eV
Surface Maximum (red dot) – 2.559 eV

Figure 4.32 (b): The MEP surface mapped plots of TP-II molecular system using DFT/B3LYP/6-31G** method.

4.5.5 Natural Bond Orbital (NBO) Analysis

The NBO analysis for TP-II molecular system using DFT/B3LYP/6-31G and DFT/B3LYP/6-31G** methods are summarised in Table 4.32 (a) and (b). Both of the computational methods (i.e. 6-31G and 6-31G** basis sets) give approximately the same NBO analysis. From the computed NBO analysis, the intra and intermolecular charge transfer interactions among bonds in TP-II molecular system mainly come from the orbitals overlap between $\sigma \rightarrow \sigma^*$, $\pi \rightarrow \pi^*$, LP $\rightarrow \pi^*$, and LP $\rightarrow \sigma^*$. With the stabilisation energies of 1.261/1.209 eV, 1.037/1.087 eV and 0.606/0.576 eV, both of the DFT/B3LYP/6-31G and DFT/B3LYP/6-31G** methods show stronger intramolecular conjugative interaction in π (C_3-C_4) $\rightarrow \pi^*$ (C_2-O_2), π (C_7-N_4) $\rightarrow \pi^*$ (C_3-C_4), and π (C_3-C_4) $\rightarrow \pi^*$ (C_7-N_4). These overlapping of $\pi \rightarrow \pi^*$ orbitals play a significant role in the structural stabilisation in TP-II molecule. Besides, intermolecular interaction between theophylline and water molecule can be observed via the orbital overlap in LP (N_4) $\rightarrow \sigma^*$(O_3-H_9) with stabilisation energy of 0.706 eV and 0.506 eV, respectively for DFT/B3LYP/6-31G and DFT/B3LYP/6-31G** methods. Furthermore, NBO analysis in Table 4.32 (a) and (b) clearly state that LP $\rightarrow \pi^*$ orbitals have considerable high $E(2)$ than $\pi \rightarrow \pi^*$ orbitals. These indicate that the transition of charge between LP $\rightarrow \pi^*$ orbitals are more intensive than $\pi \rightarrow \pi^*$ orbitals and have a larger contribution to the structural stabilisation in the TP-II molecular system. For examples, the stabilisation energies of LP (N_1) $\rightarrow \pi^*$ (O_1-C_1), LP (N_1) $\rightarrow \pi^*$ (C_2-O_2), LP (N_2) $\rightarrow \pi^*$ (O_1-C_1), LP (N_2) $\rightarrow \pi^*$ (C_3-C_4), LP (N_3) $\rightarrow \pi^*$ (C_3-C_4), and LP (N_3) $\rightarrow \pi^*$ (C_7-N_4) using DFT/B3LYP/6-31G method are 2.649 eV, 2.523 eV, 2.657 eV, 2.160 eV, 1.384 eV, and 2.506 eV,

respectively, while for DFT/B3LYP/6-31G** theory are 2.499 eV, 2.353 eV, 2.517 eV, 2.087 eV, 1.337 eV, and 2.567 eV, respectively.

Table 4.32 (a): Donor-acceptor interactions and second order perturbation energies of TP-II molecular system using DFT/B3LYP/6-31G method.

Donor NBO (i)	ED/e	Acceptor NBO (j)	ED/e	E(2) [kcal/mol]	E(2) [eV]	E(j) - E(i) [a.u]	F (i,j) [a.u]
σ (C_1-N_2)	1.983	σ* (C_4-N_4)	0.021	4.270	0.185	1.260	0.065
σ (N_1-C_2)	1.984	σ* (C_3-N_3)	0.023	4.510	0.196	1.210	0.066
σ (C_2-C_3)	1.976	σ* (C_3-C_4)	0.030	4.820	0.209	1.290	0.070
π (C_2-O_2)	1.979	π* (C_3-C_4)	0.430	5.920	0.257	0.360	0.046
π (C_3-C_4)	1.733	π* (C_2-O_2)	0.367	29.070	1.261	0.280	0.082
π (C_3-C_4)	1.733	π* (C_7-N_4)	0.416	13.980	0.606	0.250	0.055
σ (C_3-N_3)	1.982	σ* (C_4-N_2)	0.038	4.380	0.190	1.260	0.067
σ (N_3-C_7)	1.99	σ* (C_2-C_3)	0.055	4.690	0.203	1.350	0.072
σ (C_7-N_4)	1.983	σ* (C_4-N_2)	0.038	7.380	0.320	1.290	0.088
π (C_7-N_4)	1.848	π* (C_3-C_4)	0.430	23.910	1.037	0.320	0.085
LP (N_1)	1.615	π* (O_1-C_1)	0.396	61.090	2.649	0.240	0.108
LP (N_1)	1.615	π* (C_2-O_2)	0.367	58.180	2.523	0.250	0.107
LP (N_2)	1.627	π* (O_1-C_1)	0.396	61.270	2.657	0.250	0.111
LP (N_2)	1.627	π* (C_3-C_4)	0.430	49.810	2.160	0.270	0.105
LP (N_3)	1.565	π* (C_3-C_4)	0.430	31.920	1.384	0.290	0.086
LP (N_3)	1.565	π* (C_7-N_4)	0.416	57.780	2.506	0.250	0.108
LP (N_4)	1.903	σ* (O_3-H_9)	0.037	16.290	0.706	0.850	0.106

Table 4.32 (b): Donor-acceptor interactions and second order perturbation energies of TP-II molecular system using DFT/B3LYP/6-31G** method.

Donor NBO (i)	ED/e	Acceptor NBO (j)	ED/e	E(2) [kcal/mol]	E(2) [eV]	E(j) - E(i) [a.u]	F (i,j) [a.u]
σ (C_1-N_2)	1.983	σ* (C_4-N_4)	0.019	4.350	0.189	1.290	0.067
σ (N_1-C_2)	1.984	σ* (C_3-N_3)	0.021	4.460	0.193	1.230	0.066
π (C_2-O_2)	1.982	π* (C_3-C_4)	0.422	5.010	0.217	0.380	0.043
π (C_3-C_4)	1.735	π* (C_2-O_2)	0.349	27.880	1.209	0.300	0.083
π (C_3-C_4)	1.735	π* (C_7-N_4)	0.415	13.290	0.576	0.260	0.055
σ (C_3-N_3)	1.981	σ* (C_4-N_2)	0.039	4.630	0.201	1.280	0.069
σ (C_4-N_4)	1.979	σ* (C_7-H_8)	0.016	4.330	0.188	1.270	0.066
σ (N_3-C_7)	1.989	σ* (C_2-C_3)	0.060	4.930	0.214	1.340	0.074
σ (C_7-N_4)	1.981	σ* (C_4-N_2)	0.039	8.390	0.364	1.310	0.094
π (C_7-N_4)	1.844	π* (C_3-C_4)	0.422	25.070	1.087	0.340	0.088
LP (N_1)	1.626	π* (O_1-C_1)	0.377	57.630	2.499	0.260	0.110
LP (N_1)	1.626	π* (C_2-O_2)	0.349	54.260	2.353	0.270	0.108
LP (N_2)	1.637	π* (O_1-C_1)	0.377	58.040	2.517	0.270	0.112
LP (N_2)	1.637	π* (C_3-C_4)	0.422	48.120	2.087	0.280	0.105
LP (N_3)	1.565	π* (C_3-C_4)	0.422	30.830	1.337	0.300	0.086
LP (N_3)	1.565	π* (C_7-N_4)	0.415	59.200	2.567	0.260	0.112
LP (N_4)	1.906	σ* (O_3-H_9)	0.027	11.660	0.506	0.900	0.093

4.5.6 Non-Linear Optical (NLO) Properties

Table 4.33 tabulates the dipole moment (μ) and first hyperpolarizability (β_{tot}) of TP-II molecular system using DFT/B3LYP/6-31G and DFT/B3LYP/6-31G** methods. The presences of water molecule nearby the imidazole ring of the TP molecule reduces the dipole moment of the TP-II molecular system (Zaini *et al.*, 2018). In Table 4.33, the calculated dipole moment using DFT/B3LYP/6-31G method is 2.562 Debye, while for DFT/B3LYP/6-31G** method is 2.332 Debye. Both of the computational methods show that the dipole moment contributions are mainly from X (μ_x) and Z (μ_z) directions. Besides, the first polarizability (β_{tot}) of TP-II molecular system obtains via DFT/B3LYP/6-31G and DFT/B3LYP/6-31G** theories are 10.750 x 10^{-30} e.s.u and 10.130 x 10^{-30} e.s.u, respectively. These indicate that TP-II molecular system can be considered as a good NLO materials since it has higher dipole moment (μ) and first hyperpolarizability (β_{tot}) than urea (Boukabcha *et al.*, 2015; Maache *et al.*, 2016; Rahmani *et al.*, 2018; Abbaz *et al.*, 2019). Moreover, the presence of hydrogen bonding in organic molecules will evidently increase the hyperpolarizability of the molecular system (Benhalima *et al.*, 2018). TP-II molecular system with the presence of an additional hydrogen bond between the TP molecule and water molecule (N_4---H_9--O_3), shows larger first hyperpolarizability (β_{tot}) than TP-I molecular system. Hence, exhibits more NLO active nature than TP-I molecule.

Table 4.33: Computed dipole moment (μ) and first hyperpolarizability (β_{tot}) of TP-II molecular system using DFT/B3LYP/6-31G and DFT/B3LYP/6-31G** methods.

Parameters	DFT/B3LYP/6-31G	DFT/B3LYP/6-31G**
μ_x	1.757	1.304
μ_y	-0.550	-0.441
μ_z	1.781	1.882
μ [Debye]	2.562	2.332
β_{xxx}	282.087	254.497
β_{xyy}	49.420	48.307
β_{xzz}	88.792	75.660
β_{yyy}	-19.686	-19.351
β_{xxy}	-25.332	-21.117
β_{yzz}	-17.203	-14.306
β_{zzz}	-508.064	-489.042
β_{xxz}	-417.581	-382.123
β_{yyz}	-243.553	-236.753
β_{tot} [a.u]	1244.003	1172.057
β_{tot} [e.s.u]	10.750 x 10^{-30}	10.130 x 10^{-30}

4.5.7 Fourier Transform Infrared (FT-IR) Spectroscopy

Table 4.34 summarises parts of the experimental and theoretical FT-IR vibrational frequencies of the TP-II molecular system. With a total atomic number of 24, the TP-II molecule has 66 fundamental vibrational modes that quantitatively elucidate the functional groups presented in the molecular system. As can be observed in Table 4.34, both of the computational FT-IR vibrational spectrum (scaled) obtained using DFT/B3LYP/6-31G and DFT/B3LYP/6-31G** methods show satisfactory agreement with experimental data after the

employment of direct scaling technique (Che *et al.*, 2009; Marta *et al.*, 2010; Narayan, 2012; Sasaki *et al.*, 2016). Both the experimental and theoretical FT-IR results support the molecular structure of TP-II. It is worth to mention that majority of the FT-IR results in the TP-II molecular system show closer findings with the TP-I molecule since both of them have similar functional groups in the theophylline molecule, except for the water molecule which is absent from the TP-I molecular system. For example, an additional O-H stretching vibration mode from the water molecule of the TP-II molecular system can be observed at band region 3279 cm^{-1} (scaled 6-31G), 3520 cm^{-1} (scaled 6-31G**), and 3107 cm^{-1} (Experiment). Besides, band regions 3533 cm^{-1} (scaled 6-31G), 3523 cm^{-1} (scaled 6-31G**), and 3374 cm^{-1} (Experiment) are assigned to N-H stretching vibration mode. From the table, clearly noted that the C=C stretching vibrational mode from the pyrimidine ring of the TP-II molecular system can be obtained at band regions 1533 cm^{-1} (scaled 6-31G), 1536 cm^{-1} (scaled 6-31G**), and 1559 cm^{-1} (Experiment), whereas the C=C bending vibrational mode can be observed in band regions 745 cm^{-1} (scaled 6-31G), 771 cm^{-1} (scaled 6-31G**), and 746 cm^{-1} (Experiment). Furthermore, band regions between 2951 cm^{-1} to 3029 cm^{-1} (scaled 6-31G), 2939 cm^{-1} to 3014 cm^{-1} (scaled 6-31G**), and 2911 cm^{-1} to 3003 cm^{-1} (Experiment) are assigned for C-H stretching vibrational mode. Conversely, band regions 1435 cm^{-1}, 1424 cm^{-1}, 828 cm^{-1}, 610 cm^{-1} (scaled 6-31G), 1437 cm^{-1}, 1405 cm^{-1}, 807 cm^{-1}, 621 cm^{-1} (scaled 6-31G**), and 1445 cm^{-1}, 1420 cm^{-1}, 818 cm^{-1}, 615 cm^{-1} (Experiment) are all correspondence to C-H bending vibrational modes. Moreover, the C-N stretching vibration from the pyrimidine and imidazole rings of the TP-II molecular system can be observed between band regions 1177 cm^{-1} to 1358 cm^{-1} (scaled 6-31G), 1176 cm^{-1} to 1356 cm^{-1} (scaled

6-31G**), and 1199 cm^{-1} to 1320 cm^{-1} (Experiment).

Table 4.34: Experimental and computational (unscaled and scaled) FT-IR vibrational frequencies of TP-II molecular system.

Type of Vibration	DFT/B3LYP/6-31G		DFT/B3LYP/631G**		Experiment [cm^{-1}]
	Unscaled [cm^{-1}]	Scaled [cm^{-1}]	Unscaled [cm^{-1}]	Scaled [cm^{-1}]	
N-H Stretching Vibration	3673	3533	3666	3523	3374
O-H Stretching Vibration	3409	3279	3663	3520	3107
C-H Stretching Vibration	3148	3029	3136	3014	3003
C-H Stretching Vibration	3068	2951	3058	2939	2911
C=O Stretching Vibration	1732	1666	1765	1696	1655
C=C Stretching Vibration	1593	1533	1599	1536	1559
C-H Bending Vibration	1491	1435	1496	1437	1445
C-H Bending Vibration	1480	1424	1462	1405	1420
C-N Stretching Vibration	1412	1358	1411	1356	1320
C-N Stretching Vibration	1340	1289	1355	1302	1288
C-N Stretching Vibration	1223	1177	1224	1176	1199
C-H Bend Vibration	861	828	840	807	818
C=C Bend Vibration	775	745	803	771	746
C-H Bend Vibration	634	610	646	621	615

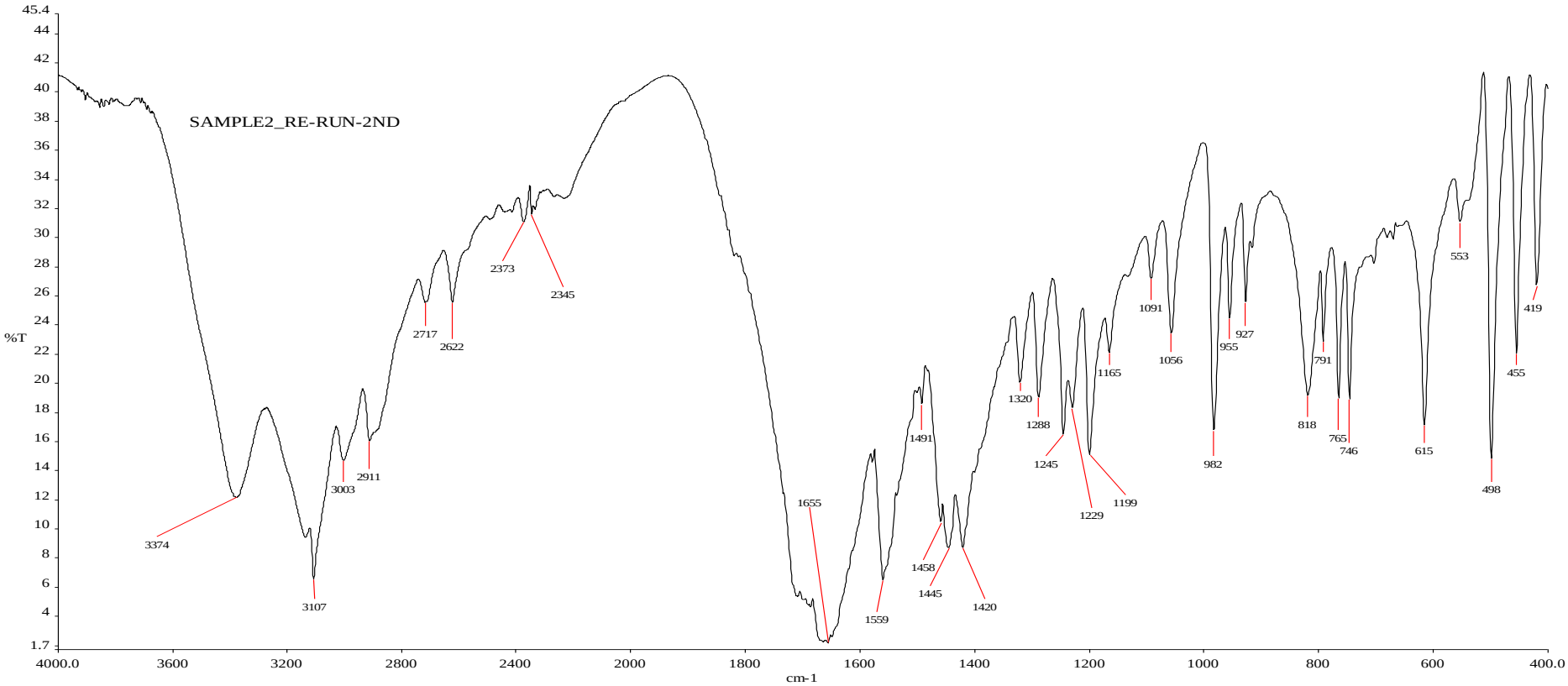

Figure 4.33: Experimental FT-IR vibrational spectrum of TP-II molecular system.

4.5.8 Size Effect Study

In order to figure out the effect of neighbouring molecules during DFT computational analysis, the single TP-II molecular system is added with additional theophylline monohydrate molecules as shown in Figure 4.34 (a), (b), (c), and (d). All the 3[TP-II], 5[TP-II], 7[TP-II], and 9[TP-II] molecular system are computed using DFT/B3LYP/6-31G and DFT/B3LYP/6-31G** level of calculations. The optimized geometry structures and calculated electronic properties are presented in this work.

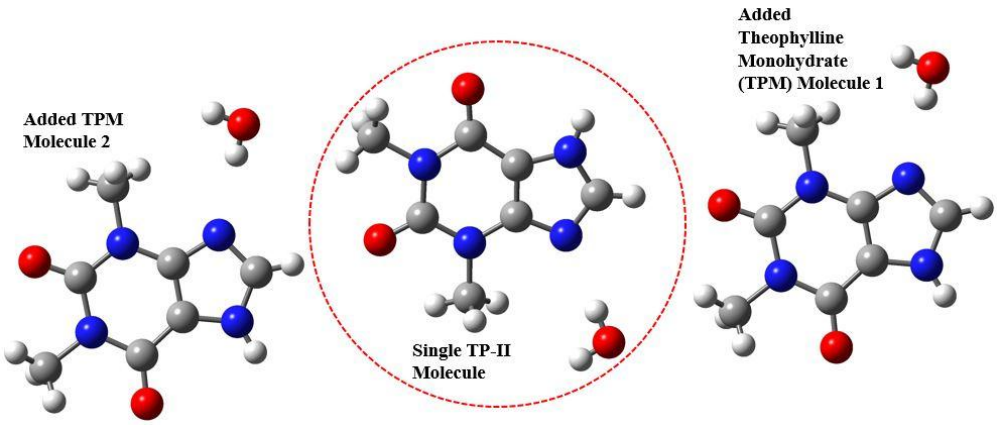

Figure 4.34 (a): The molecular structure of 3[TP-II] molecular system involved in the size effect study.

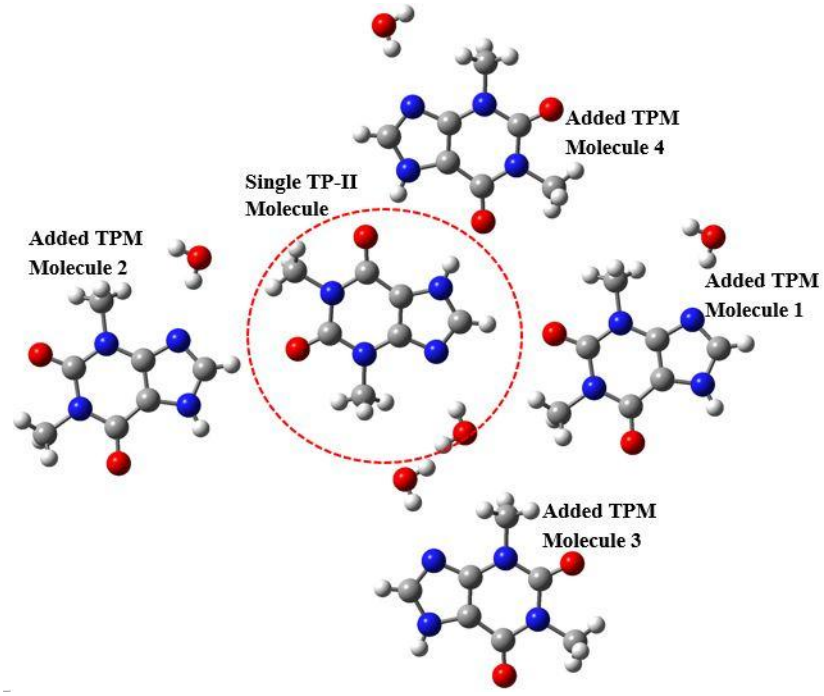

Figure 4.34 (b): The molecular structure of 5[TP-II] molecular system involved in the size effect study.

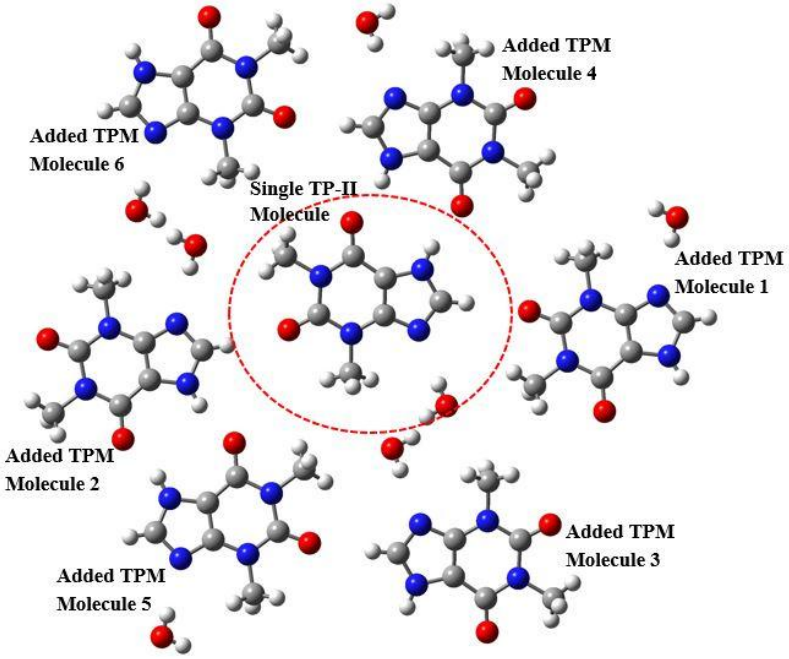

Figure 4.34 (c): The molecular structure of 7[TP-II] molecular system involved in the size effect study.

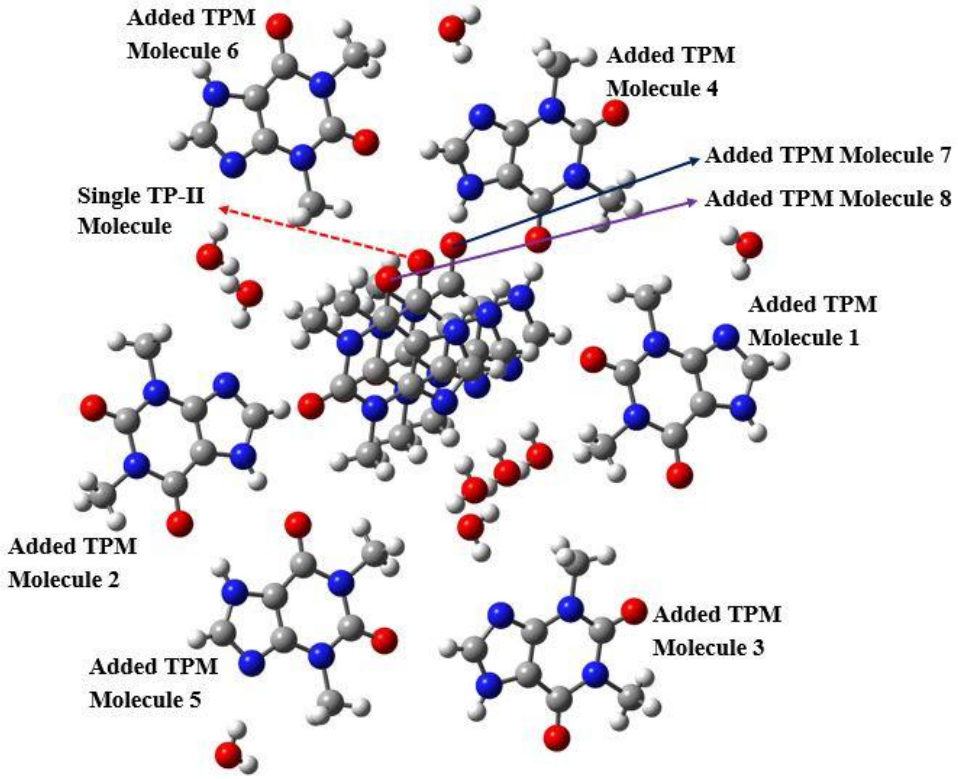

Figure 4.34 (d): The molecular structure of 9[TP-II] molecular system involved in the size effect study.

Table 4.35 (a) and (b) tabulate the optimized geometry structures of TP-II molecule obtained from TP-I, 3[TP-II], 5[TP-II], 7[TP-II], and 9[TP-II] molecular system. Again, all the optimized geometry structures of 3[TP-II], 5[TP-II], 7[TP-II], and 9[TP-II] molecular system computed via DFT/B3LYP/6-31G and DFT/B3LYP/6-31G** methods show satisfactory results with the single crystal X-ray diffraction experimental data. Clearly noticed that the increment of molecular size during geometry optimization calculation produce closer geometry parameters with experimental results. For example, the largest bond distance, bond angle, and dihedral angle percentage differences in the single TP-II molecular system using DFT/B3LYP/6-31G method are 2.112% (C_1-N_2), 1.710% (O_2-C_2-N_1), and 3.072% (O_2-C_2-C_3-N_3), respectively, whereas

for DFT/B3LYP/6-31G** method are 1.821%(C_1-N_2), 1.988% (O_2-C_2-N_1), and 3.185% (O_2-C_2-C_3-N_3), respectively. These discrepancies significantly decreased during the geometry optimization calculation in the 9[TP-II] molecular system. For DFT/B3LYP/6-31G level of calculation, the highest bond distance, bond angle, and dihedral angle percentage differences in the 9[TP-II] molecular system are further reduced to 1.602% (C_1-N_2), 0.221% (O_2-C_2-N_1), and 1.251% (O_2-C_2-C_3-N_3), while for DFT/B3LYP/6-31G** technique are decreased to 1.092%(C_1-N_2), 0.503% (O_2-C_2-N_1), and 1.024% (O_2-C_2-C_3-N_3). Figure 4.35 (a) and (b) summarise the bond distances of TP-II molecule taken from the experimental, calculated TP-I, 3[TP-II], 5[TP-II], 7[TP-II], and 9[TP-II] molecular system. With bond lengths of 1.375 Å and 1.360 Å, the bond distances C_4-N_4 and C_7-N_3 in the optimized 9[TP-II] molecular system elucidate smaller percentage differences (i.e. 0.806% and 1.343%) than the single TP-II molecular system via DFT/B3LYP/6-31G method. Besides, for DFT/B3LYP/6-31G** method, the optimized bond distances C_7-N_3, N_4-O_3, and C_7-O_3 with bond lengths of 1.348 Å, 2.907 Å, and 3.766 Å, show lower bond distance percentage differences in the optimized 9[TP-II] molecular system than the single TP-I molecular system. These reveal that the presents of neighboring molecules during DFT computational analysis strongly affect the accuracy of data because the intra and intermolecular interactions between neighbouring molecules will restrict the movement of atoms during the geometry optimization process.

Table 4.35 (a): Optimized geometry structures of TP-II, 3[TP-II], 5[TP-II], 7[TP-II], and 9[TP-II] molecular system based on size effect study using DFT/B3LYP/6-31G method.

DFT/B3LYP/6-31G					
Atoms	TP-II	3[TP-II]	5[TP-II]	7[TP-II]	9[TP-II]
Bond Distance [Å]					
O_1-C_1	1.246	1.250	1.249	1.249	1.249
C_1-N_2	1.402	1.399	1.397	1.397	1.395
N_2-C_4	1.373	1.376	1.374	1.374	1.370
C_4-C_3	1.382	1.380	1.388	1.388	1.388
N_1-C_6	1.476	1.483	1.483	1.480	1.481
C_2-O_2	1.251	1.250	1.261	1.259	1.261
C_4-N_4	1.378	1.377	1.373	1.373	1.375
N_4-C_7	1.344	1.349	1.356	1.356	1.356
C_7-N_3	1.367	1.367	1.359	1.359	1.360
N_2-C_5	1.470	1.469	1.474	1.473	1.473
N_4-O_3	2.904	2.852	2.847	2.844	2.857
C_7-O_3	3.775	3.705	3.706	3.703	3.721
Bond Angle [°]					
O_1-C_1-N_1	121.801	121.751	121.869	122.058	121.784
C_1-N_1-C_6	116.354	116.885	116.579	116.563	116.666
C_1-N_1-C_2	126.553	126.126	125.659	125.819	125.676
O_2-C_2-N_1	122.494	122.393	120.748	120.603	120.701
C_5-N_2-C_4	121.376	121.087	120.929	120.899	120.877
C_2-C_3-C_4	123.553	123.538	122.542	122.477	122.376
C_4-N_4-C_7	104.901	105.159	104.712	104.716	104.803
C_4-C_3-N_3	105.209	104.984	105.230	105.296	105.484
H_9-O_3-H_{10}	99.644	99.644	99.644	99.644	99.644
Dihedral Angle [°]					
O_1-C_1-N_1-C_6	-4.567	-4.567	-4.567	-4.567	-4.567
O_2-C_2-N_1-C_1	-179.755	-179.755	-179.755	-179.755	-179.755
C_1-N_2-C_4-C_3	0.543	0.568	0.599	0.585	0.597
C_5-N_2-C_4-C_3	-178.856	-178.842	-178.823	-178.830	-178.822
C_4-C_3-N_3-C_7	-0.169	-0.167	-0.196	-0.199	-0.204
N_2-C_4-N_4-C_7	179.903	179.925	179.965	179.955	179.962
O_2-C_2-C_3-N_3	-0.906	-0.906	-0.890	-0.887	-0.890

Table 4.35 (b): Optimized geometry structures of TP-II, 3[TP-II], 5[TP-II], 7[TP-II], and 9[TP-II] molecular system based on size effect study using DFT/B3LYP/6-31G** method.

DFT/B3LYP/6-31G**					
Atoms	TP-II	3[TP-II]	5[TP-II]	7[TP-II]	9[TP-II]
Bond Distance [Å]					
O_1-C_1	1.221	1.226	1.225	1.225	1.225
C_1-N_2	1.398	1.394	1.390	1.390	1.388
N_2-C_4	1.373	1.376	1.374	1.374	1.370
C_4-C_3	1.377	1.375	1.382	1.382	1.383
N_1-C_6	1.468	1.473	1.473	1.471	1.472
C_2-O_2	1.225	1.224	1.237	1.235	1.236
C_4-N_4	1.364	1.362	1.359	1.358	1.360
N_4-C_7	1.330	1.333	1.340	1.340	1.340
C_7-N_3	1.355	1.355	1.348	1.347	1.348
N_2-C_5	1.462	1.461	1.465	1.464	1.465
N_4-O_3	2.975	2.893	2.897	2.895	2.907
C_7-O_3	3.845	3.739	3.752	3.750	3.766
Bond Angle [°]					
O_1-C_1-N_1	121.763	121.293	121.221	121.378	121.136
C_1-N_1-C_6	116.137	116.628	116.308	116.261	116.385
C_1-N_1-C_2	126.989	126.707	126.268	126.433	126.280
O_2-C_2-N_1	122.829	122.771	121.030	120.897	121.041
C_5-N_2-C_4	121.336	121.133	121.058	121.015	121.010
C_2-C_3-C_4	123.849	123.806	122.895	122.830	122.737
C_4-N_4-C_7	104.350	104.670	104.173	104.171	104.265
C_4-C_3-N_3	104.917	104.753	105.018	105.075	105.281
H_9-O_3-H_{10}	99.644	99.644	99.644	99.644	99.644
Dihedral Angle [°]					
O_1-C_1-N_1-C_6	-4.567	-4.567	-4.567	-4.567	-4.567
O_2-C_2-N_1-C_1	-179.755	-179.755	-179.755	-179.755	-179.755
C_1-N_2-C_4-C_3	0.519	0.544	0.578	0.566	0.579
C_5-N_2-C_4-C_3	-178.871	-178.857	-178.836	-178.843	-178.834
C_4-C_3-N_3-C_7	-0.158	-0.157	-0.185	-0.187	-0.192
N_2-C_4-N_4-C_7	179.885	179.907	179.948	179.940	179.946
O_2-C_2-C_3-N_3	-0.907	-0.907	-0.887	-0.885	-0.888

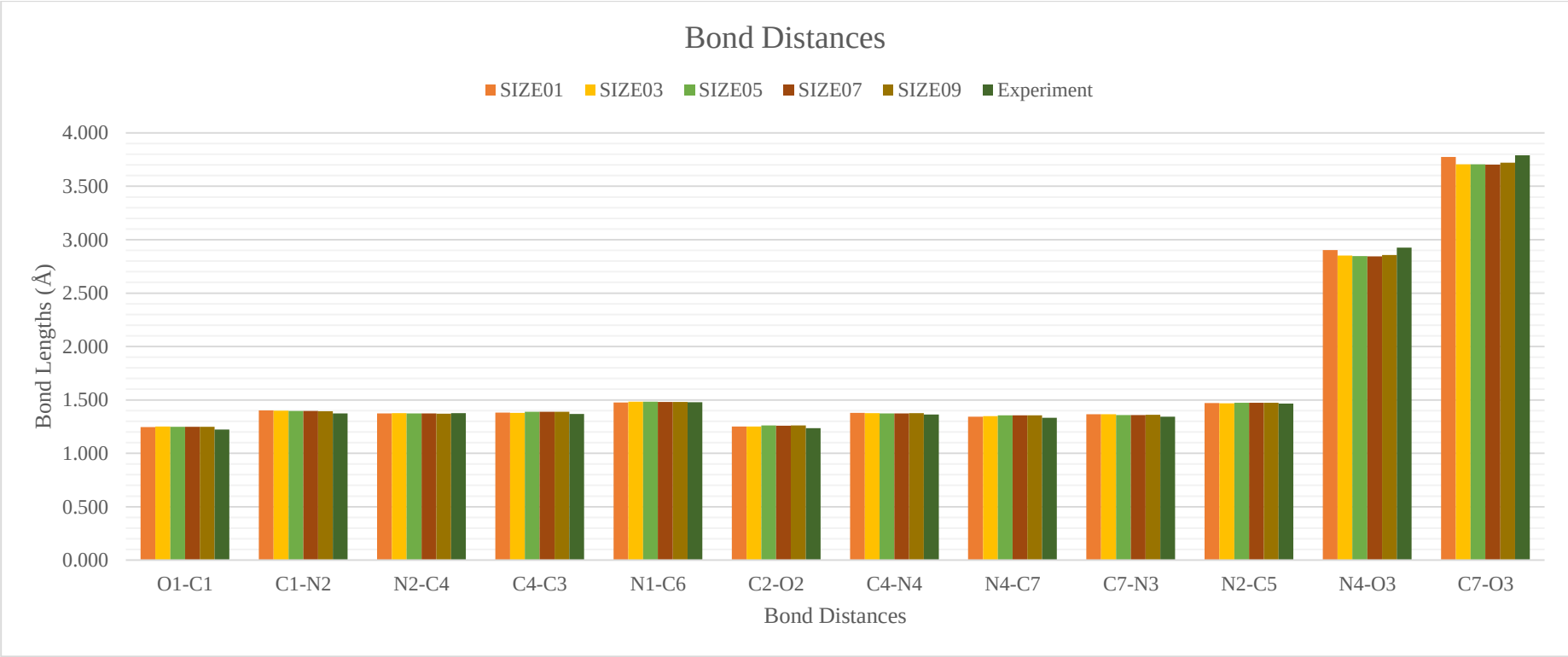

Figure 4.35 (a): Bond distances for experimental, computed TP-II, 3[TP-II], 5[TP-II], 7[TP-II], and 9[TP-II] molecular system using DFT/B3LYP/6-31G method.

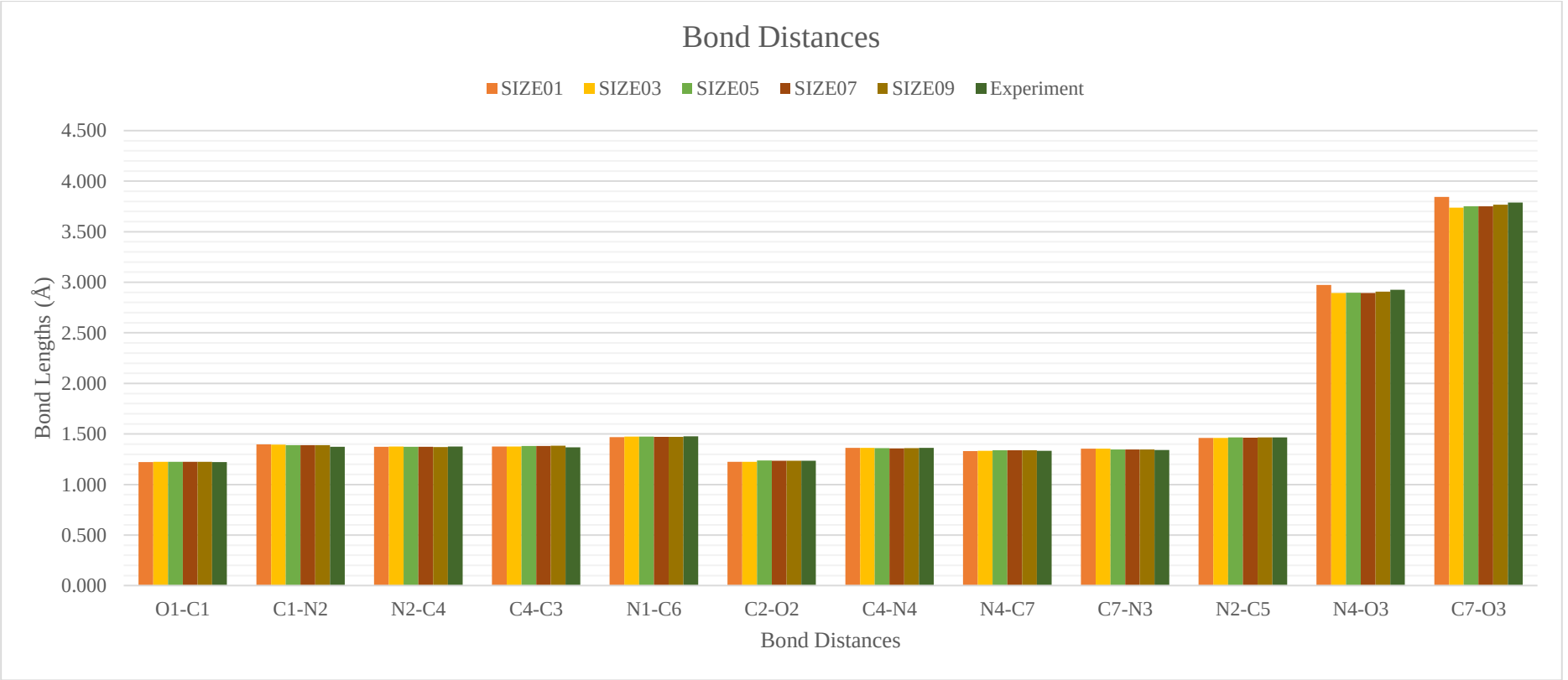

Figure 4.35 (b): Bond distances for experimental, computed TP-II, 3[TP-II], 5[TP-II], 7[TP-II], and 9[TP-II] molecular system using DFT/B3LYP/6-31G** method.

Table 4.35 (c) and (d) summarise the computed size effect electronic properties of single TP-II, 3[TP-II], 5[TP-II], 7[TP-II], and 9[TP-II] molecular system using DFT/B3LYP/6-31G and DFT/B3LYP/6-31G** methods. From the tables, the optimized total energies increase their negativity with the increment of molecular sizes. These indicate that 9[TP-I] molecular system has the largest stability as compared with TP-II, 3[TP-II], 5[TP-II], and 7[TP-II] molecular system (KUMER *et al.*, 2019). In Table 4.35 (c), the optimized total energies for 3[TP-II], 5[TP-II], 7[TP-II], and 9[TP-II] using DFT/B3LYP/6-31G method are -58542.997 eV, -97569.017 eV, -136595.636 eV, and -175620.810 eV, respectively. Besides, as stated in Table 4.35 (d), the computed total energies for 3[TP-II], 5[TP-II], 7[TP-II], and 9[TP-II] molecular system using DFT/B3LYP/6-31G** method are -58564.316 eV, -97604.658 eV, -136645.506 eV, and -175685.266 eV, respectively. From the computational data, it can be said that the computed HOMO-LUMO energy gap significantly decreased with the increment of molecular size in the TP-II molecular system. This is because the surfaces for orbitals to overlap increase with the molecular size in a system, thus easier the transfer of charge from HOMO to LUMO (Jain, 2005). The 9[TP-I] molecular system with HOMO-LUMO energy gaps of 4.485 eV (6-31G basis set) and 4.593 eV (6-31G** basis set) show closer findings with experimental results (4.580 eV) if compared with TP-II, 3[TP-II], 5[TP-II], and 7[TP-II] molecular system. Moreover, the computed dipole moments for 3[TP-II], 5[TP-II], 7[TP-II], and 9[TP-II] molecular system using DFT/B3LYP/6-31G method are 4.909 Debye, 5.515 Debye, 0.640 Debye, and 2.885 Debye, respectively, whereas for DFT/B3LYP/6-31G** method are 5.725 Debye, 4.494 Debye, 1.308 Debye, and 2.740 Debye, respectively. From the size

effect study, noticed that the accuracy of data will significantly improve when the molecular size used in computational analysis increase since it reconstructs the actual condition of the molecular system.

Table 4.35 (c): Computed electronic properties of TP-II, 3[TP-II], 5[TP-II], 7[TP-II], and 9[TP-II] molecular system based on size effect study using DFT/B3LYP/6-31G level of theory.

	DFT/B3LYP/6-31G				
	TP-II	3 [TP-II]	5 [TP-II]	7 [TP-II]	9 [TP-II]
Total Energy [eV]	-19517.293	-58542.997	-97569.017	-136595.636	-175620.810
HOMO [eV]	-6.662	-6.401	-6.412	-6.289	-6.177
LUMO [eV]	-1.633	-1.582	-1.608	-1.573	-1.693
HOMO-LUMO Energy Gap [eV]	5.029	4.819	4.804	4.716	4.485
Dipole Moment [Debye]	2.562	4.909	5.515	0.640	2.885

Table 4.35 (d): Computed electronic properties of TP-II, 3[TP-II], 5[TP-II], 7[TP-II], and 9[TP-II] molecular system based on size effect study using DFT/B3LYP/6-31G** level of theory.

	DFT/B3LYP/6-31G**				
	TP-II	3 [TP-II]	5 [TP-II]	7 [TP-II]	9 [TP-II]
Total Energy [eV]	-19524.267	-58564.316	-97604.658	-136645.506	-175685.266
HOMO [eV]	-6.403	-6.200	-6.220	-6.110	-6.031
LUMO [eV]	-1.256	-1.374	-1.407	-1.359	-1.438
HOMO-LUMO Energy Gap [eV]	5.147	4.827	4.813	4.751	4.593
Dipole Moment [Debye]	2.332	5.725	4.494	1.308	2.740

Comparison on the Polymorphisms of Acyclovir (ACV) and Theophylline (TP) Molecular System

4.6: Comparison on the Computed Electronic Properties of ACV-I, ACV-II, and ACV-III Molecular System

Table 4.36 summarises the computed electronic properties of ACV-I, ACV-II, and ACV-III molecular system using DFT/B3LYP/6-31G** and DFT/B3LYP/6-311G** level of theories. Noted that with optimized total energies of -70358.746 eV/-70376.691 eV, the stability of the ACV-I molecular system is higher than ACV-II (-70355.92 eV/-70373.84 eV) and ACV-III (-52451.747 eV/-52465.782 eV) molecular system, since it has the lowest total energies (Ali et *al.*, 2017; Chaturvedi et *al.*, 2018). Besides, with HOMO-LUMO energy gaps ranges of 4.049 eV to 4.545 eV, ACV-III molecular system is said to have lower kinetic stability, higher chemical reactivity, and softer than ACV-I (4.889 eV to 4.902 eV) and ACV-II (4.912 eV to 5.012 eV) molecular system (Bahgat and Fraihat, 2015; Ceylan *et al.*, 2016; Rajalakshmi and Nayak, 2017). The frontier molecular orbitals (i.e. HOMO energy, LUMO energy, and HOMO-LUMO energy gap) have potent usages in the characterization and determination of chemical reactivity, kinetic stability, electronic, and optical properties of a molecular system (Bahgat and Fraihat, 2015; Rahmani *et al.*, 2018). Figure 4.37 illustrates the HOMO and LUMO 3D surface mapped plots of ACV-I, ACV-II, and ACV-III molecular system. These surface plots help in the visualisation and prediction of the most reactive position of ACV-I, ACV-II, and ACV-III molecular system in π electron system. From the figure, the electron density distributions for

HOMO and LUMO in ACV-I and ACV-II molecular system are mainly localised on the guanine ring of ACV molecules and none of the electron densities distributed in the water molecules. These indicate that the electron transition of HOMO→ LUMO in the ACV-I and ACV-II molecular system implies an electron density transfer between the guanine rings of ACV molecules. For the ACV-III molecular system, the electron density distributions for HOMO are mainly localised on the guanine ring of ACV molecule, whereas the electron density distributions for LUMO are focused on the water molecules. This indicates that the electron transition of HOMO→ LUMO in ACV-III molecular system implies an electron density transfer from the guanine rings of ACV molecules to water molecules. Consequently, explained the phenomena of having narrower HOMO-LUMO energy gap in ACV-III molecular system and closer HOMO-LUMO energy gap values between ACV-I and ACV-II molecular system. From Table 4.36, with dipole moments of 14.822 Debye/14.600 Debye and first hyperpolarizabilities of 6.690 x 10^{-29} e.s.u/6.837 x 10^{-29} e.s.u, ACV-II molecular system shows highest dipole moments and first hyperpolarizabilities than ACV-I (12.384 Debye/12.274 Debye and 5.141 x 10^{-29} e.s.u/5.206 x 10^{-29} e.s.u) and ACV-III (13.083 Debye/ 13.626 Debye and 5.756 x 10^{-29} e.s.u/5.840 x 10^{-29} e.s.u) molecular system. It is figured out that ACV-II molecular system is dominated as the most suitable candidate for active NLO materials as if compare with ACV-I and ACV-III molecular system. Furthermore, higher values in dipole moments and first hyperpolarizabilities reveal that ACV-II molecular system is more polar and has a higher binding affinity than ACV-I and ACV-III molecular system (Ejuh et *al.*, 2020). These imply that ACV-II may have good therapeutic index than ACV-I and ACV-III molecular system. Figure 4.36 shows the

molecular electrostatic potential (MEP) surface mapped plots of ACV-I, ACV-II, and ACV-III molecular system. It is clearly illustrated that ACV-I, ACV-II, and ACV-III molecular system have their unique MEP surface plots. The red colour mapped plots indicate electron rich regions and are suggested to be the most probable sites for electrophilic attacks. The blue colour mapped plots represent electron deficient regions and are suggested to be the most probable sites for nucleophilic attacks. These help to predict and study the catalysis process, biological recognition process, and hydrogen bonding interaction scheme in ACV-I, ACV-II, and ACV-III molecular system (Ceylan *et al.*, 2016; Kabouchi *et al.*, 2017).

Table 4.36: The computed electronic properties (i.e. total energies, frontier molecular energies, dipole moments, and first hyperpolarizabilies) of ACV-I, ACV-II, and ACV-III molecular system.

	ACV-I		ACV-II		ACV-III	
	B3LYP/6-31G**	B3LYP/6-311G**	B3LYP/6-31G**	B3LYP/6-311G**	B3LYP/6-31G**	B3LYP/6-311G**
Total Energy (eV)	-70358.746	-70376.691	-70355.92	-70373.84	-52451.747	-52465.782
HOMO (eV)	-5.298	-5.509	-5.248	-5.478	-5.379	-5.611
LUMO (eV)	-0.409	-0.607	-0.236	-0.566	-0.834	-1.562
HOMO-LUMO Energy Gap (eV)	4.889	4.902	5.012	4.912	4.545	4.049
Dipole Moment (Debye)	12.384	12.274	14.822	14.600	13.803	13.626
First Hyperpolarizability (e.s.u)	5.141×10^{-29}	5.206×10^{-29}	6.690×10^{-29}	6.837×10^{-29}	5.756×10^{-29}	5.840×10^{-29}

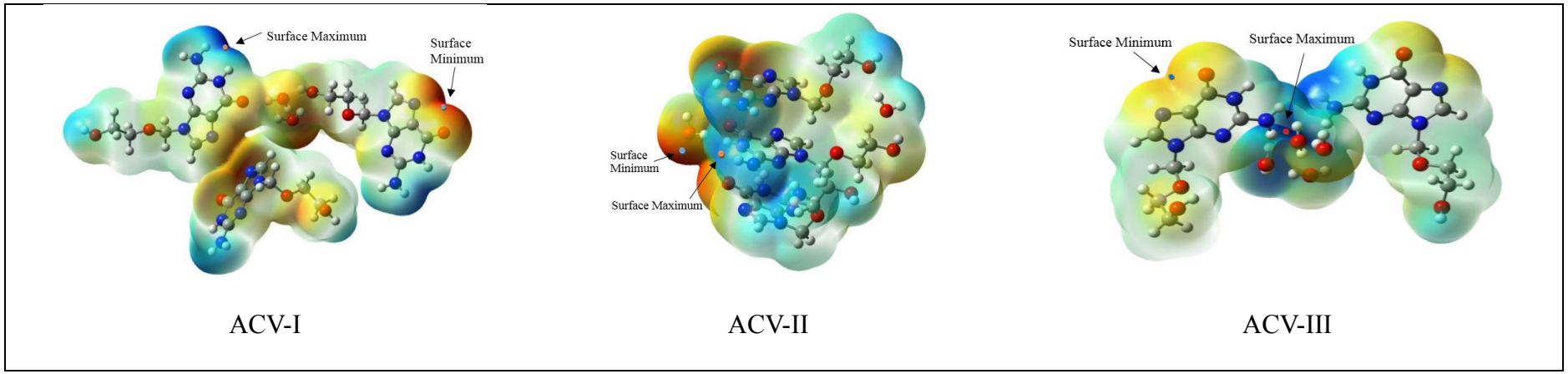

Figure 4.36: The molecular electrostatic potential (MEP) surface mapped plots of ACV-I, ACV-II, and ACV-III molecular system.

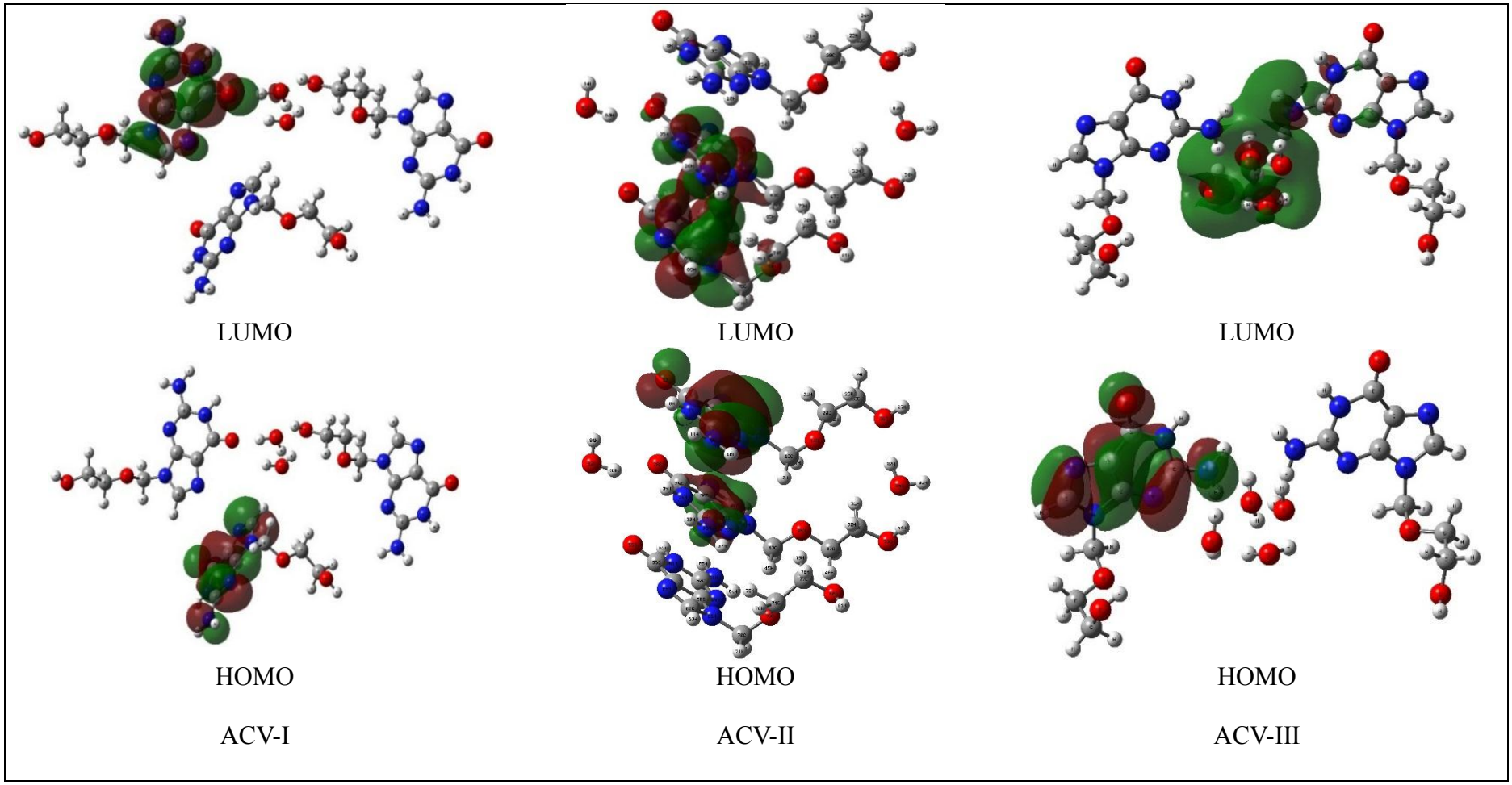

Figure 4.37: The HOMO and LUMO 3D surface mapped plots of ACV-I, ACV-II, and ACV-III molecular system.

4.7: Comparison on the Computed Electronic Properties of TP-I and TP-II Molecular System

Table 4.37 tabulates the computed electronic properties of TP-I and TP-II molecular system using DFT/B3LYP/6-31G and DFT/B3LYP/6-31G** level of theories. Noticed that with computed total energies of -19517.293 eV/-19524.267 eV, the stability of the TP-II molecular system is found to be larger than TP-I (-17438.443 eV/-17444.539 eV) molecular system, since it has lower total energies than TP-I (Kumer et *al.*, 2019). Besides, with HOMO-LUMO energy gaps ranges from 5.002 eV to 5.147 eV, both the TP-I and TP-II molecular system have closer HOMO-LUMO energy gaps within each other. This indicates that both of them (anhydrous TP-I and monohydrated TP-II) have closer kinetic stability and chemical reactivity characteristics (Holmes-Hampton *et al.*, 2014; Subhapriya, 2014). Figure 4.39 shows the HOMO and LUMO 3D surface mapped plots of the TP-I and TP-II molecular system. These surface plots help in the visualisation and prediction of the most reactive position of TP-I and TP-II molecular system in π electron system. As can be observed in the diagram, majority of the electron density distributions in both HOMO and LUMO for TP-I and TP-II molecular system are localised on the pyrimidine ring and imidazole ring of the TP molecules. Noticed that there is an absent of electron density distributions around the water molecule in the TP-II molecular system. This indicates that the presence of water molecule in TP-II molecular system has no obvious impact on the HOMO-LUMO energy gap since the electron transition from HOMO→ LUMO in TP-I and TP-II molecular system are mainly occur between the pyrimidine ring and imidazole ring of the TP molecules.

Consequently, explained the phenomena of having closer HOMO-LUMO energy gaps between TP-I and TP-II molecular system. Besides, with dipole moments of 3.642 Debye/3.481 Debye, TP-I molecular system is said to be more polar than TP-II molecular system (2.562 Debye/2.332 Debye). The existence of additional N—H—O hydrogen bonding interaction between water molecule and TP molecule in the TP-II molecular system caused it to have an increase in the first hyperpolarizability (Benhalima et *al.*, 2018). So that, with first hyperpolarizabilities of 10.750 x 10^{-30} e.s.u/10.130 x 10^{-30} e.s.u, TP-II molecular system is more suitable to consider as the potential candidate for active NLO materials than TP-I molecular system (7.598 x 10^{-30} e.s.u/7.378 x 10^{-30} e.s.u). Figure 4.38 shows the molecular electrostatic potential (MEP) surface mapped plots of the TP-I and TP-II molecular system. It is clearly illustrated that TP-I and TP-II molecular system have their unique MEP surface plots. The red colour mapped plots indicate electron rich regions and are suggested to be the most probable sites for electrophilic attacks (Benhalima *et al.*, 2018; Tribak *et al.*, 2019), while the blue colour mapped plots represent electron deficient regions and are suggested to be the most probable sites for nucleophilic attacks (Shoba, 2021). From the diagram, noticed that the presence of water molecule in the TP-II molecular system caused it to have a neutral electrostatic potential (green to colourless) on the nitrogen atoms N_4 and do not consider as one of the sites for electrophilic attacks as found in the TP-I molecular system. The MEP surface plots are significant. It helps to predict and study the catalysis process, biological recognition process and hydrogen bonding interaction scheme in TP-I and TP-II molecular system (Ceylan *et al.*, 2016; Kabouchi *et al.*, 2017).

Table 4.37: The computed electronic properties (i.e. total energies, frontier molecular energies, dipole moments, and first hyperpolarizabilities) of TP-I and TP-II molecular system.

	TP-I		TP-II	
	B3LYP/6-31G	B3LYP/6-31G**	B3LYP/6-31G	B3LYP/6-31G**
Total Energy (eV)	-17438.443	-17444.539	-19517.293	-19524.267
HOMO (eV)	-6.283	-6.083	-6.662	-6.403
LUMO (eV)	-1.282	-0.961	-1.633	-1.256
HOMO-LUMO Energy Gap (eV)	5.002	5.121	5.029	5.147
Dipole Moment (Debye)	3.642	3.481	2.562	2.332
First Hyperpolarizability (e.s.u)	7.598×10^{-30}	7.378×10^{-30}	10.750×10^{-30}	10.130×10^{-30}

TP-I TP-II

Figure 4.38: The molecular electrostatic potential (MEP) surface mapped plots of TP-I and TP-II molecular system.

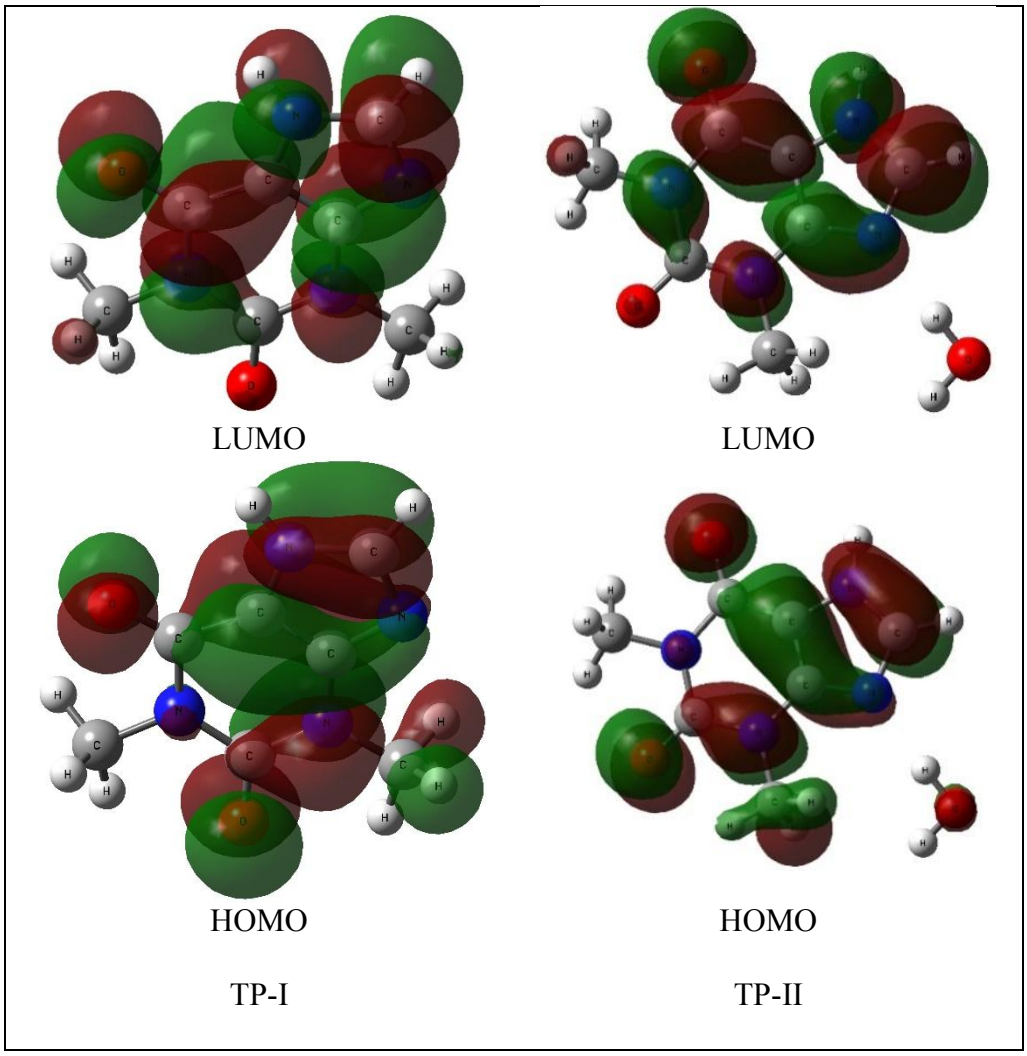

Figure 4.39: The HOMO and LUMO 3D surface mapped plots of TP-I and TP-II molecular system.

CHAPTER 5

CONCLUSION

In this research study, the geometry and electronic structures of acyclovir (ACV) and theophylline (TP) polymorphic forms (i.e. ACV-I, ACV-II, ACV-III, TP-I, and TP-II) were computed using Density Functional Theory (DFT) computational method via Gaussian 09, GaussView 5.0, and Multiwfn software packages. The polymorphism behaviors of ACV and TP drug compounds were observed via the crystallization process. ACV-I, TP-I, and TP-II compounds were obtained and the details of molecular structures were determined using the single crystal X-ray diffraction experiment.

For the ACV molecule, the optimized geometry structures of ACV-I, ACV-II, and ACV-III molecular system calculated using DFT/B3LYP/6-31G** and DFT/B3LYP/6-311G** methods meet good agreement with experimental findings. There were less than 6.000% of geometry data deviations between computed and experimental results. The optimized total energies of ACV-I, ACV-II, and ACV-III molecular system calculated via DFT/B3LYP/6-31G** method were found to be -70358.746 eV, -70355.920 eV, and -52451.747 eV, respectively, whereas for DFT/B3LYP/6-311G** technique were -70376.691 eV, -70373.840 eV, and -52465.782 eV, respectively. ACV-I molecular system with the lowest energy, was dominated to be the most stable form followed by

ACV-II and ACV-III molecular system. The HOMO-LUMO surface mapped analysis elucidate that the transition of electrons in both ACV-I and ACV-II molecular systems occurred between the guanine rings of ACV molecules, while the ACV-III molecular system involved water molecule. The HOMO-LUMO energy gaps of ACV-I and ACV-II were calculated to have a range between 4.889 eV to 5.012 eV, while a smaller HOMO-LUMO energy gap was observed in the ACV-III molecular system with ranges of 4.049 eV to 4.545 eV. The MEP surface mapped plot suggested that atoms with high electronegativity (i.e. oxygen and nitrogen) were the sites preferred for electrophilic attacks while atoms with less electronegativity (i.e. hydrogen) were the sites preferred for nucleophilic reactions. All the carbon atoms in ACV-I, ACV-II, and ACV-III molecular system were found to be neutral atoms (colourless MEP mapping) and do not take part in both electrophilic and nucleophilic reactions. The dipole moments and first hyperpolarizabilities of ACV-I, ACV-II, and ACV-III molecular system were computed and the related NLO properties were studied. Noticed that the NLO behaviors increased accompany with the increased in the values of first hyperpolarizabilities in the sequences of ACV-I → ACV-III → ACV-II. The computed FT-IR frequency band assignments were obtained and show satisfactory agreement with the geometry structures of the ACV-I, ACV-II, and ACV-III molecular system. The rotational barrier studies of ACV molecules were conducted via the PES scanning technique. It was observed that the elongation in the ACV side chain bond distance of C-O will lead to unstable conformers.

For the TP molecule, the optimized geometry structures of the TP-I and

TP-II molecular system computed via DFT/B3LYP/6-31G and DFT/B3LYP/6-31G** methods show satisfactory agreement with the single crystal X-ray diffraction data. There were not more than 4.140% of geometry data deviations between computed and experimental results. The optimized total energies of the TP-I molecular system using DFT/B3LYP/6-31G and DFT/B3LYP/6-31G** methods were -17438.443 eV and -17444.539 eV, respectively, whereas for TP-II molecular system were -19517.293 eV and -19524.267 eV, respectively. From the optimized total energies, TP-II molecular system was found to be more stable than the TP-I molecular system. The HOMO and LUMO surface mapped plots reveal that the transition of electrons in both TP-I and TP-II molecular systems mainly occurred at the pyrimidine ring and imidazole ring of the TP molecule. From the computed data, both TP-I and TP-II molecular systems had closer HOMO-LUMO energy gap ranges between 5.002 eV to 5.147 eV. The MEP surface mapped plots in TP-I molecular system suggested that atoms O_1, O_2, and N_4 were the site for the electrophilic attack, while atom H_7 is preferred for the nucleophilic reaction. In the case of the TP-II molecular system, atoms O_1, O_2, and O_3 were suggested for the electrophilic attack, while atoms H_7 and H_8 were proposed to be the sites for nucleophilic attack. The dipole moments of the TP-I molecular system calculated using DFT/B3LYP/6-31G and DFT/B3LYP/6-31G** method were found to be 3.642 Debye and 3.481 Debye, respectively, whereas for TP-II molecular system were 2.562 Debye and 2.332 Debye, respectively. As compared with urea, the TP-II molecular system exhibit better NLO properties than the TP-I molecular system. The size effect study in both TP-I and TP-II molecular system were determined. The increase in the system size will increase the data accuracy and also the computational time.

In conclusion, all the DFT computational calculations whether geometry or electronic structures in this work, able to provide useful fundamental knowledge of ACV and TP at the microscopic level. The satisfactory agreements between experimental data of FT-IR and UV-Vis spectroscopies with DFT computational results assured the reliability and the usages of DFT/B3LYP/6-31G**, DFT/B3LYP/6-311G**, and DFT/B3LYP/6-31G computational methods in the studies of ACV and TP compounds. Besides, all the computed data can act as guiding references for other researchers when dealing with ACV and TP polymorphs in future work.

5.2 Recommendation

The present study had interpreted the molecular geometry and electronic structures of ACV and TP hydrated compounds using the DFT computational approach. However, the polymorphism behaviors in both ACV and TP drug compounds are not limited to the formation of hydrates, but also exist in co-crystal and salt formation. Hence, it is vital for researchers to investigate the molecular structures and electronic properties of the co-crystal and salt polymorphism in ACV and TP using DFT/B3LYP computational methods, as it is able to provide the fundamental knowledge and may help in the screening of polymorphs during drug discovery and drug formulating processes.

REFERENCES

Abbaz, T., Bendjeddou, A. and Villemin, D., 2019. Quantum Chemical Calculations of (2-Amino, 3-Amino, 4-Amino and4-Hydrazino) Benzene Sulfonamides Compounds by DFT. *International Journal of Pharmaceutical Chemistry*, 9(1), p. e5068.

Abbaz, T., Bendjeddou, A. and Villemin, D., 2019. Density Functional Theory Studies On Molecular Structure And Electronic Properties Of sulfanilamide, Sulfathiazole, E7070 And Furosemide Molecules. *IOSR Journal of Applied Chemistry*, 12(1), pp. 60–69.

Abdel-Rahman, L. H., Abu-Dief, A.M., Moustafa, H. and Abdel-Mawgoud, A.A.H., 2020. Design and nonlinear optical properties (NLO) using DFT approach of new Cr (III), VO (II), and Ni (II) chelates incorporating tri-dentate imine ligand for DNA interaction, antimicrobial, anticancer activities and molecular docking studies. *Arabian Journal of Chemistry*, 13(1), pp. 649–670.

Abdullahi, Y. Z., 2018. *AB-Initio Investigation Of Structural, Electronic, And Adsorption Properties Of Graphitic Carbon Nitride Sheet With Embedded Transition Metal Mn And Fe Atoms*. PhD thesis, Universiti Sains Malaysia, Malaysia.

Abulyaissova, L. K., 2019. DFT-Based Molecular Conformational Analysis of a Diarylethylene Cyano-Derivative. *Journal of Structural Chemistry*, 60(2), pp. 179–185.

Agrawal, M., Kumar, A. and Gupta, A., 2017. Conformational stability, spectroscopic signatures and biological interactions of proton pump inhibitor drug lansoprazole based on structural motifs. *RSC advances*, 7(66), pp. 41573–41584.

Ahmad, F., Alam, M. J., Alam, M., Azaz, S., Parveen, M., Park, S. and Ahmad, S., 2018. Synthesis, spectroscopic, computational (DFT/B3LYP), AChE inhibition and antioxidant studies of imidazole derivative. *Journal of Molecular Structure*, 1151, pp. 327–342.

Ainurofiq, A., Dinda, K. E., Pangestika, M. W., Himawati, U., Wardhani, W. D. and Sipahutar, Y. T., 2020. The effect of polymorphism on active pharmaceutical ingredients: A review. *International Journal of Research in Pharmaceutical Sciences*, 11(2), pp. 1621–1630.

Aitipamula, S., Chow, P. S. and Tan, R. B. H., 2009. Theophylline-gentisic acid (1/1). *Acta Crystallographica Section E: Structure Reports Online*, 65(9), pp. o2126--o2127.

Aitipamula, S. and Nangia, A., 2012. Polymorphism: Fundamentals and Applications. *Supramolecular Chemistry: From Molecules to Nanomaterials*.

Akbas, E. *et al.*, 2018. Synthesis, characterization, antioxidant properties and DFT calculation of some new pyrimidine derivatives. *Phosphorus, Sulfur, and Silicon and the Related Elements*, 194(8), pp. 796-802.

Akman, F., 2017. Prediction of chemical reactivity of cellulose and chitosan based on density functional theory. *Cellulose Chemistry and Technology*, 51(3–4), pp. 253–262.

Alam, M. and Park, S., 2018. Molecular structure, spectral studies, NBO, HOMO--LUMO profile, MEP and Mulliken analysis of 3β, 6β-dichloro-5α-hydroxy-5α--cholestane. *Journal of Molecular Structure*, 1159, pp. 33–45.

Ali, A. *et al.,* 2017. DFT/B3LYP calculations, in vitro cytotoxicity and antioxidant activities of steroidal pyrimidines and their interaction with HSA using molecular docking and multispectroscopic techniques. *Bioorganic chemistry*, 73, pp. 83–99.

Alipour, M. and Mohajeri, A., 2010. Molecular Electrostatic Potential as a tool for Evaluating the Etherification Rate Constant. *The Journal of Physical Chemistry A*, 114(27), pp. 7417–7422.

Alkane Conformation, 2021, *Newman Projection and Anti-Gauche form Strain, Ryosuke University* [Online]. Available at: https://j-tradition.com/newman.html [Accessed: 1 February 2021].

Alvarez-Ros, M. C. and Palafox, M. A., 2014. Conformational analysis, molecular structure and solid state simulation of the antiviral drug acyclovir (zovirax) using density functional theory methods. *Pharmaceuticals*, 7(6), pp. 695–722.

Álvarez Ros, M.-C., 2016, *Estudio teórico de la hipoxantina y derivados*. Universidad Nacional de Educación a Distancia (España) [Online]. Available at: http://e-spacio.uned.es/fez/eserv/tesisuned:Ciencias-Mcalvarez/ALVAREZ_ROS_Margarita_Clara_Tesis.pdf [Accessed: 1 February 2021].

American, S., 2007, *How can graphite and diamond be so different if they are both composed of pure carbon?* [Online]. Available at: https://www.scientificamerican.com/article/how-can-graphite-and-diam/ [Accessed: 1 February 2021].

Andrei, K., 2011. *Solubility and physical stability improvement of natiral xanthine derivatives*. Master thesis, University of Helsinki, Finland.

Arivazhagan, M. and James, G. J., 2017. FTIR, FT-Raman Spectra, First-Order Hyperpolarizability, HOMO-LUMO, NBO, and Mulliken Charge Analyses of p-Chlorofluorobenzene. International Journal of Scientific Research in Science, Engineering and Technology, 3(5), pp. 434-448.

Asath, R. M., Premkumar, S., Rekha, T.N., Jawahar, A., Mathavan, T. and Benial, A.M.F., 2016. Vibrational spectroscopic, structural and nonlinear optical activity studies on 6-aminonicotinamide: A DFT approach. *AIP Conference Proceedings*, May 2016. AIP Publishing LLC, 1731(1), p.140050.

Asath, R. M., Premkumar, R., Mathavan, T. and Benial, A.M.F., 2017. Conformational, vibrational spectroscopic and nonlinear optical activity studies on N, N-Di-Boc-2-amino pyridine: A DFT approach. *AIP Conference Proceedings*. AIP Publishing LLC, 1832(1), pp. 140015.

Avci, D. *et al.*, 2020. Novel metal complexes containing 6-methylpyridine-2-carboxylic acid as potent α-glucosidase inhibitor: synthesis, crystal structures, DFT calculations, and molecular docking. *Molecular diversity*, pp. 1–19.

Babrah, J. *et al.*, 2007. FT-infrared spectroscopic studies of lymphoma, lymphoid and myeloid leukaemia cell lines. In: *European Conference on Biomedical Optics*. Optical Society of America, pp. 6628_28.

Bahgat, K. and Fraihat, S., 2015. Normal coordinate analysis, molecular structure, vibrational, electronic spectra and NMR investigation of 4-Amino-3-phenyl-1H-1, 2, 4-triazole-5 (4H)-thione by ab initio HF and DFT method. *Spectrochimica Acta Part A: Molecular and Biomolecular Spectroscopy*, 135, pp. 1145–1155.

Bakkiyaraj, D., 2017, *Chapter IV – Vibrational, Electronic, Docking and Reacitivity Properties of Adenine Using Spectroscopic and Computational Tools* [Online]. Available at: https://shodhganga.inflibnet.ac.in/bitstream/10603/239607/7/07_chapter4.pdf [Accessed: 1 February 2021].

Balachandran, V., Santhi, G., Karpagam, V. and Lakshmi, A., 2013. Molecular structure, spectroscopic (FT-IR, FT-Raman), NBO and HOMO--LUMO analyses, computation of thermodynamic functions for various temperatures of 2, 6-dichloro-3-nitrobenzoic acid. *Spectrochimica Acta Part A: Molecular and Biomolecular Spectroscopy*, 110, pp. 130–140.

Barakat, A. *et al.*, 2018. Quantum chemical insight into the molecular structure of l-chemosensor 1, 3-dimethyl-5-(thien-2-ylmethylene)-pyrimidine-2, 4, 6-(1 H, 3 H, 5 H)-trione: naked-eye colorimetric detection of copper (II) anions. *Journal of Theoretical and Computational Chemistry*, 17(01), p. 1850005.

Barim, E. and Akman, F., 2019. Synthesis, characterization and spectroscopic investigation of N-(2-acetylbenzofuran-3-yl) acrylamide monomer: Molecular structure, HOMO--LUMO study, TD-DFT and MEP analysis. *Journal of Molecular Structure*, 1195, pp. 506–513.

Barnes, P. J., 2013. Theophylline. *American journal of respiratory and critical care medicine*, 188(8), pp. 901–906.

Batsanov, A. S., 2010. Small Molecule Applications of X-Ray Diffraction.

Bauer, J. F., 2008. Polymorphism—A critical consideration in pharmaceutical development, manufacturing, and stability. *Journal of validation technology*, 14(5), pp. 15–24.

Benhalima, N., Djedouani, A., Rahmani, R., Chouaih, A., Hamzaoui, F. and Hadj, E., 2018. Molecular Structure, Mulliken charges, HOMO-LUMO, Electrostatic Potential and Nonlinear Optical Properties of Zwitterionic 6-methyl-2-oxo-3-[1-(ureidoiminio) ethyl]-2H-pyran-4-olate monohydrate molecule by HF and DFT methods. *World Journal of Modelling and Simulation*, 14(1), pp. 3–11.

Beran, G. J. O., 2016. Modeling polymorphic molecular crystals with electronic structure theory. *Chemical reviews*, 116(9), pp. 5567–5613.

Bharanidharan, S. and Seevakan, K., 2018. Molecular structure and Mulliken atomic charges of (2E, 6E)-2, 6-dibenzylidene-4-(4-hydroxyphenyl) cyclohexanone--A DFT method. *International Journal of Pure and Applied Mathematics*, 119(12), pp. 6211–6219.

Bhatia, A. *et al.*, 2018. Polymorphism and its Implications in Pharmaceutical Product Development. In *Dosage Form Design Parameters*, Elsevier, pp. 31–65.

Bhattacharyya, S., 2015. Fourier transform infrared spectroscopy: applications in medicine. *Journal of Physical Chemistry & Biophysics*, 5(5), p. 4.

Birnbaum, G. I., Cygler, M. and Shugar, D., 1984. Conformational features of acyclonucleosides: structure of acyclovir, an antiherpes agent. *Canadian journal of chemistry*, 62(12), pp. 2646–2652.

Bond, A. D., 2016. Single-Crystal X-ray Diffraction. In: *Analytical Techniques in the Pharmaceutical Sciences*. Springer, pp. 315–337.

Boukabcha, N., Benhalima, N., Rahmani, R., Chouaih, A. and Hamzaoui, F., 2015. Theoretical investigation of electrostatic potential and non linear optical properties of M-nitroacetanilide. *Rasayan J Chem*, 8, pp. 509–516.

Buist, A. R., Kennedy, A. R. and Manzie, C., 2014. Four salt phases of

theophylline. *Acta Crystallographica Section C: Structural Chemistry*, 70(2), pp. 220–224.

Bunaciu, A. A., Aboul-Enein, H. Y. and Fleschin, S., 2010. Application of Fourier transform infrared spectrophotometry in pharmaceutical drugs analysis. *Applied Spectroscopy Reviews*, 45(3), pp. 206–219.

Bunaciu, A. A., UdriSTioiu, E. G. and Aboul-Enein, H. Y., 2015. X-ray diffraction: instrumentation and applications. *Critical reviews in analytical chemistry*, 45(4), pp. 289–299.

Cai, Q., Xue, J., Wang, Q. and Du, Y., 2017. Solid-state cocrystal formation between acyclovir and fumaric acid: Terahertz and raman vibrational spectroscopic studies. *Spectrochimica Acta Part A: Molecular and Biomolecular Spectroscopy*, 186, pp. 29–36.

CCCBDB, 2020, *Precomputed vibrational scaling factors*, *Computational Chemistry Comparison and Benchmark DataBase* [Online]. Available at: https://cccbdb.nist.gov/vibscalejust.asp [Accessed: 1 February 2021].

Censi, R. and Di Martino, P., 2015. Polymorph impact on the bioavailability and stability of poorly soluble drugs. *Molecules*, 20(10), pp. 18759–18776.

Ceylan, Ü., Tarı, G.Ö., Gökce, H. and Ağar, E., 2016. Spectroscopic (FT--IR and UV--Vis) and theoretical (HF and DFT) investigation of 2-Ethyl-N-[(5-nitrothiophene-2-yl) methylidene] aniline. *Journal of Molecular Structure*, 1110, pp. 1–10.

Chadha, R. *et al.*, 2013. Crystal structures and physicochemical properties of four new lamotrigine multicomponent forms. *Crystal growth & design*, 13(2), pp. 858–870.

Chan, E. J., Gao, Q. and Dabros, M., 2014. Understanding the structure details when drying hydrate crystals of pharmaceuticals-interpretations from diffuse scattering and inter-modulation satellites of a partially dehydrated crystal. *Acta Crystallographica Section B: Structural Science, Crystal Engineering and Materials*, 70(3), pp. 555–567.

Chan, H. C. S., 2013. *Polymorph Prediction of Organic (Co-) Crystal Structures From a Thermodynamic Perspective.* PhD thesis, University of Bradford, England.

Chaturvedi, R. N. *et al.*, 2018. Synthesis, Biological Evaluation, Molecular Docking and DFT Study of Potent Antileishmanial Agents Based on the Thiazolo [3, 2-a] pyrimidine Chemical Scaffold. *ChemistrySelect*, 3(10), pp. 2756–2762.

Chavda, B. R., Gandhi, S.A., Dubey, R.P., Patel, U.H. and Barot, V.M., 2016. A quantitative analysis of weak intermolecular interactions & quantum chemical calculations (DFT) of novel chalcone derivatives. *AIP Conference Proceedings, May 2016.* AIP Publishing LLC, 1728 (1),

p.020251.

Che, A. F., Wan, L.S., Ling, J., Liu, Z.M. and Xu, Z.K., 2009. Recognition mechanism of theophylline-imprinted polymers: two-dimensional infrared analysis and density functional theory study. *The Journal of Physical Chemistry B*, 113(20), pp. 7053–7058.

Chemistry LibreTexts, 2016, *A.1. Molecular Orbital Theory* [Online]. Available at:https://chem.libretexts.org/Courses/Saint_Marys_College_Notre_Dame_IN/CHEM_342%3A_Bioinorganic_Chemistry/Readings/Purgatory/Chapter_3%3A_Introduction_to_Advanced_Bonding_Theories/3.2_Ligand_Field_Theory/A._Molecular_Orbital_Theory/A.1._Molecular_Orbital_ [Accessed: 1 February 2021].

ChemViz, 2000, *Background Reading for Geometry Optimizations* [Online]. Available at: https://www.shodor.org/chemviz/optimization/students/background.html [Accessed: 1 February 2021].

ChemViz, 2000, *Overview of Computational Chemistry* [Online]. Available at: https://www.shodor.org/chemviz/overview/ccbasics.html [Accessed: 1 February 2021].

Choudhary, N., Agarwal, P., Gupta, A. and Tandon, P., 2014. Quantum chemical calculations of conformation, vibrational spectroscopic, electronic, NBO and thermodynamic properties of 2, 2-dichloro-N-(2, 3-dichlorophenyl) acetamide and 2, 2-dichloro-N-(2, 3-dichlorophenyl) acetamide. *Computational and Theoretical Chemistry*, 1032, pp. 27–41.

Co., T. E., 2019, *Introduction to Fourier Transform Infrared Spectroscopy* [Online]. Available at: https://nicoletcz.cz/app/uploads/2019/03/IntroductionToFTIR.pdf [Accessed: 1 February 2021].

Computational Chemistry, 2021, [Online]. Available at: http://mason.gmu.edu/~sslayden/Chem350/manual/docs/comp-chem.pdf [Accessed: 1 February 2021].

Corp, R., 2021, *U.S. FDA Drug Definitions* [Online]. Available at: https://www.registrarcorp.com/definitions/ [Accessed: 1 February 2021].

D, A. D., 2012, *CHAPTER 8 - HYDROGEN BONDING ANALYSIS AND CHARGE TRANSFER INTERACTIONS OF 4-BENZYLOXY-2-NITROANILINE INSECTICIDE: A DENSITY FUNCTIONAL THEORETICAL STUDY IN COMBINATION WITH SPECTROSCOPIC TECHNIQUES* [Online]. Available at: https://shodhganga.inflibnet.ac.in/handle/10603/20344 [Accessed: 1 February 2021].

Daniel, D. G., 2014. The Electronic and Thermodynamic Properties of Ca doped

LaFeO3-A First Principles Study Using Density Functional Theory. Master thesis, Boise State Univerisity, United States.

David, Y., 1998, *Introduction to Computational Chemistry* [Online]. Available at: http://www.ccl.net/cca/documents/dyoung/topics-orig/compchem.html [Accessed: 1 February 2021].

Demircioğlu, Z., Kaştaş, G., Kaştaş, Ç.A. and Frank, R., 2019. Spectroscopic, XRD, Hirshfeld surface and DFT approach (chemical activity, ECT, NBO, FFA, NLO, MEP, NPA& MPA) of (E)-4-bromo-2-[(4-bromophenylimino) methyl]-6-ethoxyphenol. *Journal of Molecular Structure*, 1191, pp. 129–137.

Dezena, R. M. B., 2020. Ritonavir Polymorphism: Analytical Chemistry Approach to Problem Solving in the Pharmaceutical Industry. *Brazilian Journal of Analytical Chemistry*, 7(26), pp. 12–17.

Dheivamalar, S., Sugi, L. and Ambigai, K, 2016. Density functional theory study of exohedral carbon atoms effect on electrophilicity of nicotine: comparative analysis. *Computational Chemistry*, 4(1), pp. 17–31.

Dixit, H. and Antwerpen, B. P., 2012. *Firs-principles electronic structure calculation of transparent conducting oxide materials*. PhD thesis, University antwerpen, Belgium.

Drissi, M., Benhalima, N., Megrouss, Y., Rachida, R., Chouaih, A. and Hamzaoui, F., 2015. Theoretical and experimental electrostatic potential around the m-nitrophenol molecule. *Molecules*, 20(3), pp. 4042–4054.

Dubey, R. P., Patel, U. H. and Patel, B. D., 2018. Study on molecular structure, Spectral investigations, NBO, NLO, Hirshfeld surface analysis and Homo-Lumo energy of silver complex of 4-Amino-N-(2, 6-dimethoxypyrimidin-4-yl) benzenesulfonamide. *Inorganic and Nano-Metal Chemistry*, 48(2), pp. 110–119.

Duygu, D., Baykal, T., Açikgöz, İ. and Yildiz, K., 2009. Fourier transform infrared (FT-IR) spectroscopy for biological studies. *Gazi University Journal of Science*, 22(3), pp. 117–121.

E., P., 2016, *A very short introduction to density functional theory (DFT)* [Online]. Available at: http://physics.gu.se/~tfkhj/lecture_VIII_DFT-3.pdf [Accessed: 1 February 2021].

Ebisuzaki, Y., Boyle, P. D. and Smith, J. A., 1997. Methylxanthines. i. anhydrous theophylline. *Acta Crystallographica Section C: Crystal Structure Communications*, 53(6), pp. 777–779.

Ehteshami-Afshar, S., FitzGerald, J. M., Doyle-Waters, M. M. and Sadatsafavi, M., 2016. The global economic burden of asthma and chronic obstructive pulmonary disease. *The International Journal of Tuberculosis and Lung Disease*, 20(1), pp. 11–23.

Enkelmann, D. D., Handelmann, J., Schauerte, C. and Merz, K., 2019. Co-crystallization and polymorphic behaviour of 5-fluorouracil. *CrystEngComm*, 21(13), pp. 2130–2134.

Erdemir, F., Celepci, D. B., Aktaş, A. and Gök, Y., 2020. Synthesis, crystal structures, spectral investigations, conformational analysis and DFT studies of N-heterocyclic carbene precursors. *Journal of Molecular Structure*, 1204, p. 127519.

Fahim, A. M. and Shalaby, M. A., 2019. Synthesis, biological evaluation, molecular docking and DFT calculations of novel benzenesulfonamide derivatives. *Journal of Molecular Structure*, 1176, pp. 408–421.

Fernandes, J. A., Sardo, M., Mafra, L., Choquesillo-Lazarte, D. and Masciocchi, N., 2015. X-ray and NMR crystallography studies of novel theophylline cocrystals prepared by liquid assisted grinding. *Crystal Growth & Design*, 15(8), pp. 3674–3683.

Foresman, J.B. and Frisch, A, 1996, *Exploring chemistry with electronic structure methods (second edition)* [Online]. Available at: http://blogs.cimav.edu.mx/daniel.glossman/data/files/Libros/Exploring Chemistry With Electronic Structure Methods.pdf [Accessed: 1 February 2021].

Foroushani, F. S., 2019. *High-level computational methods: application to drug design, catalytic atmospheric reactions and thermochemistry*. PhD thesis, University of Western Australia, Australia.

Frisch, M. J. *et al.*, 2009. GAUSSIAN09. Revision E. 01. Gaussian Inc., Wallingford, CT, USA.

Fucke, K., McIntyre, G. J., Wilkinson, C., Henry, M., Howard, J. A. and Steed, J. W., 2012. New insights into an old Molecule: Interaction energies of theophylline crystal forms. *Crystal growth & design*, 12(3), pp. 1395–1401.

Gandhi, A. S. and Joshi, V., 2018, *Spectroscopic and Optical analysis of Eosin doped Strontium Tartrate Crystals Grown by Gel Growth Technique* [Online]. Available at: http://ijream.org/papers/IJREAMV04I0642080.pdf [Accessed: 1 February 2021].

Gandhi, S. A., Patel, U. H., Barot, V. M. and Varma, N. V. S., 2019. Structural analysis and charge transfer properties of a novel pyrazoline derivative: potential energy scan, XRD, DFT and molecular docking studies. *Indian Journal of Physics*, 93(10), pp. 1275–1291.

Garg, R. K. and Sarkar, D., 2016. Polymorphism control of p-aminobenzoic acid by isothermal anti-solvent crystallization. *Journal of Crystal Growth*, 454, pp. 180–185.

Gilbert, A., 2007, *Introduction to Computational Quantum Chemsitry: Theory* [Online]. Available at: http://www.srneclab.cz/lectures/MC260P87/supp/lecture2a3.pdf [Accessed: 1 February 2021].

Gong, L.-L., Du, L.-D. and Du, G.-H., 2018. Theophylline. In: *Natural Small Molecule Drugs from Plants*. Springer, pp. 469–474.

Gottlieb, S. L., Giersing, B. K., Hickling, J., Jones, R., Deal, C., Kaslow, D. C. and Group, H.V.E.C., 2019. Meeting report: Initial World Health Organization consultation on herpes simplex virus (HSV) vaccine preferred product characteristics, March 2017. *Vaccine*, 37(50), pp. 7408–7418.

El Guerdaoui, A., El Kahoui, Y., Bourjila, M., Tijar, R. and El Gridani, A., 2014. Potential Energy Surface (PES) scan of gas-phase L-proline. *International Letters of Chemistry, Physics and Astronomy*, 19(1), pp. 26–34.

Günay, N., Pir, H.A.C.E.R., Avcı, D. and Atalay, Y., 2013. NLO and NBO analysis of sarcosine-maleic acid by using HF and B3LYP calculations. *Journal of Chemistry*.

Haleblian, J. and McCrone, W., 1969. Pharmaceutical applications of polymorphism. *Journal of pharmaceutical sciences*, 58(8), pp. 911–929.

Hall, C. L., Potticary, J., Sparkes, H.A., Pridmore, N.E. and Hall, S.R., 2018. Lamotrigine ethanol monosolvate. *Acta Crystallographica Section E: Crystallographic Communications*, 74(5), pp. 678–681.

Hänninen, V.,2012, *Introduction to Computational Chemistry, Lecture 5 Basis Functions* [Online]. Available at: http://users.df.uba.ar/dmitnik/estructura3/bases/biblio/Lecture5.pdf [Accessed: 1 February 2021].

Hasegawa, K., 2012. Introduction to single crystal X-ray analysis. *The Rigaku Journal*, 28(1), pp. 14–18.

Hasnip, P. J., Refson, K., Probert, M. I., Yates, J. R., Clark, S. J. and Pickard, C. J., 2014. Density functional theory in the solid state. *Philosophical Transactions of the Royal Society A: Mathematical, Physical and Engineering Sciences*, 372(2011), p. 20130270.

Herpesviruses, H., 2007. Biology, therapy, and immunoprophylaxis. *Eds Ann Arvin, Gabriella Campadelli-Fiume et al.-Cambridge: Cambridge University Press*, 1432, p. 986.

Holmes-Hampton, G. P., Tong, W.-H. and Rouault, T. A., 2014. Biochemical and biophysical methods for studying mitochondrial iron metabolism. *Methods in enzymology*, 547, pp. 275–307.

Hu, Y., Yin, J., Chaitanya, K. and Ju, X.H., 2016. Theoretical investigation on charge transfer properties of 1, 3, 5-tripyrrolebenzene (TPB) and its derivatives with electron-withdrawing substituents. *Croatica Chemica Acta*, 89(1), pp. 81–90.

Hübschle, C. B., Sheldrick, G. M. and Dittrich, B., 2011. ShelXle: a Qt graphical user interface for SHELXL. *Journal of applied crystallography*, 44(6), pp. 1281–1284.

Hunt, P., 2008, *Molecular Orbitals and Population Analysis* [Online]. Available at: http://www.huntresearchgroup.org.uk/teaching/teaching_comp_chem_year4/L7_bonding.pdf [Accessed: 1 February 2021].

Ibeji, C. U., Adegboyega, J., Okagu, O. D. and Adeleke, B. B., 2016. Nature of ground state of benzophenone and some of its substituted derivatives: experimental and DFT study. *Journal of Applied Sciences*, 16(11), pp. 504–516.

Infrared Spectroscopy Table, 2001, [Online]. Available at: https://www.chem.ucla.edu/~bacher/General/30BL/IR/ir.html [Accessed: 1 February 2021].

Islam, N. and Chimni, S. S., 2016. DFT investigation on nonlinear optical (NLO) properties of novel borazine derivatives. *Computational and Theoretical Chemistry*, 1086, pp. 58–66.

Jain, P. K., 2005. A DFT-based study of the low-energy electronic structures and properties of small gold clusters. *Structural Chemistry*, 16(4), pp. 421–426.

Jasmine, N. J., Muthiah, P. T., Arunagiri, C. and Subashini, A., 2015. Vibrational spectra (experimental and theoretical), molecular structure, natural bond orbital, HOMO--LUMO energy, Mulliken charge and thermodynamic analysis of N′-hydroxy-pyrimidine-2-carboximidamide by DFT approach. *Spectrochimica Acta Part A: Molecular and Biomolecular Spectroscopy*, 144, pp. 215–225.

Jawaher, K. R., Indirajith, R., Krishnan, S., Robert, R. and Das, S. J., 2018. Quantum chemical calculations of Cr_2O_3/SnO_2 using density functional theory method. *Pramana*, 90(3), pp. 1–6.

Jilani, T.N., Preuss, C.V. and Sharma, S., 2020, *Theophylline*, *StatPearls* [Online]. Available at: https://www.ncbi.nlm.nih.gov/books/NBK519024/ [Accessed: 1 February 2021].

Jiang, X. et *al.*, 2014. The role of dipole moment in determining the nonlinear optical behavior of materials: ab initio studies on quaternary molybdenum tellurite crystals. *Journal of Materials Chemistry C*, 2(3), pp. 530–537.

Joshi, B. D., 2016. Chemical reactivity, dipole moment and first hyperpolarizability of aristolochic acid I. *Journal of Institute of Science and Technology*, 21(1), pp. 1–9.

Kabouchi, B., Essassi, E.M., Sahdane, T., Boughrraf, H. and Benallal, R., 2017. Theoretical and experimental investigations of structural and electronic properties of 1-Benzyl-3-methyl-quinoxalin-2 (1H)-one molecule. Journal of Materials and Environmental Sciences, 8, pp.4657-4662.

Kakkar, S., Bhattacharya, B., Reddy, C. M. and Ghosh, S., 2018. Tuning mechanical behaviour by controlling the structure of a series of theophylline co-crystals. *CrystEngComm*, 20(8), pp. 1101–1109.

Kalaiarasi, N. and Manivarman, S., 2017. AB Initio (DFT) and Vibrational Studies of the Synthesized Heterocyclic Compound 2-6-oxo-2-thioxotetrahydropyrimidin-41h-ylidene Hydrazine Carbothioamide. *Journal of New Developments in Chemistry*, 1(2), p. 100.

Kanagathara, N., Marchewka, M. K., Drozd, M., Renganathan, N. G., Gunasekaran, S. and Anbalagan, G., 2013. FT-IR, FT-Raman spectra and DFT calculations of melaminium perchlorate monohydrate. *Spectrochimica Acta Part A: Molecular and Biomolecular Spectroscopy*, 112, pp. 343–350.

Karabacak, M., Cinar, Z., Kurt, M., Sudha, S. and Sundaraganesan, N., 2012. FT-IR, FT-Raman, NMR and UV--vis spectra, vibrational assignments and DFT calculations of 4-butyl benzoic acid. *Spectrochimica Acta Part A: Molecular and Biomolecular Spectroscopy*, 85(1), pp. 179–189.

Karki, D. B. and Adhikari, N. P., 2014. First-principles DFT study for the structural stability of Hydrogen passivated graphene (H-graphene) and atomic adsorption of oxygen on H-graphene with different schemes. *arXiv preprint arXiv:1404.6446*.

Karpinski, P. H., 2006. Polymorphism of active pharmaceutical ingredients. *Chemical Engineering & Technology: Industrial Chemistry-Plant Equipment-Process Engineering-Biotechnology*, 29(2), pp. 233–237.

Karthika, M., Senthilkumar, L. and Kanakaraju, R., 2012. Theoretical studies on hydrogen bonding in caffeine--theophylline complexes. *computational and theoretical chemistry*, 979, pp. 54–63.

Katti, D. R., Sharma, A. and Katti, K. S., 2017. Predictive methodologies for design of bone tissue engineering scaffolds. In: *Materials for bone disorders*. Elsevier, pp. 453–492.

Khan, A., 2021, *Hydrogen bonds in water* [Online]. Available at: https://www.khanacademy.org/science/biology/water-acids-and-bases/hydrogen-bonding-in-water/a/hydrogen-bonding-in-water [Accessed: 1 February 2021].

Kirste, B., 2016. Applications of density functional theory to theoretical organic chemistry. ChemSci J 7: 127.

Köse, M. E., 2001. *Electronic structure analysis and density functional study of an alternating donor/acceptor polymer*. PhD thesis, Bilkent University, Turkey.

Kumar, V., Kishor, S. and Ramaniah, L. M., 2013. First-principles DFT study of some acyclic nucleoside analogues (anti-herpes drugs). *Medicinal Chemistry Research*, 22(12), pp. 5990–6001.

KUMER, A., SARKER, M. N. and Sunanda, P., 2019. The theoretical investigation of HOMO, LUMO, thermophysical properties and QSAR study of some aromatic carboxylic acids using HyperChem programming. *International Journal of Chemistry and Technology*, 3(1), pp. 26–37.

Kurth, S., Marques, M. A. L. and Gross, E. K. U., 2003. Electronic structure: Density functional theory.

Lakshmi, C. S. N., Balachandran, S., Arul, D. D., Ronaldo, A. A. and Hubert, J. I., 2019. DFT analysis on spectral and NLO properties of (2E)-3-[4-(dimethylamino) phenyl]-1-(naphthalen-2-yl) prop-2-en-1-one; a d-π-A chalcone derivative and its docking studies as a potent hepatoprotective agent. *Chemical Data Collections*, 20, p. 100205.

Li, Y., 2012. *First principles calculations of the structure and electronic properties of pentacene based organic and zinc oxide based inorganic semiconducting materials*.Master thesis, Univeristy of North Texas, Texas.

LibreTexts, C., 2019, *3.4.1. Newman Projections* [Online]. Available at: https://chem.libretexts.org/Courses/Purdue/Purdue_Chem_26100%3A_Organic_Chemistry_I_(Wenthold)/Chapter_03%3A_Structure_of_Alkanes/3.4.%09Structure_and_Conformations_of_Alkanes/3.4.1._Newman_Projections [Accessed: 1 February 2021].

LibreTexts, C., 2020, *11.2: Gaussian Basis Sets* [Online]. Available at: https://chem.libretexts.org/Bookshelves/Physical_and_Theoretical_Chemistry_Textbook_Maps/Map%3A_Physical_Chemistry_(McQuarrie_and_Simon)/11%3A_Computational_Quantum_Chemistry/11.02%3A_Gaussian_Basis_Sets [Accessed: 1 February 2021].

LibreTexts, C, 2020, *Infrared Spectroscopy Absorption Table* [Online]. Available at:

https://chem.libretexts.org/Ancillary_Materials/Reference/Reference_Tables/Spectroscopic_Parameters/Infrared_Spectroscopy_Absorption_Table [Accessed: 1 February 2021].

Lin, M., 2020. *Experimental and Numerical Study of Polymorphism in Crystallization Processes*. PhD thesis, University of Western Ontario, Canada.

Lokhande, P. K. M., Patil, D. S., Kadam, M. M. and Sekar, N., 2019. Theoretical Investigation of Optical and Nonlinear Optical (NLO) Properties of 3-Azabenzanthrone Analogues: DFT and TD-DFT Approach. *ChemistrySelect*, 4(34), pp. 10033–10045.

Looker, K.J., Magaret, A.S., Turner, K.M., Vickerman, P., Gottlieb, S.L. and Newman, L. M., 2015. Global estimates of prevalent and incident herpes simplex virus type 2 infections in 2012. *PloS one*, 10(1), p. e114989.

Looker, K. J., Magaret, A. S., May, M. T., Turner, K. M., Vickerman, P., Gottlieb, S. L. and Newman, L. M., 2015. Global and regional estimates of prevalent and incident herpes simplex virus type 1 infections in 2012. *PloS one*, 10(10), p. e0140765.

Looker, K. J. *et al.*, 2017. First estimates of the global and regional incidence of neonatal herpes infection. *The Lancet Global Health*, 5(3), pp. e300-e309.

López-Campos, J. L., Tan, W. and Soriano, J. B., 2016. Global burden of COPD. *Respirology*, 21(1), pp. 14–23.

Lu, T. and Chen, F., 2012. Multiwfn: a multifunctional wavefunction analyzer. *Journal of computational chemistry*, 33(5), pp. 580–592.

Lutker, K. M., Quiñones, R., Xu, J., Ramamoorthy, A. and Matzger, A. J., 2011. Polymorphs and hydrates of acyclovir. *Journal of pharmaceutical sciences*, 100(3), pp. 949–963.

Maache, S., Bendjeddou, A., Abbaz, T., Gouasmia, A. and Villemin, D., 2016. Molecular structure, hyperpolarizability, NBO and Fukui function analysis of a serie of 1, 4, 3, 5-oxathiadiazepane-4, 4-dioxides derived of proline. *Der Pharmacia Lettre*, 8(11), pp. 27–37.

Marinescu, M., 2018. Synthesis and Nonlinear Optical Studies on Organic Compounds in Laser-Deposited Films. In: *Applied Surface Science*. IntechOpen.

Marques, M. P. M., Valero, R., Parker, S. F., Tomkinson, J. and Batista de Carvalho, L. A., 2013. Polymorphism in cisplatin anticancer drug. *The Journal of Physical Chemistry B*, 117(21), pp. 6421–6429.

Marta, R. A., Wu, R., Eldridge, K. R., Martens, J. K. and McMahon, T. B., 2010. Infrared vibrational spectra as a structural probe of gaseous ions formed

by caffeine and theophylline. *Physical Chemistry Chemical Physics*, 12(14), pp. 3431–3442.

Masuda, T., Yoshihashi, Y., Yonemochi, E., Fujii, K., Uekusa, H. and Terada, K., 2012. Cocrystallization and amorphization induced by drug--excipient interaction improves the physical properties of acyclovir. *International Journal of Pharmaceutics*, 422(1–2), pp. 160–169.

Meenatchi, V., Agilandeshwari, R. and Meenakshisundaram, S. P., 2015. Synthesis, structure, characterization and theoretical studies of NLO active furan-2-carbohydrazide monohydrate derivative single crystals. *RSC advances*, 5(87), pp. 71076–71087.

Meepripruk, M., Bumee, R., Somphon, W. and Toh, P., 2016. Crystal growth and physical characterization of acyclovir crystallized with ascorbic acid and zinc chloride. *J. Life Sci. Technol*, 4, pp. 56–59.

Mohammed, A. A. K., (2017). *Accurate Calculations of Nonlinear Optical Properties Using Finite Field Methods*. PhD thesis, McMaster University, Canada.

Montha, M., 2012. *Supramolecular structure of the herpes antiviral agent acyclovir and related compounds*. PhD thesis, Suranaree University of Technology, Thailand.

Murti, B. T., 2017. *Experimental and computational studies on sensing of DNA damage in Alzheimer's disease*. Master thesis, Durban University of Technology, South Africa.

N.Sudha *et al.*, 2020. DENSITY FUNCTIONAL THEORY ANALYSIS AND MOLECULAR DOCKING EVALUATION OF 8-CHLOROQUINOLINE 2-CARBALDEHYDE. *Journal of Computational Chemistry & Molecular Modeling*, 4(4), pp. 463–477.

Nabati, M. and Mahkam, M., 2016. DFT Study of the Six-Membered Heterocyclic SinN6-nHn (n= 0-6): Stability and Aromaticity. *Organic Chemistry Research*, 2(1), pp. 70–80.

Nagabalasubramanian, B. P., 2012, *Chapter-6 Vibrational Frequencies, Structural Conformation Stability and HOMO-LUMO Analysis of Nicotinic Acid Ethyl Ester with Experimental (FT-IR and FT-Raman) Techniques and Quantum Mechanical Calculations* [Online]. Available at: https://www.semanticscholar.org/paper/CHAPTER-—-6-VIBRATIONAL-FREQUENCIES-%2C-STRUCTURAL-OF/bb8290dab8e05f490bb27f8fb24d0ffefd7974c5?p2df [Accessed: 1 February 2021].

Nalla, A. and Chinnala, K. M., 2017. Solubility Enhancement of Acyclovir by Solid Dispersion Method. *International Journal of Pharmaceutical Research*, 9(1), pp. 45–50.

Narayan, V., 2012. *DFT Study of Small molecules Cluster*. PhD thesis, University of Lucknow, India.

Nogueira, B. A., Milani, A., Ildiz, G. O., Paixão, J. A., Castiglioni, C. and Fausto, R., 2020. Polymorphism in 1-methylhydantoin: investigation by periodic DFT calculations and characterization of the third polymorph. *CrystEngComm*, 22(38), pp. 6347–6359.

Novena, L. M., Kumar, S. S., Athimoolam, S., Saminathan, K. and Sridhar, B., 2017. Single crystal, vibrational and computational studies of Theophylline (a bronchodilator drug) and its chloride salt. *Journal of Molecular Structure*, 1133, pp. 294–306.

Novena, L. M., Kumar, S. S. and Athimoolam, S., 2016. Improved solubility and bioactivity of theophylline (a bronchodilator drug) through its new nitrate salt analysed by experimental and theoretical approaches. *Journal of Molecular Structure*, 1116, pp. 45–55.

NPRA, 2021, *Active Pharmaceutical Ingredient (API)*, *National Pharmaceutical Regulatory Agency (NPRA)* [Online]. Available at: https://www.npra.gov.my/my/active-pharmaceutical-ingredient-api-main-page [Accessed: 1 February 2021].

Nyakung'U, W. N., 2015. *DENSITY FUNCTIONAL THEORY STUDIES ON STRUCTURAL PROPERTIES AND ENERGIES OF ISONIAZID ANALOGUES*. PhD thesis, Kenyatta University, Kenya.

O'Connor, J. J. and Robertson, E. F., 2017. Erwin schrödinger and quantum wave mechanics. *Quanta*.

Orozco, M. and Luque, J. F., 1996, *Generalization of the Molecular Electrostatic Potential for the Study of Noncovalent interactions* [Online]. Available at: https://books.google.com.my/books?id=YPnmE1N-9i8C&pg=PA181&lpg=PA181&dq=molecular+electrostatic+potential&source=bl&ots=9jjNEPqAwZ&sig=ACfU3U15jCv1FISrdgEXWat6BhjQtvXl9A&hl=en&sa=X&ved=2ahUKEwiG7YDCwbHmAhXfILcAHRhQBYM4FBDoATADegQIChAB#v=onepage&q=molecula [Accessed: 1 February 2021].

Peica, N, 2006. Vibrational spectroscopy and density functional theory calculations on biological molecules. PhD thesis, University of Würzburg, Germany.

Pereira, D. H., Ducati, L. C., Rittner, R. and Custodio, R., 2014. A study of the rotational barriers for some organic compounds using the G3 and G3CEP theories. *Journal of molecular modeling*, 20(4), pp. 1–14.

Pinar, B. A., 2017, *Fundamentals and applications of X-ray diffraction. Applications in catalysts characterization* [Online]. Available at:

https://ethz.ch/content/dam/ethz/special-interest/chab/icb/van-bokhoven-group-dam/coursework/Characterization-Techniques/2018/XRD_lecture_AnaBPinar_2017_part_1.pdf [Accessed: 1 February 2021].

Politzer, P., Laurence, P. R. and Jayasuriya, K., 1985. Molecular electrostatic potentials: an effective tool for the elucidation of biochemical phenomena. *Environmental health perspectives*, 61, pp. 191–202.

Poole, C. L. and James, S. H., 2018. Antiviral therapies for herpesviruses: current agents and new directions. *Clinical therapeutics*, 40(8), pp. 1282–1298.

Prasad, S. and Ojha, D. P., 2018. Molecular Structure, Vibrational Spectroscopic, Electronic Properties and Chemical Stability of pn-Alkylbenzoic Acids (nBAC)—a Comparison Using DFT and HF Methods. *Energy [AU]*, 4(578.12871941), pp. 578–12871941.

Prasana, J. C., Muthu, S. and Abraham, C. S., 2019. Molecular docking studies, charge transfer excitation and wave function analyses (ESP, ELF, LOL) on valacyclovir: a potential antiviral drug. *Computational biology and chemistry*, 78, pp. 9–17.

Prasanthi, N. L., Sudhir, M., Jyothi, N. and Vajrapriya, V. S., 2016. A review on polymorphism perpetuates pharmaceuticals. *Am. J. Adv. Drug Deliv*, 4, pp. 58–63.

Priya, M. K., Revathi, B. K., Renuka, V., Sathya, S. and Asirvatham, P. S., 2019. Molecular structure, spectroscopic (FT-IR, FT-Raman, 13C and 1H NMR) analysis, HOMO-LUMO energies, Mulliken, MEP and thermal properties of new chalcone derivative by DFT calculation. *Materials Today: Proceedings*, 8, pp. 37–46.

Pumpo, D. A., 2016. *Hydrogen Bonded Structures and Polymorphism in Agrochemicals*. PhD thesis, University of Bath, United Kingdom.

Rahmani, R., Boukabcha, N., Chouaih, A., Hamzaoui, F. and Goumri-Said, S., 2018. On the molecular structure, vibrational spectra, HOMO-LUMO, molecular electrostatic potential, UV--Vis, first order hyperpolarizability, and thermodynamic investigations of 3-(4-chlorophenyl)-1-(1yridine-3-yl) prop-2-en-1-one by quantum chemistry calculat. *Journal of Molecular Structure*, 1155, pp. 484–495.

Raja, M. D., Arulmozhi, S. and Madhavan, J., 2014. UV-Vis, HOMO-LUMO and Hyperpolarizability of l-Phenylalanine, 1-Phenylalaninium Benzoic Acid. *International Journal of Scientific and Engineering Research*, 5, pp. 15–173.

Rajalakshmi, K. and Nayak, D., 2017. HOMO--LUMO Analysis of Dasatinib. *Int. J. Mater. Sci*, 12, pp. 32–37.

Ramya, T., Gunasekaran, S. and Ramkumaar, G. R., 2013. Density functional theory, restricted Hartree--Fock simulations and FTIR, FT-Raman and UV--Vis spectroscopic studies on lamotrigine. *Spectrochimica Acta Part A: Molecular and Biomolecular Spectroscopy*, 114, pp. 277–283.

Raza, K., Kumar, P., Ratan, S., Malik, R. and Arora, S., 2014. Polymorphism: The Phenomenon Affecting the Performance of Drugs. SOJ Pharm Pharm Sci, 1 (2), 10. *Polymorphism: The Phenomenon Affecting the Performance of Drugs*.

Reveles, J. U. and Köster, A. M., 2004. Geometry optimization in density functional methods. *Journal of computational chemistry*, 25(9), pp. 1109–1116.

Rocha, F. S., Gomes, A. J., Lunardi, C. N., Kaliaguine, S. and Patience, G. S., 2018. Experimental methods in chemical engineering: Ultraviolet visible spectroscopy—UV-Vis. *The Canadian Journal of Chemical Engineering*, 96(12), pp. 2512–2517.

Rodríguez-López, M. T., Nesterov, V. N. and Youngblood, W. J., 2016. Polymorphism and DFT calculations of 1, 4-bis (triisopropylsilyl) buta-1, 3-diyne. *Journal of Molecular Structure*, 1107, pp. 316–321.

Rosa, R. G. T., 2014, *The Hartree-Fock Method* [Online]. Available at: http://www.ifsc.usp.br/~strontium/Teaching/Material2014-1 SFI5774 Mecanicaquantica/Seminario - Ramon - O metodo de Hartree-Fock.pdf [Accessed: 1 February 2021].

RSC, R. S. of C., 2009, *Introduction to Ultraviolet-Visible Spectroscopy (UV) - Background Theory* [Online]. Available at: https://edu.rsc.org/download?ac=11391 [Accessed: 1 February 2021].

Sachdeva, R., Soni, A., Singh, V. P. and Saini, G. S. S., 2018. Reactivity of etoricoxib based on computational study of molecular orbitals, molecular electrostatic potential surface and Mulliken charge analysis. *AIP Conference Proceedings, May 2018.* AIP Publishing LLC, 1953(1), p. 140006.

Sainz-Díaz, C. I., Francisco-Márquez, M. and Vivier-Bunge, A., 2010. Molecular structure and spectroscopic properties of polyaromatic heterocycles by first principle calculations: spectroscopic shifts with the adsorption of thiophene on phyllosilicate surface. *Theoretical Chemistry Accounts*, 125(1), pp. 83–95.

Salihović, M. *et al.*, 2014. DFT study and biological activity of some methylxanthines. *Bull. Chem. Technol. Bosnia Herzeg*, 42, pp. 31–36.

Salvaggio, M. R. and Gnann Jr, J. W., 2017. Drugs for herpesvirus infections. In: *Infectious Diseases*. Elsevier, pp. 1309–1317.

Saranya, M., Ayyappan, S., Nithya, R., Sangeetha, R. K. and Gokila, A., 2018.

Molecular structure, NBO and HOMO-LUMO analysis of quercetin on single layer graphene by density functional theory. *Digest Journal of Nanomaterials and Biostructures*, 13(1), pp. 97–105.

Sarkar, A. and Rohani, S., 2015. Cocrystals of acyclovir with promising physicochemical properties. *Journal of pharmaceutical sciences*, 104(1), pp. 98–105.

Sarma, B. and Saikia, B, 2014. Hydrogen bond synthon competition in the stabilization of theophylline cocrystals. *CrystEngComm*, 16(22), pp. 4753–4765.

Sarojini, K., Krishnan, H., Kanakam, C. C. and Muthu, S., 2012. Synthesis, X-ray structural, characterization, NBO and HOMO--LUMO analysis using DFT study of 4-methyl-N-(naphthalene-1-yl) benzene sulfonamide. *Spectrochimica Acta Part A: Molecular and Biomolecular Spectroscopy*, 96, pp. 657–667.

Sasaki, T., Kambara, O., Sakamoto, T., Otsuka, M. and Nishizawa, J. I., 2016. Single crystal growth and polarization absorption spectroscopy of theophylline anhydrous for terahertz vibrational mode assignment. *Vibrational Spectroscopy*, 85, pp. 91–96.

Schlegel, H. B., 2011. Geometry optimization. *Wiley Interdisciplinary Reviews: Computational Molecular Science*, 1(5), pp. 790–809.

ScienceDaily, 2014, *Understanding active pharmaceutical ingredients*, *International Union of Crystallography* [Online]. Available at: https://www.sciencedaily.com/releases/2014/06/140605093305.htm [Accessed: 1 February 2021].

Selected Bond Energies and Bond Lengths, 2003, [Online]. Available at: https://pdf4pro.com/view/selected-bond-energies-and-bond-lengths-55eb06.html [Accessed: 1 February 2021].

Selsi, N. J. *et al.*, 2019. Computer-aided rational design of acyclovir analogs to inhibit purine nucleoside phosphorylase. *Pharmaceutical and Biomedical Research*, 5(2), pp. 38–48.

Sena, A. M. P., 2010. *Density functional theory studies of surface interactions and electron transfer in porphyrins and other molecules*. PhD thesis, University College London, United Kingdom.

Al Shaabani, Y. A., Kadhim, B. B. and Jasim, F. H., 2016. Structural and Electronic Properties of Theophylline-InP Diamantane Drug Carrier. *American Scientific Research Journal for Engineering, Technology, and Sciences (ASRJETS)*, 19(1), pp. 130–141.

Shamshina, J. L., Cojocaru, O. A., Kelley, S. P., Bica, K., Wallace, S. P., Gurau,

G. and Rogers, R. D., 2017. Acyclovir as an ionic liquid cation or anion can improve aqueous solubility. *Acs Omega*, 2(7), pp. 3483–3493.

Sharmi, K. J., 2015, *Chapter 6 – Quantum chemical studies on structural, vibrational, NBO and hyperpolarizability of N-(1, 1-Dimenthyl-2-hydroxyethyl)-3-amino-2-hydroxypropanesulfonic acid* [Online]. Available at: https://shodhganga.inflibnet.ac.in/bitstream/10603/130988/12/12_chapter 6.pdf [Accessed: 1 February 2021].

Sherrill, C. D., 2000. An introduction to Hartree-Fock molecular orbital theory. *School of Chemistry and Biochemistry Georgia Institute of Technology*.

Shoba, D., 2021, *Chapter – V NMR, UV-Vis, IR, Raman and NBO Analysis of Methylisonicotonate with Experimental and Quantum Mechanical Studies* [Online]. Available at: https://shodhganga.inflibnet.ac.in/bitstream/10603/133096/12/12_chapter 5.pdf [Accessed: 1 February 2021].

shodhganga, 2021, *Chapter 4, Vibrational, UV Spectra, NBO, First Order Hyperpolarizability and HOMO-LUMO Analysis of 3HCHMA* [Online]. Available at: https://shodhganga.inflibnet.ac.in/bitstream/10603/148477/13/13_chapter 4.pdf [Accessed: 1 February 2021].

Shukla, M. K. and Leszczynski, J., 2006. A density functional theory study on the effect of shape and size on the ionization potential and electron affinity of different carbon nanostructures. *Chemical physics letters*, 428(4–6), pp. 317–320.

Soderberg, T., 2019, *4.4: Ultraviolet and visible spectroscopy* [Online]. Available at: https://chem.libretexts.org/Under_Construction/Purgatory/Book%3A_Organic_Chemistry_with_a_Biological_Emphasis_(Soderberg)/Chapter_04%3A_Structure_Determination_I/4.4%3A_Ultraviolet_and_visible_spectroscopy [Accessed: 1 February 2021].

Soriano, J. B. *et al.*, 2017. Global, regional, and national deaths, prevalence, disability-adjusted life years, and years lived with disability for chronic obstructive pulmonary disease and asthma, 1990--2015: a systematic analysis for the Global Burden of Disease Study 2015. *The Lancet Respiratory Medicine*, 5(9), pp. 691–706.

Sridevi, C., 2012, *Chapter V- Investigation of Molecular Structure Vibrational, Electronic, NMR and NBO Analysis of 5-Chloro-1-mentyl-4-nitro-1H-imidazole (CMNI) using AB Initio HF and DFT Calculations* [Online]. Available at: https://shodhganga.inflibnet.ac.in/bitstream/10603/23333/12/12_chapter 5.pdf [Accessed: 1 February 2021].

Sridhar, B. and Ravikumar, K., 2009. Lamotrigine, an antiepileptic drug, and its

chloride and nitrate salts. *Acta Crystallographica Section C: Crystal Structure Communications*, 65(9), pp. o460--o464.

Stone, K., 2020, *What Is an Active Pharmaceutical Ingredient (API)?* [Online]. Available at: https://www.verywellhealth.com/api-active-pharmaceutical-ingredient-2663020 [Accessed: 1 February 2021].

Studying Chemical Reactions with Gaussian, 2021, [Online]. Available at: http://www.jamberoo.org/gaussian/ts/index.html [Accessed: 1 February 2021].

Subhapriya, P., 2014, *Chapter 7 – Physicochemical Analysis of Reactants and Mesogens* [Online]. Available at: https://shodhganga.inflibnet.ac.in/bitstream/10603/49437/12/12_chapter 7.pdf [Accessed: 1 February 2021].

Suma, K. V. and Aruldhas, D., 2019, *Density Functional Theory and Non Linear Optical Activity Study On Ethyl (2E)-2-Cyano-3-(1H-Indol-3-Yl) Acrylate and Its Water-Complexes* [Online]. Available at: http://www.ijstr.org/final-print/oct2019/Density-Functional-Theory-And-Non-Linear-Optical-Activity-Study-On-Ethyl-2e-2-cyano-3-1h-indol-3-yl-Acrylate-And-Its-Water-complexes.pdf [Accessed: 1 February 2021].

Sun, C., Zhou, D., Grant, D. J. and Young Jr, V. G., 2002. Theophylline monohydrate. *Acta Crystallographica Section E: Structure Reports Online*, 58(4), pp. o368--o370.

Suna, P., Hota, P. and Misra, P. K., 2016. Experimental and theoretical studies on the structure, electronic and vibrational spectra of o/p-hydroxybenzylidene-o/p-toluidines. NISCAIR-CSIR, India, pp. 1192-1201.

Sundaraganesan, N., Meganathan, C., Anand, B., Joshua, B. D. and Lapouge, C., 2007. Vibrational spectra and assignments of 2-amino-5-iodopyridine by ab initio Hartree--Fock and density functional methods. *Spectrochimica Acta Part A: Molecular and Biomolecular Spectroscopy*, 67(3–4), pp. 830–836.

Susithra, G., Ramalingam, S., Periandy, S. and Aarthi, R., 2018. Molecular structure investigation towards pharmacodynamic activity and QSAR analysis on hypoxanthine using experimental and computational tools. *Egyptian Journal of Basic and Applied Sciences*, 5(4), pp. 313–326.

Sutor, D. J.,1958. The structures of the pyrimidines and purines. VI. The crystal structure of theophylline. *Acta Crystallographica*, 11(2), pp. 83–87.

Suwińska, K., Golankiewicz, B. and Zielenkiewicz, W., 2001. Water molecules in the crystal structure of tricyclic acyclovir. *Acta Crystallographica*

Section C: Crystal Structure Communications, 57(6), pp. 767–769.

Svensson, F., 2015. *Computational Methods in Medicinal Chemistry: Mechanistic Investigations and Virtual Screening Development*. Acta Universitatis Upsaliensis, Sweden.

Tandon, H., Chakraborty, T. and Suhag, V., 2019. A Brief Review on Importance of DFT In Drug Design. *studies*, 39, p. 46.

Tapre, A. R., 2013. *Studies on enzymatic clarification of advanced maturity stages banana pulp*. PhD thesis, Sardar Patel University, India.

Targema, M., Obi-Egbedi, N. O. and Adeoye, M. D., 2013. Molecular structure and solvent effects on the dipole moments and polarizabilities of some aniline derivatives. *Computational and Theoretical Chemistry*, 1012, pp. 47–53.

Tariq, A., Nazir, S., Arshad, A. W., Nawaz, F., Ayub, K. and Iqbal, J., 2019. DFT study of the therapeutic potential of phosphorene as a new drug-delivery system to treat cancer. *RSC advances*, 9(42), pp. 24325–24332.

Terada, K., Kurobe, H., Ito, M., Yoshihashi, Y., Yonemochi, E., Fujii, K. and Uekusa, H., 2013. Polymorphic and pseudomorphic transformation behavior of acyclovir based on thermodynamics and crystallography. *Journal of thermal analysis and calorimetry*, 113(3), pp. 1261–1267.

Thanthiriwatte, K. S. and De Silva, K. M. N., 2002. Non-linear optical properties of novel fluorenyl derivatives-ab initio quantum chemical calculations. *Journal of Molecular Structure: THEOCHEM*, 617(1–3), pp. 169–175.

Tribak, Z., Skalli, M. K. and Senhaji, O., 2019. DFT, Quantum Chemical Study and Biological Effects of a Heterocyclic Molecular. *J Biotech Biores*, 1.

Tu, G., 2008. *Studies of self-interaction corrections in density functional theory*. PhD thesis, KTH.

Ul-Haq, Z., 2016, *Introduction to Geometry Optimization* [Online]. Available at: https://th.fhi-berlin.mpg.de/sitesub/meetings/dft-workshop-2016/uploads/Meeting/May_6_Qasmi.pdf [Accessed: 1 February 2021].

Umar, Y. and Tijani, J.,2015. Density functional theory study of the rotational barriers, conformational preference, and vibrational spectra of 2-formylfuran and 3-formylfuran. *Journal of Structural Chemistry*, 56(7), pp. 1305–1312.

Valverde, C., Ribeiro, Í. N., Soares, J. V. B., Baseia, B. and Osório, F. A., 2019. Prediction of the linear and nonlinear optical properties of a schiff base derivatives via DFT. *Advances in Condensed Matter Physics*, 2019.

Varghese, A. L., Abraham, I. and George, M., 2019. DFT studies on nonlinear optical properties of N-[(Naphthalen-5-yl) methyl]-4-Nitrobenzamine.

Materials Today: Proceedings, 9, pp. 92–96.

Vidhya, V., Austine, A. and Arivazhagan, M., 2019. Quantum chemical determination of molecular geometries and spectral investigation of 4-ethoxy-2, 3-difluoro benzamide. *Heliyon*, 5(11), p. e02365.

Wang, Q., Xue, J., Wang, Y., Jin, S., Zhang, Q. and Du, Y., 2018. Investigation into tautomeric polymorphism of 2-thiobarbituric acid using experimental vibrational spectroscopy combined with DFT theoretical simulation. *Spectrochimica Acta Part A: Molecular and Biomolecular Spectroscopy*, 204, pp. 99–104.

WHO, W. H. O., 2020, *Herpes simplex virus* [Online]. Available at: https://www.who.int/news-room/fact-sheets/detail/herpes-simplex-virus [Accessed: 1 February 2021].

Wilhelm Conrad Röntgen- Biographical, 2021, *The Nobel Prize* [Online]. Available at: https://www.nobelprize.org/prizes/physics/1901/rontgen/biographical/ [Accessed: 1 February 2021].

Wired Chemist, 2021, *Common Bond Energies (D)* [Online]. Available at: http://www.wiredchemist.com/chemistry/data/bond_energies_lengths.html [Accessed: 1 February 2021].

World, C., 2007, *The shape shifters* [Online]. Available at: https://www.rsc.org/images/Shape shifters_tcm18-83943.pdf [Accessed: 1 February 2021].

Yan, Y., Chen, J.-M. and Lu, T.-B., 2013. Simultaneously enhancing the solubility and permeability of acyclovir by crystal engineering approach. *CrystEngComm*, 15(33), pp. 6457–6460.

Yin, Z., 2009. *Microscopic mechanisms of magnetism and superconductivity studied from first principle calculations*. PhD thesis, University of California, Davis.

Zaini, M. F., Razak, I. A., Khairul, W. M. and Arshad, S., 2018. Crystal structure and optical spectroscopic analyses of (E)-3-(1H-indol-2-yl)-1-(4-nitrophenyl) prop-2-en-1-one hemihydrate. *Acta Crystallographica Section E: Crystallographic Communications*, 74(11), pp. 1589–1594.

Zaitu, S., Miwa, Y. and Taga, T., 1995. A 2: 1 molecular complex of theophylline and 5-fluorouracil as the monohydrate. *Acta Crystallographica Section C: Crystal Structure Communications*, 51(9), pp. 1857–1859.

Zhang, S. and Fischer, A., 2011. A monoclinic polymorph of theophylline. *Acta Crystallographica Section E: Structure Reports Online*, 67(12), pp. o3357--o3357.

Zhou, D., 2007. An Introduction of Density Functional Theory and its Application. *Physics. Drexel. Edu*.

Zobel, J. P., 2018. *Ultrafast intersystem crossing dynamics in organic molecules*. PhD thesis, University of Vienna, Austria.